Observations of aerosol and liquid-water clouds with Dual-Field-of-View Polarization Lidar

A ground-based view on aerosol-cloud interactions

Von der Fakultät für Physik und Geowissenschaften
der Universität Leipzig
genemigte

Dissertation

zur Erlangung des akademischen Grades

Doctor rerum naturalium
Dr. rer. nat.

vorgelegt

von Diplom – Physikingenieur Cristofer Andrés Jiménez Jiménez
geboren am 10. September 1988 in Bulnes, Chile

Gutachter: Prof. Dr. Andreas Macke
Prof. Dr. Henrique Barbosa

Tag der Verleihung 20 September 2021

Bibliographic Description:

Jiménez Jiménez, Cristofer Andrés
Observations of aerosol and liquid-water clouds with Dual-Field-of-View Polarization Lidar – A ground-based view on aerosol-cloud interactions
University of Leipzig, Dissertation
182 Pages, 228 References, 30 Figures, 2 Tables (excluding the cumulative part)

Abstract: Aerosol-cloud interactions (ACI) are a big challenge to quantify the overall effect of human activities on the radiative, heat, and precipitation budgets of the atmosphere. New observational capabilities are demanded. To study the influence of aerosol particles on cloud microphysics an analysis scheme composed of newly-developed arrays is introduced. The retrieval of microphysical properties of liquid-water clouds and of the aerosol particles below the clouds from lidar observations, in a practical and replicable way, is the major challenge tackled in this work.

A lidar-based approach to derive liquid-water cloud microphysical properties from dual-field-of-view (DFOV) depolarization measurements is introduced. In addition, a new method to accurately obtain the aerosol properties below cloud layers is developed and implemented into the analysis infrastructure. Comparisons with alternative observational and modeling approaches corroborate the accuracy of both methods. The number concentration of cloud condensation nuclei (CCN) is derived from the aerosol particle extinction coefficient below the cloud, and in combination with the cloud-microphysics retrieval, they provide an aerosol-cloud scene, which allow us to study ACI. Long-term observations at the pristine location of Punta Arenas (PA), Chile, and at the polluted site of Dushanbe (DB), Tajikistan, are analyzed for this purpose. On average, similar values of cloud droplet and below-cloud CCN number concentrations, in the range of 10–150 cm^{-3}, are observed at PA. At DB, larger cloud droplet number concentrations are observed, in the order of 200–400 cm^{-3}, but much larger CCN concentrations of about 700–900 cm^{-3} are found.

The so-called ACI index ($E_{aci}^{N_d}$) is assessed from the collected data sets. The most robust estimate of $E_{aci}^{N_d}$ is obtained when calculating monthly averages over the whole measurement periods, fourteen months at PA and seven months at DB. $E_{aci}^{N_d}$ values of 0.83 ± 0.20 and 0.57 ± 0.26 are derived at PA and DB, respectively. These ACI indexes combined with satellite-based reanalysis data MERRA-2, such as the cloud albedo and cloud fraction, were used to estimate the anthropogenic radiative forcing because of to the Twomey effect, finding a radiative cooling from -0.70 to -0.17 Wm^{-2} for PA and between -1.89 and -0.66 Wm^{-2} for DB. These cooling values are slightly larger than the regional values found in the literature for the analyzed locations, although they are within the range of globally means reported during last two decades. Furthermore, the results obtained at PA show the relevance of updraft movements to trigger ACI. When considering only updraft-dominated periods, $E_{aci}^{N_d}$ is up to 50% larger than when no wind information is considered.

The new capabilities illuminated during this work may provide a big help for estimations of the cloud-mediated radiative effect and may provide a baseline to confront models dealing

with cloud microphysics in future studies.

Bibliografische Beschreibung:

Jiménez Jiménez, Cristofer Andrés
Beobachtung von Aerosolen und Flüssigwasserwolken mit Dual-Field-of-View-Polarisations-Lidar – Eine bodengebundene Ansicht der Aerosol-Wolken-Wechselwirkungen
Universität Leipzig, Dissertation
182 Seiten, 228 Literaturzitate, 30 Abbildungen, 2 Tabellen (exklusive des kumulativen Teils)

Referat:
Die Erforschung des Gesamteffektes menschlicher Aktivitäten auf den Strahlungs-, Wärme- und Niederschlagshaushalt der Atmosphäre ist eine große Herausforderung, insbesondere hinsichtlich einer genauen Berücksichtigung von Aerosol-Wolken-Wechselwirkungen (ACI). Neben einer verbesserten Modellierung, sind neue Beobachtungstechniken notwendig. Um den Einfluss von Aerosolpartikeln auf die Wolkenmikrophysik von Flüssigwasserwolken zu untersuchen, wird eine neue Lidar-Mess- und Analysemethodik eingeführt. Das neue Konzept besteht aus der gleichzeitigen Lidar-Beobachtung von Aerosoleigenschaften wenige 100 Meter unterhalb der sich bildenden Wolken und von wolkenmikrophysikalischen Eigenschaften, knapp 100 m oberhalb der Wolkenbasis, und das mit hoher zeitlicher Auflösung in einer praktischen und reproduzierbaren Weise. Dieses anspruchsvolle Konzept wird in der Arbeit vorgestellt.

Zunächst wird ein neues Lidar-Verfahren zur Ermittlung der mikrophysikalischen Eigenschaften von Flüssigwasserwolken aus sogenannten Dual-Field-of-View-Polarizations-Lidarmessungen (DFOV-Lidar) vorgestellt. Darüber hinaus wird eine neue Methode zur genauen Bestimmung der Aerosoleigenschaften unterhalb der Wolkenschichten entwickelt und in die Analyseinfrastruktur implementiert. Vergleiche mit alternativen Techniken bestätigen die Genauigkeit beider Methoden. Die Anzahlkonzentration von Wolkenkondensationskernen (CCN) wird aus dem Partikelextinktionskoeffizienten unterhalb der Wolke ermittelt (abgeschätzt). Zeitreihen der CCN-Konzentration in Kombination mit den gemessenen wolkenmikrophysikalischen Eigenschaften, z.B. Wolkenextinktionkoeffizient, effektiver Radius oder Wolkentropfenanzahlkonzentrationen (CDN-Konzentrationen), ermöglichen dann ACI zu untersuchen. Zur Demonstration der Nützlichkeit des neuen Verfahrens werden Langzeitbeobachtungen mit einem DFOV-Lidar in Punta Arenas, in Südchile, in äußerst sauberer Luft, Langzeitbeobachtungen mit einem weiteren DFOV-Lidar an einem hochverschmutzten und staubigen Standort in Zentralasien (Duschanbe, Tadschikistan) gegenübergestellt. Im Durchschnitt werden in Punta Arenas ähnliche Werte für CDN und CCN-Konzentrationen gemessen, und zwar im niedrigen Konzentrationsbereich von 10–150 cm^{-3}. In Dushanbe werden wie erwartet viel größere CDN-Konzentrationen beobachtet, etwa 200–400 cm^{-3}. Die abgeschätzte CCN-Konzentration (für eine Wasserdampfübersättigung von 0.2%) lieg dabei bei 700–900 cm^{-3}.

Der sogenannte ACI-Index ($E_{\mathrm{aci}}^{N_{\mathrm{d}}}$, relative Änderung der CDN-Konzentration N_{d} mit der

CCN-Konzentration) wird aus den gesammelten Datensätzen abgeschätzt. Der robusteste Wert von $E_{\mathrm{aci}}^{N_{\mathrm{d}}}$ gibt sich bei der Berechnung von Monatsmittelwerten über die gesamten Messperioden. Für Punta Arenas und Dushanbe wurden $E_{\mathrm{aci}}^{N_{\mathrm{d}}}$-Werte von 0.83 ± 0.20 bzw. 0.57 ± 0.26 gefunden, die zur Abschätzung des Strahlungsantriebs durch den Twomey-Effekt verwendet werden. Eine Strahlungskühlung von -0.70 bis -0.17 Wm^{-2} wird für Punta Arenas und zwischen -1.89 und -0.66 Wm^{-2} für Dushanbe gefunden. Diese Ergebnisse stimmen mit globalen Schätzungen des wolken-bezogenen, direkten Aerosoleffekts überein, sind aber etwas größer als die Werte, die üblicherweise an den betrachteten Standorten gefunden werden. Darüber hinaus zeigen die in Punta Arenas erhaltenen Ergebnisse die Bedeutung von Aufwindbereichen in der ACI-Berechnungen auf. Wenn nur Wolkenmessungen während der (mit einem Doppler-Lidar) gemessenen Aufwindbereiche berücksichtigt werden, ist $E_{\mathrm{aci}}^{N_{\mathrm{d}}}$ um bis zu 50% größer als in dem Fall ohne Berücksichtigung von aufwärts und abwärts gerichteten Vertikalwinden. Nur während der Aufwindphase können Aerosolpartikel durch die Wolkenbasis in die Wolke eindringen und die mikrophysikalischen Wolkeneigenschaften beeinflussen.

Die neuen Möglichkeiten, die in dieser Arbeit beleuchtet wurden, leisten einen Beitrag zu einer detaillierteren und realtitätsnäheren Berücksichtigung von Aerosoleffekten in der Wolkenmodellierung und können somit zu einer verbesserten Abschätzung des direkten Strahlungseffekts durch Wolken beitragen.

Table of Contents

Chapter 1

Introduction

The climate system is changing significantly. Since the second part of the 20th century the planet has been getting warmer, and despite the fact that the debate in politics and social media remains vigorous, among scientists there is a clear consensus: This is extremely likely due to the increment of human-made emissions since the massive industrialization started in the 18th century, and the consequent effects on the environment will be devastating for human and natural systems, making global warming a big threat for life on Earth [IPCC, 2014]. Climate change is not only an environmental issue but an ethical one. Those who are least responsible will suffer the gravest consequences, while most of wealthier nations, with a much larger historical contribution, expect less grave consequences and will likely be more prepared, culturally, economically, and technologically, for adaptation. Attention has to be devoted towards this issue, called climate injustice.

Climate change needs to be faced urgently. Actions need to be performed opportunely, carefully and efficiently, meaning that major efforts need to be undertaken from governments to people now and in the near future. With the goal of keeping global temperature rise below 2 K, the Paris Agreement constitutes one of the biggest political and economical commitments in history [Glanemann et al., 2020]. But to achieve such a milestone, a close cooperation among nations is required, and it is key that the decision process in the next years (and decades) goes side by side with the current best scientific knowledge of the climate system in all its aspects. The fateful future-climate scenario is encouraging scientists to study the atmosphere, the surface, the oceans, and their interactions for a better understanding from the physical, chemical, and biological point of view. Two atmospheric protagonists in climate are aerosol and clouds, whose complexity make it difficult for scientists to predict key information about future climate, such as temperature and precipitation changes in the next decades. This knowledge, with the best precision as possible, is crucial to plan the future in terms of climate actions.

Atmospheric clouds are vital for life on Earth. They cool the planet, transport heat and moisture, and distribute water over the surface in the form of precipitation. They cover perpetually about two thirds of the planet, interact with solar short-wave and terrestrial thermal radiation, and thus play a major role in the energy balance [Lohmann et al., 2016].

Clouds are important components in understanding climate change and therefore must be accurately represented in large-scale weather and climate models so that we can make realistic future-climate predictions [Simpson et al., 2014]. However, a tricky aspect of clouds is their close relation with aerosol particles, which provide the nucleation site for the formation of droplets and ice crystals.

Atmospheric aerosol particles, by serving as cloud condensation nuclei (CCN) or ice-nucleating particles (INP) and by interacting with incoming solar and outgoing terrestrial radiation, are of major relevance for the energy balance and the water cycle of the planet. Aerosol has always been present in the atmosphere. Before the industrialization, most aerosol in the atmosphere originated from natural sources. At the present time, and since the industrialization period, a considerable amount of aerosol comes from anthropogenic sources, affecting the radiative budget of the total atmosphere, as far as we know, in opposite manner and with similar magnitude as the emissions of CO_2 [Myhre et al., 1998, 2013]. Nowadays, the amount of anthropogenic aerosol varies from one quarter to two thirds of the total aerosol amount in the atmosphere [Boucher et al., 2013], and its relevance besides climate is wide, e.g., long-range-transported aerosol is important for fertilizing land and oceans [Jickells et al., 2005; Carslaw et al., 2010], at high concentrations particles affect visibility, which can be an issue in aviation [Moses and Akinyemi, 2017], and fine particles can be detrimental for human's respiratory system, positioning aerosol emissions as a health problem in highly polluted areas [Braga et al., 2001; WHO, 1999]. For this reason, anthropogenic aerosol emission will tend to decrease in the next decades, a factor to keep in mind when studying the role of aerosol in the climate system.

Aerosol effects on climate were mentioned in the first report of the Intergovernmental Panel on Climate Change (IPCC) in the early nineteen-nineties, but the knowledge at that time was inadequate to estimate their magnitude or even sign. Since then, the number of aerosol-caused climate effects considered and the estimates of their cumulative magnitude have grown steadily [Andreae et al., 2005]. At present, the best estimate of the global and annual mean anthropogenic radiative forcing between 1750 and 2011, due to aerosol-radiation interactions (ARI), varies from -0.85 to $+0.15$ Wm^{-2} and due to aerosol-cloud interactions from -1.9 to -0.1 Wm^{-2}. The latter effect exhibits the largest uncertainty among all forcing precursors, making cloud-related aerosol effects the major source of uncertainty in our knowledge of the anthropogenic climate forcing [Myhre et al., 2013; Boucher et al., 2013].

This uncertainty and our incomplete knowledge about cloud microphysical processes [Grabowski et al., 2019; Morrison et al., 2020] leave the question to what extent clouds and aerosol will be affected by temperature changes unsolved, keeping aerosol and clouds as a great source of poorly understood feedback mechanisms that make future-climate predictions rather unconfident [Dufresne and Bony, 2008]. Do we live in a world with weak aerosol cooling and thus low climate sensitivity, in which case future-climate change may be expected to be relatively benign? Or do we live in a highly forced, highly sensitive world with a very uncertain and worrying future that may bring a much faster temperature rise than how is generally predicted? [Andreae et al., 2005] These are questions that cannot be categorically answered yet. The demand of knowledge about aerosol-cloud interactions and of ways to

reduce the large uncertainties is the main motivation of this thesis.

Despite the large uncertainties, current estimations suggest that today anthropogenic aerosol emissions cool the planet [Myhre et al., 2013]. For this reason, aerosol particles gain further attention as they may be key for the conception of actions to counteract the greenhouse-gas-induced warming. For this purpose, so-called geoengineering schemes aim to deliberately intervene in the Earth's climate system at the large scale, and this is nowadays one of the most rapidly growing areas of climate research as a potential option for tackling global warming. Geoengineering (or climate engineering) represents an alternative way to solve the climate problem, not by mitigation, but by altering the radiative budget of the planet either by removing carbon dioxide or by manipulating solar radiation fluxes [Cao et al., 2015]. Some of the ideas to manipulate solar radiation are 1) to inject aerosol particles in the stratosphere to scatter more sunlight [Robock et al., 2009], 2) to inject aerosol particles in the higher troposphere to reduce cirrus cloudiness [Mitchell et al., 2009; Storelvmo and Herger, 2014; Penner et al., 2015; Gasparini and Lohmann, 2016], or 3) to inject sea spray in the marine boundary layer to increment cloud reflectivity [Latham, 1990; Latham et al., 2008; Cooper et al., 2013; Salter et al., 2008; Jenkins and Forster, 2013a,b; Alterskjaer et al., 2012]. These possibilities evaluated in academia and politics would have the most significant physical potential to contribute notably towards achieving the 1.5 or 2 K temperature goal of the Paris Agreement over the next few decades [Lawrence et al., 2018].

These possible actions involving aerosol usage are highly controversial, mainly because of the mistrust evoked by the idea of messing around with climate, given the fact that human activities started the warming in the first place. *Such schemes aim to deal with the symptoms over the causes* [Kiehl, 2006]. Nevertheless, there is agreement that the window of opportunity to avoid breaching the Paris climate target of staying well below 2 K warming is narrowing sharply, and initiatives to study and develop geoengineering technologies are gaining traction as a potential last resort [Pearce, 2019]. However, the employment of geoengineering methods may carry various side effects and unexpected consequences in the environment that may result in a climate much less suitable for human life than without these measures [Korhonen et al., 2010]. Before large-scale implementation of any geoengineering scheme, we need to fully explore and evaluate the associated mechanisms, impacts, and risks of climate engineering [Cao et al., 2015]. If we want to make progress in this direction, a robust understanding of aerosol-cloud interactions (ACI) is inevitable.

There is no doubt that CCN and INP influence cloud microstructure, precipitation-forming processes [Guichard and Couvreux, 2017; Morrison et al., 2020], and the meteorological and radiative responses of clouds and the atmosphere [Wild et al., 2013; Matus and L'Ecuyer, 2017]. These effects impact both the atmospheric circulation systems and the thermodynamic and radiative energy budgets over a cascade of scales from local to global [Rosenfeld et al., 2014b]. Global models cannot resolve clouds at all but rather use cloud parameterizations. Incorporating the cloud-aerosol processes accurately in such cloud parameterization schemes is rather challenging, and despite decades of research, cloud microphysics, precipitation and aerosol interactions remain as a weak point in all models regardless of the resolution [Boucher et al., 2013]. To make progress, models must be able to handle all nat-

ural and man-made aerosol types from the emission over regional and long-range transport to deposition and the interaction of the different aerosol types with clouds. Until we reach a good representation of aerosol properties, aerosol vertical layering, and the complex interactions of aerosol in the climate system in numerical models, the predictions of actionable scientific scenarios will remain uncertain [Schwartz et al., 2014].

Progress cannot be made without observations to confront models. Strong efforts of continuous, long-term observations of aerosol, clouds, and meteorological conditions (especially of the vertical-wind fields) by means of active remote sensing with Doppler cloud radar, aerosol-cloud lidar, and Doppler wind lidars around the globe are required to obtain a significantly improved understanding of the physical processes of aerosol-cloud interaction. Droplet formation, the evolution of the liquid and ice phases, the development of precipitation, and the impact of organized vertical motions, turbulence, and entrainment processes must be covered by observations [Schmidt et al., 2015].

Liquid-cloud processes are of particular interest because of their not yet fully determined susceptibility to atmospheric dynamics [Silver et al., 2020] and atmospheric aerosol particles that act as CCN [Mülmenstädt and Feingold, 2018]. In warm liquid clouds, the droplet number concentration (N_d) is of central interest for the understanding of cloud physics and for quantifying the effective radiative forcing via aerosol-cloud interactions. The best known interaction is the change of N_d due to changes in the concentration of aerosol particles acting as CCN within a cloud. The albedo of a cloud is dependent on N_d [Twomey, 1977] as it is the cloud lifetime [Albrecht, 1989]. To simultaneously observe clouds and aerosol is known to be a difficult task, even more complicated is to attribute changes in cloud radiative effects to aerosol particles, because one must exclude, or at least account for, other meteorological and surface factors contributing to the observed differences in cloud properties [Rosenfeld et al., 2014b]. Different observational approaches have been used to quantify this interaction, but a wide spread of results exists in the literature [Block, 2018; Schmidt et al., 2015].

Long-term collocated observations of micro- and macro-physical properties of aerosol and clouds and their surrounding environment at well-equipped sites are needed. Such observations would provide an important resource for quantifying the response of clouds to aerosol and for validating parameterizations of these processes in models [Grosvenor et al., 2018]. One emerging opportunity to fulfil the observational demand is the lidar technique, as such instruments can continuously measure both aerosol and clouds with high vertical and temporal resolution. In this context, the ground-based remote-sensing group of the Leibniz Institute for Tropospheric Research (TROPOS) has performed pioneering research by developing the Dual-Field-of-View (DFOV) Raman technique during the past two decades [Wandinger, 1998; Schmidt et al., 2013].

The technique allows the retrieval of aerosol particle extinction coefficients close to the base of liquid-water cloud layers and of cloud microphysical properties such as cloud droplet effective radius and cloud droplet number concentration in the lower part of the cloud layer. In this way, the most direct impact of aerosol particles on cloud microphysical properties could be assessed, and new insights into the dependency of aerosol-cloud interaction on vertical wind were possible by adding a Doppler lidar into the analysis [Schmidt et al., 2014,

2015]. However, the method is only applicable during nighttime and signal averaging of the order of 10–30 minutes is required to reduce the impact of signal noise on the observations to a tolerable level. Therefore, cloud properties cannot be resolved at scales of 100–300 m horizontal resolution or 10–60 s. The difficulty to measure strong Raman signals hampers the replicability of this approach. A high-power laser and a large telescope are needed. This is an important point, since ground-based networks to provide a quasi-global coverage will be essential to adequately constrain global modeling of the aerosol indirect effect [Lohmann et al, 2007]. Robust and easy-to-implement methods need to be developed. The present PhD thesis is motivated by the results from Schmidt et al. [2013, 2014, 2015], and one of the goals is to improve the DFOV measurement concept towards daytime observations and shorter signal averaging times (towards time scales allowing us to resolve single updrafts and downdrafts).

The major outcome of this thesis is the development of a new lidar-based technique to observe microphysical properties of liquid-water clouds by means of a DFOV polarization lidar [Jimenez et al., 2017, 2018, 2019, 2020a,b]. The methodology is based on the multiple-scattering effect on depolarization measurements, which is strongly dependent on cloud microphysical properties. The new technique can be applied during day and night with temporal resolution of a few seconds. Such resolution enables us to separate the data set into individual updraft and downdraft periods, allowing the assessment of the so-called aerosol-cloud-interaction index in great detail. The new method requires only minor instrumental upgrades, i.e., one extra measurement channel in a standard polarization lidar. It could therefore be implemented, after extensive tests, in three autonomous systems of Polly type (POrtabLe Lidar sYstem) [Engelmann et al., 2016] deployed by TROPOS at different locations. The long-term data sets gathered in this way further demonstrate the potential of the new approach to evaluate aerosol-cloud interactions under various environmental conditions.

The content of the thesis is distributed as follows. In Chapter 2, a description of the state-of-the-art knowledge on aerosol-cloud interactions is given, and the research questions are outlined. Chapter 3 provides an overview of lidar methodologies to assess aerosol-cloud interaction in warm clouds. The steps followed during this thesis and the array of developments are described here. Chapter 4 presents the three articles published in response to the research questions. Chapter 5 discusses the potential of the new technique and further applications in the long term. Finally, Chapter 6 presents the summary and conclusions of the work.

Chapter 2

Aerosol, clouds and their interaction - State of the art and research questions

As mentioned in the Introduction, human activities influence the aerosol burden in the atmosphere, affecting climate to an uncertain extent. This chapter is intended to summarize our current knowledge about aerosol, clouds, and the processes involved in their interaction, with emphasis on the observational aspects that need attention to improve our predictions about future climate. The end of the chapter illuminates in which concrete direction the thesis is tuned and what are the research questions to be addressed in the cumulative part.

2.1 Aerosol and clouds

A useful quantity to study the impact of individual agents on climate, such as aerosol, is the radiative forcing (RF): a temporary imbalance between the energy received from the sun and the energy radiated back to space [Myhre et al., 2013]. The RF induced by aerosol via absorption and scattering of radiation has been commonly known as direct effect. A subsequent effect exerted by highly absorbing aerosols is that they warm the ambience of clouds, thus affecting atmospheric heating rates. This effect can enhance evaporation and reduce cloudiness [Hansen et al., 1997; Ackerman et al., 2000b]. If absorbing aerosol is present above clouds, the heating may strengthen the temperature inversion and reduce the entrainment of dry air at the cloud top, which leads to enhanced cloudiness [Johnson et al., 2004]. These changes in cloud properties also affect precipitation formation processes, which in turn feed back to the cloud dynamic properties in highly nonlinear ways [Rosenfeld et al., 2014b]. This heating-related forcing, known as semi-direct effect, and the direct effect are nowadays combined into the term of aerosol-radiation interactions, and to date the best estimate of the related RF between 1750 and 2011 is -0.35 [-0.85, 0.15] Wm^{-2} [Myhre et al., 2013].

This large range of values reflects the difficulty to estimate aerosol effects globally, given

their strong variations in space and time, physicochemical properties, and the challenging task of separating natural and human-made emissions [Ramachandran et al., 2012; Carslaw et al., 2013]. Despite the large error, according to the last IPCC report [Myhre et al., 2013; Boucher et al., 2013], the radiation-mediated radiative effect stands as a problem with high level of understanding, which is an improvement since the previous report, with a rather medium-low level of understanding [Forster et al., 2007].

With much larger magnitude and uncertainty, cloud-mediated aerosol effects are thought to contribute with an RF of -0.9 Wm^{-2}, with an error bar from -1.9 to -0.1 Wm^{-2}, i.e., they are the most uncertain among all contributions considered in the IPCC report [Boucher et al., 2013]. The large error bar comes from our incomplete knowledge about how clouds evolve at given aerosol and meteorological conditions.

2.1.1 Aerosol effect on liquid-water clouds

Warm clouds cover on average one third of the planet, representing about half of all clouds [Lohmann et al., 2016]. Those clouds are mostly formed in the planetary boundary layer (PBL) and are thought to be the primary mediator of aerosol radiative forcing via ACI [Heyn et al., 2020]. Low clouds have a strong cooling effect by reflecting much of the incoming solar energy back to space, whereas high, semitransparent clouds have a net warming effect by shielding the upwelling thermal emission from escaping to space [Rosenfeld et al., 2014b].

Most impacts on warm clouds are realized via changes in droplet number concentration. Clouds formed in an ambience with large CCN concentration, e.g., in a polluted area, have more and smaller droplets than clouds with the same amount of water in a pristine environment. More droplets increase the overall droplet surface area and hence the cloud optical thickness, which in turn enhances the cloud albedo. More reflective clouds, due to increased CCN concentrations, allow less radiation to reach the ground and therefore lead to a radiative cooling of the surface. This effect, known as Twomey effect [Twomey, 1959, 1977] (or cloud-albedo effect), is well known to manifest in ship tracks [Chen et al., 2012], but this specific case contributes only with a RF of about -0.0005 Wm^{-2} [Schreier et al., 2007; Boucher et al., 2013], while recent estimations based on polarimetric satellite observations attribute a global anthropogenic RF of about -1.1 Wm^{-2} to the Twomey effect [Hasekamp et al., 2019]. The magnitude of this effect is related to the amount of available aerosol particles that act as CCN and on their ability to allow activation.

An increased number of CCN, and hence N_d, reduces the mean droplet size. Smaller droplets reduce the collision efficiency and thus suppress precipitation, because less droplets can reach drizzle sizes, which increases the liquid-water content and extends the lifetime of the cloud [Albrecht, 1989; Rosenfeld, 1999]. The suppression of drizzle leads initially to higher cloud cover and hence to a cooling. Drizzle has however a stabilization function for the boundary layer, as a result of a heating of the cloud, when water vapor condenses, and a cooling of the sub-cloud region where drizzle droplets evaporate. This effect inhibits vertical mixing, a critical process for the maintenance of marine stratocumulus clouds [Albrecht, 1989]. Furthermore, smaller droplets evaporate faster, which increases entrainment and

causes further evaporation and thus reduces the vertical extent and ultimately the lifetime of the cloud, in this way counteracting the Twomey effect [Lohmann et al., 2016]. Besides the decreased effective radius, an increased cloud droplet number can also carry a broader size spectrum, which leads to an increased coalescence efficiency and reduces the lifetime of the cloud [Wang et al., 2020].

Another aspect to be considered is that, if the air above the boundary layer is dry, the enhanced cloud-top cooling and the associated enhanced cloud-top entrainment in polluted clouds causes faster evaporation of cloud droplets. This effect leads again to a reduced liquid-water content of polluted clouds compared with clean clouds [Ackerman et al., 2004].

Depending on cloud type, meteorological conditions, dynamics, and feedback mechanisms, the evaporation of liquid water may become a primary effect counteracting precipitation suppression [Stevens et al., 1998; Lu and Seinfeld, 2005; Small et al., 2009]. In conclusion, there is a web of mechanisms that shape the microphysical structure of clouds, which need to be better understood and quantified. Some evidence suggests that aerosol effects often occur such that a perturbation of the system in one direction creates a compensating effect in another. According to Stevens and Feingold [2009], despite decades of research, establishing climatically meaningful relationships between aerosol, clouds, and precipitation has proved to be frustratingly difficult. Furthermore, the existence and importance of a lifetime effect has been questioned in modeling studies that found statistically similar lifetimes of polluted and clean clouds [Ackerman et al., 2004; Jiang et al., 2006]. The extent of aerosol effects on cloud albedo and lifetime of liquid-water clouds is still an open question, and the effects on cold clouds remain even more complicated as discussed in the following.

2.1.2 Aerosol effect on ice-containing clouds

A further aerosol effect in the case of convective clouds is that smaller droplets take longer to freeze, i.e., doing it at higher altitudes above cloud base compared to pristine clouds. When the latent heat is released higher up in the atmosphere, updrafts can be enhanced, thus affecting cloud-top height and temperature. This so-called thermodynamic effect can potentially lead to an increased warming cloud greenhouse effect [Quaas et al., 2009; Koren et al., 2005].

Higher in the atmosphere, at lower temperatures, aerosol influences cold-cloud microphysics and dynamics. As aerosol particles facilitate the formation of ice via multiple possible ways such as immersion, condensation, deposition, or contact freezing, they can affect the composition and radiative properties of ice-containing clouds [Lohmann, 2017] and can sensitively impact the tropospheric water cycle by altering the precipitation budget [Mülmenstädt et al., 2015]. Increased INP concentrations can result in the rapid glaciation of supercooled liquid water due to the Wegener-Bergeron-Findeisen process [Findeisen, 1938], due to which ice grows at expenses of liquid droplets in an environment subsaturated for liquid water but supersaturated for ice. When INPs have soluble coatings, ice does not form by deposition but via immersion freezing. Because immersion freezing occurs at lower temperatures than deposition (or contact) freezing, more droplets will remain supercooled, which reduces

precipitation efficiency and makes clouds more reflective (deactivation effect) [Hoose et al., 2008]. Whether the glaciation or deactivation mechanism dominates, how large they are, and hence to what degree these effects contribute to the radiative forcing of aerosol is still a matter of debate [Lohmann et al., 2016; Boucher et al., 2013; Schwartz et al., 2014; Fan et al., 2016; Ansmann et al., 2019].

2.1.3 Cloud processes

Liquid-cloud properties are not only influenced by ACI but by a number of other processes as well, which complicates the identification and quantification of aerosol-cloud relationships. Cloud processes are manifold and complex, and part of the complexity arises during the aerosol activation process, which determines the number of droplets nucleated. Additional complexity results from mixing processes, which evaporate droplets and release aerosol [Abdul-Razzak et al., 1998], and also from collision and coalescence, which initiate precipitation formation.

Prediction of cloud droplet number concentration N_d is essential to large-scale weather and climate modeling. In warm clouds N_d is determined firstly by activation mostly taking place at cloud base. Nucleated particles must undergo significant condensational growth while avoiding coagulational scavenging [Westervelt et al., 2014]. How many droplets effectively activate depends on the number concentration, size distribution, and physico-chemical properties of the aerosol as well as on ambient conditions such as the maximum supersaturation of the system. Updrafts, usually generated from turbulence, convection, or gravity waves [Quaas et al., 2020], are key in this process, as upwelling motions yield a supersaturated ambience, enabling the activation of new droplets. This process can be sufficiently well described by the Köhler theory [Köhler, 1936], when thermodynamic equilibrium can be assumed for the air parcel. Regarding the aerosol particles serving as CCN, recent studies have found that aerosol composition, which determines aerosol solubility, is of minor relevance for the efficiency of particles acting as CCN, whereas the particle size is a more decisive factor for the activation efficiency [Dusek et al., 2006; Gong et al., 2020]. Too small particles may not reach the critical size to activate. Giant particles may consume the available water vapor too fast, reducing the maximum supersaturation that can be reached. In both cases low concentrations of droplets are the result [Ghan et al., 1998].

Other processes that determine the number concentration N_d are the evaporation due to lateral and cloud-top entrainment (e.g., in downdrafts), losses due to coalescence, and wet removal via collection by precipitation [Grosvenor et al., 2018].

2.1.4 Modeling droplet number concentration N_d

Proper representation of the formation and evolution of cloud and precipitation particles is key for numerical cloud modeling [Grabowski et al., 2019]. To simulate clouds, models need to solve the dynamic equations of motion of the air that forms the clouds, the thermodynamic processes that energize the cloud, and the microphysical processes of aerosol nucleation into cloud droplets, their coalescence into raindrops, the nucleation of ice in the cloud, and

the development of cloud ice and precipitation. Aerosol conditions can have very different impacts at different scales, because primary effects that can be observed at the individual cloud scale can be either buffered or amplified by system response and adjustments at larger scales. The assessment must hence be performed at several scales ranging from the individual cloud element (few kilometers and tens of minutes), through the scale of the cloud lifecycle (tens to few hundred kilometers and few to 24 h), to regional (few hundred to thousands of kilometers and few days) and global extent at climate time scales [Rosenfeld et al., 2014b].

Cloud parcel calculations are too costly to be applied in large-scale global models. Hence, aerosol activation has to be parameterized [Simpson et al., 2014]. Several formulations exist that diagnose N_d as a function of updraft speed and parameters describing the aerosol particle size distribution and chemical composition [Abdul-Razzak et al., 1998; Barahona and Nenes, 2007]. However, despite such schemes can produce similar results at a given framework, important questions such as the representation of vertical wind at cloud scale and the accuracy of the available activation schemes used in climate models remain unanswered [Donner et al., 2016]. Activation schemes need more testing against observations under real environmental conditions and with observed updrafts, aerosol composition, and size distributions. Closure experiments are required, in which predictions of N_d, from CCN number concentration and updraft measurements, must be evaluated with independent measurements of N_d [e.g., Snider et al., 2003; Conant et al., 2006]. Cloud-resolving models dealing with the whole web of processes that shape cloud microphysics, besides droplet activation, need confrontation with observations as well [Grabowski et al., 2019; Morrison et al., 2020]. Closure studies need to be performed at strategic locations with given aerosol and ambient conditions, e.g., for comparing pristine marine against polluted continental conditions [Grosvenor et al., 2018].

2.2 Aerosol radiative effect via ACI in liquid-water clouds

The overall aerosol effect on clouds is reflected in the planetary albedo (A), whose perturbation induces a radiative forcing at the top of the atmosphere F_aci [Gryspeerdt et al., 2017]:

$$F_\mathrm{aci} = -F^{\downarrow}\mathrm{d}A, \tag{2.1}$$

where $F^{\downarrow}$ denotes the down-welling shortwave radiation, which remains relatively constant over time over the globe, but varies seasonally in the hemispheres.

Given the variety of pathways, a practical strategy to address cloud-mediated aerosol effects is to separate the total forcing into the instantaneous effect, i.e., the Twomey effect characterized by N_d changes, and into adjustments, which consider the net forcing due to further effects of an increased droplet number concentration on cloud processes. Those adjustments are manifested in changes in the liquid-water path (L_w) and in the cloud fraction (f_c) [Goren and Rosenfeld, 2014].

A can be decomposed into a clear- (A_clr) and cloudy-sky part (A_c), each contributing

according to the cloud fraction f_c:

$$A = (1 - f_c)A_{clr} + f_c A_c. \tag{2.2}$$

Eq. (2.2) can be differentiated with respect to the perturbation, which is the change in CCN concentration (N_{CCN}). Considering that aerosol may affect N_d, L_w, and f_c, dA takes firstly the form [Ghan et al., 2016]:

$$\mathrm{d}A = \left(\frac{\partial A}{\partial f_c} \frac{\partial f_c}{\partial_{\ln} N_{CCN}} + f_c \frac{\partial A_c}{\partial_{\ln} N_{CCN}} \right) \Delta \ln N_{CCN}. \tag{2.3}$$

Here, the notation $\partial_{\ln} N_{CCN} \equiv \partial \ln N_{CCN}$ was introduced, and the effect of aerosol on clear-sky albedo (due to ARI) has been omitted. From Eq. (2.2), it follows that $\frac{\partial A}{\partial f} = A_c - A_{clr}$. Given the dependency between cloud albedo and optical depth, which depends on N_d and L_w [Ackerman et al., 2000a; Quaas et al., 2008], the second term in Eq. (2.3) can be approximated as:

$$\begin{aligned} \frac{\partial A_c}{\partial_{\ln} N_{CCN}} &= \left(\frac{\partial A_c}{\partial_{\ln} N_d} \frac{\partial_{\ln} N_d}{\partial_{\ln} N_{CCN}} + \frac{\partial A_c}{\partial_{\ln} L_w} \frac{\partial_{\ln} L_w}{\partial_{\ln} N_{CCN}} \right) \\ &\approx \frac{A_c(1 - A_c)}{3} \left(\frac{\partial_{\ln} N_d}{\partial_{\ln} N_{CCN}} + \frac{5}{2} \frac{\partial_{\ln} L_w}{\partial_{\ln} N_{CCN}} \right). \end{aligned} \tag{2.4}$$

Finally, we get:

$$\mathrm{d}A = \left[(A_c - A_{clr}) \frac{\partial f_c}{\partial_{\ln} N_{CCN}} + \frac{f_c A_c (1 - A_c)}{3} \left(\frac{\partial_{\ln} N_d}{\partial_{\ln} N_{CCN}} + \frac{5}{2} \frac{\partial_{\ln} L_w}{\partial_{\ln} N_{CCN}} \right) \right] \Delta \ln N_{CCN}. \tag{2.5}$$

A_c, A_{clr}, and f_c are parameters that can be obtained, e.g., from passive satellite multi-spectral observations. The partial derivatives and the variation between preindustrial and present-day aerosol conditions ($\Delta \ln N_{CCN}$) are however the main obstacles to evaluate Eq. (2.5). The best known is the term $\frac{\partial_{\ln} N_d}{\partial_{\ln} N_{CCN}}$ bonded to the Twomey effect, which takes positive values in most of the observational studies reported [Schmidt et al., 2015]. The combined effect of aerosol on cloud fraction f_c and on liquid-water path L_w is likely small compared to the Twomey effect, as there is no clear consensus whether they are positive or negative.

For the quantification of F_{aci}, a profound understanding of ACI and the ACI-involved processes is needed. Observations are essential to achieve this task. Long-term data sets to account for regional, seasonal, and inter-annual variations of the various ACI are required.

2.2.1 Aerosol-cloud-interaction index E_{aci}^X

To evaluate the cloud response to aerosol using observations, proxies have been commonly used to describe aerosol burden as well as cloud properties. Among the aerosol proxies being used are the aerosol extinction coefficient [Feingold et al., 2003; Schmidt et al., 2014, 2015], the aerosol optical depth (AOD) [Kaufman and Fraser, 1997], the light scattering coefficient

[Kim et al., 2003], aerosol particle number concentration [Lu et al., 2008; Painemal and Zuidema, 2013], the so-called aerosol index (optical thickness multiplied by the Ångström exponent), and the CCN number concentration [McComiskey et al., 2009].

As for the cloud, the properties considered to evaluate the Twomey effect can be the cloud extinction coefficient α, the droplet effective radius R_e, or the droplet number concentration N_d. The so-called efficiency index (E^X_aci), or ACI index, or cloud susceptibility, with $X = \alpha$, R_e, or N_d, can be estimated by applying a log-log regression to collocated data [Feingold et al., 2003; McComiskey and Feingold, 2008; Schmidt et al., 2015]. Using the number concentration N_d as proxy for the cloud and the CCN concentration N_CCN for aerosol, the index is defined as

$$E^{N_\mathrm{d}}_\mathrm{aci} = \frac{\partial_{\ln} N_\mathrm{d}}{\partial_{\ln} N_\mathrm{CCN}}. \tag{2.6}$$

At constant water path, and because $\alpha \propto N_\mathrm{d}^{1/3}$ and $R_\mathrm{e} \propto N_\mathrm{d}^{-1/3}$, it can be easily shown that

$$E^{R_\mathrm{e}}_\mathrm{aci} = E^{\alpha}_\mathrm{aci} = \frac{1}{3} E^{N_\mathrm{d}}_\mathrm{aci}. \tag{2.7}$$

Here, the $E^{R_\mathrm{e}}_\mathrm{aci}$ index is defined as the negative derivative so that it also takes positive values. Regardless which cloud proxy is used, the E^X_aci values obtained can be converted into a common index (e.g., $E^{N_\mathrm{d}}_\mathrm{aci}$).

A similar index can be defined for the adjustments in Eq. (2.5), i.e., the first and third partial derivatives can be written as

$$E^{f}_\mathrm{aci} = \frac{\partial f_\mathrm{c}}{\partial_{\ln} N_\mathrm{CCN}} \tag{2.8}$$

and

$$E^{L_\mathrm{w}}_\mathrm{aci} = \frac{\partial_{\ln} L_\mathrm{w}}{\partial_{\ln} N_\mathrm{CCN}}. \tag{2.9}$$

The difficulty to estimate the indexes in Eqs. (2.6), (2.8) and (2.9) lies mainly in the hard task of measuring the aerosol-cloud relationships independently of other influences. $E^{N_\mathrm{d}}_\mathrm{aci}$ can be assessed directly from measurements of N_CCN and N_d under the right environmental conditions, e.g., when updraft motions dominate. However, cloud fraction and liquid-water path are influenced by many environmental conditions such as the relative humidity (RH), which obscure the aerosol-cloud relationships. A useful quantity to assess these relationships is the droplet number concentration N_d, which can be used as a mediating variable to account for the confounding influence of the relative humidity [Gryspeerdt et al., 2016, 2019]. For this reason N_d has become a fundamental quantity for assessing the cloud-mediated aerosol radiative effect.

$$\mathrm{d}A = \left[(A_\mathrm{c} - A_\mathrm{clr}) \frac{\partial f_\mathrm{c}}{\partial_{\ln} N_\mathrm{d}} + \frac{f_\mathrm{c} A_\mathrm{c} (1 - A_\mathrm{c})}{3} \left(1 + \frac{5}{2} \frac{\partial_{\ln} L_\mathrm{w}}{\partial_{\ln} N_\mathrm{d}} \right) \right] \frac{\partial_{\ln} N_\mathrm{d}}{\partial_{\ln} N_\mathrm{CCN}} \Delta \ln N_\mathrm{CCN}. \tag{2.10}$$

All mentioned proxies can be obtained with spaceborne sensors, but questions about the accuracy remain open, especially in the case of the cloud droplet number concentration and the aerosol properties, which mainly interact at the cloud base. In the next section, an overview of current approaches to estimate $E^{N_\mathrm{d}}_\mathrm{aci}$ is given.

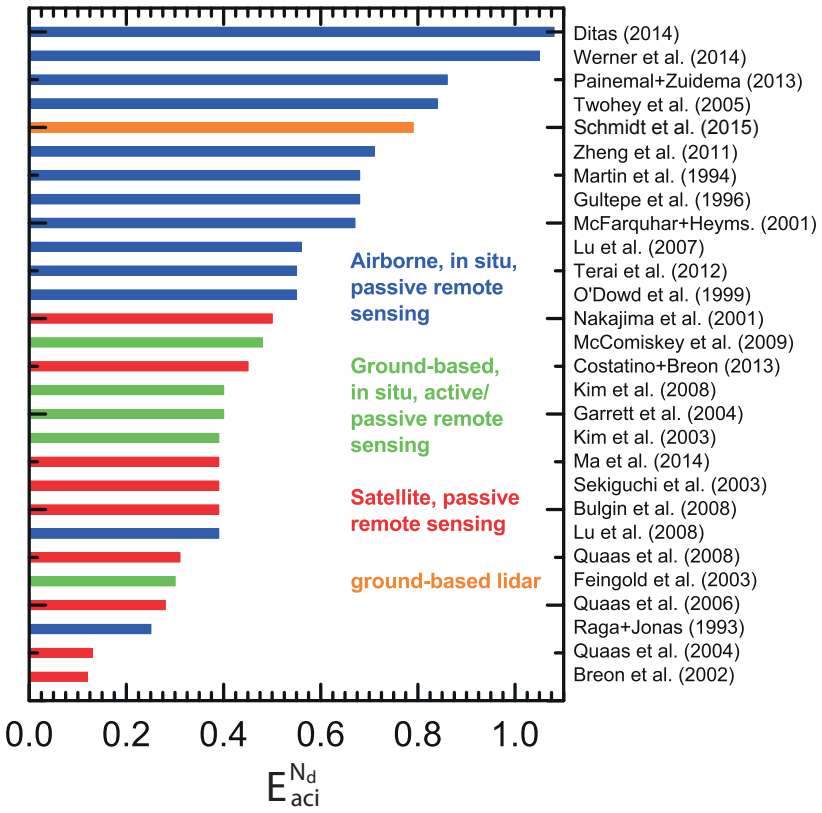

Figure 2.1: Values of $E_{\mathrm{aci}}^{\mathrm{N_d}}$ collected by Schmidt et al. [2015]. Different methods (in-situ measurements, remote sensing) and observational platforms (aircraft, satellite, ground based) are sketched. The orange bar shows the results obtained by Schmidt et al. [2015].

2.2.2 Observational approaches for $E_{\mathrm{aci}}^{N_\mathrm{d}}$

The cloud-albedo effect was first described by Twomey [1959]. Twomey [1977] roughly estimated that a 10% increase in CCN leads to an increase of 2.5% in optical thickness, i.e., $E_{\mathrm{aci}}^{R_\mathrm{e}} = 0.25$ or $E_{\mathrm{aci}}^{N_\mathrm{d}} = 0.75$. Since then, multiple studies have attempted to assess this index resulting in a spread of values, but with clear differences between the different techniques employed. In Figure 2.1, a summary of $E_{\mathrm{aci}}^{N_\mathrm{d}}$ values provided by Schmidt et al. [2015] is presented. Values obtained with satellite-based approaches lie in the lower part of the physically-possible range, while airborne in-situ approaches are found on the top of the range (close to one).

Spaceborne observations

On a global perspective, satellite observations are the most attractive to assess E_{aci}^{X} [Quaas et al., 2004, 2006, 2008], with $X = \{N_\mathrm{d}, R_\mathrm{e}, f, \text{or } L_\mathrm{w}\}$. Satellite platforms deliver global, horizontally distributed, long-term data sets. These capabilities added to the fact that they

observe cloud properties from above, the same perspective as relevant for the cloud albedo, suits spaceborne platforms as a profitable tool to evaluate the Twomey effect. However, there are systematic issues that satellite retrievals have to deal with. Firstly, the distinction between cloudy and cloud-free regions is problematic and may hamper the distinction between aerosol and cloud. This problem is especially severe for thin clouds with a low optical thickness [Schmidt, 2014]. Secondly, aerosol and cloud properties cannot be derived in the same grid point of observation, as clouds prevent the detection of aerosols below the cloud. Therefore, aerosol properties have to be derived in neighboring grid points, which do not necessarily correlate to the cloud in the same way as the region below the cloud. The joint and entangled occurrence of ACI, bonded to updraft movements, is also a major obstacle, and the fact that information on the height of the aerosol and cloud layers is not available can contribute to the usage of decoupled data.

In the case of satellite remote sensing, with horizontal resolutions of kilometers so that updraft and downdraft regions cannot be resolved, $E_{\mathrm{aci}}^{N_{\mathrm{d}}}$ must be generally interpreted with care. Even if the horizontal resolution would be high (a few 100 m) in satellite retrievals, the fact that most cloud information is related to cloud-top areas and that vertical wind observations directly below the cloud are not available will generally prohibit an accurate determination of $E_{\mathrm{aci}}^{N_{\mathrm{d}}}$ from space, limiting the results to the lower part of the physically-possible range, i.e., between 0.1 and 0.4 [e.g., Quaas et al., 2004, 2006, 2008; Nakajima et al., 2001; Kim et al., 2003; Sekiguchi et al., 2003]. Costantino et al. [2013] showed that by including vertical information of the aerosol burden obtained with space lidar, the coupled cases can be better isolated, which improves the estimates of E_{aci}^{X}. Additionally, Hasekamp et al. [2019] used estimates of the so-called aerosol index, instead of the aerosol optical thickness, and obtained values of $E_{\mathrm{aci}}^{N_{\mathrm{d}}}$ betwen 0.55 and 0.66, which shows that there is room for improvements.

Satellite-derived statistical relationships yield a global annual mean radiative forcing due to the cloud-albedo effect of about -0.2 Wm^{-2} [Quaas et al., 2008], which is much smaller than the values based on models. Combination of satellite products with models yields an anthropogenic aerosol forcing of -1.2 ± 0.4 Wm^{-2} [Quaas et al., 2009], which is in moderate agreement with current estimates based on model results only [Myhre et al., 2013]. However, models carry large uncertainties inherent to assumptions and parameterizations used to characterize the emissions and transport of aerosol, and also to represent the physical processes involving aerosol such as cloud and precipitation formation and their interaction with radiation [Stevens et al., 1998]. We still need to be cautious with these estimates. McComiskey and Feingold [2012] performed calculations of the radiative effect of aerosol by varying the $E_{\mathrm{aci}}^{N_{\mathrm{d}}}$ values over nearly the entire range (from about 0.03 to 0.85). They found values from -0.2 to -3.9 Wm^{-2}. This huge range of radiative forcing confirms the need of more accurate and appropriate assessments of E_{aci}^{X}.

Airborne in-situ observations

In contrast to satellite retrievals, approaches based on airborne in-situ measurements have provided the largest $E_{\mathrm{aci}}^{N_{\mathrm{d}}}$ values (close to 1) [McFarquhar et al., 2001; Painemal and Zuidema, 2013; Zheng et al., 2011] and values even larger than 1 have been reported [Werner et al., 2014]. The capability of performing detailed measurements of aerosol as well as cloud microphysical and radiative properties with high resolution makes airborne platforms suitable for studying cloud susceptibility to aerosol, with potential focus on cloud processes [Schmidt, 2014]. Not only the particle number concentration can be measured, but also valuable additional information such as the CCN concentration at several supersaturation levels and the chemical composition of the particles can be included in the analysis, as done by Lu et al. [2008], who considered the meteorological situation (wind, relative humidity, dewpoint temperature) as well.

As shown by Shinozuka et al. [2015], when using the optical properties of aerosol, a maximum value of about 0.75 can be obtained for $E_{\mathrm{aci}}^{N_{\mathrm{d}}}$, because the extinction depends on the size and the number concentration of particles (which can act as CCN). However, the number concentration of particles larger than 50 nm (size at which particles can reach their critical size and activate) can in most of the cases be parametrized as proportional to $(\alpha_{\mathrm{par}})^{\chi}$, with the aerosol extinction coefficient α and a conversion parameter χ that depends on the aerosol type and size distribution [Mamouri and Ansmann, 2016]. Practically, the exponent $\chi < 1$ imposes a limit to the maximum $E_{\mathrm{aci}}^{N_{\mathrm{d}}}$ that one can get using the extinction coefficient as proxy instead of N_{CCN}. The corresponding efficiency index in terms of the extinction coefficient can be derived as follows:

$$E_{\mathrm{aci}}^{N_{\mathrm{d}},\alpha_{\mathrm{par}}} = \frac{\partial_{\ln} N_{\mathrm{d}}}{\partial_{\ln} \alpha_{\mathrm{par}}} = \chi E_{\mathrm{aci}}^{N_{\mathrm{d}}}. \tag{2.11}$$

The variety of properties provided from such approaches, by combining airborne with ground-based observations, can help us to evaluate the impact of the aerosol proxy chosen on E_{aci}^{X}, such as the extinction coefficient (or optical depth) and CCN concentration. However, airborne in-situ field campaigns are usually restricted to a short time periods, which limits the statistical value of the assembled data set. Furthermore, the costs of such campaigns limit such assessments in different contrasting locations and in the long term.

2.2.3 Strategies to evaluate $E_{\mathrm{aci}}^{N_{\mathrm{d}}}$ from observations

The spread of the reported values of $E_{\mathrm{aci}}^{N_{\mathrm{d}}}$ reflects first of all the use of different technical approaches and methods (different combinations of in-situ measurements, active remote sensing, and passive remote sensing). Secondly, differences in cloud evolution over the oceans and over continental sites may have also contributed to the large range of values found. Different conditions regarding aerosol types and mixtures and the strong contrast in the occurrence frequency, strength, and duration (temporal length) of up- and down-draft features over oceanic and continental sites are important factors in this respect. Orographic aspects, the pronounced diurnal cycle of the planetary boundary layer, and heterogeneous heating of the

ground have also to be taken into account when studying cloud formation and evolution over land [Schmidt et al., 2015].

As we learned from Schmidt [2014], to keep track of a clear scientific question, it is reasonable to distinguish the achievable goals of the various approaches. The spatial and temporal resolution as well as the observed quantities will define the usage of the cloud susceptibility E_{aci}^{X}. The Twomey effect originates mainly from the upward transport of cloud parcels that were affected by ACI at the cloud base. During the transport, the cloud parcels are exposed to a number of other cloud processes (as explained in Sect. 2.1.3), which diminish the overall influence of aerosol particles on the cloud.

Satellite-derived relationships, based on an integrated view of aerosol and clouds, provide a picture on the net resultant cloud radiative effect. To improve our knowledge regarding cloud processes, aerosol-cloud relationships have to be derived considering only the cloud base region, where most of the activation occurs.

Furthermore, as shown by Reutter et al. [2009], it is meaningful to define aerosol- and updraft-limited regimes of cloud droplet formation. In the case of an aerosol-limited regime, updrafts are strong, water-vapor supersaturation is usually >0.5%, and the cloud droplet number concentration is directly proportional to the aerosol particle number concentration, so that $E_{\mathrm{aci}}^{N_{\mathrm{d}}}$ is high (and close to 1). In the case of an updraft-limited regime, updraft strength is low, water-vapor supersaturation is usually <0.2%, and the respective $E_{\mathrm{aci}}^{N_{\mathrm{d}}}$ values may be as low as 0.2–0.5.

To significantly contribute to the field of ACI research, a large number of observations are required to produce statistically significant constraints on subgrid-scale cloud parameterizations used in weather and climate models, from which many are developed on the basis of a few cases studies. Strong efforts of continuous, long-term observations of aerosol, clouds, and meteorological conditions (especially of the vertical-wind fields) around the globe by means of active remote sensing at well equipped supersites are required to obtain a significantly improved understanding of the physical processes of ACI. Droplet formation, the evolution of the ice phase, the development of precipitation, and the impact of organized vertical motions, turbulence, and entrainment processes must be covered by observations [Schmidt et al., 2015]. Only active-remote-sensing instruments can provide an integral picture of the vertical structure of aerosol and clouds, and the works of Feingold et al. [2003], Kim et al. [2003], and McComiskey et al. [2009] are pioneering in this area. These ground-based studies combined aerosol data measured at the surface or at low heights with mostly column-integrated cloud properties, which were retrieved from radiometer observations or from combined cloud radar and radiometer observations. Those approaches have found $E_{\mathrm{aci}}^{N_{\mathrm{d}}}$ values between 0.3 and 0.5. A more recent study has found values between 0.25 and 0.72, with the largest values obtained for low liquid-water paths (between 20–50 gm^{-2}) [Zheng et al., 2019]. The lower values found for larger L_{w} suggest a diminished cloud microphysical response to aerosol loading, presumably due to enhanced condensational growth processes and enlarged particle sizes.

2.2.4 ACI studies based on lidar

To improve the assessment of $E_{\mathrm{aci}}^{N_{\mathrm{d}}}$, new experimental (profiling) methods need to be developed to allow an improved and more direct observation of the impact of different aerosol types and mixtures on the evolution of liquid-water clouds occurring in the height range from the upper PBL to the tropopause. Active remote sensing is a powerful technique to continuously and coherently monitor the evolution and lifecycle of clouds in their natural environment. Aerosol properties can vary strongly with height and as lidar can provide vertically resolved information about aerosols, it suits as an attractive option for studies of the aerosol effect on clouds.

Using solely lidar, progress has been recently made with the development of new techniques to study ACI in liquid-water clouds. Schmidt et al. [2013, 2014] introduced the so-called Dual-Field-Of-View (DFOV) Raman technique, which allows observations of the aerosol particle extinction coefficient close to cloud base of a liquid-water cloud layer and to retrieve, at the same time, cloud microphysical properties such as cloud droplet effective radius and cloud droplet number concentration in the lower part of the cloud layer. The potential of a novel cloud lidar based on Raman measurements at two fields of view (FOVs) combined with a Doppler lidar [Bühl et al., 2013] to provide new insight into the influence of aerosol particles on the evolution of pure liquid-water altocumulus layers was investigated. These clouds are usually optically thin enough so that lidar can provide information of cloud optical and microphysical properties and of up- and down-draft characteristics throughout the cloud layer from base to top. In this way, the most direct impact of aerosol particles on cloud microphysical properties could be evaluated. Simultaneous aerosol and liquid-water cloud observations were not evaluated before in other ACI studies, in which lidar was used to characterize aerosol as well as cloud properties.

The method is based on the multiple-scattering effect that takes place in liquid-water clouds. The dependency of this effect on the cloud microphysical properties can be exploited by measuring Raman signals at two FOVs, which contain information about the size and extinction coefficient of cloud droplets. The method permits the unambiguous retrieval of vertically-resolved profiles of the cloud properties without assumptions concerning the vertical structure of the cloud. However, as the method is based on weak inelastic scattering, it is only applicable during nighttime, and signal averaging of the order of 10–30 minutes is required to reduce the impact of signal noise on the observations to a tolerable level. As a consequence, cloud properties cannot be resolved on scales of 100–200 m horizontal resolution or 10–30 s. Therefore, only cases with almost no temporal variation in cloud properties, such as cloud base height, can be assessed with this technique. After three years of measurements during 2010–2013, only 29 non-drizzling purely liquid-water cloud layers (mainly altocumulus) finally remained for the statistical analysis. $E_{\mathrm{aci}}^{N_{\mathrm{d}}}$ was found to be close to 0.8 during updraft periods and below 0.4 when ignoring vertical-wind information in the analysis [Schmidt et al., 2015]. The highest values were obtained when considering aerosol properties down to 1000 meters below cloud base and cloud properties up to 70 meters above cloud base.

At higher penetration depths, the cloud response is noticeably reduced, which can partially explain the lower values obtained from ground-based active/passive remote-sensing approaches [Feingold et al., 2003; Kim et al., 2003; McComiskey et al., 2009] and the much lower E_{aci}^{X} values delivered by passive satellite remote sensing. For continental air masses, and considering the whole cloud extent, Schmidt [2014] found an $E_{\mathrm{aci}}^{N_{\mathrm{d}}}$ value of 0.13±0.07, which differs by almost an order of magnitude from the $E_{\mathrm{aci}}^{N_{\mathrm{d}}}$ value obtained when using only the lowermost 70 m of the cloud. This result confirms the need of a better understanding of the aerosol effects on clouds on a vertical basis. Cloud-base ACI studies are relevant to evaluate cloud processes, while as for the Twomey effect the whole cloud needs to be considered.

In conclusion, measurements of aerosol, clouds, and their environment over the continents in polluted as well as pristine environments and covering all cloud types (convective and stratiform cloud systems) are required to improve our knowledge on the impact of human-made aerosol on cloud formation. To make progress, these measurements need to be performed automatically around the clock, and the methodology to assess aerosol-cloud interactions must be developed and standardized.

2.3 Research questions

The need for a profound understanding of ACI was motivated in the first chapter. In in this second chapter, current knowledge and methodologies to address ACI were described and discussed. In this section, the research questions and challenges concerning observational and analysis methodologies are outlined. Comments to provide some context are added to each question.

1. How can we improve the assessment of $E_{\mathrm{aci}}^{N_{\mathrm{d}}}$ using ground-based lidar systems?

   The studies of Schmidt et al. [2013, 2014, 2015] showed for the first time the assessment of $E_{\mathrm{aci}}^{N_{\mathrm{d}}}$ based on simultaneous observations of aerosol and clouds with lidar. The coarse resolution and limitation to nighttime of the technique, additionally to the difficulty to retrieve the aerosol information in cloudy periods, are issues that demand technical developments in order to increase the robustness of such approaches based on lidar.

2. Linked to the first question, is it possible to extend the DFOV concept proposed by Schmidt et al. [2013] to polarization measurements in a practical way to assess cloud microphysical properties with high temporal resolution and towards daytime?

   Polarization measurements have been shown to be sensitive to cloud microphysical properties when light undergoes multiple scattering. In fact, polarization-based approaches can be found in the literature [e.g., Roy et al., 1999; Veselovskii et al., 2006; Donovan et al., 2015]. However, practical and replicable schemes have not been proposed yet. To improve our knowledge about ACI, as many stations as possible need to be able to perform aerosol and cloud observations. This requirement prompted the idea of developing the new concept of DFOV polarization lidar. To improve the DFOV

measurement concept towards daytime observations and shorter signal averaging times (towards time scales allowing us to resolve individual, single updrafts and downdrafts) the so-called Dual-Field-of-View depolarization (DFOV-Depol) method was developed, which comprises the major outcome of the thesis.

3. How can a lidar instrument be calibrated to obtain accurate retrievals of the aerosol and cloud properties?

   Another goal of this thesis is to deliver an analysis environment that is able to process the lidar data automatically and to perform the calibrations of the instrument in terms of polarization and detection efficiency. Only in this way, high-quality observations for $E_{\mathrm{aci}}^{N_{\mathrm{d}}}$ assessment are possible, given the complexity of the interaction. The analytical aspects to robustly retrieve the aerosol and cloud properties are discussed and new methodologies are proposed.

4. How can a standard lidar be upgraded into a DFOV polarization lidar?

   Lidar systems with polarization capabilities that also possess a second FOV to observe the near vertical range can in principle be expanded by adding a second near-range telescope measuring cross-polarized light. The technical means to realize this concept and to characterize the system need to be developed.

5. How important is it to consider vertical-wind information in the assessment of E_{aci}^{X}?

   Information about the vertical-wind speed, as provided by the ongoing measurement campaign in Punta Arenas (`https://dacapo.tropos.de/`), can be used to investigate the differences between the $E_{\mathrm{aci}}^{N_{\mathrm{d}}}$ for updrafts and the one when no wind information is considered.

6. How different are the aerosol and cloud conditions in different regions of the planet, when observed with lidar systems possessing equivalent capabilities? And how large is the cloud response to aerosol in each of these regions?

   As explained previously, cloud properties depend on aerosol conditions. From long-term measurements in places with contrasting conditions, clear differences should be observed. The data obtained in the measurement campaign at the pristine location of Punta Arenas, Chile, and the data from the polluted continental area of Dushanbe in Tajikistan can be evaluated to answer these questions. Both systems have DFOV polarization capabilities.

7. How does the temporal scale affect estimates of $E_{\mathrm{aci}}^{N_{\mathrm{d}}}$? And what are the consequences of considering data sets of different scales in ACI research?

   High temporal resolution, continuous, and long-term observations can provide insight into the scale dependency of $E_{\mathrm{aci}}^{N_{\mathrm{d}}}$. Single data in one cloud, single clouds over a given period, or temporal averages, e.g., monthly, seasonal, or annual averages, can be considered to estimate the index.

8. How relevant are the $E_{\mathrm{aci}}^{N_{\mathrm{d}}}$ values that can be obtained with the new approach for the aerosol-cloud-albedo effect?

   The efficiency index $E_{\mathrm{aci}}^{N_{\mathrm{d}}}$ needs to be brought into a radiative-forcing context. The two locations to be investigated, the pristine marine Punta Arenas and the polluted continental Dushanbe, should give us insights into the importance of assessing aerosol-cloud interactions locally for the conception of strategies towards better constraints of the aerosol radiative effect globally.

These questions are answered in a series of three research articles [Jimenez et al., 2019, 2020a,b], three conference contributions [Jimenez et al., 2017, 2018, 2020c], and in Chapter 5, presenting further results obtained in the long term. A detailed explanation on how these questions have been tackled is given in Chapter 3.

Chapter 3

Lidar measurements of aerosol-cloud interaction – Overview of applied methodologies

This chapter provides an overview on the lidar technique with focus on the most recent developments to characterize liquid-water clouds and aerosol properties, both essential for ACI research, as explained in Section 2.2. The observational capabilities of a lidar system is the central matter here. In this context, an array of developments to assure a robust retrieval of the aerosol and cloud properties using a lidar system is presented. Most of the attention is devoted to a new method to retrieve microphysical properties of liquid-water clouds, the development of which responds to the need of useful and replicable solutions to characterize clouds.

3.1 Multiple-scattering lidar

Lidar systems emit laser pulses and measure the backscattered photons, which provide vertically-resolved information of the scattering agents present in the atmosphere. Although lidars are mostly deployed for aerosol research, liquid and ice clouds are also detected, but those cannot be described with the traditional single-scattering approach because multiple-scattering (MS) events take place when the light travels through the cloud. The denser a cloud, the more relevant will be the MS effect [Mooradian et al., 1979; Bissonette et al., 1994]. How the MS affects the lidar return depends on the geometrical and spectral characteristics of the lidar instrument, but also on the macro- and micro-physical properties of the cloud layers [Bissonnette et al., 1995; Chaikovskaya, 2008]. Therefore, a variety of models have been developed to characterize the lidar return in MS regime and thus to correct the MS effect on lidar signals [e.g., Eloranta, 1998; Hogan, 2008; Hogan and Battaglia, 2008; Wandinger, 1998; Katzev et al., 1997; Chaikovskaya and Zege, 2004]. Additionally, several attempts have been undertaken to explore the potential of lidar to retrieve optical and microphysical properties of liquid-water clouds from measured MS-affected lidar returns [e.g.,

Roy et al., 1999; Bissonnette et al., 2005, 2006; Veselovskii et al., 2006; Kim et al., 2010]. The challenging instrumental (multiple-field-of-view lidar) and analytical requirements (off-line MS model) have limited the application of those approaches by the aerosol-lidar community, mainly because of the lack of practical easy-to-implement relationships. In the next sections, two documented and tested lidar-based approaches to assess microphysical parameters of liquid-water clouds are introduced.

3.2 DFOV-Raman technique

Investigations of the multiple-scattering effect and its relation to cloud microphysics have been conducted at TROPOS during the last two decades. They allowed the development of a robust lidar approach for the retrieval of profiles of cloud extinction coefficient and effective radius without assumptions on the vertical structure of the liquid-water cloud [Schmidt et al., 2013]. The method is based on the measurement of the Raman return at two different receiver FOVs and the application of a fast forward radiative-transfer model that can compute Raman returns of liquid-water clouds in the multiple-scattering regime [Schmidt et al., 2013]. From now on, this method is referred to as DFOV-Raman technique. This thesis takes over this research branch, with the first goal of searching for improvements of the ACI analysis and of the retrieval capabilities of the DFOV lidar system MARTHA (Multiwavelength Atmospheric Raman lidar for Temperature, Humidity, and Aerosol profiling) [Mattis et al., 2004, 2008]. This section provides an overview about the fundamentals of the method, with its potential applications and limitations.

When the laser beam reaches the cloud, multiple near-forward (NF) scattering occurs before and also after one near-backward (NB) scattering event, which sends the light back towards the lidar receiver. The scattering events, which define the spatial journey of the laser photons through the cloud, occur inside a long but narrow volume defined by the laser divergence and the cloud properties. Fig. 3.1(d) presents a photograph from the MARTHA system measuring during a cloudy period. It shows us an integral picture of how the MS affects the return of light towards the surface as a whole. The spatial features of that journey are closely related to the phase function of the cloud droplets. The larger the sphere is, the more elongated is the phase function and hence the narrower is the multiple-scattering horizontal cross-section, as shown in Fig. 3.1(a) and (c). The one NB scattering event can take place either by a cloud droplet or an air molecule.

A Raman lidar can measure the return of nitrogen molecules, which possess an almost isotropic phase function. This feature gives an advantage to Raman signals over elastic ones, as those contain information about the droplet size due to the multiple NF scattering and one isotropic NB scattering event, making the modeling of the lidar returns much simpler than for the elastic case [Malinka and Zege, 2003]. Regarding elastic signals, the phase function of droplets in the NB direction exhibits strong oscillations that hamper the size-depending features of the NF scattering phase function.

Following the recommendations of Malinka and Zege [2007], a DFOV-Raman system was built at TROPOS. The system measures at one narrow FOV of 0.5 mrad (FOV_{in}) and

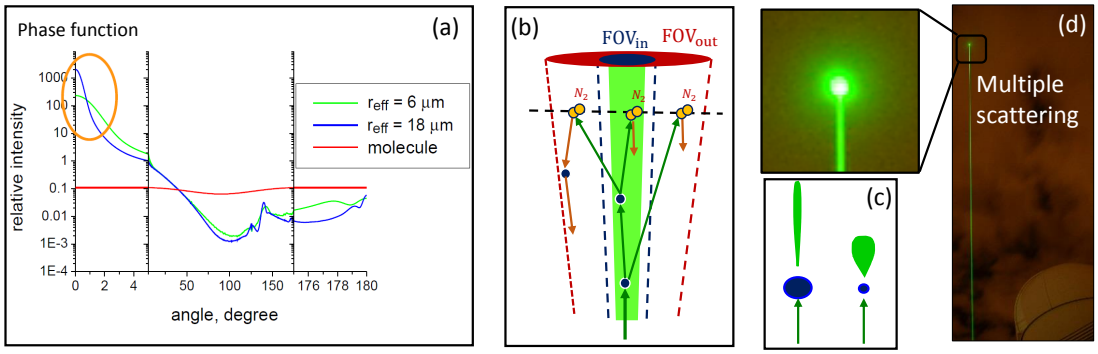

Figure 3.1: Panel (a) shows the phase function versus scattering angle for two different droplet sizes. The almost isotropic molecular phase function is shown in red. A schematic view of FOV configuration of a Raman DFOV lidar system is shown in (b), and (c) illustrates the size dependency between the droplet size and the elongation of the phase function in the near-forward direction. Finally, (d) presents a picture of the MS effect taking place at the cloud layer hit with the laser beam of the MARTHA system.

additionally at a wide FOV of 2.0 mrad (FOV_{out}), with the form of a ring that excludes the inner narrow FOV (Fig. 3.1(b)). In the retrieval scheme, the cloud is divided in homogeneous layers, and the cloud extinction coefficient and effective radius in each layer are obtained via an iterative minimization procedure. The task of the algorithm is to find the best estimate of the cloud parameters using the Raman signals and an on-line forward MS model to simulate the lidar returns [Malinka and Zege, 2003]. This approach allowed retrievals of the cloud microphysical properties for night-time measurement cases from 2010 to 2013, and with the aerosol information retrieved using the traditional lidar approach (see A.3.1 and A.2.2), ACI studies as described in Chapter 2 were possible [Schmidt et al., 2014, 2015].

However, the DFOV-Raman technique requires strong returns and thus a large receiver (e.g., 80 cm diameter in the MARTHA system). It can only be applied during nighttime and it needs stable cloud layers so that the signal can be averaged over 20–40 minutes. Manually operated measurements, during nighttime and with long averaging periods, with a careful signal processing are necessary to apply the DFOV-Raman approach. As concluded by Schmidt [2014], this strategy might not help us to make further advances into ACI research, as much more, continuous, measurements need to be performed in the long term, including daytime and if possible with higher temporal resolution.

3.3 Single-FOV polarization lidar

As mentioned in the previous section, the NB scattering hampers the size-dependency of the NF scattering. However, a quantity that might buffer the oscillations on the NB phase function is the depolarization ratio, which in fact also depends to a certain extent on the droplet size. Analyzing outputs of the Monte-Carlo multiple-scattering model of the Earth-

CARE simulator ECSIM [Donovan et al., 2010; Illingworth et al., 2015], Donovan et al. [2015] found a relation between the vertical extent and depolarization of the lidar return and the droplet size and extinction coefficient. Using co- and cross-polarized signals, Donovan et al. [2015] developed an optimal estimation approach to retrieve the cloud properties by using the lidar signals as input and look-up tables from an off-line MS model. As a first step to a more practical solution, in the framework of this thesis this approach, called from now on Single-FOV depolarization (SFOV-Depol) technique, was implemented in our lidar system MARTHA.

The SFOV-Depol approach requires very well calibrated polarization signals with errors of less than 5%, which is quite difficult to obtain given the systematic effects on polarization channels, which are difficult to correct [Mattis et al., 2009; Freudenthaler, 2016a]. In order to implement the SFOV-Depol approach into the MARTHA system, a new calibration approach was developed and experimentally tested. To minimize systematic effects, the method is based on three independent receiver telescopes designed to collect the total, co-, and cross-polarized returns. Because of the strong elastic signals from liquid-cloud layers, a practical solution was to build small telescopes of 50-mm diameter, which are large enough to measure good lidar echoes. The design of the lidar receiver, the calibration approach, its implementation into the MARTHA system, and comparisons with the state-of-the-art polarization lidar BERTHA [Haarig et al., 2017] were documented in a first publication: **Jimenez et al. [2019]**.

The calibration approach is based on the different sensitivities to polarized light that the three channels exhibit and includes polarizing effects associated to the emission unit. It allows a full characterization of the lidar system, and the calibration can be performed at any given measurement as long as there are depolarizing agents in the atmosphere, such as clouds or non-spherical particles. The calibration is done in the same time slot as the measurement to be analyzed, and the polarization efficiencies can be assessed directly without the need of estimating them experimentally [e.g., Mattis et al., 2009]. These features represent an advantage over traditional methods. This development was motivated by the first research question concerning improvements for better assessment of the $E_{\mathrm{ACI}}^{\mathrm{N_d}}$ index, as the SFOV-Depol approach might extend the measurement capacities towards daytime and better temporal resolution (3–5 minutes). The new capabilities also provide an answer to part of the third question, which points out the need of methodologies to calibrate the aerosol and cloud products.

In the next step, cloud measurements were performed at daytime and also during the night to find cases in which the DFOV-Raman method as well as the SFOV-Depol method could be successfully applied. The DFOV-Raman scripts were provided by J. Schmidt (former PhD student at TROPOS), and the SFOV-Depol code, including the required look-up tables, was provided by D. Donovan from KNMI (Royal Netherlands Meteorological Institute). The code initialization was adapted to our measurement environment.

3.3.1 Comparison between DFOV-Raman and SFOV-Depol methods

After the analysis of several measurement cases, it was found that the SFOV-Depol and the DFOV-Raman methods deliver similar values of extinction coefficient, but quite different resuts for the effective radius. This finding can be seen in the case of the 2 April 2017 shown in Fig. 3.2. Here a stratocumulus layer was present at about 2.2 km height during the whole period. Five sections of the period were selected to perform the retrieval. Fig. 3.3 shows the results obtained for section 5 from 02:25–02:45 UTC. Fig. 3.3(a) shows the inputs for the retrieval schemes, i.e., the Raman signals from the $\mathrm{FOV_{in}}$ and $\mathrm{FOV_{out}}$ and the depolarization ratio δ for the SFOV-Depol method. The minimization procedure for the SFOV-Depol method is initialized with the calibrated co- and cross-polarized signals ($P_{\parallel}$ and $P_{\perp}$), so that the depolarization ratio $\delta = P_{\perp}/P_{\parallel}$. To initialize the retrieval schemes, the cloud base height is determined. The SFOV-Depol method uses the parallel return and the DFOV-Raman method the Raman return of the $\mathrm{FOV_{out}}$, so that different cloud base heights are obtained.

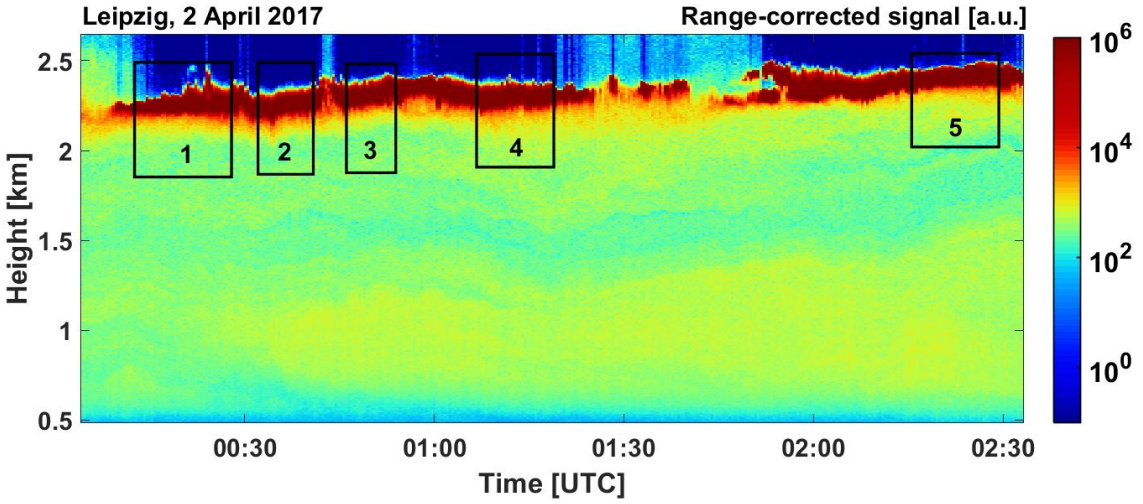

Figure 3.2: Quicklook of lidar range-corrected signal on 2 April 2017. Five periods were selected to apply the retrieval.

Fig. 3.3(b) shows the extinction values obtained with both lidar approaches and additionally the profile of the extinction coefficient obtained with the traditional single-scattering method, which as usual underestimates the extinction coefficient because of the MS effect. The extinction values of the DFOV-Raman and SFOV-Depol methods agree quite well. Almost-zero values were delivered by the DFOV-Raman method in the lowest 35 meters, which agree with the difference on the cloud base height that the SFOV-Depol method use. In the case of the effective radius, shown in Fig. 3.3(c), the results are quite different. The question is, which result is closer to the real one. On one side, the drawback of the DFOV-Raman technique is the long averaging period, which could make clouds to appear thinner when strong variations are present at the cloud base. This seems not to be the case here (see section 5 in Fig. 3.2). Furthermore, this effect is more relevant for the extinction coefficient.

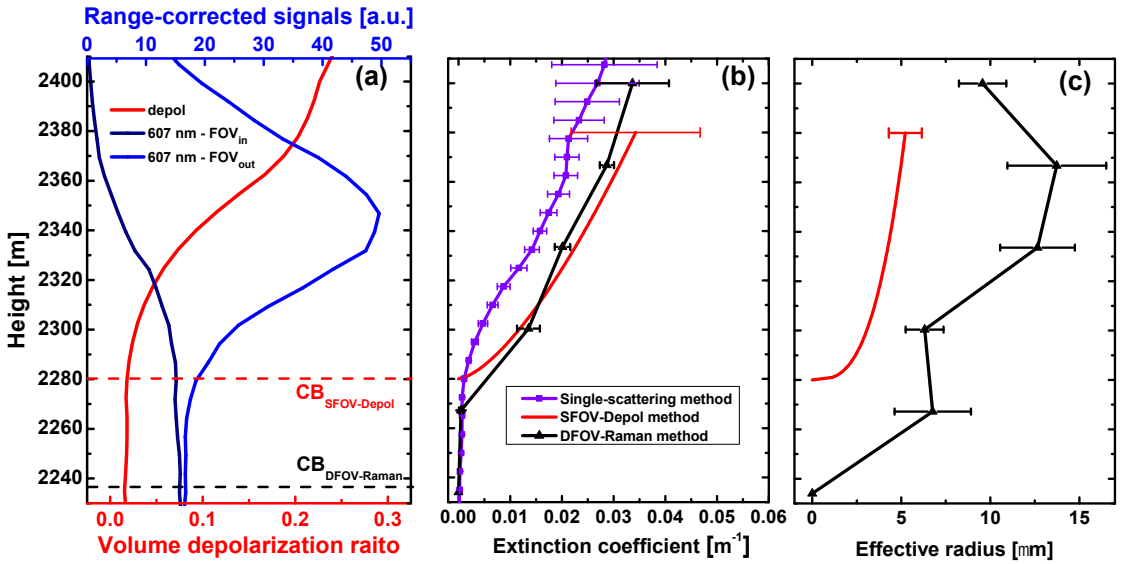

Figure 3.3: (a) Raman signals at 607 nm and depolarization ratio for retrieval of microphysical properties of the section 5 in Fig. 3.2, (b) retrieved cloud extinction coefficient with both methods and by using the traditional Raman method, (c) retrieved cloud droplet effective radius from the DFOV-Raman (black) and SFOV-Depol (red) methods. CB are the cloud base heights determined with each method.

The issue seems to be related to the SFOV-Depol approach.

The SFOV-Depol method exploits the features of the co- and cross-polarized signals. The effective radius depends mainly on the width of the signals, i.e., the narrower the lidar return is at the cloud, the smaller is the effective radius (see Fig. 3 in Donovan et al. [2015]). To perform the optimal estimation of the cloud parameters, a complicated treatment of the lidar data is needed, which at the end limits the results of the retrieval to the lower part of the possible values of effective radius. This may lead to the difference of a factor of 2 from the DFOV-Raman approach. This comparison study was summarized in a conference contribution [Jimenez et al., 2018].

3.4 Dual-FOV depolarization approach

The discrepancies between the two approaches discussed above put in question the potential of the SFOV-Depol approach, which left us with not much advance into new ways to measure cloud properties during daytime and with high temporal resolution. Therefore, guided by the studies of Roy et al. [1999], Bissonnette et al. [2005], and Veselovskii et al. [2006], a new attempt was to use depolarization measurements with more than one FOV. The most useful and convincing approach for us was the one based on a system that measures depolarization with two FOVs (Fig. 3.4(a)). The techniques using multiple FOVs are based either on elastic total or cross-polarized signals, but a dual-FOV depolarization (DFOV-Depol) approach has

not been proposed before. This idea was conceived after looking at the droplet phase function, closely related to the droplet size as shown in Fig. 3.4(b) and in Sect. 3.2, in conjuntion with the second important feature in the depolarization ratio, sketched in Fig. 3.4(c) for the case of double scattering. The depolarization of light takes place in the NB direction. It is zero at exactly 180°, i.e., depolarization for water droplets occurs exclusively in the multiple-scattering regime. The depolarizing of light can be described with Mie theory and can be physically understood from the angular scattering properties of single water spheres [Sassen and Petrilla, 1986]. The accumulation of several NF scattering processes potentiates the horizontal features of the depolarization at the NB direction, as illustrated in Fig. 3.4(d) by multiplying the NF phase function and the NB depolarization for the double-scattering example. These functions indicate that when we measure the depolarization ratio at two FOVs, we can assess its horizontal features, which are closely linked to the effective radius.

The idea was introduced in a conference contribution [Jimenez et al., 2017], and the formal description of the approach was published in a second research article: **Jimenez et al. [2020a]**. The DFOV-Depol approach is based on an accurate multiple-scattering model [Zege et al., 1995; Zege and Chaikovskaya, 1999; Chaikovskaya, 2008], which allows us to establish practical relationships between the cloud extinction coefficient and the effective radius and the depolarization ratio measured at two FOVs. In Jimenez et al. [2020a], the attention was focused on the validity of our simulations by comparing our model with alternative model approaches that deal with multiple scattering. The new retrieval approach is valid for a cloud system under subadiabatic equilibrium, which was shown to be a valid assumption for the cases in which updraft conditions prevail [Merk et al., 2016; Foth and Pospichal, 2017; Barlakas et al., 2020; Kim et al., 2008]. In this article, we derived the relationships that are needed for different lidar configurations, including the configurations of our MARTHA and Polly systems [Jimenez et al., 2020d]. Finally, by providing solutions for four FOV combinations, this article precisely answers the second research question regarding the extent of the capabilities of the lidar system MARTHA.

The new high-resolution and daytime capabilities of the novel method give us also an answer to the first research question. In-depth aerosol-cloud-interaction studies can be largely improved by resolving cloud properties at scales of 15–120 s (or 100–200 m horizontal resolution), which allow us to identify single updraft periods. The newly available products, i.e., the collocated observation of aerosol, cloud, vertical wind, and water-vapor mixing ratio from Raman channels [Dai et al., 2018], offer the opportunity to conduct closure studies to confront microphysical schemes from the scales of large eddies to the meso- and global scale [Morrison et al., 2020; Simpson et al., 2014]. The long-term monitoring also brings the opportunity for assessment studies focused on the Twomey effect. The DFOV-Depol approach has shown its potential in several studies using measurements at different locations, which were conducted in the framework this thesis.

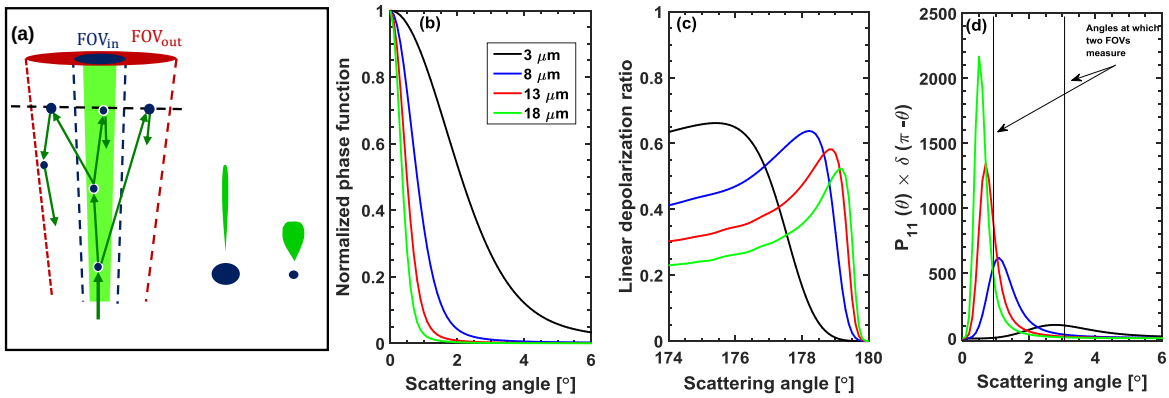

Figure 3.4: (a) Schematic view of the FOV configuration and of the size dependency of the NF scattering, (b) phase function in the NF direction for four droplet sizes (normalized to the maximum at 0°), (c) droplet linear depolarization ratio as a function of scattering angle in the NB direction, and (d) phase function multiplied with the depolarization ratio at $\theta_b = \pi - \theta_f$ (in c).

3.4.1 Calibration of the lidar system

The third research question is related to the calibration of the lidar system. This is a very important issue for accurate retrievals not only of the cloud properties, but also of the aerosol properties below cloud base.

In the case of the MARTHA system, we upgraded the lidar with three telescopes that were calibrated using the method introduced in Jimenez et al. [2019] and measured at a FOV_{out} of 1.6 mrad. The MARTHA system possesses additionally one co- and one cross-polarized channel at a FOV_{in} of 0.5 mrad, but their calibration was flawed by unknown systematic effects in the emission and reception of polarized light. Using our calibrated depolarization ratio at FOV_{out} in cloud-free periods, an accurate calibration of the polarization channels at the FOV_{in} was possible. This effort is described in Appendix B.

One issue about measuring at liquid-water clouds is that they scatter much more light than aerosol particles. This can eventually saturate any of the polarization channels, inducing an underestimation of the lidar return and hence errors on the cloud-microphysical products. If any of the four polarization channels is saturated, the data bin is discarded. The detectors being used at TROPOS reach maximums of 120–145 MHz. A maximum count rate allowed of 100 MHz was set. Up to this count rate, the dead-time approach can provide accurate corrected signals, as concluded by Wiesen [2020], who studied this issue on the laboratory and with DFOV-Depol lidar data.

Another matter regarding system calibration is the assessment of the lidar constant of the elastic and/or Raman channels. These calibration constants are needed to retrieve aerosol properties in cloudy cases, which is not possible with the traditional elastic and Raman approaches. In Appendix A, a new so-called bottom-up approach developed to retrieve the aerosol properties below cloud base, either by using only the elastic signals or by using elastic

and Raman signals when they are available, is presented.

3.4.2 DFOV-Depol measurement cases

To evaluate the performance of the new DFOV-Depol approach, the method was applied to the same measurement example as shown in Sect. 3.4, i.e., the 2 April 2017, for the five periods selected in Fig. 3.2. The depolarization observations at the two FOVs, calibrated according to Jimenez et al. [2019] and to Appendix B, were used to initialize the new retrieval scheme. The profiles of extinction coefficient and effective radius for the five periods are summarized in Fig. 3.5 and in Fig 3.6, where the mean values of each profile are plotted. Here, very good agreement between the DFOV-Raman and DFOV-Depol results can be noted. There are some differences, but both profiles agree within their error bars. For all five periods, we can also confirm the systematic effect in the SFOV-Depol retrieval, i.e., a general underestimation of the effective radius. However, the temporal evolution follows a similar behavior as for the other two methods, showing that there might be a bias in the SFOV-Depol approach. Furthermore, good agreement of the extinction coefficient was found among the three methods for the whole period.

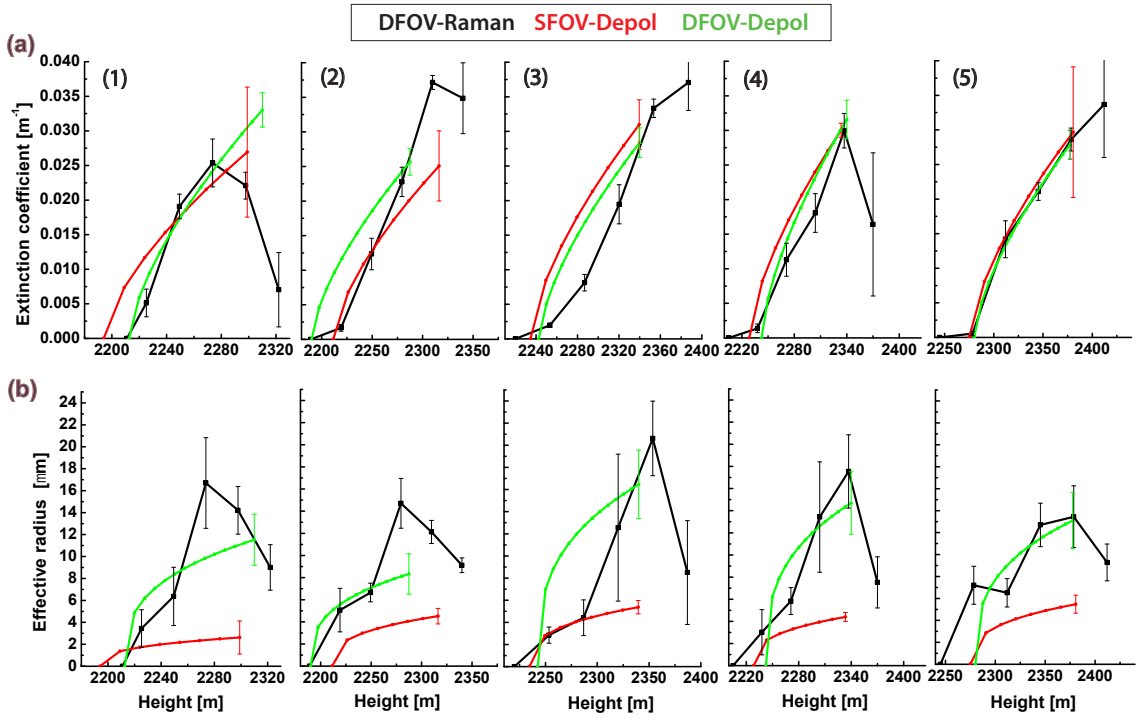

Figure 3.5: (a) Profiles of the extinction coefficient for the five periods selected in Fig. 3.2, (b) profiles of effective radius. The five periods are presented from left to right and the axes have been exchanged with respect to Fig. 3.3.

The good agreement between the DFOV-Raman and DFOV-Depol methods shows the potential of the new approach to retrieve cloud microphysical properties. The whole analy-

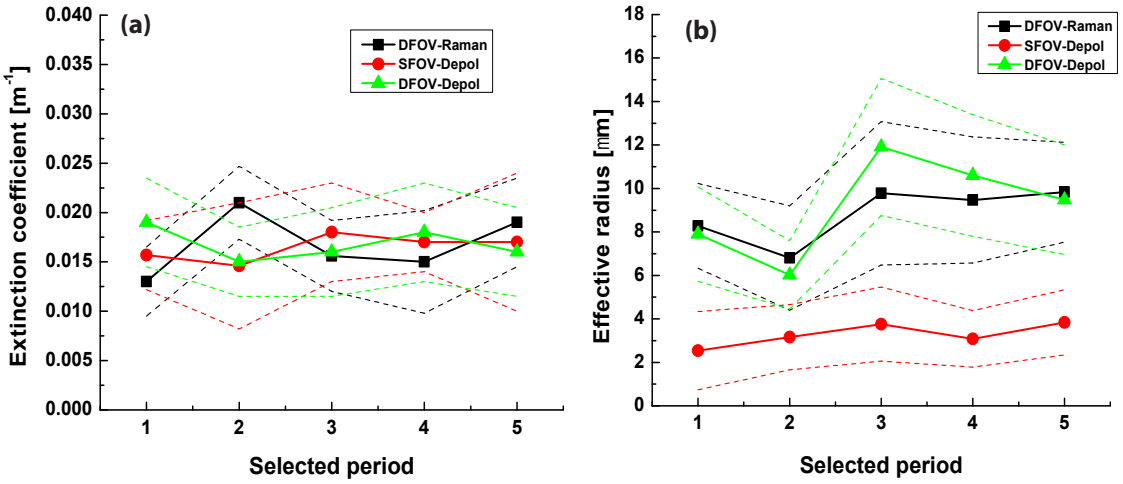

Figure 3.6: Time series of the profile mean values of the extinction coefficient (a) and effective radius (b) obtained for the five periods selected in Fig. 3.2. The dashed lines indicate the respective standard deviations.

sis of the measurements between 2017 and 2019 is ongoing work, but after analyzing more cases that fulfill the requirements mentioned in Sect. 3.2, it was found that both methods do not always agree in the temporal evolution of the products in one single cloud, but on average they deliver similar values. The long-term averages of the profiles retrieved with both approaches corroborate this agreement. Fig. 3.7 (a), (b), and (c) show the mean profiles of droplet number concentration, effective radius, and liquid-water content, respectively. Results obtained with the DFOV-Raman method are plotted in black and consider measurements performed at Leipzig between 2010 and 2017 (39 profiles, about 18 hours). The results obtained with the DFOV-Depol method during 2017–2018 are shown in green (800 profiles, about 40 hours). The temporal variability of both methods is indicated by the dashed line. The effective radii from the DFOV-Depol retrieval are about 10% smaller than those from the DFOV-Raman method, and the number concentrations N_d are 20–25% larger. Ignoring the fact that the mean profiles cover different periods, one can conclude that the results agree within the typical errors of those retrievals, which corroborates the consistency of both approaches.

These results contributed to the validation section in Costa-Surós et al. [2020]. In this publication, outputs from the large-domain large-eddy model ICON-LEM were used. The model simulated the cloud situation over central Europe on 2 May 2013 and a perturbed scenario with double CCN concentration as a reference for 1985. Considering the average profiles of model and observations, good agreement between the model results for 2013 and the lidar observations, as shown in Fig. 3.7, can be noted. The consistency of these results gives us a rough indication that models and observational approaches might be going towards the right direction in terms of their products.

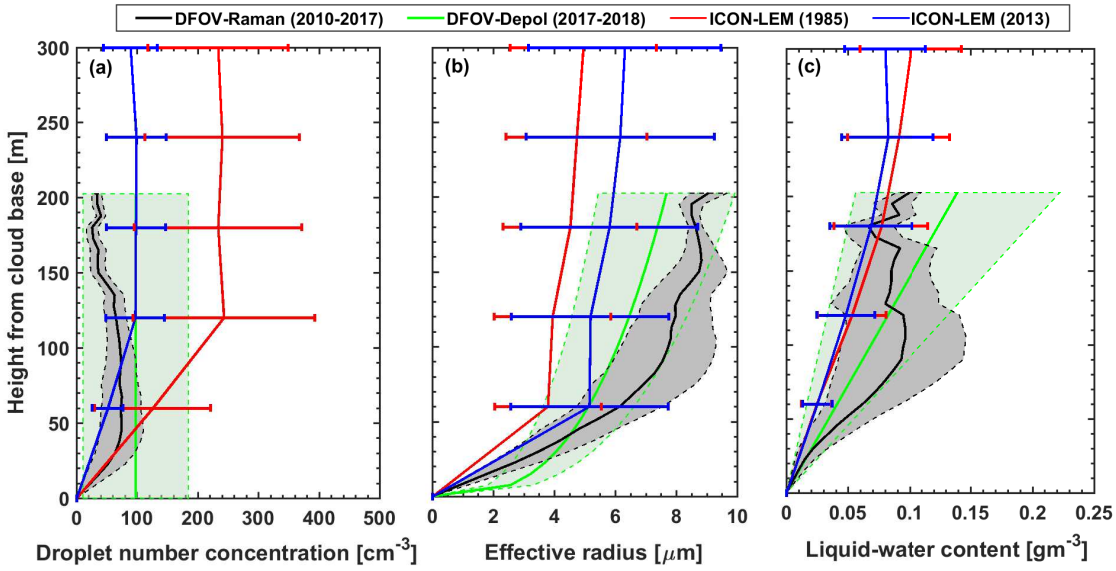

Figure 3.7: Comparison of the cloud microphysical properties observed with the DFOV lidar and ICON outputs for a present-day (blue) and a 1985 scenario (red) with double CCN burden.

3.5 Implementation of the DFOV-Depol approach into the standardized lidar system Polly

With the DFOV-Depol method as principal outcome, in the previous sections new developments to answer the first three research questions were presented. This section deals with the fourth and fifth research question and provides the first steps to address questions 6 and 7.

The need of long-term continuous measurements with high temporal resolution motivated the development of the new technique. In a first step, the method was tested experimentally in the MARTHA system. As "testbed" this system helped us to confirm the consistency of our approach. But the MARTHA system cannot fulfill the long-term and continuous requirements. The DFOV-Depol method needs to be operational for network standard lidars, such as the Polly system [Engelmann et al., 2016], part of the Polly network [Baars et al., 2016], which also supports larger European networks, i.e., the EARLINET (European Aerosol Research Lidar Network) [Pappalardo et al., 2014] and Cloudnet [Illingworth et al., 2007; Bühl et al., 2016], both coordinated by ACTRIS (https://www.actris.eu/), a multinational effort to build up the necessary aerosol-cloud monitoring infrastructure to improve our knowledge about atmospheric processes with focus on the present societal and environmental challenges, such as climate change.

The Polly system is a multiwavelength polarization Raman lidar. The development and construction of the system is led by the lidar group at TROPOS. More than 10 systems have been constructed and distributed mostly over Europe during the last 15 years. The experience in lidar research of the remote-sensing group resulted in a state-of-the-art standard system,

also used as reference to evaluate the performance of other lidar instruments [Belegante et al., 2018]. The capabilities of such systems are essential to deliver quality-assured data sets at strategic locations [e.g., Hofer et al., 2020a; Griesche et al., 2020] and to detect extreme atmospheric events [e.g., Haarig et al., 2018; Ohneiser et al., 2020; Floutsi et al., 2021]. The Polly system was chosen as "workhorse" for the application of the DFOV-Depol scheme.

Among the channels of the Polly system, there are polarization channels (total and cross-polarized) at two wavelengths (355 and 532 nm), which measure at 1 mrad FOV. Additionally, the system possesses a near-range telescope that measures at 2 mrad FOV. These qualities, which all Polly systems share, make the task of upgrading the system into a DFOV-Depol lidar straight forward. By adding an additional telescope that can measure cross-polarized returns, the Polly system was upgraded. The system upgrade, the calibration, and the analysis of two case studies are summarized in a third publication: **Jimenez et al. [2020b]**.

The article responds fully to the fourth research question, with the integration of the DFOV-Depol approach into the Polly system of the LACROS mobile platform (http://lacros.rsd.tropos.de/), currently located at the pristine location of Punta Arenas (Chile) for the two-year measurement campaign DACAPO-PESO (Dynamics, Aerosol, Cloud And Precipitation Observations in the Pristine Environment of the Southern Ocean, https://dacapo.tropos.de). The observations with the aerosol/cloud lidar, a Doppler lidar for vertical wind, and a cloud radar as main profiling instruments are intended to disentangle the different processes involved in the formation of clouds, precipitation, and their radiative impact. The clean near-pristine conditions make the location in southern Chile a favorable environment for aerosol-cloud-interaction studies.

In Jimenez et al. [2020b], Case 1 was used to discuss the uncertainties of the retrieval approach and also to compare our results with radar-based retrievals of the effective radius in a liquid cloud layer [Frisch et al., 2002]. The good agreement between the two approaches confirms the retrieval capabilities of a Polly system with FOVs of 1 and 2 mrad, and adds to the comparisons presented in Sect. 3.4.2, it corroborates that the approach is working and that the products are accurate enough for providing aerosol and cloud data sets for conducting ACI studies. The second case presented in Jimenez et al. [2020b], motivated by the fifth question, highlights the extended potential of the new approach to conduct detailed updraft- and downdraft-resolved ACI studies, when vertical wind information from a Doppler lidar is integrated into the analysis. The high-resolution products of aerosol and cloud properties (1-minute resolution) allowed the isolation of individual updraft and downdraft periods, and the assessment of the ACI efficiency index $E_{\mathrm{aci}}^{\mathrm{N_d}}$ confirms the need of accounting for the vertical wind information, so that a representative index can be obtained.

Within the cumulative part of the thesis, i.e., the three research articles presented in Chapter 4, the first five questions are addressed in detail. The last three questions, regarding the cloud conditions at several contrasting environments and the application of the lidar-based ACI studies to improve our understanding of the influence of aerosol on clouds, have not been addressed yet. To deal with these questions, further work has been done. We equipped three further Polly instruments with polarization channels at two FOVs. These lidars are or were operated in the High Arctic (at 85–90° N) on board the German icebreaker

Polarstern from September 2019 to September 2020, at Dushanbe, Tajikistan, in polluted and dusty conditions in Central Asia since June 2019, and at Limassol, Cyprus, in the polluted and dusty Eastern Mediterranean since summer 2020. A fourth DFOV Polly lidar will start long-term monitoring at Mindelo, Cabo Verde, in the outflow regime of pollution and dust from western and central Africa in 2021. A mobile DFOV Polly will be moved to New Zealand for further ACI studies in the Southern Ocean in 2022. All these field activities will be used to characterize ACI in the case of liquid-water clouds under very different aerosol and meteorological conditions in future studies. Results obtained in near-pristine conditions at Punta Arenas and in the dusty polluted environment of Dushanbe are discussed in Chapter 5 to address the research questions 6, 7, and 8.

Chapter 4

Research results

This chapter presents the cumulative part of the dissertation. The following publications are considered:

- Polarization lidar: an extended three-signal calibration approach, by Cristofer Jimenez, Albert Ansmann, Ronny Engelmann, Moritz Haarig, Jörg Schmidt, and Ulla Wandinger, in *Atmospheric Measurements Techniques*, **12**, 1077-1093, 2019.
- The dual-field-of-view polarization lidar technique: A new concept in monitoring aerosol effects in liquid-water clouds – Theoretical framework, by Cristofer Jimenez, Albert Ansmann, Ronny Engelmann, David Donovan, Aleksey Malinka, Jörg Schmidt, Patric Seifert, and Ulla Wandinger, in *Atmospheric Chemistry and Physics*, **20**, 15247–15263, 2020.
- The dual-field-of-view polarization lidar technique: A new concept in monitoring aerosol effects in liquid-water clouds – Case studies, by Cristofer Jimenez, Albert Ansmann, Ronny Engelmann, David Donovan, Aleksey Malinka, Patric Seifert, Robert Wiesen, Martin Radenz, Zhenping Yin, Johannes Bühl, Jörg Schmidt, Boris Barja, and Ulla Wandinger, in *Atmospheric Chemistry and Physics*, **20**, 15265–15284, 2020.

4.1 First publication: Polarization lidar: an extended three-signal calibration approach

The content of this chapter has already been published under the title "Polarization lidar: an extended three-signal calibration approach" by Cristofer Jimenez, Albert Ansmann, Ronny Engelmann, Moritz Haarig, Jörg Schmidt, and Ulla Wandinger. In 2019, the paper was published under the Creative Commons Attribution 4.0 License in Atmospheric Measurements Techniques with the doi: 10.5194/amt-12-1077-2019 (see `https://doi.org/10.5194/amt-12-1077-2019`). Reprinted with permission by the authors from Atmospheric Measurements Techniques, 12, 1077-1093, 2019.

Atmos. Meas. Tech., 12, 1077–1093, 2019
https://doi.org/10.5194/amt-12-1077-2019

Atmospheric Measurement Techniques
Open Access
EGU

Polarization lidar: an extended three-signal calibration approach

Cristofer Jimenez[1], **Albert Ansmann**[1], **Ronny Engelmann**[1], **Moritz Haarig**[1], **Jörg Schmidt**[2], **and Ulla Wandinger**[1]

[1]Leibniz Institute for Tropospheric Research, Leipzig, 04318, Germany
[2]University of Leipzig, Institute for Meteorology, Leipzig, 04103, Germany

Correspondence: Cristofer Jimenez (cristofer.jimenez@tropos.de)

Received: 19 October 2018 – Discussion started: 27 November 2018
Revised: 24 January 2019 – Accepted: 25 January 2019 – Published: 18 February 2019

Abstract. We present a new formalism to calibrate a three-signal polarization lidar and to measure highly accurate height profiles of the volume linear depolarization ratios under realistic experimental conditions. The methodology considers elliptically polarized laser light, angular misalignment of the receiver unit with respect to the main polarization plane of the laser pulses, and cross talk among the receiver channels. A case study of a liquid-water cloud observation demonstrates the potential of the new technique. Long-term observations of the calibration parameters corroborate the robustness of the method and the long-term stability of the three-signal polarization lidar. A comparison with a second polarization lidar shows excellent agreement regarding the derived volume linear polarization ratios in different scenarios: a biomass burning smoke event throughout the troposphere and the lower stratosphere up to 16 km in height, a dust case, and also a cirrus cloud case.

1 Introduction

Atmospheric aerosol particles influence the evolution of clouds and the formation of precipitation in complex and not well-understood ways. Strong efforts are needed to improve our knowledge about aerosol–cloud interaction and the parameterization of cloud processes in atmospheric (weather and climate) models and weather forecasts and especially to decrease the large uncertainties in future climate predictions (IPCC, 2014; Huang et al., 2007; Fan et al., 2016). In addition to more measurements in contrasting environments with different climatic and air pollution conditions, new experimental (profiling) methods need to be developed to allow an improved and more direct observation of the impact of different aerosol types and mixtures on the evolution of liquid-water, mixed-phase, and ice clouds occurring in the height range from the upper planetary boundary layer to the tropopause. Active remote sensing is a powerful technique to continuously and coherently monitor the evolution and life cycle of clouds in their natural environment.

Recently, Schmidt et al. (2013a, b, 2015) introduced the so-called dual-field-of-view (dual-FOV) Raman lidar technique, which allows us to measure aerosol particle extinction coefficients (used as aerosol proxy) close to cloud base of a liquid-water cloud layer and to retrieve, at the same time, cloud microphysical properties such as cloud droplet effective radius and cloud droplet number concentration (CDNC) in the lower part of the cloud layer. In this way, the most direct impact of aerosol particles on cloud microphysical properties could be determined. However, the method is only applicable after sunset (during nighttime) and signal averaging of the order of 10–30 min is required to reduce the impact of signal noise on the observations to a tolerable level. As a consequence, cloud properties cannot be resolved on scales of 100–200 m horizontal resolution or 10–30 s. To improve the dual-FOV measurement concept towards daytime observations and shorter signal averaging times (towards timescales allowing us to resolve individual, single updrafts and downdrafts) we developed the so-called dual-FOV polarization lidar method (Jimenez et al., 2017, 2018). This technique makes use of strong depolarization of transmitted linearly polarized laser pulses in water clouds by multiple scattering of laser photons by water droplets (with typical number concentrations of 100 cm^{-3}). This novel polarization lidar method can be applied to daytime observations with resolutions of 10–30 s. An extended description of the method is in preparation (Jimenez et al., 2019).

Highly accurate observations of the volume linear depolarization ratio are of fundamental importance for a successful

retrieval of cloud microphysical properties by means of the new polarization lidar technique. In this article (Part 1 of a series of several papers on the dual-FOV polarization lidar technique), we present and discuss our new polarization lidar setup and how the lidar channels are calibrated. The basic product of a polarization lidar is the volume linear depolarization ratio, defined as the ratio of the cross-polarized to the co-polarized atmospheric backscatter intensity, and is derived from lidar observations of the cross- and co-polarized signal components, or alternatively, from the observation of the cross-polarized and total (cross- + co-polarized) signal components. Cross- and co-polarized denote the plane of linear polarization, orthogonal and parallel to the linear polarization plane of the transmitted laser light, respectively. Reichardt et al. (2003) proposed a robust concept to obtain high-quality depolarization ratio profiles by simultaneously measuring three signal components, namely the cross- and co-polarized signal components and additionally the total elastic backscatter signal. We will follow this idea as described in Sect. 2. Reichardt et al. (2003) assumed that the laser pulses are totally linearly polarized. Recent studies, however, have shown that the transmitted laser pulses can be slightly elliptically polarized (David et al., 2012; Freudenthaler, 2016; Bravo-Aranda et al., 2016; Belegante et al., 2018). We will consider this effect in our extended approach of the three-channel depolarization technique. We further extend the formalism by considering realistic strengths of cross talk among the three channels and we propose a practical inversion scheme based on the determination of the instrumental constants for the retrieval of high-temporal-resolution volume depolarization ratio profiles.

The article is organized as follows. In Sect. 2, the lidar instrument is described. The new methodology to calibrate the lidar system and to obtain high-quality depolarization ratio observations is outlined in Sect. 3. Section 4 presents and discusses atmospheric measurements performed to check and test the applicability of the new methodology. Concluding remarks are given in Sect. 5.

2 Lidar setup

A sketch of the instrumental setup, providing an overview of the entire lidar system, is shown in Fig. 1. MARTHA (Multiwavelength Tropospheric Raman lidar for Temperature, Humidity, and Aerosol profiling) has a powerful laser transmitting in total 1 J per pulse at a repetition rate of 30 Hz and has an 80 cm telescope. It is thus well designed for tropospheric and stratospheric aerosol observations (Mattis et al., 2004, 2008, 2010; Schmidt et al., 2013b, 2014, 2015; Jimenez et al., 2017, 2018). MARTHA belongs to the European Aerosol Research Lidar Network (EARLINET) (Pappalardo et al., 2014). We implemented a new three-signal polarization lidar receiver unit to the left side of the large telescope (see Fig. 1). The new receiver setup is composed of three independent telescopes co-aligned with the lidar transmitter.

Figure 2 provides details of the new polarization-sensitive channels. Each of the small receiver telescopes consists of 2 in. (50.8 mm) achromatic lens with a focal length of 250 mm. An optical fiber with an aperture of 400 µm is placed at the focal point of the lens. The resulting FOV is 1.6 mrad. The receivers have in principle the same overlap function since they are identical and are implemented into the large telescope at the same distance from the laser beam axis. The laser-beam receiver-FOV overlap (obtained theoretically) is complete at about 650 m above the lidar (Stelmaszczyk et al., 2005).

A 2 mm ball lens is placed at the output of the fiber (scrambler in Fig. 2) in order to remove the small sensitivity of the interference filter to the changing incidence angle of backscattered light in the near-range. A spatial attenuation unit which consists of two optical fibers is integrated in the receiver setup, replacing the usual setup with neutral density filters. The distance between the two fibers with a given aperture and thus the strength of the incoming lidar return signal can be changed. The attenuation factor depends on the square of the distance between the fibers and on the numerical aperture of the fibers, for example, signal attenuation by a factor of about 100 when the distance is 25 mm and about 1000 with 79 mm of distance.

The purpose of the new receiver system is to measure accurate profiles of the volume depolarization ratio in clouds between 1 and 12 km in height. For the separation of the polarization components two of the three polarization telescopes are equipped with a linear polarization filter (see Fig. 2, linear polarizer) in front of the entrance lens. In the alignment process, the cross-polarized axis is found when the count rates are at the minimum. The co-polarized channel is then rotated by 90° compared to the cross-polarized filter position. Because it is set manually, the difference between the true polarization axis of the filters may not be 90°. However, in this approach we will assume that it is 90° since the impact of small variations in the pointing angles of the polarization filters can be eventually neglected (see Appendix A). Additionally, a small tilt between the finally obtained polarization plane of the receiver unit and the true polarization state (main plane of linear polarization) of the transmitted laser pulses is expected and thus assumed in the methodology outlined in Sect. 3.

3 Methodology

In Sect. 3.1, we begin with definitions and equations that allow us to describe the transmission of polarized laser pulses into the atmosphere; backscatter, extinction, and depolarization of polarized laser radiation by the atmospheric constituents; and the influence of the receiver setup on the depolarization ratio measurements. As a first step in this the-

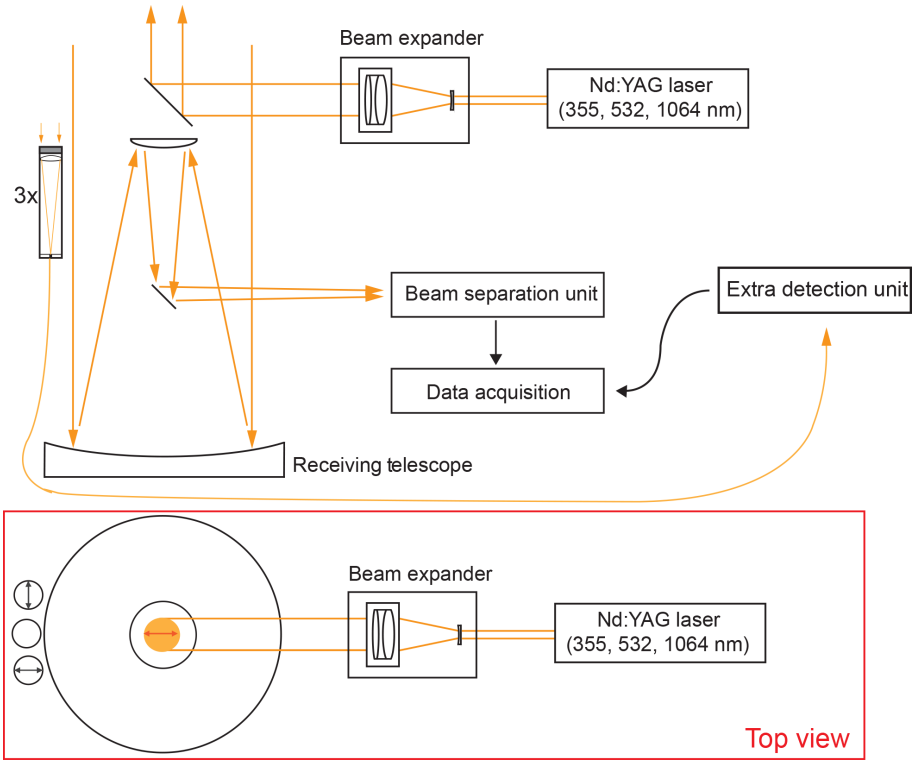

Figure 1. Overview of the EARLINET lidar MARTHA. The three-signal receiver unit of the new polarization lidar setup (details are shown in Fig. 2) is integrated into the MARTHA telescope construction (left side in both of the sketches). The outgoing laser beam is 54 cm away from the new polarization-sensitive receiver unit. The main plane of linear polarization of the laser pulses and the polarization sensitivity of cross- and co-polarized receiver channels are indicated by arrows in the top-view sketch.

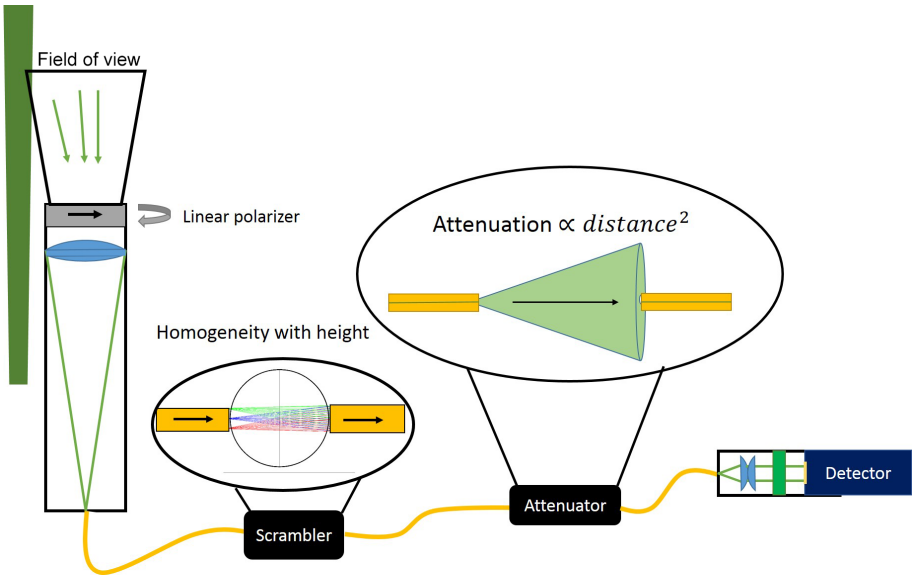

Figure 2. Sketch of one of the three identical receiver channels of the three-signal polarization lidar. The different parts are explained in the text.

oretical framework we will derive three lidar equations for our three measured signal components. In Sect. 3.2, we then present the derivation of the new three-signal method for the determination of the volume depolarization ratio starting from the three lidar equations (one for each channel) defined in Sect. 3.1.

3.1 Theoretical background: three-signal polarization lidar

We follow the explanations and part of the notation of Freudenthaler (2016), Bravo-Aranda et al. (2016), and Belegante et al. (2018) in the description of the lidar setup, from the laser source (as part of the transmitter unit) to the detector unit (as part of the receiver block), and regarding the interaction of the polarized laser light photons with atmospheric particles and molecules by means of the Müller–Stokes formalism (Chipman, 2009). A Stokes vector describes the flux and the state of polarization of the transmitted laser radiation pulses, and Müller matrices describe how the optical elements of the transmitter and receiver units and the atmospheric constituents change the Stokes vector. The laser beam is expanded before transmission into the atmosphere. In most polarization lidar applications it is assumed that the transmitted laser radiation is totally linearly polarized. But this is not the case in practice. In our approach, we therefore take into consideration that the transmitted wave front contains a non-negligible small amount of cross-polarized light after passing through the beam expander. Additionally, we consider a small-angular misalignment, described by angle α between the main polarization plane of the laser beam and the orientation of the respective polarization plane, defined by the polarization filters in front of the telescopes of the receiver unit of our three-channel polarization lidar configuration described in Sect. 2 (these considerations can be visualized in Fig. 3).

The transmitted radiation $P_0(z)$ of the laser pulse can be written as the sum

$$P_0 = P_{0,\parallel} + P_{0,\perp}, \tag{1}$$

with the co- and cross-polarized light components, $P_{0,\parallel}$ and $P_{0,\perp}$, with polarizations parallel and orthogonal to the main plane of laser light polarization. We introduce the so-called cross-talk term ε_1:

$$\varepsilon_1 = \frac{P_{0,\perp}}{P_{0,\parallel}}, \tag{2}$$

which describes the small amount of cross-polarized light in the laser beam after leaving the transmission block of the lidar towards the atmosphere. Now we can write

$$P_0 = (1+\varepsilon_1)\, P_{0,\parallel}. \tag{3}$$

The transmitted electromagnetic wave front is then given by the Stokes vector (Lu and Chipman, 1996).

$$\boldsymbol{I}_{\mathrm{L}} = P_{0,\parallel} \begin{pmatrix} 1+\varepsilon_1 \\ 1-\varepsilon_1 \\ 0 \\ 0 \end{pmatrix} = P_0 \begin{pmatrix} 1 \\ \frac{1-\varepsilon_1}{1+\varepsilon_1} \\ 0 \\ 0 \end{pmatrix} \tag{4}$$

The misalignment between the polarization axis of the transmitted light and the co-polarized receiver channel (defined by the respective polarization filter in front of the detector) is characterized by angle α and described by the rotation Müller matrix (Bravo-Aranda et al., 2016); here we adopt the notation for the trigonometric functions used in Freudenthaler (2016), i.e., $\cos(2\alpha) := c_{2\alpha}$ and $\sin(2\alpha) := s_{2\alpha}$:

$$\begin{aligned} \mathbf{R}(\alpha) &= \begin{pmatrix} 1 & 0 & 0 & 0 \\ 0 & \cos(2\alpha) & -\sin(2\alpha) & 0 \\ 0 & \sin(2\alpha) & \cos(2\alpha) & 0 \\ 0 & 0 & 0 & 1 \end{pmatrix} \\ &= \begin{pmatrix} 1 & 0 & 0 & 0 \\ 0 & c_{2\alpha} & -s_{2\alpha} & 0 \\ 0 & s_{2\alpha} & c_{2\alpha} & 0 \\ 0 & 0 & 0 & 1 \end{pmatrix}. \end{aligned} \tag{5}$$

Then the incident field after backscattering by atmospheric particles and molecules, and before passing the receiver block, can be written as (Freudenthaler, 2016)

$$\begin{aligned} \boldsymbol{I}_{\mathrm{in}} &= \mathbf{F}\mathbf{R}(\alpha)\boldsymbol{I}_{\mathrm{L}} = F_{11} \begin{pmatrix} 1 & 0 & 0 & 0 \\ 0 & a & 0 & 0 \\ 0 & 0 & -a & 0 \\ 0 & 0 & 0 & 1-2a \end{pmatrix} \\ &\quad \begin{pmatrix} 1 & 0 & 0 & 0 \\ 0 & c_{2\alpha} & -s_{2\alpha} & 0 \\ 0 & s_{2\alpha} & c_{2\alpha} & 0 \\ 0 & 0 & 0 & 1 \end{pmatrix} P_0 \begin{pmatrix} 1 \\ \frac{1-\varepsilon_1}{1+\varepsilon_1} \\ 0 \\ 0 \end{pmatrix}, \\ \boldsymbol{I}_{\mathrm{in}} &= F_{11} P_0 \begin{pmatrix} 1 \\ \frac{1-\varepsilon_1}{1+\varepsilon_1} c_{2\alpha} a \\ -\frac{1-\varepsilon_1}{1+\varepsilon_1} s_{2\alpha} a \\ 0 \end{pmatrix}, \end{aligned} \tag{6}$$

with the atmospheric polarization parameter

$$a = \frac{1-\delta}{1+\delta}. \tag{7}$$

The scattering matrix $\mathbf{F}$ describes the interaction of the laser photons with the atmospheric particles and molecules. F_{11} and δ are the backscatter coefficient and the volume linear depolarization ratio, respectively.

The true volume backscatter coefficient ($\beta := F_{11}$) is given by

$$\beta = \beta_{\parallel} + \beta_{\perp} = (1+\delta)\,\beta_{\parallel}, \tag{8}$$

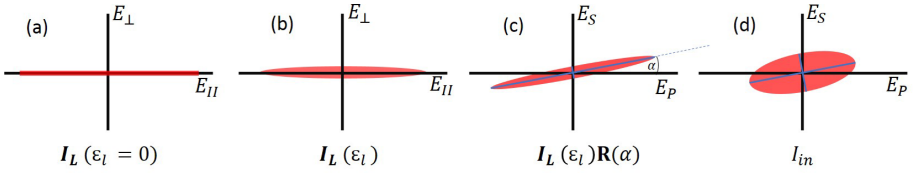

Figure 3. (a) Polarization state of the light generated by the laser (100 % linearly polarized); $\boldsymbol{E}$ denotes electromagnetic field. **(b)** The laser radiation is elliptically polarized after passing the beam expander (see Fig. 1). **(c)** The receiving cross- and co-polarized signal channels ($\boldsymbol{E}_\mathrm{S}$ and $\boldsymbol{E}_\mathrm{P}$) are usually not perfectly aligned to the main polarization plane of the laser radiation, i.e., $\alpha > 0$. **(d)** Polarization plane in the receiver for light which has been backscattered and depolarized by the atmosphere.

with the backscatter contributions for the co- and cross-polarization planes (with respect to the true polarization planes given by the transmitted laser pulses). The volume linear depolarization ratio is defined as

$$\delta\,(z) = \frac{\beta_\perp\,(z)}{\beta_\parallel\,(z)}. \tag{9}$$

Figure 3 illustrates the different polarization states and configurations of the original laser pulses (Fig. 3a) and after leaving the beam expander as elliptically polarized laser light (Fig. 3b). The receiver block may be not well aligned to the main plain of laser radiation so that the photomultiplier measures different cross- and co-polarized signal components with respect the outgoing cross- and co-polarized laser light components in Fig. 3b. The rotated polarization axis is represented in Fig. 3c, and after being backscattered and depolarized, the incident polarization plane has the form as shown in Fig. 3d.

To distinguish the apparent measured volume backscatter coefficient, determined from the actually measured co- and cross-polarized signal components which are related to the incident field $\boldsymbol{I}_\mathrm{in}$ (Eq. 6, see Fig. 3c), we introduce index "in" and have the following relationships and links to the (true) laser light polarization plane:

$$\beta_\mathrm{in} = \beta_{\parallel,\mathrm{in}} + \beta_{\perp,\mathrm{in}} = \beta, \tag{10}$$

$$\beta_{\parallel,\mathrm{in}} - \beta_{\perp,\mathrm{in}} = \frac{1-\varepsilon_1}{1+\varepsilon_1} c_{2\alpha} a\beta. \tag{11}$$

Now using Eq. (10) (describing the first term of $\boldsymbol{I}_\mathrm{in}$ in Eq. 6) and Eq. (11) (describing the second term of $\boldsymbol{I}_\mathrm{in}$ in Eq. 6), the apparent backscatter components $\beta_{\parallel,\mathrm{in}}$ and $\beta_{\perp,\mathrm{in}}$ can be written as

$$\beta_{\parallel,\mathrm{in}} = \left(1 + \frac{(1-\delta)}{(1+\delta)}\frac{(1-\varepsilon_1)}{(1+\varepsilon_1)} c_{2\alpha}\right)\beta/2, \tag{12}$$

$$\beta_{\perp,\mathrm{in}} = \left(1 - \frac{(1-\delta)}{(1+\delta)}\frac{(1-\varepsilon_1)}{(1+\varepsilon_1)} c_{2\alpha}\right)\beta/2. \tag{13}$$

These three backscattering components (Eqs. 10, 12, and 13) can be measured separately using the three different telescopes of our polarization lidar described in Sect. 2.

It is worthwhile to mention that polarization lidars typically have two detection channels, either a cross-polarized and a parallel-polarized channel or a cross-polarized and so-called total channel. A commonly used method for the calibration is to insert an additional polarization filter into the optical path of the receiver unit and to rotate or tilt a $\lambda/2$ plate (Liu and Wang, 2013; Engelmann et al., 2016; McCullough et al., 2017). For these calibrations an extra measurement period is required. This calibration can introduce new and significant uncertainties (Biele et al., 2000; Freudenthaler et al., 2009; Mattis et al., 2009; Haarig et al., 2017).

As mentioned in the introduction, the concept to calibrate a lidar depolarization receiver by using three channels was proposed by Reichardt et al. (2003). The method consists of an absolute calibration procedure based on the measurement of elastically backscattered light with three detection channels for measuring co-, cross-, and totally polarized backscatter components.

To determine the number of counts that the detection channels measure, Müller matrices representing the optical path of each channel would need to be added to Eq. (6). Nevertheless, in this approach we follow the view adopted by Reichardt et al. (2003), in which the traditional lidar equation is used to characterize the lidar channels.

Let us now introduce the lidar equations for these three signals. Following Reichardt et al. (2003), the number of photons N_i that a lidar detects at height z (above the full overlap height) with channel i is given by

$$N_i\,(z) = P_0\left(\eta_{\parallel,i}\beta_{\parallel,\mathrm{in}}\,(z) + \eta_{\perp,i}\beta_{\perp,\mathrm{in}}\,(z)\right) T^2(z)/z^2. \tag{14}$$

P_0 is the number of emitted laser photons and $\eta_{\parallel,i}$ and $\eta_{\perp,i}$ are the optical efficiencies regarding the co- and cross-polarized components ($\beta_{\parallel,\mathrm{in}}$ and $\beta_{\perp,\mathrm{in}}$) of the backscattered light that arrives at the channel-i detector. These efficiencies include instrumental constants that contain the total transmittance through all optical components and gain of the detectors and attenuation in the path of each channel. T denotes the atmospheric single-path transmission and is the same for all three detection channels (co-, cross-, and total) since the extinction is independent of the state of polarization of the light. Rearrangements lead to the following versions of the lidar equations for the cross- (S) and co-polarized (P) channels:

$$N_i\,(z) = P_0\,\eta_{\parallel,i}\left(\beta_{\parallel,\mathrm{in}}\,(z) + D_i\beta_{\perp,\mathrm{in}}\,(z)\right) T^2(z)/z^2, \tag{15}$$

or

$$N_i(z) = P_0\,\eta_{\perp,i}\left(D_i^{-1}\beta_{\parallel,\mathrm{in}}(z) + \beta_{\perp,\mathrm{in}}(z)\right)T^2(z)/z^2. \quad (16)$$

Here D_i denotes the so-called efficiency ratio (Reichardt et al., 2003), and it is defined as

$$D_i := \frac{\eta_{\perp,i}}{\eta_{\parallel,i}}. \quad (17)$$

The absence of optical elements before the polarization filters (such as the telescope itself and beam splitters) avoids further polarization effects, such as diattenuation and retardation, described in detail by Freudenthaler (2016). Moreover, since we employed the same filter model in the optical path of the channels P and S, we assumed that $D_\mathrm{P} = D_\mathrm{S}^{-1}$. In the case of the total signal component ($i = \mathrm{tot}$) we assume that $D_\mathrm{tot} = 1$ and we introduce the overall efficiency η_tot for simplicity reasons. The numbers of photons measured with each of the three channels ($i = \mathrm{P}, \mathrm{S}, \mathrm{tot}$) are then given by

$$N_\mathrm{P}(z) = P_0\eta_{\parallel,\mathrm{P}}\left(\beta_{\parallel,\mathrm{in}}(z) + D_\mathrm{P}\beta_{\perp,\mathrm{in}}(z)\right)T^2(z)/z^2, \quad (18)$$

$$N_\mathrm{S}(z) = P_0\eta_{\perp,\mathrm{S}}\left(\beta_{\perp,\mathrm{in}}(z) + D_\mathrm{S}^{-1}\beta_{\parallel,\mathrm{in}}(z)\right)T^2(z)/z^2, \quad (19)$$

$$N_\mathrm{tot}(z) = P_0\eta_\mathrm{tot}\beta_\mathrm{in}(z)\,T^2(z)/z^2. \quad (20)$$

After further rearranging we finally obtain

$$\frac{N_\mathrm{P}(z)\,z^2}{\eta_{\parallel,\mathrm{P}}P_0T^2(z)} = \beta_{\parallel,\mathrm{in}}(z) + D_\mathrm{P}\beta_{\perp,\mathrm{in}}(z), \quad (21)$$

$$\frac{N_\mathrm{S}(z)\,z^2}{\eta_{\perp,\mathrm{S}}P_0T^2(z)} = \beta_{\perp,\mathrm{in}}(z) + D_\mathrm{S}^{-1}\beta_{\parallel,\mathrm{in}}(z), \quad (22)$$

$$\frac{N_\mathrm{tot}(z)\,z^2}{\eta_\mathrm{tot}P_0T^2(z)} = \beta_\mathrm{in}(z). \quad (23)$$

To consider, in the next step, receiver misalignment and cross-talk effects, we introduced the parameters $\varepsilon_\mathrm{l} = \frac{P_{0,\perp}}{P_{0,\parallel}}$ (Eq. 2), describing the small amount of cross-polarized light in the laser beam after leaving the transmission block into the atmosphere, and the rotation angle α describing the angular misalignment between the transmitter and receiver units. To also consider the receiver–channel cross talk, we further introduce ε_r, defined by $\varepsilon_\mathrm{r} = D_\mathrm{S}^{-1} = D_\mathrm{P}$. The receiver cross-talk value is typically $\varepsilon_\mathrm{r} \leq 10^{-3}$ (according to the filter manufacturer) as here the only element to consider is the polarization filter in front of the telescopes. Now combining Eqs. (10), (12), and (13) with Eqs. (21)–(23), we can write

$$\begin{aligned}\frac{N_\mathrm{P}(z)\,z^2}{\eta_{\parallel,\mathrm{P}}P_0T^2(z)} &= \beta_{\parallel,\mathrm{in}}(z) + \varepsilon_\mathrm{r}\beta_{\perp,\mathrm{in}}(z)\\ &= \left(1 + \varepsilon_\mathrm{r} + \frac{(1-\delta(z))}{(1+\delta(z))}\frac{(1-\varepsilon_\mathrm{l})}{(1+\varepsilon_\mathrm{l})}(1-\varepsilon_\mathrm{r})c_{2\alpha}\right)\\ &\quad\cdot\beta(z)/2, \quad (24)\end{aligned}$$

$$\begin{aligned}\frac{N_\mathrm{S}(z)\,z^2}{\eta_{\perp,\mathrm{S}}P_0T^2(z)} &= \beta_{\perp,\mathrm{in}}(z) + \varepsilon_\mathrm{r}\beta_{\parallel,\mathrm{in}}(z)\\ &= \left(1 + \varepsilon_\mathrm{r} - \frac{(1-\delta(z))}{(1+\delta(z))}\frac{(1-\varepsilon_\mathrm{l})}{(1+\varepsilon_\mathrm{l})}(1-\varepsilon_\mathrm{r})c_{2\alpha}\right)\\ &\quad\cdot\beta(z)/2, \quad (25)\end{aligned}$$

$$\frac{N_\mathrm{tot}(z)\,z^2}{\eta_\mathrm{tot}P_0T^2(z)} = \beta_\mathrm{in}(z) = \beta(z). \quad (26)$$

Until this point, the analytical procedure has been based on the assumption that the polarization filters in front of the cross- and co-polarized telescopes are pointing 90° with respect to each other. However, in the general case, when their angular deviation with respect to their respective components is different (E_P to $E_\parallel$ and E_S to $E_\perp$), Eqs. (24) and (25) have a different angular component. In this approach, we keep this assumption for the development of a simple calibration procedure. In Appendix A, the general case is evaluated (angle P to $S \neq 90°$), and based on a measurement example, we demonstrated that the impact of this assumption can be neglected in our system.

3.2 Determination of calibration constants and the volume linear depolarization ratio

Outgoing from Eqs. (24)–(26) we will define instrumental (interchannel) constants which are required to calibrate the lidar in the experimental practice and which are also used in the determination of the volume linear depolarization ratio. The equations for the determination of the depolarization ratios will be given. Three different ways can be used to determine the linear depolarization ratio profiles.

Considering Eq. (26) and the sum of Eqs. (24) and (25), we can write

$$\frac{N_\mathrm{tot}(z)}{\eta_\mathrm{tot}} = \frac{1}{1+\varepsilon_\mathrm{r}}\left(\frac{N_\mathrm{P}(z)}{\eta_{\parallel,\mathrm{P}}} + \frac{N_\mathrm{S}(z)}{\eta_{\perp,\mathrm{S}}}\right). \quad (27)$$

Equation (27) is independent of the transmission cross-talk factor ε_l and of the rotation of the receiver axis (and thus rotation angle α) but depends on the receiver cross-talk factor ε_r.

Let us introduce the interchannel instrumental constants

$$X_\mathrm{P} = \frac{\eta_\mathrm{tot}}{(1+\varepsilon_\mathrm{r})\,\eta_{\parallel,\mathrm{P}}}, \quad (28)$$

$$X_\mathrm{S} = \frac{\eta_\mathrm{tot}}{(1+\varepsilon_\mathrm{r})\,\eta_{\perp,\mathrm{S}}}, \quad (29)$$

$$X_\delta = \frac{\eta_{\parallel,\mathrm{P}}}{\eta_{\perp,\mathrm{S}}} = \frac{X_\mathrm{S}}{X_\mathrm{P}}, \quad (30)$$

and the signal ratios R_P, R_S, and R_δ

$$R_\mathrm{P}(z) = N_\mathrm{P}(z)/N_\mathrm{tot}(z), \quad (31)$$

$$R_\mathrm{S}(z) = N_\mathrm{S}(z)/N_\mathrm{tot}(z), \quad (32)$$

$$R_\delta(z) = N_\mathrm{S}(z)/N_\mathrm{P}(z). \quad (33)$$

By using these definitions, Eq. (27) (after multiplication with $\frac{\eta_\mathrm{tot}}{N_\mathrm{tot}(z)}$) can be rearranged to

$$X_\mathrm{P}R_\mathrm{P}(z) + X_\mathrm{S}R_\mathrm{S}(z) = 1. \quad (34)$$

Equation (34) is only valid for the case of an almost ideal polarization lidar receiver unit, i.e., when $D_S^{-1} = D_P(= \varepsilon_r)$. This is not the case for most lidar systems in which the receiver and separation unit may introduce differences between the transmission ratios D_S^{-1} and D_P. In the next step, we form the difference of Eq. (34) for altitude z_j minus Eq. (34) for altitude z_k and obtain

$$X_\delta\left(z_j, z_k, t\right) = -\frac{R_P\left(z_j, t\right) - R_P\left(z_k, t\right)}{R_S\left(z_j, t\right) - R_S(z_k, t)}. \tag{35}$$

In the same way, when Eq. (27) is multiplied by $\frac{\eta_{\perp,S}}{N_S(z)}$ and $\frac{\eta_{\parallel,P}}{N_P(z)}$, we can derive Eqs. (36) and (37), respectively.

$$X_S\left(z_j, z_k, t\right) = \frac{R_P^{-1}\left(z_j, t\right) - R_P^{-1}\left(z_k, t\right)}{R_\delta\left(z_j, t\right) - R_\delta\left(z_k, t\right)} \tag{36}$$

$$X_P\left(z_j, z_k, t\right) = \frac{R_S^{-1}\left(z_j, t\right) - R_S^{-1}\left(z_k, t\right)}{R_\delta^{-1}\left(z_j, t\right) - R_\delta^{-1}\left(z_k, t\right)} \tag{37}$$

t denotes time.

In the conventional three-signal calibration approach, each signal is normalized to a reference altitude; by doing so the efficiencies of the three channels $\eta_{\parallel,P}$, $\eta_{\perp,S}$, and η_{tot} cancel themselves from the equations. Then the ratios between the three normalized signals are calculated. The retrieval of the volume depolarization ratio is performed by solving a system of two equations and two unknowns: the volume depolarization ratio at a reference height $\delta(z_0)$ and the volume depolarization ratio at all heights $\delta(z)$ (Reichardt et al., 2003).

In this extended three-signal calibration procedure, the signals are not normalized to a reference height z_0; instead, we directly divide the signals, obtaining the ratios R_P, R_S, and R_δ. By then taking the difference between two altitudes (and not the ratio) we subtract the cross talk in the emission and reception (ε_l and ε_r) and the angular misalignment ($c_{2\alpha}$). The difference additionally offers a better performance in terms of error propagation compared to the ratio. In this way, the so-called interchannel constants (X_δ, X_S, and X_P) remain in the equations and they can be estimated by evaluating Eqs. (35), (36), and (37), respectively. Although we can estimate these three constants, we have to note that the number of unknowns are actually two X_P and X_S, with the third constant X_δ being the ratio of them (please see Eq. 30); i.e., Eq. (35) is equivalent to Eq. (36) divided by Eq. (37).

Given the form of Eqs. (35)–(37), observable differences between the height points z_j and z_k are needed for its evaluation. In practice, only altitude regions should be selected in the determination of X_P, X_S, and X_δ where significant changes in the depolarization ratio occur, e.g., in liquid-water clouds in which multiple scattering by droplets produces steadily increasing depolarization with increasing penetration of laser light into the cloud (Donovan et al., 2015; Jimenez et al., 2017, 2018). Long measurement periods should be considered for the evaluation of Eqs. (35)–(37). All pairs of data points (z_j and z_k in a certain height range, defined according to the ratio of signals) in all single measurements (in time t) provide an array with many observations of the interchannel constants. Averaging these arrays we obtain a trustworthy estimate of these constants for the retrieval of the volume depolarization ratio (please see Fig. 6).

To derive the linear depolarization ratio, we divide Eq. (25) by Eq. (24).

$$\begin{aligned}\frac{N_S}{N_P}\frac{\eta_{\parallel,P}}{\eta_{\perp,S}} &= X_\delta R_\delta \\ &= \frac{(1+\varepsilon_r)(1+\varepsilon_l) - \frac{(1-\delta)}{(1+\delta)}(1-\varepsilon_l)(1-\varepsilon_r)c_{2\alpha}}{(1+\varepsilon_r)(1+\varepsilon_l) + \frac{(1-\delta)}{(1+\delta)}(1-\varepsilon_l)(1-\varepsilon_r)c_{2\alpha}}\end{aligned} \tag{38}$$

Furthermore, we introduce the total cross-talk factor ξ_{tot},

$$\xi_{tot} = \frac{(1+\varepsilon_r)(1+\varepsilon_l)}{(1-\varepsilon_l)(1-\varepsilon_r)c_{2\alpha}} \geq 1, \tag{39}$$

which takes account of the combined effect of the emitted elliptically polarized wave front ε_l, of the angular misalignment between emitter and receiver (described by the rotation angle α), and of the cross talk among receiver channels described by ε_r. The factor ξ_{tot} would be equal to 1 if the emitted laser pulses are totally linearly polarized, misalignment of the receiver unit could be avoided, and cross talk among receiver channels would be negligible.

Now Eq. (38) can be rewritten after dividing the numerator and denominator by $(1-\varepsilon_l)(1-\varepsilon_r)c_{2\alpha}$ and rearranging the equation:

$$X_\delta R_\delta = \frac{\xi_{tot} - \frac{(1-\delta)}{(1+\delta)}}{\xi_{tot} + \frac{(1-\delta)}{(1+\delta)}}, \tag{40}$$

and the volume depolarization ratio can be obtained from Eq. (40) after rearrangement,

$$\delta(R_\delta, X_\delta, \xi_{tot}) = \frac{1 - \xi_{tot} + X_\delta R_\delta\,(1+\xi_{tot})}{1 + \xi_{tot} + X_\delta R_\delta\,(1-\xi_{tot})}. \tag{41}$$

As shown in Eq. (41), the volume depolarization ratio can be calculated by using the ratio R_δ between the cross- and co-polarized signals and when the constants X_δ and ξ_{tot} are known. As a first step of the calibration, the interchannel constant X_δ (together with X_P and X_S) is obtained from the measurements by evaluating Eqs. (35)–(37) in the selected height range (with variations in the depolarization) at each measurement time t. Then ξ_{tot} can be estimated in a region (defined by height z_{mol}) with dominating Rayleigh backscattering for which the volume depolarization ratio, δ_{mol}, is assumed as constant and known. Behrendt and Nakamura (2002) theoretically estimated a value of the linear depolarization ratio caused by molecules of 0.0046 for a lidar system whose interference filters have a full width at half maximum (FWHM) = 1.0 nm. However, Freudenthaler et al. (2016) have found a

value of 0.005 ± 0.012 based on long-term measurements in aerosol and cloud-free tropospheric height regions. We used this value and we have considered the propagation of this systematic uncertainty in our calculations. Thus, from Eq. (41) ξ_{tot} is given by

$$\xi_{\mathrm{tot}} = \left(\frac{1-\delta_{\mathrm{mol}}}{1+\delta_{\mathrm{mol}}}\right)\left(\frac{1+X_\delta R_\delta(z_{\mathrm{mol}})}{1-X_\delta R_\delta(z_{\mathrm{mol}})}\right). \quad (42)$$

By calculating the ratio between Eqs. (24) and (26) (co to total) or the ratio between Eqs. (25) and (26) (cross- to total), the volume depolarization ratio can also be derived:

$$\delta(R_{\mathrm{S}}, X_{\mathrm{S}}, \xi_{\mathrm{tot}}) = \frac{1-\xi_{\mathrm{tot}}(1-2X_{\mathrm{S}}R_{\mathrm{S}})}{1+\xi_{\mathrm{tot}}(1-2X_{\mathrm{S}}R_{\mathrm{S}})}, \quad (43)$$

$$\delta(R_{\mathrm{P}}, X_{\mathrm{P}}, \xi_{\mathrm{tot}}) = \frac{1-\xi_{\mathrm{tot}}(2X_{\mathrm{P}}R_{\mathrm{P}}-1)}{1+\xi_{\mathrm{tot}}(2X_{\mathrm{P}}R_{\mathrm{P}}-1)}. \quad (44)$$

In summary, the volume linear depolarization ratio can be calculated after the determination of the constants X_{P}, X_{S}, X_δ, and ξ_{tot}. Then the signal ratio profiles $R_{\mathrm{P}}(z)$, $R_{\mathrm{S}}(z)$, and $R_\delta(z)$ are required and calculated within Eqs. (31), (32), and (33), and by considering Eqs. (41), (43), and (44) the depolarization ratio can finally be calculated by using the pair of signals N_{S} and N_{P}, the pair N_{S} and N_{tot}, or the pair N_{P} and N_{tot}, respectively. However, the expected errors in the retrievals are not the same for all of these pairs since they present different sensitivities to changes in the depolarization ratio, obtaining the largest uncertainties when the pair N_{P} and N_{tot} is used.

4 Observations

4.1 Application of the calibration approach to a measurement case

To test the method introduced in Sect. 3, the measurement case from 19 September 2017 was analyzed and the results are presented in this section. Figure 4 provides an overview of the atmospheric situation. An aerosol layer reached up to about 2.8 km in height and was topped by a persistent, shallow altocumulus deck with a cloud base height at 2.6–2.7 km a.g.l. (above ground level).

Although the time resolution of the lidar measurements is 30 s, to reduce computing time and signal noise, we consider 5 min average measurements. Figure 5 shows the three range-corrected signals of the polarization lidar, the signal ratios as defined by Eqs. (31)–(33), and the corresponding inverse ratios for a 5 min measurement as an example.

In the next step of the data analysis and calibration procedure, we selected the height range from a few meters below cloud base up to 240 m above cloud base for each 5 min averaging period t. Then we computed the instrumental inter-channel ratios $X_{\mathrm{P}}(z_j, z_k, t)$, $X_{\mathrm{S}}(z_j, z_k, t)$, and $X_\delta(z_j, z_k, t)$ with Eqs. (37), (36), and (35), respectively. Height resolution was 7.5 m. The result is shown in Fig. 6.

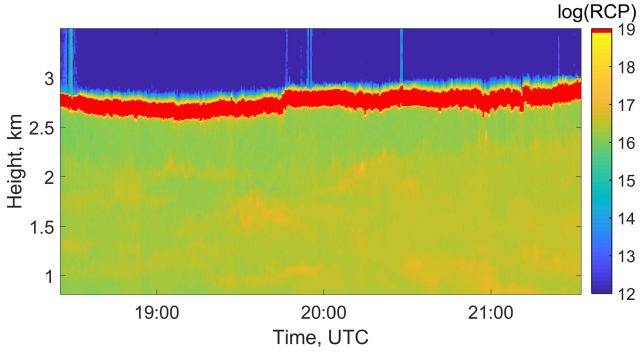

Figure 4. Range-corrected 532 nm total backscatter signal (RCP) measured on 19 September 2017 with 30 s and 7.5 m vertical resolution.

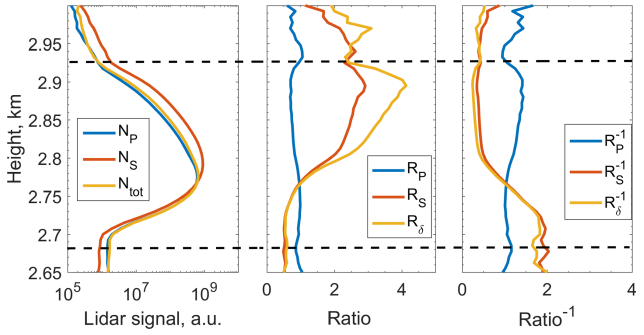

Figure 5. Example of a 5 min profile of range-corrected lidar signals from the channels, signal ratios, and inverse ratios. The calibration procedure considers all signals of the 3 h measurement period shown in Fig. 4. The dashed line indicates the range in which the calibration calculations were carried out.

The mean values of the constants with the respective statistical error based on Fig. 6 are $X_{\mathrm{P}} = 0.965 \pm 0.012$, $X_{\mathrm{S}} = 0.108 \pm 0.005$, and $X_\delta = 0.110 \pm 0.006$. The reason for these low uncertainties is that the calibration is performed in a cloudy region so that every channel shows high count rates and thus high signal-to-noise ratios.

Using the constant X_δ and evaluating Eq. (42) in the particle-free region of the 3 h measurement period, a mean value of $\xi_{\mathrm{tot}} = 1.118 \pm 0.008$ for the total cross talk was obtained. Given the form of the equations to retrieve the profiles of volume depolarization ratio (Eqs. 35–37), the propagated uncertainty associated with ξ_{tot} does not vary largely with height, which leads to a large percentage uncertainty on the retrieval of the volume linear depolarization ratio in the region with low depolarization ratios, also characterized by low signal strengths. Table 1 summarize the retrieved instrumental constants for the measurement case presented.

Figure 7 presents the height profiles of the volume linear polarization ratio computed by means of Eqs. (41), (43), and (44). Good agreement among the different solutions is visible. However, the depolarization ratios obtained from the channels N_{P} and N_{tot} (blue) show the largest uncertainties,

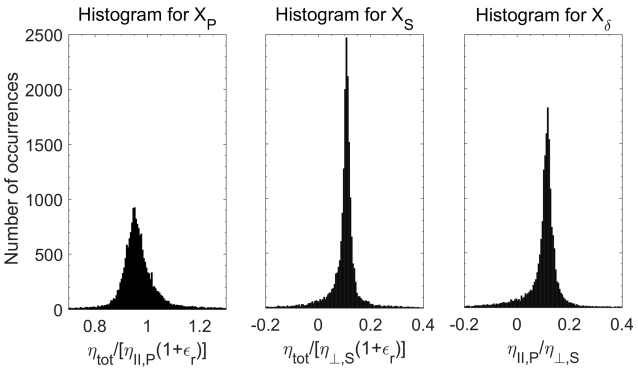

Figure 6. Histograms for the interchannel constants X_P, X_S, and X_δ. Each point corresponds to a combination of z_j and z_k in a 5 min period, obtaining about 18 000 data points for this 3 h measurement case.

Table 1. Values of the instrumental interchannel constants and cross-talk factor determined for the measurement case presented.

Instrumental constant	Value
X_P	0.965 ± 0.012
X_S	0.108 ± 0.005
X_δ	0.110 ± 0.006
ξ_{tot}	1.118 ± 0.008

especially above the cloud layer. The profile-mean absolute uncertainties from the ground up to the cloud top (3.1 km) for $\delta(R_P, X_P)$, $\delta(R_S, X_S)$, and $\delta(R_\delta, X_\delta)$ are 0.034, 0.0139, and 0.0137, respectively. The three derived depolarization ratios agree well in the cloud region. Differences appear in the upper part of the cloud caused by strongly reduced count rates due to the strong attenuation of all the channels, in order to avoid signal saturation at low level clouds.

Figure 8 presents the volume depolarization ratio with 30 s temporal resolution. The signal ratio R_δ and the constant X_δ were used. These profiles are the basis for the retrieval of the microphysical properties of the liquid-water cloud. The results will be discussed in a follow-up article (Jimenez et al., 2019).

To validate the new system and the calibration procedure a comparison among the measurements of the volume linear depolarization ratio with the lidar systems MARTHA and BERTHA (Backscatter Extinction Lidar Ratio Temperature and Humidity profiling Apparatus) is presented in Fig. 9. The observations were conducted at Leipzig (51° N, 12° E) on 29 May 2017 with the presence of a dust layer between 2 and 5 km and a cirrus cloud at 11 km (see Fig. 9a). Good agreement in the dust layer can be noted, while the cirrus cloud shows differences between the two systems. That difference can be attributed to the fact that the BERTHA system is pointing 5° with respect to the zenith, while the MARTHA system points to the zenith (0°). This could lead to specular

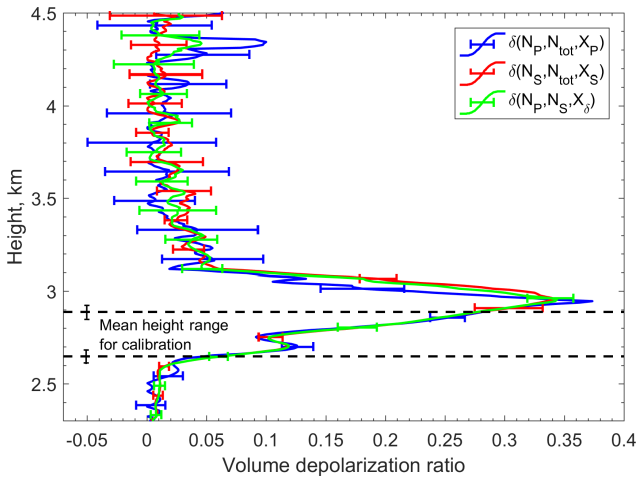

Figure 7. Profiles of the volume linear depolarization ratio for the 3 h period in the cloud region, using the three pairs of signal ratios presented in Eqs. (41), (43), and (44). The error bars include the statistical and systematical uncertainties. The dashed lines indicate the mean height range (of 240 m) at which the calculation of the interchannel constants was performed.

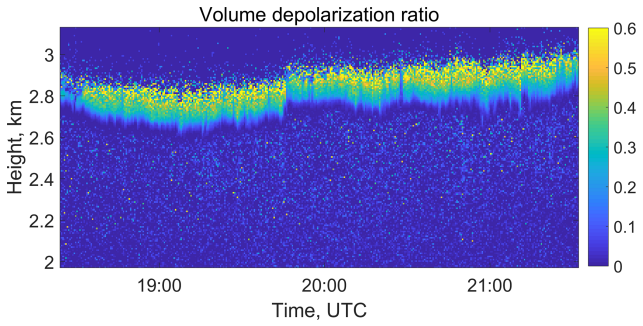

Figure 8. Volume linear depolarization ratio for the entire 3 h period, shown in Fig. 4. The temporal resolution is 30 s.

reflection by horizontally oriented ice crystals reducing the depolarization ratio in the case of the MARTHA system.

A second measurement period during a unique event with a dense biomass burning smoke layer in the stratosphere on 22 August 2017 was considered for comparison (Haarig et al., 2018). Here very good agreement for the layer between 5 and 7 km and also for the layer at 14 km was obtained, confirming the good performance of the systems and of the respective calibration procedures, extended three-signal method in MARTHA, and $\Delta 90°$ method in the BERTHA system.

4.2 Temporal stability of the polarization lidar calibration and performance

The time series of the interchannel constant X_δ obtained from MARTHA observations between days 120 and 320 of 2017 is presented in Fig. 10. The respective time series of

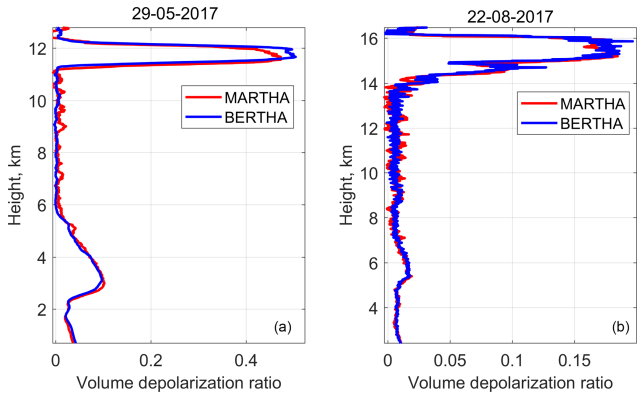

Figure 9. Volume linear depolarization ratio obtained with MARTHA (extended three-signal method) and BERTHA ($\Delta 90°$ method) on **(a)** 29 May 2017, 20:20–20:45 UTC (with smooth 27 bins) and **(b)** 22 August 2017, 20:45–23:15 UTC (Haarig et al., 2018). The systems were calibrated independently. The systems were located at a distance of 80 m.

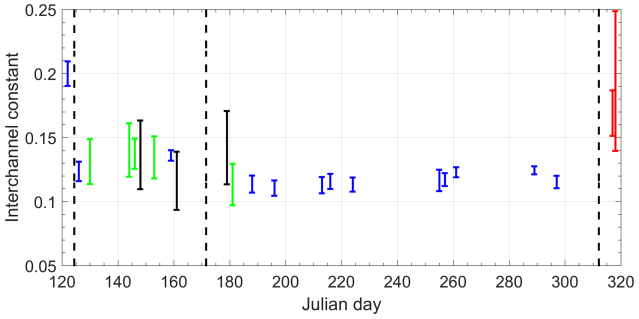

Figure 10. Time series of the interchannel calibration constant X_δ measured from the end of April to mid-November 2017. The vertical bars show the uncertainty in the retrieval. The calibration procedure was based on lidar measurements in liquid-water clouds (blue) and cirrus clouds (green) and during optically thick cumulus events (black) and Saharan dust periods (red). The dashed lines indicate the days when changes in the attenuation configuration of the channels were made.

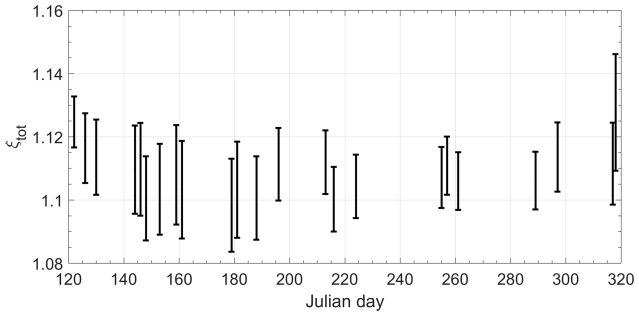

Figure 11. Time series of the total cross-talk factor ξ_{tot} measured in 2017. The vertical bars show the uncertainty in the retrieval, which includes the statistical error from the determination of the interchannel constants and systematical errors from the value considered in the molecular region 0005 ± 00012.

ξ_{tot} is given in Fig. 11. As can be seen, the calibration values show the lowest uncertainties in the interchannel constants (of about 4 %) when altocumulus layers with a stable cloud base and moderate light extinction were present. Higher uncertainty levels were observed in the case of cirrus clouds (green, 11 %) and the Saharan dust layer (red, 17 %). In the case of very thick cumulus clouds (black), the mean uncertainty was 21 %. One reason for these differences in the uncertainty of X_δ is that the system was optimized for the observation of low-altitude liquid-water clouds, for which the detection channels need large attenuation to avoid saturation of the detectors in the cloud layer. This setup prohibited an optimum detection of high-level dust layers and ice clouds due to the low signal strength for these cases. Furthermore, liquid clouds are favorable for calibration because the volume depolarization ratio increases very smoothly as a result of the increasing multiple scattering impact. At these conditions, a large number of measurement pairs for heights z_j and z_k with different depolarization ratios are available. Some slight changes of X_δ occurred when the attenuation configuration of the polarization receivers was changed. Small day-to-day changes were caused by small variations in the response of each detector with time.

In Fig. 10 the retrieved values of ξ_{tot} are shown; small variations can be seen but they remain much lower than the uncertainties, and no stronger variations can be noted with changes in the attenuation or changes of the calibration medium (water cloud, cirrus, Saharan dust layer). In 2017, the mean value $\xi_{tot} = 1.109 \pm 0.009$.

5 Summary and conclusions

In this work a new formalism to calibrate polarization lidar systems based on three detection channels has been presented. We propose a simple lidar polarization receiver, based on three telescopes (one for each channel) with a polarization filter on the front (in the case of the cross- and co-polarized channels). This setup removes the effect of the receiver optics on the polarization state of the collected backscattered light, simplifying the measurement concept. The derivation of the volume linear depolarization ratio considering the instrumental effects on the proposed system was described in Sect. 3. Here there are three effects considered: the emitted laser beam (after beam expander) is slightly elliptically polarized (ε_l), there is an angular misalignment (α) of the receiver unit with respect to the main polarization plane of the emitted laser pulses, and there is a small cross-talk amount in the detection channels (co- and cross-) (ε_r). These instrumental parameters can be summarized into one single constant, the so-called total cross talk (ξ_{tot}).

The methodology does not require a priori knowledge about the behavior of the instrument in terms of polariza-

tion and permits the determination of the so-called interchannel constants X_P, X_S, and X_δ, which depend on the attenuation and detector response of each channel, and thus it is expected to vary among different measurement days. In the free-aerosol region the total cross talk can also be estimated by means of long-term measurements. In our case we estimated a mean value of $\xi_{tot} = 1.109 \pm 0.009$. The calibration is based on actual lidar measurement periods, providing large numbers of input data for accurate estimation of the mean value of the instrumental constants. However, it needs a strong depolarizing medium for its application, such as dust layers and also water clouds, which depolarize the light due to multiple scattering in droplets or due to single scattering of ice particles.

A case study of a liquid-water cloud observation was presented. The 3 h period demonstrates the potential of the new technique for the retrieval of accurate high-temporal-resolution depolarization profiles. The method is simple to implement and allows high-quality depolarization ratio studies. Temporal studies indicated the robustness and stability of the three-signal lidar system over long time periods. A comparison with a second polarization lidar shows excellent agreement regarding the derived volume linear polarization ratio of biomass burning smoke throughout the troposphere and the lower stratosphere up to 16 km in height.

Data availability. The lidar data used for this research can be accessed by request to the Leibniz Institute for Tropospheric Research.

Appendix A: General case regarding the rotation of the polarization filters with respect to the true polarization axis of the emitted light

For the derivation outlined in Sect. 3 it is assumed that the polarization filters in front of the cross- and co-polarized telescopes are pointing 90° with respect to each other. However, in the general case, when their angular deviation with respect to their respective components is different (E_P to $E_\parallel$ and E_S to $E_\perp$), Eqs. (24) and (25) have a different angular component. In this Appendix we analyze this general case and discuss the need of implementation depending on the results obtained.

We define the angles α_P and α_S as the angular misalignment of the channels E_P and E_S with respect to $E_\parallel$ and $E_\perp$, respectively (see Fig. A1). We rewrite Eqs. (24)–(26), we factorize by $(1+\varepsilon_r)$, and to simplify the expression we adopt the polarization parameter $a = \frac{(1-\delta)}{(1+\delta)}$ again. We do not use the short notation of the cosine adopted in Sect. 3.

$$\frac{N_P(z)\,z^2}{\eta_{\parallel,P}\,P_0 T^2(z)} = \beta_{\parallel,in}(z) + \varepsilon_r \beta_{\perp,in}(z)$$
$$= (1+\varepsilon_r)\left(1 + a(z)\frac{(1-\varepsilon_l)}{(1+\varepsilon_l)}\frac{(1-\varepsilon_r)}{(1+\varepsilon_r)}\cos(2\alpha_P)\right)$$
$$\cdot\,\beta(z)/2 \tag{A1}$$

$$\frac{N_S(z)\,z^2}{\eta_{\perp,S}\,P_0 T^2(z)} = \beta_{\parallel,in}(z) + \varepsilon_r \beta_{\perp,in}(z)$$
$$= (1+\varepsilon_r)\left(1 - a(z)\frac{(1-\varepsilon_l)}{(1+\varepsilon_l)}\frac{(1-\varepsilon_r)}{(1+\varepsilon_r)}\cos(2\alpha_S)\right)$$
$$\cdot\,\beta(z)/2 \tag{A2}$$

$$\frac{N_{tot}(z)\,z^2}{\eta_{tot}\,P_0 T^2(z)} = \beta_{in}(z) = \beta(z) \tag{A3}$$

In a way similar to how we defined ξ_{tot}, we define the total cross-talk factor for the co- and cross-polarized channels.

$$\xi_P = \frac{(1+\varepsilon_r)(1+\varepsilon_l)}{(1-\varepsilon_l)(1-\varepsilon_r)\cos(2\alpha_P)} \geq 1 \tag{A4}$$

$$\xi_S = \frac{(1+\varepsilon_r)(1+\varepsilon_l)}{(1-\varepsilon_l)(1-\varepsilon_r)\cos(2\alpha_S)} \geq 1 \tag{A5}$$

The three-signal polarization equation (Eq. 27) can be rewritten in a general form, when adding Eqs. (A1) and (A2) and considering Eq. (A3):

$$\left(\frac{N_P(z)}{\eta_{\parallel,P}} + \frac{N_S(z)}{\eta_{\perp,S}}\right) = (1+\varepsilon_r)\,(1+a(z)(\xi_P^{-1} - \xi_S^{-1})/2)\frac{N_{tot}(z)}{\eta_{tot}}. \tag{A6}$$

The term $\xi_P^{-1} - \xi_S^{-1}$ depends on the difference of the cosines of $2\alpha_P$ and $2\alpha_S$. We define the parameter ξ_S^P, which accounts for the difference of the impact of the polarization channels.

$$\xi_S^P := (\xi_P^{-1} - \xi_S^{-1})/2$$

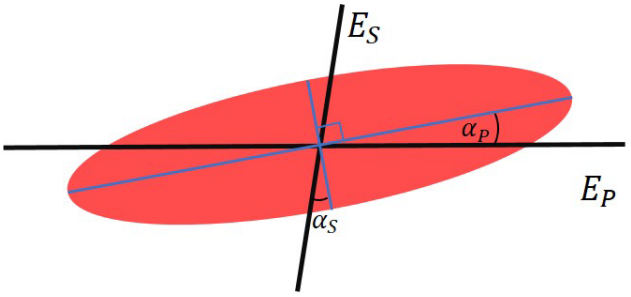

Figure A1. Scheme of the observation of the polarization state of the backscattered light (similar to Fig. 3). The co-polarized and cross-polarized channels are misaligned with respect to their components at angles α_P and α_S, respectively.

$$= \frac{(1-\varepsilon_l)(1-\varepsilon_r)}{2(1+\varepsilon_l)(1+\varepsilon_r)}(\cos(2\alpha_P) - \cos(2\alpha_S)) \tag{A7}$$

This factor can be positive or negative, depending on which polarization filter is more misaligned, and it is equal to zero when they point 90° with respect to each other. Equation (A6) can be expressed as

$$\left(\frac{N_P(z)}{\eta_{\parallel,P}} + \frac{N_S(z)}{\eta_{\perp,S}}\right) = (1+\varepsilon_r)\,(1+\xi_S^P a(z))\frac{N_{tot}(z)}{\eta_{tot}}. \tag{A8}$$

We adopt the notation

$$\Delta R_P(z_j, z_k) = R_P(z_j) - R_P(z_k) \tag{A9}$$

to account for the difference among the signal ratios R_P, R_S, and R_δ, between the polarization parameter a, and between the ratios a/R_S and a/R_P at the heights z_j and z_k. In an way equivalent to how we derived Eqs. (35)–(37) we can obtain a general solution for the instrumental interchannel constants:

$$X_P(z_j, z_k) = \frac{\Delta R_S^{-1}(z_j, z_k) + \xi_S^P \Delta\left(\frac{a}{R_S}(z_j, z_k)\right)}{\Delta R_\delta^{-1}(z_j, z_k)}, \tag{A10}$$

$$X_S(z_j, z_k) = \frac{\Delta R_P^{-1}(z_j, z_k) + \xi_S^P \Delta\left(\frac{a}{R_P}(z_j, z_k)\right)}{\Delta R_\delta(z_j, z_k)}, \tag{A11}$$

$$X_\delta(z_j, z_k) = \frac{-\Delta R_P(z_j, z_k) + \xi_S^P \frac{\Delta a(z_j, z_k)}{X_P}}{\Delta R_S(z_j, z_k)}. \tag{A12}$$

In an absolute sense it would not be possible to determine the interchannel constants X_P, X_S, and X_δ without knowing the polarization parameter (or the depolarization ratio); however, the impact on Eqs. (A10)–(A12) of their respective second term can be very small since it depends on the difference of the cosines of small angles, for example, if $2\alpha_P = 5°$ and $2\alpha_S = 10°$, using Eq. (A7) $\xi_S^P = 0.005\frac{(1-\varepsilon_l)(1-\varepsilon_r)}{(1+\varepsilon_l)(1+\varepsilon_r)}$. Considering this small effect, a first guess of the polarization parameter would be sufficient to solve Eqs. (A10)–(A12).

Calculating the three ratios among Eqs. (A1), (A2), and (A3), we can obtain the volume linear depolarization ratio,

similarly to how it was performed for Eqs. (41), (43), and (44).

$$\delta(R_S, X_S, \xi_S) = \frac{1-\xi_S\,(1-2X_S R_S)}{1+\xi_S\,(1-2X_S R_S)} \tag{A13}$$

$$\delta(R_P, X_P, \xi_P) = \frac{1-\xi_P\,(2X_P R_P-1)}{1+\xi_P\,(2X_P R_P-1)} \tag{A14}$$

$$\delta(R_\delta, X_\delta, \xi_P, \xi_S) = \frac{1+\frac{\xi_S}{\xi_P} X_\delta R_\delta - \xi_S(1-X_\delta R_\delta)}{1+\frac{\xi_S}{\xi_P} X_\delta R_\delta + \xi_S(1-X_\delta R_\delta)} \tag{A15}$$

$$a = \frac{1-\delta}{1+\delta} \tag{A16}$$

In the measurement example presented, we performed an iterative computation procedure to determine the interchannel calibration constants and the cross-talk factors. Using Eqs. (A10)–(A12), in a first run we determined the interchannel constants when we assume $\xi_S^P = 0$, i.e., $\alpha_P = \alpha_S$. A first guess of the volume depolarization ratio using each pair of signals is obtained (Eqs. A13–A15), and then the corresponding cross talks ξ_P and ξ_S are determined by imposing a mean value of $\delta = 0.005 \pm 0.012$ in the free-aerosol region (Freudenthaler et al., 2016b). The second run takes the values of $\xi_S^P \neq 0$ and of the polarization parameter $a\,(z,t)$ (Eqs. A14 and A16) from the first run and the interchannel constants are computed again. Figure A2 shows the results of performing the calibration iteratively. Small differences between the values obtained in the first and second run can be noted; in fact, the variations are smaller than the error of the respective constants, and we can see that after the second run, all values remain practically constant. The mean values of the instrumental constants after six iterations are listed in Table A1.

In this measurement case we found a value for $\xi_S^P = -0.008$. Due to this small value there are no important variations between the first guess and the second run; therefore we conclude that by assuming $\xi_S^P = 0$ a fast and practical inversion procedure is possible. However, in cases with larger differences between α_P and α_S, an iterative procedure as described above would be needed.

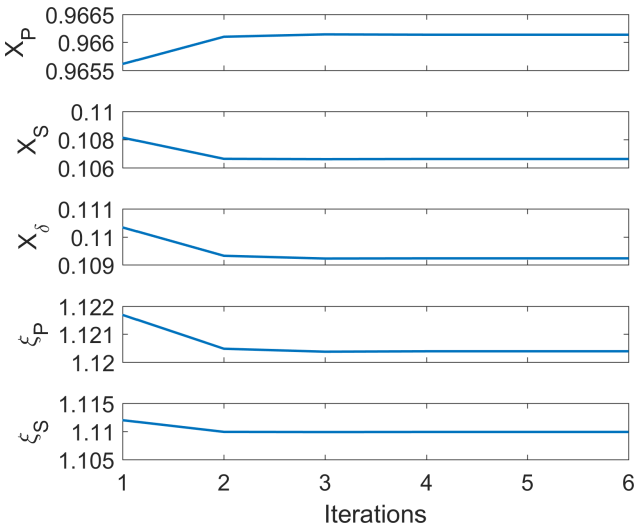

Figure A2. Instrumental channels obtained with an iterative procedure. We did not include the error bars since they are much larger than the variations among runs.

Table A1. Results of the instrumental constants after using the iterative procedure (six runs).

Instrumental constant	Value
X_P	0.966 ± 0.011
X_S	0.106 ± 0.005
X_δ	0.109 ± 0.006
ξ_P	1.120 ± 0.007
ξ_S	1.110 ± 0.007

This general solution for the lidar three-signal problem converges to the same results when we also consider that the receiver cross talk can eventually be different for the channels P and S. In that case we would have $\varepsilon_{r,P}$ and $\varepsilon_{r,S}$, which would also lead to two constants ξ_P and ξ_S to determine. For simplicity this section only discussed the effect of the different angular misalignment of channels P and S.

Appendix B: Description of the variables used in the approach

z	Height.
a	Atmospheric polarization parameter. Varies with height z.
δ	Atmospheric volume depolarization ratio, so that $\delta = \frac{1-a}{1+a}$.
δ_{mol}	Volume depolarization ratio in the free-aerosol region. Assumed constant and known.
β	Backscattering coefficient. Equal to the element F_{11} from the atmospheric scattering matrix.
β_{in}	Backscatter that arrives at the receiver and it is measured by the total channel $\beta_{\mathrm{in}} = \beta$ in our system ($D_{\mathrm{tot}} = 1$).
$\beta_{\parallel,\mathrm{in}}$	Parallel component of the arriving backscatter.
$\beta_{\perp,\mathrm{in}}$	Cross component of the arriving backscatter.
T	Atmospheric transmission path for the lidar equation.
P_0	Number of emitted photons.
ε_{l}	Portion of the emitted radiation polarized in the cross direction ($\perp$), called cross talk of the emitter.
$\boldsymbol{I}_{\mathrm{L}}$	Stokes vector describing the emitted radiation in terms of the polarization state.
$\mathbf{F}$	Scattering matrix of the atmosphere. The element F_{11} corresponds to the backscattering coefficient β.
$\boldsymbol{I}_{\mathrm{in}}$	Stokes vector describing the arriving radiation after being transmitted, backscattered, and depolarized by the atmosphere.
$c_{2\alpha}$	$\cos(2\alpha)$, α denotes the rotation between the polarization axis of the emission with respect to the reception.
$\mathbf{R}(\alpha)$	Rotation matrix to consider the effect of the rotation α between emission and receiver polarization plane.
$N_i(z)$	Number of photons measured by each detector (i = P, S, tot) at height z.
$\eta_{\parallel,\mathrm{P}}$	Constant describing the efficiency of channel P to component $\parallel$.
$\eta_{\perp,\mathrm{S}}$	Constant describing the efficiency of channel S to component $\perp$.
η_{tot}	Constant describing the efficiency of the total channel (tot) to the sum of the components $\parallel + \perp$.
D_i	Efficiency ratio of each channel $= \eta_{\perp,i}/\eta_{\parallel,i}$ (i = P,S). $D_{\mathrm{tot}} \equiv 1$ (ideal).
ε_{r}	So-called cross talk of the receiver. $\varepsilon_{\mathrm{r}} = D_{\mathrm{P}} = D_{\mathrm{S}}^{-1}$ (ideal case).
X_{P}	So-called interchannel constant, similar to the gain ratio used in previous studies (η^*). $\eta_{\mathrm{tot}}/[\eta_{\parallel,\mathrm{P}}(1+\varepsilon_{\mathrm{r}})]$.
X_{S}	$\eta_{\mathrm{tot}}/[\eta_{\perp,\mathrm{S}}(1+\varepsilon_{\mathrm{r}})]$.
X_δ	$\eta_{\parallel,\mathrm{P}}/\eta_{\perp,\mathrm{S}} = X_{\mathrm{S}}/X_{\mathrm{P}}$.
R_{P}	Ratio of signals $N_{\mathrm{P}}(z)/N_{\mathrm{tot}}(z)$.
R_{S}	Ratio of signals $N_{\mathrm{S}}(z)/N_{\mathrm{tot}}(z)$.
R_δ	Ratio of signals $N_{\mathrm{S}}(z)/N_{\mathrm{P}}(z)$.
ξ_{tot}	So-called total cross talk of the system (ideal case). It summarizes the three instrumental effects considered (ε_{l}, $c_{2\alpha}$ and ε_{r}).
ξ_{P}	Total cross talk of the P channel (nonideal case).
ξ_{S}	Total cross talk of the S channels (nonideal case).
$\xi_{\mathrm{S}}^{\mathrm{P}}$	$= (\xi_{\mathrm{P}}^{-1} - \xi_{\mathrm{S}}^{-1})/2$.
$\Delta R_i(z_j, z_k)$	$= R_i(z_j) - R_i(z_k)$.

Additional information about the extended three-signal calibration approach

- The extinction coefficient is assumed to be independent of the polarization state of the light. This assumption permits the simplification of the three lidar equations, making possible the determination of the instrumental constants.
- The effects of the emission and reception in terms of polarization can be summarized into one total cross-talk constant ξ_{tot} (in the ideal case), or into two total cross talk constant ξ_{P} and ξ_{S} for the nonideal case (Appendix A).
- Differences with previous studies in terms of the nomenclature are present:
  - In our approach ε denotes cross talk, and not the error angle of the $\Delta 90$ calibration as denoted in previous studies. The cross talk has usually been denoted by G_{S} and H_{S} (Freudentaler, 2016).
  - D_i denotes the efficiency ratio (Reichardt et al., 2003), while in recent studies D denotes the diattenuation parameter.

  The total channel is assumed to be ideal in terms of polarization, i.e., $D_{\mathrm{tot}} = 1$.
- No diattenuation and retardation are considered in the emission and reception units.

Author contributions. The theoretical framework was developed by CJ in close cooperation with AA, MH, and UW. RE, JS, and CJ contributed in the setup of the lidar instrument. CJ wrote the computing code for the analysis. CJ and MH performed the measurements and analyzed the data of the MARTHA and BERTHA systems, respectively. CJ and AA prepared the paper in cooperation with MH.

Competing interests. The authors declare that they have no conflict of interest.

Acknowledgements. This research was partially funded by the program DAAD/Becas Chile, grant no. 57144001. This activity is supported by the ACTRIS Research Infrastructure (EU H2020-R&I), grant agreement no. 654109.

We thank Ilya Serikov for the fruitful discussions on the topic. We would like to acknowledge the three anonymous referees for their valuable feedback given during the revision process.

The publication of this article was funded by the Open Access Fund of the Leibniz Association.

Edited by: Vassilis Amiridis
Reviewed by: three anonymous referees

References

Behrendt, A. and Nakamura, T.: Calculation of the calibration constant of polarization lidar and its dependency on atmospheric temperature, Opt. Express, 10, 805–817, 2002.

Belegante, L., Bravo-Aranda, J. A., Freudenthaler, V., Nicolae, D., Nemuc, A., Ene, D., Alados-Arboledas, L., Amodeo, A., Pappalardo, G., D'Amico, G., Amato, F., Engelmann, R., Baars, H., Wandinger, U., Papayannis, A., Kokkalis, P., and Pereira, S. N.: Experimental techniques for the calibration of lidar depolarization channels in EARLINET, Atmos. Meas. Tech., 11, 1119–1141, https://doi.org/10.5194/amt-11-1119-2018, 2018.

Biele, J., Beyerle, G., and Baumgarten, G.: Polarization lidar: Corrections of instrumental effects, Opt. Express, 7, 427–435, 2000.

Bravo-Aranda, J. A., Belegante, L., Freudenthaler, V., Alados-Arboledas, L., Nicolae, D., Granados-Muñoz, M. J., Guerrero-Rascado, J. L., Amodeo, A., D'Amico, G., Engelmann, R., Pappalardo, G., Kokkalis, P., Mamouri, R., Papayannis, A., Navas-Guzmán, F., Olmo, F. J., Wandinger, U., Amato, F., and Haeffelin, M.: Assessment of lidar depolarization uncertainty by means of a polarimetric lidar simulator, Atmos. Meas. Tech., 9, 4935–4953, https://doi.org/10.5194/amt-9-4935-2016, 2016.

Chipman, R. A.: Mueller matrices in: Handbook of Optics, Volume I, 3rd edn., chap. 14, McGraw-Hill, 2009.

David, G., Miffre, A., Thomas, B., and Rairoux, P.: Sensitive and accurate dual-wavelength UV-VIS polarization detector for optical remote sensing of tropospheric aerosols, Appl. Phys. B, 108, 197–216, https://doi.org/10.1007/s00340-012-5066-x, 2012.

Donovan, D. P., Klein Baltink, H., Henzing, J. S., de Roode, S. R., and Siebesma, A. P.: A depolarisation lidar-based method for the determination of liquid-cloud microphysical properties, Atmos. Meas. Tech., 8, 237–266, https://doi.org/10.5194/amt-8-237-2015, 2015.

Engelmann, R., Kanitz, T., Baars, H., Heese, B., Althausen, D., Skupin, A., Wandinger, U., Komppula, M., Stachlewska, I. S., Amiridis, V., Marinou, E., Mattis, I., Linné, H., and Ansmann, A.: The automated multiwavelength Raman polarization and water-vapor lidar Polly^{XT}: the neXT generation, Atmos. Meas. Tech., 9, 1767–1784, https://doi.org/10.5194/amt-9-1767-2016, 2016.

Fan, J., Wang, Y., Rosenfeld, D., and Liu, X.: Review of Aerosol-Cloud Interactions: Mechanisms, significance, and Challenges, J. Atmos. Sci., 73, 4221–4252, https://doi.org/10.1175/JAS-D-16-0037.1, 2016.

Freudenthaler, V.: About the effects of polarising optics on lidar signals and the $\Delta 90$ calibration, Atmos. Meas. Tech., 9, 4181–4255, https://doi.org/10.5194/amt-9-4181-2016, 2016.

Freudenthaler, V., Esselborn, M., Wiegner, M., Heese, B., Tesche, M., Ansmann, A., Müller, D., Althausen, D., Wirth, M., Fix, A., Ehret, G., Knippertz, P., Toledano, C., Gasteiger, J., Garhammer, M., and Seefeldner, M.: Depolarization ratio profiling at several wavelengths in pure Saharan dust during SAMUM 2006, Tellus B, 61, 165–179, https://doi.org/10.1111/j.1600-0889.2008.00396.x, 2009.

Freudenthaler, V., Seefeldner, M., Groß, S., and Wandinger, U.: Accuracy of Linear Depolarisation Ratios in Clean Air Ranges Measured with POLIS-6 at 355 and 532 NM, EPJ Web Conf., 119, 25013, https://doi.org/10.1051/epjconf/201611925013, 2016.

Haarig, M., Ansmann, A., Althausen, D., Klepel, A., Groß, S., Freudenthaler, V., Toledano, C., Mamouri, R.-E., Farrell, D. A., Prescod, D. A., Marinou, E., Burton, S. P., Gasteiger, J., Engelmann, R., and Baars, H.: Triple-wavelength depolarization-ratio profiling of Saharan dust over Barbados during SALTRACE in 2013 and 2014, Atmos. Chem. Phys., 17, 10767–10794, https://doi.org/10.5194/acp-17-10767-2017, 2017.

Haarig, M., Ansmann, A., Baars, H., Jimenez, C., Veselovskii, I., Engelmann, R., and Althausen, D.: Depolarization and lidar ratios at 355, 532, and 1064 nm and microphysical properties of aged tropospheric and stratospheric Canadian wildfire smoke, Atmos. Chem. Phys., 18, 11847–11861, https://doi.org/10.5194/acp-18-11847-2018, 2018.

Huang, Y., Chameides, W. L., and Dickinson, R. E.: Direct and indirect effects of anthropogenic aerosols on regional precipitation over east Asia, J. Geophys. Res., 112, D03212, https://doi.org/10.1029/2006JD007114, 2007.

IPCC: Climate Change 2014: Synthesis Report. Contribution of Working Groups I, II and III to the Fifth Assessment Report of the Intergovernmental Panel on Climate Change, edited by: Core Writing Team, Pachauri, R. K., and Meyer, L. A., IPCC, Geneva, Switzerland, 151 pp., available at: https://www.ipcc.ch/report/ar5/syr/ (last access: 8 February 2019), 2014.

Jimenez, C., Ansmann, A., Donovan, D., Engelmann, R., Malinka, A., Schmidt, J., and Wandinger, U.: Retrieval of microphysical properties of liquid water clouds from atmospheric lidar measurements: Comparison of the Raman dual field of view and the depolarization techniques, Proc. SPIE, 10429, 1042907, https://doi.org/10.1117/12.2281806, 2017.

Jimenez, C., Ansmann, A., Donovan, D., Engelmann, R., Schmidt, J., and Wandinger, U.: Comparison between two lidar methods to retrieve microphysical properties

of liquid water clouds, EPJ Web Conf., 176, 01032, https://doi.org/10.1051/epjconf/201817601032, 2018.

Jimenez, C., Ansmann, A., Engelmann, R., Malinka, A., Schmidt, J., and Wandinger, U.: Retrieval of microphysical properties of liquid water clouds from atmospheric lidar measurements: dual field of view depolarization technique, in preparation, 2019.

Liu, B. and Wang, Z.: Improved calibration method for depolarization lidar measurement, Opt. Express, 21, 14583–14590, https://doi.org/10.1364/OE.21.014583, 2013.

Lu, S. Y. and Chipman, R. A.: Interpretation of Mueller matrices based on polar decomposition, J. Opt. Soc. Am. A, 13, 1106–1113, 1996.

Mattis, I., Ansmann, A., Müller, D., Wandinger, U., and Althausen, D.: Multiyear aerosol observations with dualwavelength Raman lidar in the framework of EARLINET, J. Geophys. Res., 109, D13203, https://doi.org/10.1029/2004JD004600, 2004.

Mattis, I., Müller, D., Ansmann, A., Wandinger, U., Preißler, J., Seifert, P., and Tesche, M.: Ten years of multiwavelength Raman lidar observations of free-tropospheric aerosol layers over central Europe: Geometrical properties and annual cycle, J. Geophys. Res., 113, D20202, https://doi.org/10.1029/2007JD009636, 2008.

Mattis, I., Tesche, M., Grein, M., Freudenthaler, V., and Müller, D.: Systematic error of lidar profiles caused by a polarization-dependent receiver transmission: quantification and error correction scheme, Appl. Optics, 48, 2742–2751, 2009.

Mattis, I., Seifert, P., Müller, D., M. Tesche, Hiebsch, A., Kanitz, T., Schmidt, J., Finger, F., Wandinger, U., and Ansmann, A.: Volcanic aerosol layers observed with multiwavelength Raman lidar over central Europe in 2008–2009, J. Geophys. Res., 115, D00L04, https://doi.org/10.1029/2009JD013472, 2010.

McCullough, E. M., Sica, R. J., Drummond, J. R., Nott, G., Perro, C., Thackray, C. P., Hopper, J., Doyle, J., Duck, T. J., and Walker, K. A.: Depolarization calibration and measurements using the CANDAC Rayleigh–Mie–Raman lidar at Eureka, Canada, Atmos. Meas. Tech., 10, 4253–4277, https://doi.org/10.5194/amt-10-4253-2017, 2017.

Pappalardo, G., Amodeo, A., Apituley, A., Comeron, A., Freudenthaler, V., Linné, H., Ansmann, A., Bösenberg, J., D'Amico, G., Mattis, I., Mona, L., Wandinger, U., Amiridis, V., Alados-Arboledas, L., Nicolae, D., and Wiegner, M.: EARLINET: towards an advanced sustainable European aerosol lidar network, Atmos. Meas. Tech., 7, 2389–2409, https://doi.org/10.5194/amt-7-2389-2014, 2014.

Reichardt, J., Baumgart, R., and McGee, T. J.: Three-signal method for accurate measurements of depolarization ratio with lidar, Appl. Optics, 42, 4909–4913, 2003.

Schmidt, J., Ansmann, A., Bühl, J., Baars, H., Wandinger, U., Müller, D., and Malinka, A. V.: Dual-FOV Raman and Doppler lidar studies of aerosol-cloud interactions: Simultaneous profiling of aerosols, warm-cloud properties, and vertical wind, J. Geophys. Res.-Atmos., 119, 5512–5527, 2013a.

Schmidt, J., Wandinger, U., and Malinka, A.: Dual-field-of-view Raman lidar measurements for the retrieval of cloud microphysical properties, Appl. Optics, 52, 2235–2247, 2013b.

Schmidt, J., Ansmann, A., Bühl, J., and Wandinger, U.: Strong aerosol–cloud interaction in altocumulus during updraft periods: lidar observations over central Europe, Atmos. Chem. Phys., 15, 10687–10700, https://doi.org/10.5194/acp-15-10687-2015, 2015.

Stelmaszczyk, K., Dell'Aglio, M., Chudzyński, S., Stacewicz, T., and Wöste, L.: Analytical function for lidar geometrical compression form-factor calculations, Appl. Optics, 44, 1323–1331, 2005.

4.2 Second publication: The dual-field-of-view polarization lidar technique: A new concept in monitoring aerosol effects in liquid-water clouds – Theoretical framework

The content of this chapter has already been published under the title "The dual-field-of-view polarization lidar technique: A new concept in monitoring aerosol effects in liquid-water clouds – Theoretical framework" by Cristofer Jimenez, Albert Ansmann, Ronny Engelmann, David Donovan, Aleksey Malinka, Jörg Schmidt, Patric Seifert, and Ulla Wandinger. In 2020, the paper was published under the Creative Commons Attribution 4.0 License in Atmospheric Chemistry and Physics with the doi: 10.5194/acp-20-15247-2020 (see `https://doi.org/10.5194/acp-20-15247-2020`). Reprinted with permission by the authors from Atmospheric Chemistry and Physics, 20, 15247–15263, 2020.

Atmos. Chem. Phys., 20, 15247–15263, 2020
https://doi.org/10.5194/acp-20-15247-2020

Atmospheric Chemistry and Physics
Open Access
EGU

The dual-field-of-view polarization lidar technique: a new concept in monitoring aerosol effects in liquid-water clouds – theoretical framework

Cristofer Jimenez[1], Albert Ansmann[1], Ronny Engelmann[1], David Donovan[2], Aleksey Malinka[3], Jörg Schmidt[4], Patric Seifert[1], and Ulla Wandinger[1]

[1]Leibniz Institute for Tropospheric Research, Leipzig, Germany
[2]Royal Netherlands Meteorological Institute (KNMI), De Bilt, the Netherlands
[3]National Academy of Sciences of Belarus, Minsk, Belarus
[4]Institute of Meteorology, University of Leipzig, Leipzig, Germany

Correspondence: Cristofer Jimenez (jimenez@tropos.de)

Received: 14 May 2020 – Discussion started: 7 July 2020
Revised: 6 October 2020 – Accepted: 19 October 2020 – Published: 8 December 2020

Abstract. In a series of two articles, a novel, robust, and practicable lidar approach is presented that allows us to derive microphysical properties of liquid-water clouds (cloud extinction coefficient, droplet effective radius, liquid-water content, cloud droplet number concentration) at a height of 50–100 m above the cloud base. The temporal resolution of the observations is on the order of 30–120 s. Together with the aerosol information (aerosol extinction coefficients, cloud condensation nucleus concentration) below the cloud layer, obtained with the same lidar, in-depth aerosol–cloud interaction studies can be performed. The theoretical background and the methodology of the new cloud lidar technique is outlined in this article (Part 1), and measurement applications are presented in a companion publication (Part 2) (Jimenez et al., 2020a). The novel cloud retrieval technique is based on lidar observations of the volume linear depolarization ratio at two different receiver fields of view (FOVs). Extensive simulations of lidar returns in the multiple scattering regime were conducted to investigate the capabilities of a dual-FOV polarization lidar to measure cloud properties and to quantify the information content in the measured depolarization features regarding the basic retrieval parameters (cloud extinction coefficient, droplet effective radius). Key simulation results and the overall data analysis scheme developed to obtain the aerosol and cloud products are presented.

1 Introduction

Aerosol–cloud–precipitation interaction is an important branch of atmospheric research and one of the main uncertainty sources in climate predictions (IPCC, 2014). Significant efforts are undertaken to investigate the role of aerosol particles in liquid-water, mixed-phase, and cirrus cloud formation processes, by means of ground-based, airborne, and spaceborne observations with an increasing contribution of active remote sensing (Grosvenor et al., 2018). Ground-based lidar is the most favorable technique to continuously monitor aerosol layers and the evolution of clouds within these layers. Regarding liquid-water clouds, lidar permits us to measure aerosol properties directly below the cloud base and liquid-droplet microphysical properties just above the cloud base and thus to quantify the relationship between changing aerosol conditions and changing cloud properties very sensitively and with high temporal resolution. The impact of upward and downward motions which strongly influence the levels of water vapor supersaturation during droplet formation, and thus control how many of the aerosol particles will be activated to become cloud droplets, can be investigated in these aerosol–cloud-interaction (ACI) studies by adding or integrating a vertically pointing Doppler lidar to the remote sensing facility (Schmidt et al., 2014, 2015).

The new dual-FOV (field of view) polarization lidar technique, introduced in this article, is a follow-up development of the dual-FOV Raman lidar technique (Schmidt et al.,

2013) which allows us to determine the effective radius of cloud droplets and the cloud light-extinction coefficient, and to derive the liquid water content and cloud droplet number concentration within the lowest 100 m of a liquid-water cloud layer. Together with aerosol properties such as the particle extinction coefficient or the estimated cloud condensation nucleus (CCN) concentration in air parcels, which enter the cloud environment in updrafts from below, the influence of aerosol particles on the evolution of the cloud layer can be monitored in detail.

Lidar observations of liquid-water cloud properties make use of the relationship between the strength of multiple scattering caused by water droplets and the size and amount of these droplets. In the case of the dual-FOV Raman lidar technique, nitrogen Raman backscatter signals are measured at two different receiver FOVs to provide the necessary information about multiple scattering. The advantage of the Raman lidar is that the measured multiple scattering contribution (forward scattering of laser photons by cloud droplets) is unambiguously linked to the effective radius of the droplets. This method delivers the most robust and reliable observations of microphysical properties of liquid-water clouds. However, nitrogen Raman signals are weak so that observations are restricted to nighttime hours and signal averaging times of 10–30 min are usually needed to reduce the impact of signal noise on the lidar products to a tolerable level. Thus, the investigation of the influence of aerosols on the evolution of the cloud system with high resolution of seconds to minutes at day and nighttime is not possible with the Raman lidar. Furthermore, because of these long signal integration times a bias in the retrieval products, caused by averaging of backscatter signals during periods with a varying cloud base height resulting from up and downward motions, must be kept in consideration in the data interpretation (Schmidt et al., 2013, 2014). This problem is largely overcome in the case of the novel dual-FOV polarization lidar technique with respective short signal integration times.

The requirement for observations during day and night and temporal resolutions on the order of 30–120 s to resolve different phases of cloud evolution and to study, for example, the impact of individual updraft events of given duration and strength on cloud droplet nucleation for given aerosol conditions was therefore the main motivation for the development of this alternative lidar measurement concept (Jimenez et al., 2017, 2018). A polarization lidar transmits linearly polarized laser pulses and detects the cross- and co-polarized signal components. "Co-" and "cross-" denote the planes of polarization parallel and orthogonal to the plane of linear polarization of the transmitted laser pulses, respectively. The volume linear depolarization ratio is defined as the ratio of the cross- to the co-polarized signal and yields the information on the ratio of the cross-to-co-polarized backscatter coefficient. The depolarization ratio is sensitively influenced by multiple scattering in water clouds and varies, for example, with receiver FOV, cloud height, and number concentration and size of the droplets as will be explained in this article. Comparably strong cloud elastic-backscatter signals are the basis for this method so that no restrictions to nighttime hours are given and a high temporal resolution can be achieved. The light-depolarizing effect is different for different FOVs and this difference sensitively depends on the effective radius of the droplets. The strength of the change in light depolarization with height inside the cloud layer provides a direct measurement of the cloud light-extinction coefficient. All this is outlined in Sect. 3.

The article is organized as follows: in Sect. 2, a brief review of lidar methods for liquid-water cloud observations is given. Section 3 provides the theoretical background regarding the multiple scattering effects and the relationship between the microphysical properties of the liquid-water clouds and the observable cloud depolarization ratio profiles induced by multiple scattering. The simulation model is introduced in Sect. 3.3. The development of the cloud retrieval scheme is outlined in Sect. 4 based on extensive simulation studies. In Sect. 5, the uncertainties in the retrieved cloud properties are discussed. Section 6 presents the lidar data analysis regarding the aerosol properties (below the investigated cloud layer) obtained with the same lidar. Section 7 finally summarizes all cloud and aerosol data analysis procedures and provides a final table with all data analysis steps. After the detailed description of the methodology in this Part 1, a dual-FOV polarization lidar setup is described in Part 2 (Jimenez et al., 2020a). This lidar performed continuous aerosol and cloud observations at Punta Arenas (53° S) in southern Chile in pristine marine conditions of the Southern Ocean within the framework of a 2-year field campaign. In Part 2, two case studies are discussed to demonstrate the potential of the new lidar approach to study aerosol–cloud interaction of liquid water clouds.

2 Multiple scattering lidar

Here, we provide a brief overview of lidar applications in liquid-water cloud research. The use of lidar to derive cloud properties from measurements of multiple scattering contributions to the return signals has a long tradition. Strong forward scattering of incident laser photons occurs on the way up to the in-cloud backscatter region and on the way back to the lidar (Mooradian et al., 1979). The multiple scattering (MS) effect depends on the geometrical and spectral characteristics of the lidar instrument and on the geometrical and microphysical properties of the cloud layers (Bissonnette et al., 1995; Chaikovskaya, 2008).

Several models are available to simulate the MS contribution to the lidar return signal (e.g., Eloranta, 1998; Hogan, 2008; Wandinger, 1998; Katsev et al., 1997; Chaikovskaya and Zege, 2004; Donovan et al., 2015), and many attempts have been undertaken to explore the potential of lidar to retrieve optical and microphysical properties of liquid-water

clouds from measured multiple scattering effects (e.g., Pal and Carswell, 1985; Roy et al., 1999; Bissonnette et al., 2005; Kim et al., 2010; Schmidt et al., 2013; Donovan et al., 2015). A promising way is the use of a lidar measuring cloud backscatter signals at several FOVs. Bissonnette et al. (2005) proposed a multiple-FOV approach based on the measurement of total elastic-backscattering returns in combination with Monte Carlo simulations. Roy et al. (1999) has introduced a robust approach based on cross-polarized returns at multiple FOVs, allowing the assessment of the droplet size distribution.

The information content in multiple-FOV polarization lidar returns was then systematically (theoretically and experimentally) studied by Veselovskii et al. (2006). This work demonstrated the ability of a multiple-FOV lidar to investigate cloud microphysical properties in very great detail. One of the conclusions from this analysis is that the use of six FOVs would be optimal and would allow an accurate retrieval of droplet sizes, amount, and light-extinction coefficient. However, the realization of a lidar receiver with six well-calibrated FOVs is challenging. Thus, in this study we propose a dual-FOV polarization lidar approach (in Part 1) and demonstrate that such an attempt is easy to realize and provides high-quality cloud measurements (in Part 2). The sensitivity of such a dual-FOV lidar system to cloud microphysical properties depends on the selected pair of FOVs and on the altitude of the target (Malinka and Zege, 2003; Veselovskii et al., 2006) as shown below.

Donovan et al. (2015) recently presented a new approach of a single-FOV polarization lidar-based method for the observation of liquid-water clouds. The retrieval is based on computed look-up tables of the cross- and co-polarized signal strength as a function of cloud microphysical properties. The cloud light-extinction coefficient and droplet effective radius can be retrieved by applying a Bayesian optimal estimation procedure. We will compare our results with the ones obtained with the method suggested by Donovan et al. (2015).

3 Methodological background and cloud simulation model

In this section, we provide the theoretical background of the dual-FOV polarization lidar method developed. In Sect. 3.1, we begin with an overview of the retrievable cloud microphysical and observable optical properties of liquid-water clouds. Afterwards, we demonstrate how the measured volume linear depolarization ratio is related to the strength of multiple scattering (MS) as a function of receiver FOV and given cloud properties (Sect. 3.2). This provides the first insight into the relationship between light depolarization, cloud extinction, and droplet effective radius that we want to determine. Then we introduce the MS simulation model (Sect. 3.3) that was used to develop the dual-FOV polarization lidar technique (presented in Sects. 4 and 5) and show comparisons to demonstrate that the MS model is able to simulate real-world cloud scenarios, multiple scattering processes, and lidar backscatter signals.

3.1 Basic cloud microphysical and optical properties

As outlined and summarized by Schmidt et al. (2013, 2014) and Donovan et al. (2015), the basic properties characterizing a liquid-water cloud layer are the cloud droplet number concentration N_d, the cloud droplet effective radius R_e, the cloud droplet (single scattering) light-extinction coefficient α, and the liquid-water content w_l. The liquid-water content of droplets in a given volume is defined as follows:

$$\begin{aligned} w_\mathrm{l} &= \frac{4}{3}\pi\rho_\mathrm{w}\int_0^\infty n(r)r^3\mathrm{d}r \\ &= \frac{4}{3}\pi\rho_\mathrm{w}\left(\frac{\int_0^\infty n(r)r^3\mathrm{d}r}{\int_0^\infty n(r)\mathrm{d}r}\right)\int_0^\infty n(r)\mathrm{d}r \\ &= \frac{4}{3}\pi\rho_\mathrm{w}R_\mathrm{v}^3N_\mathrm{d}, \end{aligned} \tag{1}$$

with the total droplet number concentration $N_\mathrm{d} = \int_0^\infty n(r)\mathrm{d}r$, the volume mean droplet radius R_v of a given droplet size distribution $n(r)$, and the liquid-water density ρ_w. The droplet number concentration $n(r)$ is described by a modified gamma size distribution (see Eq. 2 in Schmidt et al., 2014).

The light-extinction coefficient of the cloud layer can be approximated by

$$\alpha = 2\pi\int_0^\infty n(r)r^2\mathrm{d}r = 2\pi R_\mathrm{s}^2N_\mathrm{d} \tag{2}$$

in the case that the droplets are large in comparison to the laser wavelength. R_s denotes the surface mean droplet radius. Besides the cloud extinction coefficient, the droplet effective radius

$$R_\mathrm{e} = \frac{\int_0^\infty n(r)r^3\mathrm{d}r}{\int_0^\infty n(r)r^2\mathrm{d}r} = \frac{N_\mathrm{d}R_\mathrm{v}^3}{N_\mathrm{d}R_\mathrm{s}^2} \Rightarrow R_\mathrm{s}^2 = \frac{R_\mathrm{v}^3}{R_\mathrm{e}} \tag{3}$$

is used to characterize an observed liquid-water cloud layer. By combining Eqs. (1), (2), and (3) we can write the following for the liquid-water content:

$$w_\mathrm{l} = \frac{2}{3}\rho_\mathrm{w}\alpha R_\mathrm{e}\,. \tag{4}$$

Based on in situ measurements in warm stratified clouds Martin et al. (1994) found that the cubic power of the measured effective radius and the cubic power of the volume mean droplet radius follow a linear relationship, defining the parameter k:

$$k = \frac{R_\mathrm{v}^3}{R_\mathrm{e}^3}\,. \tag{5}$$

This linear relationship suggests that, in most cases, a modified gamma function (Eq. 2 in Schmidt et al., 2014, Eq. 6 in Donovan et al., 2015) can describe the droplet size distribution. Lu and Seinfeld (2006) compiled a list of k values for stratiform clouds based on a literature review. The k range of 0.75 ± 0.15 represents well the values found for continental air masses. For marine stratocumulus k was slightly larger (around 0.8).

From Eqs. (2), (3), and (5) an expression for the cloud droplet number concentration can be obtained:

$$N_\mathrm{d} = \frac{1}{2\pi k} \alpha R_\mathrm{e}^{-2}. \tag{6}$$

Equations (4) and (6) permit the calculation of the liquid water content w_l and the droplet number concentration N_d from lidar measurements of the cloud extinction coefficient α and the droplet effective radius R_e as already outlined by Schmidt et al. (2013, 2014). In the next sections, we evaluate the possibilities of retrieving information about these two cloud parameters from lidar measurements of depolarization ratios caused by multiple scattering. The investigation is based on simulations with an analytical model (introduced in Sect. 3.3) which can compute the co- and cross-polarized lidar returns in multiple scattering regimes of pure liquid-water clouds.

3.2 Relationship between light depolarization and multiple scattering

It is well known that the polarization state of photons scattered in the strictly backward direction remain invariant in the case of spherical particles. In dense water clouds (multiple scattering regime), however, one or more forward scattering events take place, so the backscatter process that allows the return of laser photons to the receiver telescope within the lidar FOV occurs at a scattering angle close to but different from 180°. In this case, multiple scattering causes depolarization of the incident linearly polarized laser light (Sassen and Petrilla, 1986; Zege and Chaikovskaya, 1996).

To provide an easy-to-follow overview of the polarimetric behavior in lidar-relevant multiple scattering regimes, we consider first a simple case of double scattering, as illustrated in Fig. 1, consisting of forward scattering of laser photons by one droplet at height z_f at a small scattering angle θ_f followed by backward scattering by another droplet at height z_b at a large angle $\theta_\mathrm{b} = \pi - \theta_\mathrm{f}$ (around 180°).

The Stokes vector describing the resulting polarization state with respect to the initial coordinate system, which we relate to the laser beam polarization state, can be obtained as follows:

$$\boldsymbol{A}(\theta_\mathrm{f}, \theta_\mathrm{b}, \phi) = \mathbf{B}^{\mathrm{sc}\to\mathrm{cc}}(\phi)\mathbf{P}(\theta_\mathrm{b})\mathbf{P}(\theta_\mathrm{f})\mathbf{B}^{\mathrm{cc}\to\mathrm{rc}}(\phi)\boldsymbol{A}_\mathrm{lin}. \tag{7}$$

$\boldsymbol{A}_\mathrm{lin}$ denotes the Stokes vector for the 100 % linearly polarized laser pulses, associated with the initial laser polarization plane ($\boldsymbol{e}_{\parallel\mathrm{cc}}$, $\boldsymbol{e}_{\perp\mathrm{cc}}$, $\boldsymbol{e}_z$). The transformation matrix $\mathbf{B}^{\mathrm{cc}\to\mathrm{rc}}(\phi)$ enables the transition from the Cartesian coordinate system

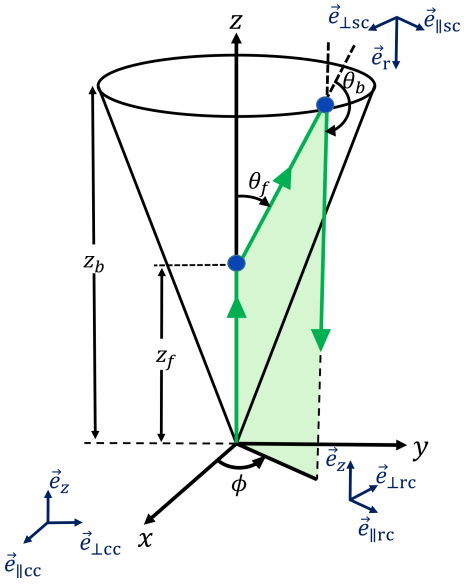

Figure 1. Scattering geometry for one forward and one backward scattering event.

(cc, $\boldsymbol{e}_{\parallel\mathrm{cc}}$, $\boldsymbol{e}_{\perp\mathrm{cc}}$, $\boldsymbol{e}_z$ coordinates in Fig. 1) to the ϕ-rotated system (rc, $\boldsymbol{e}_{\parallel\mathrm{rc}}$, $\boldsymbol{e}_{\perp\mathrm{rc}}$, $\boldsymbol{e}_z$ coordinates) followed by the scattering of the incident wave front. $\mathbf{P}$ represents the single scattering matrix defined for an isotropic media (Zege and Chaikovskaya, 2000). The matrices $\mathbf{P}(\theta_\mathrm{f})$ and $\mathbf{P}(\theta_\mathrm{b})$ denote the forward and backward scattering. The transformation matrix $\mathbf{B}^{\mathrm{sc}\to\mathrm{cc}}$ finally enables the transition from the scattering-coordinate system (sc, $\boldsymbol{e}_{\parallel\mathrm{sc}}$, $\boldsymbol{e}_{\perp\mathrm{sc}}$, $\boldsymbol{e}_\mathrm{r}$ coordinates in Fig. 1) to the original Cartesian system (cc) (Wandinger, 1994).

From the Stokes vector $\boldsymbol{A}(\theta_\mathrm{f}, \theta_\mathrm{b}, \phi)$ we can extract the co- and cross-polarized lidar signal components $S_\parallel$ and $S_\perp$. In Fig. 2b, the computed azimuthal patterns (in the backscatter plane orthogonal to the z axis in Fig. 1) of the co- and cross-polarized signal components for scattering angles from 170 to 180° are shown for four different droplet sizes. Those azimuthal patterns can be observed with imaging polarization lidars, which are supplied with a charged coupled device matrix as a photo-receiving element (Roy et al., 2004). But a common lidar receiver collects the scattered light over the entire azimuthal range and stores it as one signal. However, by selecting a certain receiver FOV, we define the range of scattering angles θ_f and θ_b that a lidar can detect in the multiple scattering regime, and by measuring lidar return signals at different FOVs and thus for different ranges of θ_f and θ_b, a way is opened to derive information about the droplet sizes as emphasized in Fig. 2a–d. This is the basic idea of combining lidar measurements at different FOVs to retrieve the effective radius of the droplets and, in the next step, further cloud properties as will be described in Sect. 4.

From the two observed lidar signal components, $S_\perp$ and $S_\parallel$ backscattered at height z_b, the so-called volume or, in the case of dense water clouds, droplet linear depolarization ratio

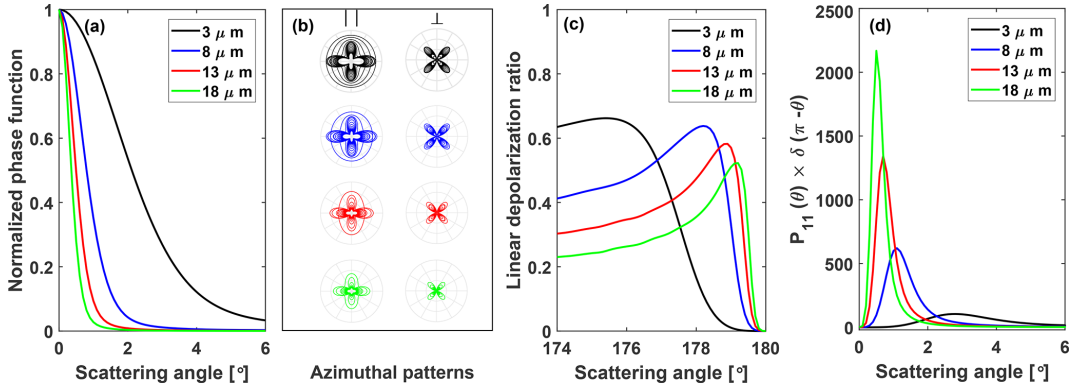

Figure 2. **(a)** Normalized scattering matrix element P_{11} (normalized to the maximum at 0° scattering angle) as a function of forward scattering angle θ_f for four droplet effective radii (given as numbers), **(b)** azimuthal patterns (computed with the MS model for the entire range of azimuthal angles from 0 to 2π; see Fig. 1) of the co-polarized $\parallel$ and the cross-polarized $\perp$ signal components at scattering angles θ_b between 170 and 189.5° for the different droplet diameters, **(c)** droplet linear depolarization ratio $\delta = S_\perp / S_\parallel$ with the lidar signal components $S_\perp$ and $S_\parallel$ (obtained from azimuthal integration over the range from $\phi = 0$–2π in **b**) as a function of the backscattering angle θ_b from 174° to 180° for the four droplet sizes, and **(d)** scattering matrix element $P_{11}(\theta)$ at θ_f (in **a**) multiplied by the depolarization ratio at $\theta_b = \pi - \theta_f$ (in **c**).

defined as

$$\delta(z_b) = \frac{S_\perp(z_b)}{S_\parallel(z_b)} \tag{8}$$

is obtained. After forward scattering, the laser photons are backscattered at a certain backscatter angle θ_b. The dependence of the depolarization ratio on the backscatter angle θ_b is shown in Fig. 2c for the four droplet effective radii. It can be seen that the depolarization ratio increases to considerable values when the scattering angle deviates from 180°. This sensitivity of the non-180° backscattering angle θ_b on light depolarization and the strong forward scattering peak in Fig. 2a are the features used in the dual-FOV polarization lidar technique to retrieve the basic cloud microphysical properties. Figure 2a, c, and d provide an impression of the sensitive impact of cloud droplet size on measurable lidar quantities and thus suggest again that polarization lidars operated at two FOVs have the potential to derive R_e and subsequently also the cloud extinction coefficient α. Both R_e and α are closely linked to the cloud droplet number concentration N_d (see Eq. 6). The relationship between MS-induced light depolarization measured at several FOVs and the cloud droplet size characteristics has already been illuminated and discussed in previous studies (Veselovskii et al., 2006; Roy et al., 2016). In the next sections, we will show that a dual-FOV polarization lidar can already provide trustworthy information about the size and extinction coefficient in the cloud base region of liquid water clouds.

To emphasize the dominating impact of the receiver FOV on the measured multiple scattering effects let us, at the end of this subsection, compare the influence of the laser beam width and divergence, receiver telescope area, and the receiver field of view on the observable cloud volume. In the case of a receiver FOV of 1 mrad, the lidar sees or observes a geometrical cross section (circular area in the horizontal plane at cloud base height z_{bot}) of about 0.8, 7, and 20 m^2 for a cloud with base height at 1, 3, and 5 km, respectively. The observable cross sections increase to about 3, 28, and 80 m^2 when using a 2 mrad FOV. In contrast, in the case of a 30 cm receiver telescope (and a theoretical FOV of 0 mrad), the monitored circular cloud area at the cloud base is less than 0.1 m^2. Also, the divergence of the laser beam (0.1 to 0.2 mrad) has only a minor impact on the amount of backscattered photons (and MS effects). The illuminated cloud cross section at cloud base is always < 1 m^2 for a cloud base height of < 5 km. So, the FOV clearly determines the cloud volume (geometrical cross section at cloud base times 50–100 m laser beam penetration depth into the cloud) available for MS cloud studies with lidar.

3.3 Multiple scattering model

After presenting the principle relationship between the measured linear depolarization ratio, forward scattering, and droplet size, next we introduce the multiple scattering model used to develop our retrieval method presented in Sect. 4. The simulation model allows us to simulate realistic cloud scenarios with varying cloud height, droplet number concentration, cloud extinction coefficient, and droplet size distribution and the resulting co- and cross–polarized lidar signal components $S_\parallel$ and $S_\perp$ for given lidar configuration parameters such as laser beam divergence and receiver FOV.

In several articles, the radiative transfer problem of polarized light undergoing multiple scattering in an optically dense medium has been analytically addressed, and several solutions have been proposed and tested (Zege et al., 1995; Zege and Chaikovskaya, 1999, 2000). The so-called small-angle approximation is used. This solution is justified in the

case of a narrow and pronounced forward scattering peak of the droplet scattering phase function which in turn is the case when the droplet size (on the order of 5–20 µm) is large compared to the laser wavelength (532 nm). Such an elongated forward-phase-function medium allows a simplification of Green's matrix. The vector equation can thus be split into a system of scalar-like equations which are simpler and include less integral terms than the original ones and can thus be solved by using well developed radiative-transfer-equation techniques.

The Stokes vector $\boldsymbol{A}$ has the general form $\boldsymbol{A} = (I, Q, U, V)^{\mathrm{T}} = (S_{\parallel} + S_{\perp}, S_{\parallel} - S_{\perp}, U, V)^{\mathrm{T}}$ and the Stokes vector is $\boldsymbol{A}_{\mathrm{lin}} = (1, 1, 0, 0)^{\mathrm{T}}$ in the case of linearly polarized laser pulses (in x direction in Fig. 1) in Eq. (7).

The first element of the Stokes vector is the light intensity I which satisfies the radiative transfer equation using the single scattering matrix element $P_{11}(\theta)$ (shown after normalization in Fig. 2a). The Q component of the Stokes vector describes the linear polarization and satisfies the same equation but with the "modified" angular scattering function that equals $(P_{22} \pm P_{33})/2$ with the sign "+" for the forward and "−" for backward scattering. P_{22} and P_{33} are also elements of the scattering matrix **P**. In this way, the Stokes vector components can be solved separately as a scalar radiative transfer problem (Zege and Chaikovskaya, 2000). The more elongated the phase function, the more accurate the solution. This solution is not restricted to single and double scattering events. It simulates multiple forward scattering processes and one backscattering process. The approach offers high accuracy for optical depths up to 5 together with high computing efficiency (Chaikovskaya, 2008). The authors emphasized the potential of the model for developing new retrieval techniques.

The modeled components I and Q enable the calculations of the cross- and co-polarized returns $S_{\perp}(z_{\mathrm{b}})$ and $S_{\parallel}(z_{\mathrm{b}})$ for backscatter height z_{b} within a liquid-water cloud layer,

$$\boldsymbol{I}(\boldsymbol{X}(z_{\mathrm{b}}), \boldsymbol{G}) = S_{\parallel}(z_{\mathrm{b}}) + S_{\perp}(z_{\mathrm{b}}), \tag{9}$$

$$\boldsymbol{Q}(\boldsymbol{X}(z_{\mathrm{b}}), \boldsymbol{G}) = S_{\parallel}(z_{\mathrm{b}}) - S_{\perp}(z_{\mathrm{b}}). \tag{10}$$

The geometrical vector $\boldsymbol{G}(\Theta_{\mathrm{ldiv}}, \Theta_{\mathrm{fov}}, d_{\mathrm{lb}}, d_{\mathrm{m1}}, d_{\mathrm{m2sd}})$ required to solve Eqs. (9) and (10) provides all necessary information about the lidar configuration, such as the full divergence angle of the laser beam Θ_{ldiv}, the beam diameter d_{lb}, the FOV full divergence angle of the receiver Θ_{fov}, the diameter of the primary receiver telescope d_{m1} and its respective secondary mirror shadow d_{m2sd}. The atmospheric state vector $\boldsymbol{X}(z_{\mathrm{b}}, \alpha(z_{\mathrm{b}}), R_{\mathrm{e}}(z_{\mathrm{b}}))$ provides the cloud information, i.e., cloud extinction coefficient $\alpha(z_{\mathrm{b}})$ (assumed as the scattering coefficient) and effective radius R_{e} at height z_{b}.

The linear depolarization ratio according to Eqs. (8)–(10) is then given by

$$\delta(z_{\mathrm{b}}) = \frac{I(z_{\mathrm{b}}) - Q(z_{\mathrm{b}})}{I(z_{\mathrm{b}}) + Q(z_{\mathrm{b}})}. \tag{11}$$

3.4 Model quality check: comparison with ECSIM Monte Carlo simulations and CALIPSO multiple scattering observations

We investigated to what extent the MS model used is able to simulate real-world polarization lidar observations and thus can be used to develop new lidar analysis methods with a focus on clouds. We compared our simulations with results obtained with the Monte Carlo simulation model ECSIM (EarthCARE Simulator) (Donovan et al., 2015, 2010) and observations with the CALIPSO (Cloud–Aerosol Lidar and Infrared Pathfinder Satellite Observation) lidar (Hu et al., 2007). EarthCARE (Earth Clouds, Aerosols and Radiation Explorer) is a planned spaceborne lidar and radar mission, designed within a co-operation of the European Space Agency (ESA) and the Japan Aerospace Exploration Agency (JAXA) (Illingworth et al., 2015). Based on the 4×4 α–R_{e} combinations ($4\ \alpha(z_{\mathrm{b}})$ values in the range from 5 to 26 km^{-1}, $4\ R_{\mathrm{e}}(z_{\mathrm{b}})$ values in the range from 3 to 15 µm), we performed more than 200 different simulations for these 16 cloud scenarios by considering cloud penetration depths from 10 to 70 m (with step width of 10 m), two different FOVs of 0.5 and 2.0 mrad, and assuming a liquid-cloud layer with a cloud base height at 3000 m. We compared the obtained volume depolarization ratio with respective values simulated with the Monte Carlo simulation model ECSIM in Fig. 3a. As can be seen, our simulations (δ(our model)) are in good agreement with results of the sophisticated Monte Carlo model. Both models agree for most of the depolarization ratio, except for the largest penetration depth exhibiting values close to 0.1. On average the depolarization ratios obtained with ECSIM are larger than our values by 0.016. The small differences indicate that our method delivers a realistic picture of multiple scattering in liquid-water clouds. The growing disagreement for depolarization ratios > 0.05 is caused by different assumptions and implementations regarding the considered narrow ranges of the small-angle forward scattering processes and the one wide-angle backscattering process in the different models.

In a second approach, we compared our simulations with CALIPSO polarization lidar observations. Hu et al. (2007) investigated the relationship between the ratio of the total, cloud-integrated lidar return signal $\overline{\gamma}$ (from cloud top to base in the case of the CALIPSO lidar) to the one caused by single scattering ($\overline{\gamma}_{\mathrm{ss}}$ caused by one backscattering process) and the respective cloud-integrated linear depolarization ratio $\overline{\delta}$. This study was based on observations with ground-based and spaceborne lidars supported by sophisticated Monte Carlo simulations of the multiple scattering impact on the observed cloud lidar returns. By performing a polynomial regression analysis to all observations they found the following best matching relationship:

$$\frac{\overline{\gamma}}{\overline{\gamma}_{\mathrm{ss}}} = \left(\frac{1 - \overline{\delta}}{1 + \overline{\delta}}\right)^2. \tag{12}$$

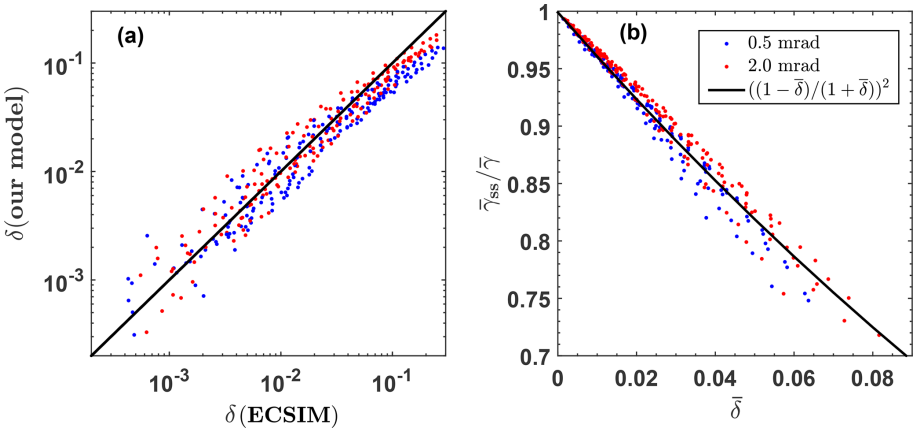

Figure 3. (a) Comparison of the volume linear depolarization ratios $\delta(z)$ computed with our analytical MS model and computed with ESA's Monte Carlo model ECSIM (more details in the text, 1 : 1 line is given as solid diagonal line) and **(b)** comparison of our computations of the relationship between the single-scattering-to-total-scattering-attenuated-backscatter ratio $\overline{\gamma}_{ss}/\overline{\gamma}$ and the cloud-integrated depolarization ratio $\overline{\delta}$ (red and black circles) with the respective values for this relationship as retrieved from CALIPSO multiple scattering observations (solid black line). For the two different FOVs (0.5 mrad in blue, 2.0 mrad in red) 4×4 $R_e(z_{ref}) - \alpha(z_{ref})$ combinations are considered together with different cloud penetration depths Δz_{ref} from 10 to 70 m (with 10 m step width). All in all more than 200 simulations are included in each of the panels **(a)** and **(b)**.

The measured cloud-integrated CALIPSO lidar signal $\overline{\gamma}$ results from single plus multiple scattering events and corresponds to the respective cloud-integrated depolarization ratio $\overline{\delta}$ for a given receiver FOV full angle Θ.

In Fig. 3b, the relationship presented by Hu et al. (2007) is shown as a solid black line. As can be seen, our individual simulations for the two FOVs (red and black circles) are in good agreement with Eq. (12) (black solid line in Fig. 3b), which again corroborates that our model describes well the link between cloud multiple scattering and light depolarization.

4 Retrieval of microphysical properties from polarization lidar observations at two FOVs

Based on simulations, the goal is to establish a method that allows us to retrieve R_e and α from measured δ values at two FOVs, and afterwards to determine w_l and N_d by means of R_e and α. Therefore a large number of polarization lidar measurements for the full range of observable parameters were simulated with the MS model and formed the basis for the development of the new dual-FOV lidar measurement and data analysis concept.

To generate the input scenes, first the vertical profiles are computed and for this we assume that the cloud system develops at subadiabatic equilibrium, as first proposed by Albrecht et al. (1990). Recent experimental (Foth and Pospichal, 2017; Merk et al., 2016) and modeling studies (Barlakas et al., 2020) have shown that this assumption is appropriate to be applied in remote-sensing retrieval methods (Donovan et al., 2015). Such an subadiabatic system considers a reduction in the water content, compared to the adiabatic one, due to evaporation triggered by the entrainment of drier air masses caused by downward transport from above the cloud top.

Our data analysis scheme introduced below will deliver the cloud microphysical products for a height z_{ref} that is 50–100 m above the cloud base height z_{bot}. The respective cloud penetration depth for laser light pulses is defined as

$$\Delta z_{ref} = z_{ref} - z_{bot}\,. \tag{13}$$

For convenience, we use $\Delta z_{ref} = 75$ m in the following discussion. Following the methodological approach as outlined by Donovan et al. (2015), we assume that the cloud droplet number concentration N_d (Eq. 6) is height-independent and the liquid water content $w_l(z)$ increases linearly with height (see Fig. 4). The profile of the liquid-water content (Eq. 4) can thus be expressed by

$$w_l(z) = \Gamma_l \Delta z, \tag{14}$$

with the gradient of the liquid-water content $\Gamma_l = \mathrm{d}w_l/\mathrm{d}z$ for subadiabatic cloud conditions and the column depth

$$\Delta z = z - z_{bot}\,. \tag{15}$$

Cloud droplets form at cloud base and then grow by water uptake at supersaturation conditions in updraft regions. According to Eqs. (4) and (14) we can write

$$\Gamma_l \Delta z = \frac{2}{3}\rho_w \alpha(z) R_e(z)\,. \tag{16}$$

By using Eqs. (6) and (16) and forming the ratio $\Gamma_l \Delta z / N_d$ we obtain

$$\frac{\Gamma_l \Delta z}{N_d} = \frac{4\pi k \rho_w}{3} R_e^3(z) \tag{17}$$

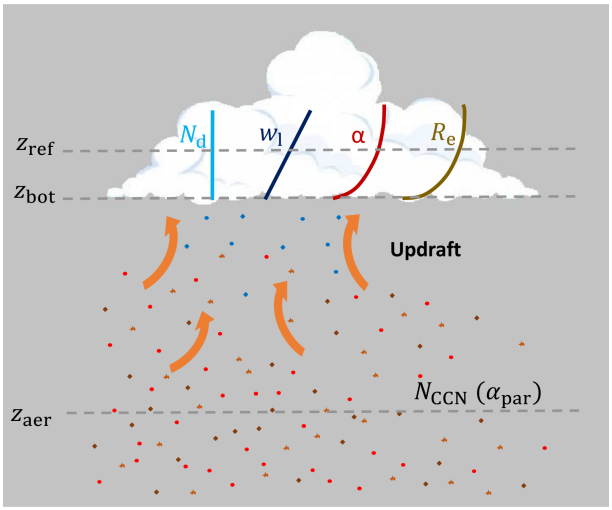

Figure 4. Illustration of the overall concept to investigate aerosol–cloud interaction by combining observations of cloud microphysical properties at height z_{ref} 50–100 m above the cloud base at z_{bot} with aerosol properties (particle extinction coefficient α_{par}, cloud condensation nucleus concentration N_{CCN}) measured at height z_{aer} several hundreds of meters below the cloud base. The indicated height profiles of cloud microphysical properties are used in the simulations to develop the new cloud retrieval scheme. Subadiabatic conditions in the lowest part of the cloud layer are assumed with an height-independent droplet number concentration $N_d(z)$ and a linearly increasing liquid-water content $w_l(z)$. The profiles of the cloud extinction coefficient $\alpha(z)$ and the droplet effective radius $R_e(z)$ are then computed with Eqs. (21) and (18), respectively. All cloud parameters are zero at cloud base.

and for $R_e(z)$

$$R_e(z) = \left(\frac{3\Gamma_l \Delta z}{4\pi \rho_w k N_d}\right)^{1/3}. \quad (18)$$

Further treatment leads to the link between $R_e(z)$ and $R_e(z_{ref})$,

$$R_e(z) = R_e(z_{ref})\left(\frac{z - z_{bot}}{z_{ref} - z_{bot}}\right)^{1/3}. \quad (19)$$

The $R_e(z)$ profile is shown in Fig. 4.

To obtain the profile of the cloud extinction coefficient $\alpha(z)$ used in the simulations we combine Eqs. (16) and (18),

$$\Gamma_l \Delta z = \frac{2}{3}\rho_w \alpha(z)\left(\frac{3\Gamma_l \Delta z}{4\pi \rho_w k N_d}\right)^{1/3}. \quad (20)$$

Rearrangement yields

$$\alpha(z) = \left(\frac{3\Gamma_l \Delta z}{\rho_w}\right)^{2/3}\left(\frac{\pi k N_d}{2}\right)^{1/3}. \quad (21)$$

Finally, we can write

$$\alpha(z) = \alpha(z_{ref})\left(\frac{z - z_{bot}}{z_{ref} - z_{bot}}\right)^{2/3}. \quad (22)$$

The profile of $\alpha(z)$ is sketched in Fig. 4 as well.

We used then the profiles in Fig. 4, described by Eqs. (6), (14), (18), and (21), to simulate the corresponding cross- and co-polarized lidar backscatter returns and the volume depolarization ratio (Eq. 11). We performed computations at two receiver FOVs for 720 different cloud scenarios (defined by the state vector $\boldsymbol{X}$) by using Eqs. (9)–(10). The input parameters (10 values for $\alpha(z_{ref})$, 9 values for $R_e(z_{ref})$, and 8 cloud base altitudes z_{bot}) are given in Table 1. Overall cloud depth was 200 m. Vertical resolution or step width in the computations was 7.5 m, which corresponds to the vertical resolution of the lidar observations introduced in Part 2 (Jimenez et al., 2020a).

Figure 5 shows the profiles of the linear depolarization ratios δ_{in} and δ_{out} for the inner and outer FOVs, i.e., for FOV_{in} of 1 mrad and for FOV_{out} of 2 mrad for four different profiles of the cloud extinction coefficient α and four different profiles of the effective radius R_e of the droplets. The simulated cloud layer is at 3 km height. A monotonic increase in the volume linear depolarization ratio is visible because of the increasing contribution of multiple scattering processes to the amount of backscattered laser photons with increasing cloud penetration depths. With an increasing number of cloud droplets and thus increasing light extinction, the probability of multiple scattering and thus the strength of depolarization increase strongly.

The striking feature in Fig. 5 is the clear dependence of δ_{in}/δ_{out} on the droplet effective radius $R_e(z_{ref})$. In principle, we can show a similar figure by combining different backscatter signals measured with lidar at two different FOVs. However, the comparison of all these combinations clearly revealed that the optimum retrieval of the cloud effective radius (as shown in Fig. 5c) is only possible by means of the co- and cross-polarized signal components observed at different FOVs.

According to Fig. 5c it is recommended to use the lidar observations in the lowest part of the liquid-water cloud to retrieve the cloud microphysical properties. To obtain robust values of the cloud depolarization ratios at the two different FOVs (with low signal noise impact) we integrate, in the next step, the depolarization ratio from the cloud base to a fixed reference altitude (see Fig. 4),

$$\overline{\delta}_{in}(z_{bot}, z_{ref}) = \frac{\int_{z_{bot}}^{z_{ref}} S_{\perp,in}(z)dz}{\int_{z_{bot}}^{z_{ref}} S_{\parallel,in}(z)dz}, \quad (23)$$

$$\overline{\delta}_{out}(z_{bot}, z_{ref}) = \frac{\int_{z_{bot}}^{z_{ref}} S_{\perp,out}(z)dz}{\int_{z_{bot}}^{z_{ref}} S_{\parallel,out}(z)dz}, \quad (24)$$

and further define the dual-FOV ratio of depolarization ratios,

$$\overline{\delta}_{rat}(z_{bot}, z_{ref}) = \frac{\overline{\delta}_{in}(z_{bot}, z_{ref})}{\overline{\delta}_{out}(z_{bot}, z_{ref})}. \quad (25)$$

To check the sensitivity of the dual-FOV retrieval method to the selected pair of FOVs, we used the logarithmic deriva-

Table 1. Lidar and liquid-water cloud input parameters used in the simulations with the MS model.

FOV, full solid angle, Θ_{in} (mrad)	0.5, 1.0. 1.5, 2.0, 2.5
FOV, full solid angle, Θ_{out} (mrad)	1.0, 1.5, 2.0, 2.5, 3.0
Cloud base height (km)	1.0, 1.5, 2.0, 2.5, 3.0, 3.5, 4.0, 5.0
$\alpha(\Delta z_{ref})$ (km^{-1}) for $\Delta z_{ref} = 75$ m	5.2, 7.8, 10.4, 13.0, 15.6, 18.2, 20.8, 23.4, 26.0, 28.6
$R_e(\Delta z_{ref})$ (µm) for $\Delta z_{ref} = 75$ m	3.6, 4.7, 5.8, 6.9, 7.9, 9.4, 10.8, 12.6, 14.4

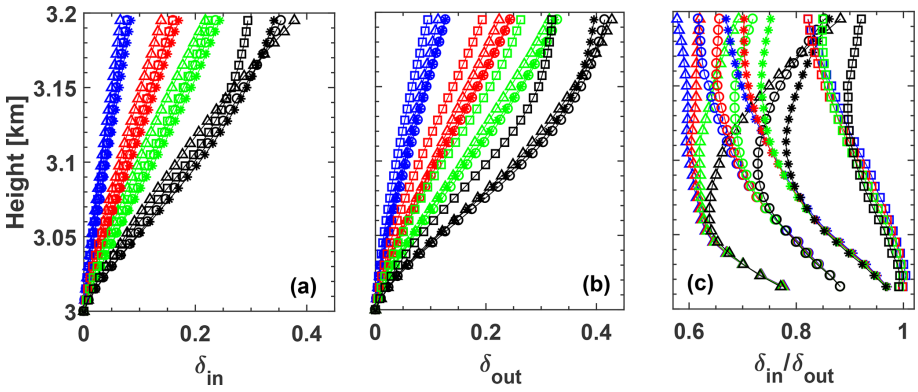

Figure 5. Simulated depolarization ratio profiles for **(a)** FOV_{in} of 1 mrad, **(b)** FOV_{out} of 2 mrad, and **(c)** profiles of the ratio $\delta_{in}(z)/\delta_{out}(z)$. $\alpha(z_{ref})$ values are 5.2 km^{-1} (blue), 10.4 km^{-1} (red), 15.6 km^{-1} (green), and 26.0 km^{-1} (black) (see Table 1, z_{ref} =75 m above the cloud base at $z_{bot} = 3$ km). Different symbols indicate different simulated $R_e(z_{ref})$ values (3.6 µm (triangle), 5.8 µm (circle), 7.9 µm (star), and 14.4 µm (square)). A clear dependence of $R_e(z_{ref})$ on $\delta_{in}(z)/\delta_{out}(z)$ is visible up to about 100 m above the cloud base.

tive of the observables and the retrievable parameters, as proposed by Malinka and Zege (2007). We performed simulations with FOVs from 0.5 to 3.0 mrad and found that the highest sensitivity to the droplet effective radius is given for the case with the highest FOV_{out}-to-FOV_{in} ratio. However, the selection of FOV_{in} of 1 mrad and FOV_{out} of 2 mrad as used in the following was found to be sufficiently sensitive for liquid-water cloud studies and, on the other hand, a good compromise when keeping cloud inhomogeneities in consideration. Besides, this choice of FOVs allow us to upgrade our Polly systems (Engelmann et al., 2016) into a Dual-FOV Polarization lidar simply by adding one cross-polarized channel. This topic will be discussed in Part 2. The backscatter signals may be different for the two FOVs not only because of the different multiple scattering contributions, but also because of the differences in the amount of photon backscatter from different cloud cross sections and cloud volumes (defined by cloud height and FOV) as a result of inhomogeneities in cloud properties that may vary in the horizontal plane.

In Fig. 6, an overview of all simulations of $\overline{\delta}_{rat}$ and $\overline{\delta}_{in}$ for 90 cloud scenarios (all possible combinations of cloud extinction and effective radii in Table 1) are shown for a cloud layer at $z_{bot} = 3$ km and FOVs of 1 and 2 mrad. As mentioned, the depolarization ratio values are integrated over the lowest 75 m of the cloud layer. Again, a clear dependence of $\overline{\delta}_{rat}$ on the effective radius R_e at z_{ref} (75 m above the cloud base) is visible in Fig. 6a. The dominating impact of the cloud extinction coefficient on $\overline{\delta}_{in}$ is shown in Fig. 6b.

In Fig. 7a, the relationship between $\overline{\delta}_{rat}$ and effective radius $R_e(z_{ref})$ is presented for all cloud layers with base heights from 1 to 5 km and FOVs of 1 and 2 mrad. The horizontal bars indicate the influence of the cloud extinction coefficient for each of the simulated nine effective radii for the eight cloud layers. A polynomial regression is applied to each of the eight cloud simulation data sets and the respective cubic polynomial fits (Eq. 26) are shown as colored curves in Fig. 7a. To perform the regression the mean values of $\overline{\delta}_{rat}$ over α were considered.

Equation (26) is now used in our dual-FOV method to derive the droplet effective radius $R_e(z_{ref})$ from the measurements of $\overline{\delta}_{rat}$ for the integration length $\Delta z_{ref} = 75$ m:

$$R_e(z_{ref}) = R_0 + R_1 \times \overline{\delta}_{rat} + R_2 \times \overline{\delta}^2_{rat} + R_3 \times \overline{\delta}^3_{rat}\,. \qquad (26)$$

The polynomial coefficients R_0, R_1, R_2, and R_3 are given in Table 2. For a given cloud base altitude, we obtained the appropriate curve by interpolating the two nearest curves (computed by means of the Table 2 values) for the adjacent heights.

In the second step of the retrieval, the cloud extinction coefficient $\alpha(z_{ref})$ is determined by using the derived effective radius and the measured integrated depolarization ratio $\overline{\delta}_{in}$ inserted in the quadratic polynomial fit,

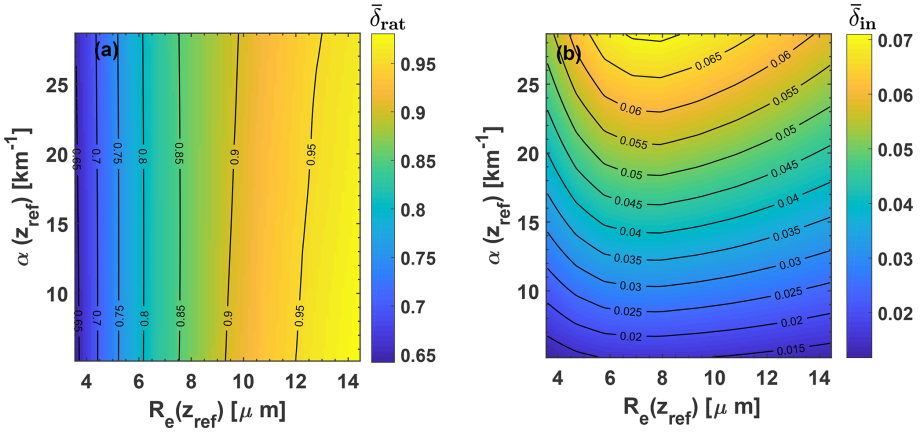

Figure 6. **(a)** Ratio $\overline{\delta}_{rat}(z_{bot}, z_{ref})$ of depolarization ratios (see Eq. (25), integration height range of $\Delta z_{ref} = 75$ m) as a function of droplet effective radius $R_e(z_{ref})$ and cloud extinction coefficient $\alpha(z_{ref})$. Cloud base z_{bot} is at 3 km height, z_{ref} is thus at 3.075 km height. **(b)** Integrated depolarization ratio $\overline{\delta}_{in}(z_{bot}, z_{ref})$ as a function of $R_e(z_{ref})$ and $\alpha(z_{ref})$. Isolines of $\overline{\delta}_{rat}$ in **(a)** show the strong dependence of $\overline{\delta}_{rat}$ on the effective radius. The $\overline{\delta}_{in}$ isolines in **(b)** highlight the dominating influence of the extinction coefficient on $\overline{\delta}_{in}$. The figures are based on 720 simulated cloud scenarios for each of the FOVs of 1 and 2 mrad.

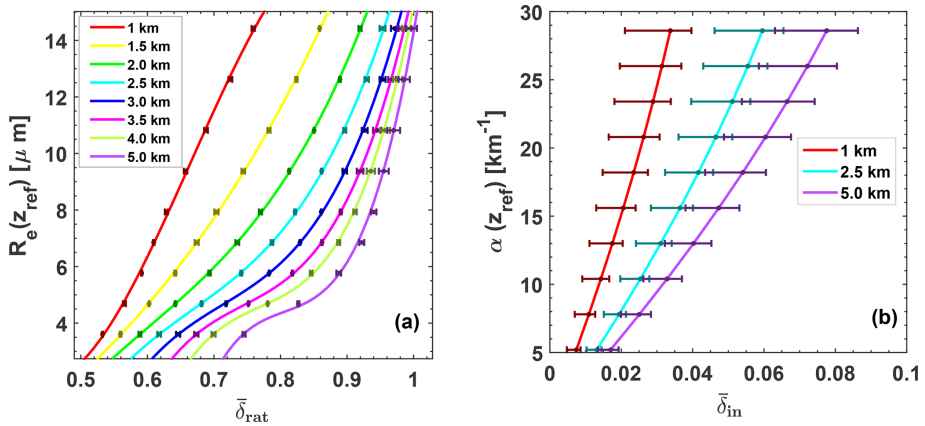

Figure 7. **(a)** Droplet effective radius $R_e(z_{ref})$ as a function of $\overline{\delta}_{rat} = \overline{\delta}_{in}/\overline{\delta}_{out}$ for $\Delta z_{ref} = 75$ m and **(b)** relationship between the measured $\overline{\delta}_{in}$ for FOV = 1 mrad and cloud extinction coefficient α. Eight different cloud layers with base height z_{bot} from 1 to 5 km height (given as numbers in the panels) are simulated in **(a)**, and three different layers are simulated in **(b)**. For each cloud layer (indicated by different colors) simulations with all combinations of R_e–α profile pairs (in Table 1) are performed. The small bars in **(a)** indicate the range of possible δ_{rat} values for the whole range of α values at a given R_e value, which indicate the very low influence of α on the R_e retrieval (simulated α range is given in Table 1). A polynomial regression is applied to the mean values of $\overline{\delta}_{rat}$. This regression analysis is performed for each of the eight cloud layers. The cubic model (Eq. 26) for each cloud layer is indicated as thick solid colored line. The bars in **(b)** indicate the range of possible δ_{in} values for a given α value. Here, the length of the bars indicate the relatively strong R_e influence on the $\alpha(z_{ref})$ retrieval (simulated R_e range is given in Table 1). The respective regression analysis leads here to the thick solid lines calculated with Eq. (27).

$$\alpha(z_{ref}) = \alpha_0(R_e, z_{bot}) + \alpha_1(R_e, z_{bot}) \times \overline{\delta}_{in} + \alpha_2(R_e, z_{bot}) \times \overline{\delta}_{in}^2 . \quad (27)$$

The coefficients $\alpha_0(R_e, z_{bot})$, $\alpha_1(R_e, z_{bot})$, and $\alpha_2(R_e, z_{bot})$ are obtained from a polynomial regression analysis applied to each simulation data set for a given cloud layer characterized by z_{bot} and $R_e(z_{ref})$ as well as the given inner FOV. Figure 7b shows the relationship between the different parameters.

The two-step retrieval is finally explained again in Fig. 8 for a cloud layer with cloud base height of 3 km, z_{ref} at 75 m above cloud base height, and FOVs of 1 and 2 mrad. To show again the low dependency of $\overline{\delta}_{rat}$ on cloud extinction, all 10 simulations with $\alpha(z_{ref})$ values from 5.2 to 28.6 km^{-1} are presented. A clear relationship between $\overline{\delta}_{rat}$ and $R_e(z_{ref})$ according to Eq. (26) is given. Figure 8b is the basis for the second step of the retrieval. Here, the polynomial fits (Eq. 27) of the $\alpha(z_{ref})$ vs. $\overline{\delta}_{in}$ simulations are used and shown in Fig. 8b for the nine discrete effective radius values in Table 1. Thus,

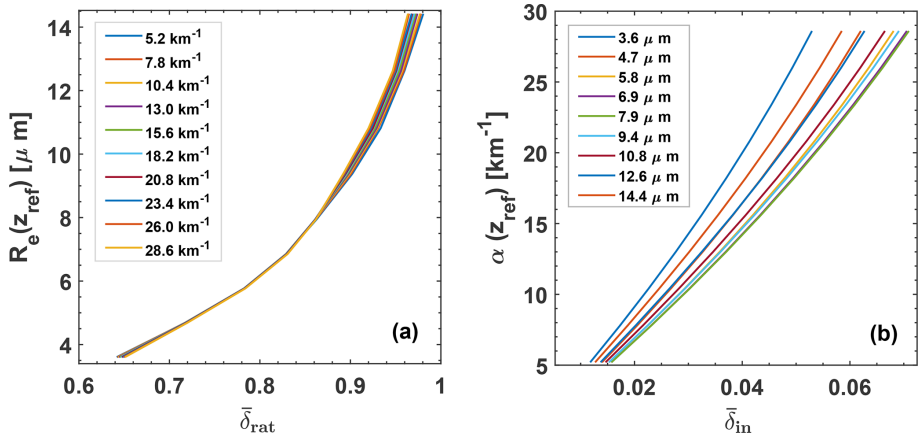

Figure 8. Two-step approach to derive $R_e(z_{ref})$ and $\alpha(z_{ref})$ from $\overline{\delta}_{rat}(z_{bot}, z_{ref})$ and $\overline{\delta}_{in}(z_{bot}, z_{ref})$ for a liquid cloud layer with $z_{bot} = 3$ km and $z_{ref} = 3.075$ km. In the first step **(a)**, $\overline{\delta}_{rat}$ is used to determine $R_e(z_{ref})$ by means of Eq. (26), and in the second step **(b)**, $\overline{\delta}_{in}$ and R_e (from step 1) are used to determine $\alpha(z_{ref})$ with Eq. (27). In **(a)**, all simulations with all available combinations of R_e–α profile pairs are shown to indicate the low impact of α (given as numbers) on the retrieval. In **(b)**, the relationship between $\overline{\delta}_{in}$ and α for nine R_e values (given as numbers) are shown to indicate the comparably large influence of R_e on the α retrieval.

Table 2. Polynomial coefficients used in the computation of R_e with Eq. (26).

Height (km)	1.0	1.5	2.0	2.5	3.0	3.5	4.0	5.0
$\Theta_{in} = 0.5$ mrad, $\Theta_{out} = 2.0$ mrad								
R_3	−441.36	15.423	22.617	15.927	13.407	12.16	13.044	18.049
R_2	405.55	−29.724	−26.928	−12.61	−5.4525	−0.98796	−0.25593	−5.329
R_1	−56.13	58.634	43.376	29.091	20.206	13.875	10.145	7.6976
R_0	−1.7577	−10.776	−7.5234	−4.8777	−3.1182	−1.7942	−0.89156	0.039517
Limits δ_{rat}	0.231	0.235	0.243	0.251	0.258	0.266	0.273	0.286
	−0.433	−0.530	−0.616	−0.685	−0.738	−0.780	−0.812	−0.859
$\Theta_{in} = 0.5$ mrad, $\Theta_{out} = 3.0$ mrad								
R_3	81.663	42.223	16.662	6.3751	2.6949	1.0601	1.5411	6.4387
R_2	−113.59	−52.42	−16.483	0.82019	9.207	14.553	16.473	13.649
R_1	94.713	55.496	33.1	20.212	12.215	6.2326	2.2924	−1.4903
R_0	−11.187	−6.4306	−3.7067	−2.0188	−0.8682	0.080457	0.79579	1.729
Limits δ_{rat}	0.163	0.172	0.183	0.194	0.206	0.217	0.228	0.249
	−0.413	−0.524	−0.616	−0.686	−0.739	−0.778	−0.808	−0.848
$\Theta_{in} = 1.0$ mrad, $\Theta_{out} = 2.0$ mrad								
R_3	−84.414	113.3	166.93	225.94	310.96	408.5	528.35	830.46
R_2	161.7	−206.18	−322.73	−458.62	−657.33	−889.14	−1177.2	−1917.2
R_1	−50.452	158.26	232.73	330.11	479.21	658	884.29	1479.7
R_0	−3.0039	−40.491	−55.768	−78.64	−115.45	−160.89	−219.53	−377.74
Limits δ_{rat}	0.525	0.539	0.555	0.570	0.585	0.600	0.613	0.637
	−0.747	−0.845	−0.907	−0.944	−0.964	−0.976	−0.983	−0.991
$\Theta_{in} = 1.0$ mrad, $\Theta_{out} = 3.0$ mrad								
R_3	41.408	41.372	55.974	78.481	111.98	156.57	215.13	404.41
R_2	−72.367	−62.602	−87.735	−131.56	−200.01	−293.79	−420.61	−844.39
R_1	75.554	55.203	63.881	88.371	131.71	194.52	283.18	592.99
R_0	−17.638	−12.128	−13.111	−17.875	−27.104	−41.088	−61.577	−136.28
Limits δ_{rat}	0.370	0.393	0.418	0.442	0.466	0.489	0.512	0.553
	−0.713	−0.836	−0.908	−0.945	−0.965	−0.974	−0.978	−0.978

to avoid large errors in the $\alpha(z_{\mathrm{ref}})$ retrieval, $R_{\mathrm{e}}(z_{\mathrm{ref}})$ from step 1 is used to select the right curve for the $\alpha(z_{\mathrm{ref}})$ determination.

Finally, after the derivation of the droplet extinction coefficient $\alpha(z_{\mathrm{Ref}})$ and the droplet effective radius $R_{\mathrm{e}}(z_{\mathrm{ref}})$ as independent variables, we can compute the liquid-water content $w_{\mathrm{l}}(z_{\mathrm{ref}})$ with Eq. (4) and the droplet number concentration $N_{\mathrm{d}}(z_{\mathrm{ref}})$ with Eq. (6), in the same way as presented by Schmidt et al. (2013, 2014).

The polynomial coefficients to retrieve $R_{\mathrm{e}}(z_{\mathrm{ref}})$, in Table 2, for the pair of FOVs 0.1 and 2.0 mrads, and the matrices containing the values of $\overline{\delta}_{\mathrm{in}}$ for given values of $R_{\mathrm{e}}(z_{\mathrm{ref}})$ and $\alpha(z_{\mathrm{ref}})$, to generate the quadratic polynomials for the second step of the retrieval, i.e to derive $\alpha(z_{\mathrm{ref}})$, from the obtained $R_{\mathrm{e}}(z_{\mathrm{ref}})$ and the observation of $\overline{\delta}_{\mathrm{in}}$, can be found in Jimenez et al. (2020b).

5 Retrieval uncertainties

With Eqs. (26) and (27) the retrieval of the effective radius and extinction coefficient is possible. In this section, we illuminate the underlying uncertainties in the retrieval of these cloud parameters. First, we consider the assumption about the vertical structure of the cloud, i.e., a subadiabatic cloud system. Whether the cloud conditions are adiabatic or subadiabatic is not an important issue as in both systems the water content increases linearly with height. When the real water content or number concentration profiles differ slightly from our assumptions (of a linearly increasing w_{l} and height-independent N_{d}), the monotonic form of the simulated observables ($\overline{\delta}_{\mathrm{in}}$ and $\overline{\delta}_{\mathrm{rat}}$) as a function of droplet size and extinction coefficient (in Fig. 7) would still hold for cases in which the vertical profiles differ from the theoretical ones, as long as the height-averaged values are the same. However, in cases with very different profiles, e.g., in cases with vertically homogeneous cloud properties, the retrieval curves may change. As a consequence, the interpretation of cloud observations, e.g., during downdraft situations, should be interpreted with care because our basic assumption of a linearly increasing w_{l} and height-constant N_{d} may be no longer valid.

The retrieval of the effective radius $R_{\mathrm{e}}(z_{\mathrm{ref}})$ of the cloud droplets needs the ratio of depolarization ratios $\overline{\delta}_{\mathrm{rat}}$ and the cloud base height z_{bot} as input. The relationship between $R_{\mathrm{e}}(z_{\mathrm{ref}})$ and $\overline{\delta}_{\mathrm{rat}}$ is also a function of the cloud extinction coefficient $\alpha(z_{\mathrm{ref}})$. We can estimate the uncertainties caused by the uncertainty $\pm\Delta\overline{\delta}_{\mathrm{rat}}$ in the $\overline{\delta}_{\mathrm{rat}}$ measurement by calculating

$$\pm\sigma_{\mathrm{ran},R_{\mathrm{e}}}(\Delta\overline{\delta}_{\mathrm{rat}}) = \left[R_0 + R_1 \times (\overline{\delta}_{\mathrm{rat}} \pm \Delta\overline{\delta}_{\mathrm{rat}}) + R_2 \times (\overline{\delta}_{\mathrm{rat}} \pm \Delta\overline{\delta}_{\mathrm{rat}})^2 + R_3 \times (\overline{\delta}_{\mathrm{rat}} \pm \Delta\overline{\delta}_{\mathrm{rat}})^3\right] - R_{\mathrm{e}} \quad (28)$$

and by taking half of the respective uncertainty bars.

Systematic retrieval uncertainties $\sigma_{\mathrm{sys},R_{\mathrm{e}}}$ arise from the use of the model (polynomial functions in Fig. 7), the uncertainties in the determined cloud base height Δz_{bot} (we assume ± 15 m), and the influence of the cloud extinction coefficient (the uncertainty is denoted here as $\Delta\alpha$ and given by the range of values in Table 1 from 5.2 to 28.6 Mm^{-1}). From the extended error simulations and from the analysis with real (observational) data we conclude that

$$\sigma_{\mathrm{sys},R_{\mathrm{e}}}(\Delta\alpha) \approx 0.15 R_{\mathrm{e}}(z_{\mathrm{ref}}), \quad (29)$$

$$\sigma_{\mathrm{sys},R_{\mathrm{e}}}(\Delta z_{\mathrm{bot}}) \approx 0.10 R_{\mathrm{e}}(z_{\mathrm{ref}}). \quad (30)$$

On average, input uncertainties may partly cancel out and the mean uncertainty is given by

$$\sigma_{\mathrm{sys},R_{\mathrm{e}}}(\Delta\alpha, \Delta z_{\mathrm{bot}}) = \sqrt{\sigma_{\mathrm{sys},R_{\mathrm{e}}}(\Delta\alpha)^2 + \sigma_{\mathrm{sys},R_{\mathrm{e}}}(\Delta z_{\mathrm{bot}})^2}. \quad (31)$$

The influence of measurement uncertainties on the retrieval of $\alpha(z_{\mathrm{ref}})$ is estimated by considering the standard deviation $\pm\Delta\overline{\delta}_{\mathrm{in}}$ in the computation,

$$\pm\sigma_{\mathrm{ran},\alpha}(\Delta\overline{\delta}_{\mathrm{rat}}) = \left[\alpha_0 + \alpha_1 \times (\overline{\delta}_{\mathrm{in}} \pm \Delta\overline{\delta}_{\mathrm{in}}) + \alpha_2 \times (\overline{\delta}_{\mathrm{in}} \pm \Delta\overline{\delta}_{\mathrm{in}})^2\right] - \alpha. \quad (32)$$

In a similar way to that described above for the systematic uncertainty in R_{e}, we estimated $\sigma_{\mathrm{sys},\alpha}$ with $\Delta z_{\mathrm{bot}} \pm 15$ m and by using ΔR_{e} according to Eq. (31) in the second retrieval step to obtain $\alpha(z_{\mathrm{ref}})$. Again, from many simulations we concluded that

$$\sigma_{\mathrm{sys},\alpha}(\Delta R_{\mathrm{e}}) \approx 0.08\alpha(z_{\mathrm{ref}}), \quad (33)$$

$$\sigma_{\mathrm{sys},\alpha}(\Delta z_{\mathrm{bot}}) \approx 0.15\alpha(z_{\mathrm{ref}}). \quad (34)$$

The overall mean systematic uncertainty may be given by

$$\sigma_{\mathrm{sys},\alpha}(\Delta R_{\mathrm{e}}, \Delta z_{\mathrm{bot}}) = \sqrt{\sigma_{\mathrm{sys},\alpha}(\Delta R_{\mathrm{e}})^2 + \sigma_{\mathrm{sys},\alpha}(\Delta z_{\mathrm{bot}})^2}. \quad (35)$$

6 Retrieval of cloud-relevant aerosol properties and aerosol–cloud-interaction parameters

6.1 Lidar-derived aerosol properties

For completeness of the theoretical Part 1, we briefly introduce the aerosol parameters needed for the ACI studies. Examples of aerosol observations with the multiwavelength polarization Raman lidar Polly (portable lidar system) (Engelmann et al., 2016) used in Part 2 and upgraded to a dual-FOV polarization lidar can be found in Baars et al. (2016) and Hofer et al. (2017, 2020). The sketch in Fig. 4 illustrates our overall concept of lidar-based ACI studies. The aerosol parameters are measured with the lidar at the smaller FOV ($\mathrm{FOV}_{\mathrm{in}}$) several hundreds of meters below the cloud base. The cloud- and ACI-relevant aerosol proxies are the particle extinction coefficient $\alpha_{\mathrm{par}}(z)$ and the cloud condensation nucleus concentration $N_{\mathrm{CCN}}(z)$. The methodology to derive

N_{CCN} profiles from measurements of particle optical properties is outlined in Mamouri and Ansmann (2016). A brief summary of the method, denoted as the POLIPHON (Polarization Lidar Photometer Networking) method, is given here.

A specific problem in ACI studies is the retrieval of the particle backscatter and extinction profiles below extended liquid-water cloud layers in the first step. The required calibration of the lidar profiles in clear air (in pure Rayleigh scattering conditions), i.e., in the upper troposphere and lower stratosphere, is then not possible. In these cases with aerosol backscatter signals up to cloud base height z_{bot} only, the so-called lidar constant is required in the retrieval of aerosol properties. The determination of the lidar constant (considering all instrumental constants, such as laser pulse energy and receiver telescope area, in the basic lidar equation) following the procedure of Wiegner and Geiß (2012) is performed during cloud-free situations before or after the passage of the cloud fields or during periods with cloud holes so that clear air layers (Rayleigh scattering regime) are available for the lidar calibration. Subsequently, the determined lidar constant is used during the cloudy periods in the data analysis to retrieve the backscatter coefficient profiles up to the base of the optically dense water clouds again following the procedure of Wiegner and Geiß (2012).

By means of height profiles of the aerosol particle depolarization ratio and the particle backscatter coefficient, the POLIPHON data analysis separates particle backscatter and extinction contribution of the three basic aerosol types (marine aerosol, mineral dust, anthropogenic haze). The aerosol-type-dependent 532 nm extinction coefficients below the cloud base z_{bot} are then converted into particle number concentrations and respective CCN concentrations (for a water supersaturation level of 0.2 % or relative humidity over water of 100.2 %) as described by Mamouri and Ansmann (2016).

For pure marine conditions, we obtain N_{CCN} from α_{par} by using the following conversion:

$$N_{CCN} = 7(\alpha_{par})^{0.85}, \tag{36}$$

with N_{CCN} per cubic centimeter (cm^{-3}) and α_{par} in units of inverse megameter (Mm^{-1}). For urban haze conditions (central European pollution conditions), we apply

$$N_{CCN} = 25(\alpha_{par})^{0.95} \tag{37}$$

and for desert dust

$$N_{CCN} = 4(\alpha_{par})^{0.9}. \tag{38}$$

The N_{CCN} values assume that all dry particles with radius > 50 nm (marine, urban) and > 100 nm are potential cloud condensation nuclei. The parameterization holds for an ambient relative humidity of 60 % relative humidity for continental fine-mode aerosol and 80 % relative humidity in the case of marine particles. Respective water-uptake effects by aerosol particles are considered and corrected in Eqs. (36) and (37). In the case of hydrophobic dust particles, no water uptake effect is considered and corrected.

The uncertainty in the basic aerosol-type-dependent extinction coefficients and in the retrieved N_{CCN} values is on the order of 20 % and 50 %–100 %, respectively. However, aircraft comparisons (Düsing et al., 2018; Haarig et al., 2019) and long-term field studies at a central European background station (Schmale et al., 2018) revealed that the uncertainty is typically on the order of 50 % for lidar-derived CCN estimates. It should be emphasized at the end that the Raman lidar Polly permits the retrieval of profiles of the water-vapor mixing ratio and relative humidity (RH) (Dai et al., 2018) so that, in principle, actual RH measurements are available for the required aerosol water uptake effects in the N_{CCN} conversion procedure as described by Mamouri and Ansmann (2016)

6.2 Aerosol–cloud-interaction (ACI) parameter

The study of the influence of aerosol particles on liquid-water cloud evolution and cloud microphysical properties is based on two ACI parameters defined as follows (Feingold et al., 2001; McComiskey et al., 2009; Schmidt et al., 2013, 2014):

$$E_{ACI,\alpha_{par}}(N_d, \alpha_{par}) = d\ln(N_d)/d\ln(\alpha_{par}) \tag{39}$$

and

$$E_{ACI,N_{CCN}}(N_d, N_{CCN}) = d\ln(N_d)/d\ln(N_{CCN}). \tag{40}$$

The so-called nucleation-efficiency parameter $E_{ACI,\alpha_{par}}$ describes the relative change of the cloud droplet number concentration N_d with a relative change in the particle extinction coefficient α_{par}. Correspondingly, $E_{ACI,N_{CCN}}$ characterizes the relative increase in N_d with a relative increase in the cloud condensation nucleus concentration N_{CCN}. The higher the ACI value, the stronger the impact of the observed aerosol conditions on the cloud microphysical properties.

7 Summary

We presented a new polarization-based lidar approach to derive microphysical properties of pure liquid-water clouds. Extended simulations with a multiple scattering model were performed regarding the relationship between cloud microphysical and light-extinction properties and the cloud depolarization ratio measured with lidar at two different FOVs. These simulations served as the basis for the development of the new dual-FOV polarization lidar method. An extended error analysis was performed as well. The new dual-FOV polarization lidar technique can be combined with the POLIPHON method, which allows the profiling of CCN concentrations below the cloud base. In Table 3, the full data analysis scheme of the dual-FOV polarization lidar is shown. All steps of the data analysis procedure from the determination of the

Table 3. Overview of the cloud and aerosol retrieval procedure (step-by-step data analysis). The data analysis starts with a precise determination of the cloud base height z_{bot}. The cloud products are given at the reference height z_{ref}, 75 m above the cloud base height z_{bot}. In the estimation of the ACI efficiency, particle extinction and cloud condensation nucleus concentration at z_{aer}, usually several hundreds of meters below the cloud base, are considered.

Parameter	Symbol	Equation	Uncertainty
Cloud base height	z_{bot}		0.1 %–1 %
Cloud depolarization ratios	$\overline{\delta}_{in}(z_{bot}, z_{ref})$	Eq. (23)	5 %
	$\overline{\delta}_{out}(z_{bot}, z_{ref})$	Eq. (24)	5 %
	$\overline{\delta}_{rat}(z_{bot}, z_{ref})$	Eq. (25)	10 %–15 %
Droplet effective radius	$R_e(z_{ref})$	Eq. (26)	15 %
Cloud extinction coefficient	$\alpha(z_{ref})$	Eq. (27)	15 %–20 %
Liquid water content	$w_l(z_{ref})$	Eq. (4)	25 %
Cloud droplet number concentration	$N_d(z_{ref})$	Eq. (6)	25 %–75 %
Aerosol depolarization ratio	$\delta_{par}(z)$		5 %–10 %
Aerosol extinction coefficient	$\alpha_{par}(z_{aer})$		20 %
Cloud condensation nucleus concentration	$N_{CCN}(z_{aer})$	Eqs. (36)–(38)	30 %–100 %
Aerosol–cloud-interaction efficiency	$E_{ACI,\alpha_{par}}(N_d, \alpha_{par})$	Eq. (39)	
Aerosol–cloud-interaction efficiency	$E_{ACI,N_{CCN}}(N_d, N_{CCN})$	Eq. (40)	

cloud microphysical properties and the aerosol proxies to the ACI parameters are listed.

In our follow-up article (Jimenez et al., 2020a), we describe how we implemented the novel dual-FOV polarization lidar technique into a Polly instrument which is now being used in a long-term field campaign in Punta Arenas, southern Chile, at the southern-most tip of South America. The field site is surrounded by the Southern Ocean. Pristine marine conditions prevail. Continental and especially anthropogenic aerosol sources usually play a negligible role regarding their influence on cloud evolution and properties in this region of the world. We present two case studies of this campaign in Part 2. Case 1 is used to explain the full aerosol and cloud data analysis scheme in detail. This case study includes an uncertainty discussion and comparisons with alternative approaches to derive cloud microphysical properties such as the single-FOV polarization lidar technique (Donovan et al., 2015). Based on case 2, the potential of the new lidar technique to improve ACI studies in the case of liquid-water clouds is highlighted.

Data availability. The simulation products to perform the retrieval of microphysical properties can be found at https://doi.org/10.5281/zenodo.4107137 (Jimenez et al., 2020b).

Author contributions. CJ and AA prepared the manuscript. CJ developed the method and performed the MS simulations. The analytical MS code was developed and provided by AM. DD performed the simulations with the ECSIM MS model. AA, RE, DD, AM, JS, and UW contributed to the design of the simulations study and to the discussion of the results.

Competing interests. The authors declare that they have no conflict of interest.

Special issue statement. This article is part of the special issue "EARLINET aerosol profiling: contributions to atmospheric and climate research". It is not associated with a conference.

Acknowledgements. The authors would like to thank the TROPOS lidar team members for their support and numerous fruitful discussions during the last 5 years.

Financial support. This research has been supported by the DAAD/Becas Chile (grant no. 57144001) and the ACTRIS Research Infrastructure (EU H2020-R&I) (grant no. 654109).

The publication of this article was funded by the Open Access Fund of the Leibniz Association.

Review statement. This paper was edited by Eduardo Landulfo and reviewed by two anonymous referees.

References

Albrecht, B. A., Fairall, C. W., Thomson, D. W., White, A. B., Snider, J. B., and Schubert, W. H.: Surface-based remote sensing of the observed and the adiabatic liquid water content of stratocumulus clouds, Geophys. Res. Lett., 17, 89–92, https://doi.org/10.1029/GL017i001p00089, 1990.

Ansmann, A., Mamouri, R.-E., Hofer, J., Baars, H., Althausen, D., and Abdullaev, S. F.: Dust mass, cloud condensation nuclei, and ice-nucleating particle profiling with polarization

lidar: updated POLIPHON conversion factors from global AERONET analysis, Atmos. Meas. Tech., 12, 4849–4865, https://doi.org/10.5194/amt-12-4849-2019, 2019.

Baars, H., Kanitz, T., Engelmann, R., Althausen, D., Heese, B., Komppula, M., Preißler, J., Tesche, M., Ansmann, A., Wandinger, U., Lim, J.-H., Ahn, J. Y., Stachlewska, I. S., Amiridis, V., Marinou, E., Seifert, P., Hofer, J., Skupin, A., Schneider, F., Bohlmann, S., Foth, A., Bley, S., Pfüller, A., Giannakaki, E., Lihavainen, H., Viisanen, Y., Hooda, R. K., Pereira, S. N., Bortoli, D., Wagner, F., Mattis, I., Janicka, L., Markowicz, K. M., Achtert, P., Artaxo, P., Pauliquevis, T., Souza, R. A. F., Sharma, V. P., van Zyl, P. G., Beukes, J. P., Sun, J., Rohwer, E. G., Deng, R., Mamouri, R.-E., and Zamorano, F.: An overview of the first decade of Polly^{NET}: an emerging network of automated Raman-polarization lidars for continuous aerosol profiling, Atmos. Chem. Phys., 16, 5111–5137, https://doi.org/10.5194/acp-16-5111-2016, 2016.

Barlakas, V., Deneke, H., and Macke, A.: The sub-adiabatic model as a concept for evaluating the representation and radiative effects of low-level clouds in a high-resolution atmospheric model, Atmos. Chem. Phys., 20, 303–322, https://doi.org/10.5194/acp-20-303-2020, 2020.

Bissonnette, L. R., Bruscaglioni, P., Ismaelli, A., Zaccanti, G., Cohen, A., Benayahu, Y., Kleiman, M., Egert, S., Flesia, C., Schwendimann, P., Starkov, A. V., Noormohammadian, M., Oppel, U. G., Winker, D. M., Zege, E. P., Katsev, I. L., and Polonsky, I. N.: LIDAR multiple scattering from clouds, Appl. Phys. B, 60, 355–362, https://doi.org/10.1007/BF01082271, 1995.

Bissonnette, L. R., Roy, G., and Roy, N.: Multiple-scattering-based lidar retrieval: method and results of cloud probings, Appl. Optics, 44, 5565–5581, 2005.

Bissonnette, L. R., Roy, G., and Tremblay, G.: Lidar-Based Characterization of the Geometry and Structure of Water Clouds, J. Atmos. Ocean. Tech., 24, 1364–1376,https://doi.org/10.1175/JTECH2045.1, 2006.

Chaikovskaya, L.: Remote sensing of clouds using linearly and circularly polarized laser beams: techniques to compute signal polarization, in: Light Scattering Reviews, edited by: Kokhanovsky, A. A., Springer Praxis Books, Berlin and Heidelberg, Germany, 191–228, https://doi.org/10.1007/978-3-540-48546-9_6, 2008.

Chaikovskaya, L. and Zege, E.: Theory of polarized lidar sounding including multiple scattering, J. Quant. Spectrosc. Ra., 88, 21–35, https://doi.org/10.1016/j.jqsrt.2004.01.002, 2004.

Chaikovskaya, L., Zege, E., Katzev, I., Hirschberger, M., and Oppel, U.: Lidar returns from multiply scattered media in multiple-field-of-view and CCD lidars with polarization devices: comparison of semi-analytical solution and Monte Carlo data, Appl. Optics, 48, 623–632, 2009.

Dai, G., Althausen, D., Hofer, J., Engelmann, R., Seifert, P., Bühl, J., Mamouri, R.-E., Wu, S., and Ansmann, A.: Calibration of Raman lidar water vapor profiles by means of AERONET photometer observations and GDAS meteorological data, Atmos. Meas. Tech., 11, 2735–2748, https://doi.org/10.5194/amt-11-2735-2018, 2018.

Donovan, D., Voors, R., van Zadelhoff, G.-J., and Acarreta, J.-R.: ECSIM Model and Algorithms Document, KNMI Tech. Rep.: ECSIM-KNMI-TEC-MAD01-R, available at: https://www.academia.edu/33712449/ECSIM_Model_and_Algorithms_Document (last access: 28 November 2020), 2010.

Donovan, D. P., Klein Baltink, H., Henzing, J. S., de Roode, S. R., and Siebesma, A. P.: A depolarisation lidar-based method for the determination of liquid-cloud microphysical properties, Atmos. Meas. Tech., 8, 237–266, https://doi.org/10.5194/amt-8-237-2015, 2015.

Düsing, S., Wehner, B., Seifert, P., Ansmann, A., Baars, H., Ditas, F., Henning, S., Ma, N., Poulain, L., Siebert, H., Wiedensohler, A., and Macke, A.: Helicopter-borne observations of the continental background aerosol in combination with remote sensing and ground-based measurements, Atmos. Chem. Phys., 18, 1263–1290, https://doi.org/10.5194/acp-18-1263-2018, 2018.

Eloranta, E. W.: Practical model for the calculations of multiply scattered lidar returns, Appl. Optics, 37, 2464–2472, 1998.

Engelmann, R., Kanitz, T., Baars, H., Heese, B., Althausen, D., Skupin, A., Wandinger, U., Komppula, M., Stachlewska, I. S., Amiridis, V., Marinou, E., Mattis, I., Linné, H., and Ansmann, A.: The automated multiwavelength Raman polarization and water-vapor lidar Polly^{XT}: the neXT generation, Atmos. Meas. Tech., 9, 1767–1784, https://doi.org/10.5194/amt-9-1767-2016, 2016.

Feingold, G., Remer, L., Ramaprasad, J., and Kaufman, Y.: Analysis of smoke impact on clouds in Brazilian biomass burning regions: An extension of Twomey's approach, J. Geophys. Res., 106, 907–922, https://doi.org/10.1029/2001JD000732, 2001.

Foth, A. and Pospichal, B.: Optimal estimation of water vapour profiles using a combination of Raman lidar and microwave radiometer, Atmos. Meas. Tech., 10, 3325–3344, https://doi.org/10.5194/amt-10-3325-2017, 2017.

Giannakaki, E., Kokkalis, P., Marinou, E., Bartsotas, N. S., Amiridis, V., Ansmann, A., and Komppula, M.: The potential of elastic and polarization lidars to retrieve extinction profiles, Atmos. Meas. Tech., 13, 893–905, https://doi.org/10.5194/amt-13-893-2020, 2020.

Grosvenor, D. P., Sourdeval, O., Zuidema, P., Ackerman, A., Alexandrov, M. D., Bennartz, R., Boers, R., Cairns, B., Chiu, J. C., Christensen, M., Deneke, H., Diamond, M., Feingold, G., Fridlind, A., Hünerbein, A., Knist, C., Kollias, P., Marshak, A., McCoy, D., Merk, D., Painemal, D., Rausch, J., Rosenfeld, D., Russchenberg, H., Seifert, P., Sinclair, K., Stier, P., van Diedenhoven, B., Wendisch, M., Werner, F., Wood, R., Zhang, Z., and Quaas, J.: Remote sensing of droplet number concentration in warm clouds: A review of the current state of knowledge and perspectives, Rev. Geophys., 56, 409–453, https://doi.org/10.1029/2017RG000593, 2018.

Haarig, M., Walser, A., Ansmann, A., Dollner, M., Althausen, D., Sauer, D., Farrell, D., and Weinzierl, B.: Profiles of cloud condensation nuclei, dust mass concentration, and ice-nucleating-particle-relevant aerosol properties in the Saharan Air Layer over Barbados from polarization lidar and airborne in situ measurements, Atmos. Chem. Phys., 19, 13773–13788, https://doi.org/10.5194/acp-19-13773-2019, 2019.

Hofer, J., Althausen, D., Abdullaev, S. F., Makhmudov, A. N., Nazarov, B. I., Schettler, G., Engelmann, R., Baars, H., Fomba, K. W., Müller, K., Heinold, B., Kandler, K., and Ansmann, A.: Long-term profiling of mineral dust and pollution aerosol with multiwavelength polarization Raman lidar at the Central Asian site of Dushanbe, Tajikistan: case studies, Atmos. Chem. Phys., 17, 14559–14577, https://doi.org/10.5194/acp-17-14559-2017, 2017.

Hofer, J., Ansmann, A., Althausen, D., Engelmann, R., Baars, H., Abdullaev, S. F., and Makhmudov, A. N.: Long-term profiling of aerosol light extinction, particle mass, cloud condensation nuclei, and ice-nucleating particle concentration over Dushanbe, Tajikistan, in Central Asia, Atmos. Chem. Phys., 20, 4695–4711, https://doi.org/10.5194/acp-20-4695-2020, 2020.

Hogan, R. J.: Fast Lidar and Radar Multiple-Scattering Models. Part I: Small-Angle Scattering Using the Photon Variance-Covariance Method, J. Atm. Sci., 65, 3621–3635, https://doi.org/10.1175/2008JAS2642.1, 2008.

Holben, B. N., Eck, T. F., Slutsker, I., Tanré, D., Buis, J. P., Setzer, A., Vermote, E., Reagan, J. A., Kaufman, Y. J., Nakajima, T., Lavenu, F., Jankowiak, I., and Smirnov, A.: AERONET – a federated instrument network and data archive for aerosol characterization, Remote Sens. Environ., 66, 1–16, 1998.

Hu, Y., Vaughan, M., Liu, Z., Lin, B., Yang, P., Flittner, D., Hunt, B., Kuehn, R., Huang, J., Wu, D., Rodier, S., Powell, K., Trepte, C., and Winker, D.: The depolarization – attenuated backscatter relation: CALIPSO lidar measurements vs. theory, Opt. Express, 15, 5327–5332, 2007.

Illingworth, A. J., Barker, H. W., Beljaars, A., Ceccaldi, M., Chepfer, H., Clerbaux, N., Cole, J., Delanoe, J., Domenech, C., Donovan, D. P., Fukuda, S., Hirakata, M., Hogan, R. J., Huenerbein, H., Kollias, P., Kubota, T., Nakajima, T., Nakajima, T. Y., Nishizawa, T., Ohno, Y., Okamoto, H., Oki, R., Sato, K., Satoh, M., Shephard, M., Velázquez-Blázquez, A., Wandinger, U., Wehr, T., and Zadelhoff, G.-J.: The EARTHCARE satellite: the next step forward in global measurements of clouds, aerosols, precipitation and radiation, B. Am. Meteorol. Soc., 96, 1311–1332, https://doi.org/10.1175/BAMS-D-12-00227.1, 2015.

IPCC: Climate Change 2014: Synthesis Report, Contribution of Working Groups I, II and III to the Fifth Assessment Report of the Intergovernmental Panel on Climate Change, edited by: Core Writing Team, Pachauri, R. K., and Meyer, L. A., IPCC, Geneva, Switzerland, 151 pp., available at: https://www.ipcc.ch/pdf/assessment-report/ar5/syr/SYR_AR5_FINAL_full.pdf (last access: 28 November 2020), 2014.

Jimenez, C., Ansmann, A., Donovan, D., Engelmann, R., Malinka, A., Schmidt, J., and Wandinger, U.: Retrieval of microphysical properties of liquid water clouds from atmospheric lidar measurements: Comparison of the Raman dual field of view and the depolarization techniques, Proc. SPIE, 10429, 1042907, https://doi.org/10.1117/12.2281806, 2017.

Jimenez, C., Ansmann, A., Donovan, D., Engelmann, R., Schmidt, J., and Wandinger, U.: Comparison between two lidar methods to retrieve microphysical properties of liquid water clouds, EPJ Web Conf., The 28th International Laser Radar Conference, June 2017, Bucharest, Romania, 17601032, https://doi.org/10.1051/epjconf/201817601032, 2018.

Jimenez, C., Ansmann, A., Engelmann, R., Donovan, D., Malinka, A., Seifert, P., Radenz, M., Yin, Z., Wiesen, R., Bühl, J., Schmidt, J., Wandinger, U., and Barja, B.: The dual-field-of-view polarization lidar technique: a new concept in monitoring aerosol effects in liquid-water clouds – case studies, Atmos. Chem. Phys., 20, 15265–15284, https://doi.org/10.5194/acp-20-15265-2020, 2020a.

Jimenez, C., Ansmann, A., and Malinka, A.: Files to retrieve effective radius and extinction coefficient in liquid clouds from depolarization observations at two FOVs, Zenodo, https://doi.org/10.5281/zenodo.4107137, 2020b.

Katsev, L., Zege, E., Prikhach, A., and Polonsky, I.: Efficient technique to determine backscattered light power for various atmospheric and oceanic sounding and imaging systems, JOSA A, 14, 1338–46, 1997.

Kim, D., Cheong, H., Kim, Y., Volkov, S., and Lee, J.: Optical Depth and Multiple Scattering Depolarization in Liquid Clouds, Opt. Rev., 17, 507–512, 2010

Lu, M.-L. and Seinfeld, J. H.: Effect of aerosol number concentration on cloud droplet dispersion: A large-eddy simulation study and implications for aerosol indirect forcing, J. Geophys. Res., 111, D02207, https://doi.org/10.1029/2005JD006419, 2006.

Malinka, A. V, and Zege, E. P.: Analytical modeling of Raman lidar return, including multiple scattering, Appl. Optics, 42, 1075–1081, 2003.

Malinka, A. V. and Zege, E. P.: Possibilities of warm cloud microstructure profiling with multiple-field-of-view Raman lidar, Appl. Optics 46, 8419–8427, 2007.

Mamouri, R.-E. and Ansmann, A.: Potential of polarization lidar to provide profiles of CCN- and INP-relevant aerosol parameters, Atmos. Chem. Phys., 16, 5905–5931, https://doi.org/10.5194/acp-16-5905-2016, 2016.

Martin, G. M., Johnson, D. W., and Spice, A.: The measurement and parameterization of effective radius of droplets in warm stratocumulus clouds, J. Atmos. Sci., 51, 1823–1842, https://doi.org/10.1175/1520-0469(1994)051<1823:TMAPOE>2.0.CO;2, 1994.

McComiskey, A., Feingold, G., Frisch, A. S., Turner, D. D., Miller, M. A., Chiu, J. C., Min, Q., and Ogren, J. A.: An assessment of aerosol-cloud interactions in marine stratus clouds based on surface remote sensing, J. Geophys. Res., 114, D09203, https://doi.org/10.1029/2008JD011006, 2009.

Merk, D., Deneke, H., Pospichal, B., and Seifert, P.: Investigation of the adiabatic assumption for estimating cloud micro- and macrophysical properties from satellite and ground observations, Atmos. Chem. Phys., 16, 933–952, https://doi.org/10.5194/acp-16-933-2016, 2016.

Mooradian, G., Geller, M., Stotts, L., Stephens, D., and Krautwald, R: Blue-green pulsed propagation through fog, Appl. Optics, 18, 429–441, https://doi.org/10.1364/AO.18.000429, 1979.

Pal, S. and Carswell, A.: Polarizaiton anisotropy in lidar multiple scattering from atmospheric clouds, Appl. Optics, 24, 3464–3471, 1985.

Roy, G., Bissonnette, L., Bastille, C., and Vallé, G.: Retrieval of droplet-size density distribution from multiple-field-of-view cross-polarized lidar signals: theory and experimental validation, Appl. Optics, 38, 5202–5210, 1999.

Roy, G., Cao, X., Tremblay, G., and Bernier, R.: On depolarization lidar-based method for determination of liquid-cloud microphysical properties, EPJ Web Conf., 11916002, https://doi.org/10.1051/epjconf/201611916002, 2016.

Roy, N., Roy, G., Bissonnette, L. R., and Simard, J.-R.: Measurement of the azimuthal dependence of cross-polarized lidar returns and its relation to optical depth, Appl. Optics, 43, 2777–2785, https://doi.org/10.1364/AO.43.002777, 2004.

Sassen, K. and Petrilla, R.: Lidar depolarization from multiple scattering in marine stratus clouds, Appl. Optics, 25, 1450–1459, https://doi.org/10.1364/AO.25.001450, 1986.

Schmale, J., Henning, S., Decesari, S., Henzing, B., Keskinen, H., Sellegri, K., Ovadnevaite, J., Pöhlker, M. L., Brito, J., Bougiatioti, A., Kristensson, A., Kalivitis, N., Stavroulas, I., Carbone, S., Jefferson, A., Park, M., Schlag, P., Iwamoto, Y., Aalto, P., Äijälä, M., Bukowiecki, N., Ehn, M., Frank, G., Fröhlich, R., Frumau, A., Herrmann, E., Herrmann, H., Holzinger, R., Kos, G., Kulmala, M., Mihalopoulos, N., Nenes, A., O'Dowd, C., Petäjä, T., Picard, D., Pöhlker, C., Pöschl, U., Poulain, L., Prévôt, A. S. H., Swietlicki, E., Andreae, M. O., Artaxo, P., Wiedensohler, A., Ogren, J., Matsuki, A., Yum, S. S., Stratmann, F., Baltensperger, U., and Gysel, M.: Long-term cloud condensation nuclei number concentration, particle number size distribution and chemical composition measurements at regionally representative observatories, Atmos. Chem. Phys., 18, 2853–2881, https://doi.org/10.5194/acp-18-2853-2018, 2018.

Schmidt, J., Wandinger, U., and Malinka, A.: Dual-field-of-view Raman lidar measurements for the retrieval of cloud microphysical properties, Appl. Optics, 52, 2235–2247, https://doi.org/10.1364/AO.52.002235, 2013.

Schmidt, J., Ansmann, A., Bühl, J., Baars, H., Wandinger, U., Müller, D., and Malinka, A. V.: Dual-FOV Raman and Doppler lidar studies of aerosol-cloud interactions: simultaneous profiling of aerosols, warm-cloud properties, and vertical wind, J. Geophys. Res., 119, 5512–5527, https://doi.org/10.1002/2013JD020424, 2014.

Schmidt, J., Ansmann, A., Bühl, J., and Wandinger, U.: Strong aerosol–cloud interaction in altocumulus during updraft periods: lidar observations over central Europe, Atmos. Chem. Phys., 15, 10687–10700, https://doi.org/10.5194/acp-15-10687-2015, 2015.

Shinozuka, Y., Clarke, A. D., Nenes, A., Jefferson, A., Wood, R., McNaughton, C. S., Ström, J., Tunved, P., Redemann, J., Thornhill, K. L., Moore, R. H., Lathem, T. L., Lin, J. J., and Yoon, Y. J.: The relationship between cloud condensation nuclei (CCN) concentration and light extinction of dried particles: indications of underlying aerosol processes and implications for satellite-based CCN estimates, Atmos. Chem. Phys., 15, 7585–7604, https://doi.org/10.5194/acp-15-7585-2015, 2015.

Veselovskii, I., Korenskii, M., Griaznov, V., Whiteman, D., McGill, M., Roy, G., and Bissonnette, L.: Information content of data measured with a multiple-field-of-view lidar, Appl. Optics, 45, 6839–6847, 2006.

Wandinger, U.: Theoretische und experimentelle Studien zur Messung stratosphärischen Aerosols sowie zum Einfluss der Mehrfachstreuung auf Wolkenmessungen mit einem Polarisations-Raman-Lidar, PhD thesis, University of Hamburg, Germany, 78–83, 1994.

Wandinger, U.: Multiple-scattering influence on extinction- and backscatter-coefficient measurements with Raman and high-spectral-resolution lidars, Appl. Optics, 37, 417–427, https://doi.org/10.1364/AO.37.000417, 1998.

Wiegner, M. and Geiß, A.: Aerosol profiling with the Jenoptik ceilometer CHM15kx, Atmos. Meas. Tech., 5, 1953–1964, https://doi.org/10.5194/amt-5-1953-2012, 2012.

Zege, E. and Chaikovskaya L.: New approach to the polarized radiative transfer problem, J. Quant. Spectrosc. Ra., 55, 19–31, 1996.

Zege, E. and Chaikovskaya, L.: Polarization of multiple-scattered lidar return from clouds and ocean water, J. Opt. Soc. Am., 16, 1430–1438, 1999.

Zege, E. and Chaikovskaya, L.: Approximate theory of linearly polarized light propagation through a scattering medium, J. Quant. Spectrosc. Ra., 66, 413–435, 2000.

Zege, E., Katsev, I., and Polonsky, I.: Analytical solution to LIDAR return signals from clouds with regard to multiple scattering, Appl. Phys. B, 60, 345–353, 1995.

4.3 Third publication: The dual-field-of-view polarization lidar technique: A new concept in monitoring aerosol effects in liquid-water clouds – Case studies

The content of this chapter has already been published under the title "The dual-field-of-view polarization lidar technique: A new concept in monitoring aerosol effects in liquid-water clouds – Case studies" by Cristofer Jimenez, Albert Ansmann, Ronny Engelmann, David Donovan, Aleksey Malinka, Patric Seifert, Robert Wiesen, Martin Radenz, Zhenping Yin, Johannes Bühl, Jörg Schmidt, Boris Barja, and Ulla Wandinger. In 2020, the paper was published under the Creative Commons Attribution 4.0 License in Atmospheric Chemistry and Physics with the doi: 10.5194/acp-20-15265-2020 (see `https://doi.org/10.5194/acp-20-15265-2020`). Reprinted with permission by the authors fro Atmospheric Chemistry and Physics, 20, 15265–15284, 2020.

Atmos. Chem. Phys., 20, 15265–15284, 2020
https://doi.org/10.5194/acp-20-15265-2020

Atmospheric Chemistry and Physics Open Access EGU

The dual-field-of-view polarization lidar technique: a new concept in monitoring aerosol effects in liquid-water clouds – case studies

Cristofer Jimenez[1], Albert Ansmann[1], Ronny Engelmann[1], David Donovan[2], Aleksey Malinka[3], Patric Seifert[1], Robert Wiesen[1], Martin Radenz[1], Zhenping Yin[1,4,5], Johannes Bühl[1], Jörg Schmidt[6], Boris Barja[7], and Ulla Wandinger[1]

[1]Leibniz Institute for Tropospheric Research, Leipzig, Germany
[2]Royal Netherlands Meteorological Institute (KNMI), De Bilt, the Netherlands
[3]National Academy of Sciences of Belarus, Minsk, Belarus
[4]School of Electronic Information, Wuhan University, Wuhan, China
[5]Key Laboratory of Geospace Environment and Geodesy, Ministry of Education, Wuhan, China
[6]Institute of Meteorology, University of Leipzig, Leipzig, Germany
[7]Atmospheric Research Laboratory, University of Magallanes, Punta Arenas, Chile

Correspondence: Cristofer Jimenez (jimenez@tropos.de)

Received: 19 May 2020 – Discussion started: 7 July 2020
Revised: 6 October 2020 – Accepted: 24 October 2020 – Published: 8 December 2020

Abstract. In a companion article (Jimenez et al., 2020), we introduced a new lidar method to derive microphysical properties of liquid-water clouds (cloud extinction coefficient, droplet effective radius, liquid-water content, cloud droplet number concentration N_d) at a height of 50–100 m above the cloud base together with aerosol information (aerosol extinction coefficients, cloud condensation nuclei concentration N_{CCN}) below the cloud layer so that detailed studies of the influence of given aerosol conditions on the evolution of liquid-water cloud layers with high temporal resolution solely based on lidar observations have become possible now. The novel cloud retrieval technique makes use of lidar observations of the volume linear depolarization ratio at two different receiver field of views (FOVs). In this article, Part 2, the new dual-FOV polarization lidar technique is applied to cloud measurements in pristine marine conditions at Punta Arenas in southern Chile. A multiwavelength polarization Raman lidar, upgraded by integrating a second polarization-sensitive channel to permit depolarization ratio observations at two FOVs, was used for these measurements at the southernmost tip of South America. Two case studies are presented to demonstrate the potential of the new lidar technique. Successful aerosol–cloud-interaction (ACI) studies based on measurements with the upgraded aerosol–cloud lidar in combination with a Doppler lidar of the vertical wind component could be carried out with 1 min temporal resolution at these pristine conditions. In a stratocumulus layer at the top of the convective boundary layer, we found values of N_d and N_{CCN} (for 0.2 % water supersaturation) ranging from 15–100 and 75–200 cm^{-3}, respectively, during updraft periods. The studies of the aerosol impact on cloud properties yielded ACI values close to 1. The impact of aerosol water uptake on the ACI studies was analyzed with the result that the highest ACI values were obtained when considering aerosol proxies (light-extinction coefficient α_{par} or N_{CCN}) measured at heights about 500 m below the cloud base (and thus for dry aerosol conditions).

1 Introduction

Numerous details and aspects of aerosol–cloud interaction (ACI) are not well understood and thus not well considered and parameterized in weather and climate models. The reason for this gap in our knowledge is closely linked to the lack of adequate measurements, observational concepts, instrumentation, tools, and techniques for a detailed, continuous (camera-like) monitoring of cloud processes in a variety of aerosol environmental and meteorological conditions. Such continuous monitoring is only possible in well-

designed ground-based remote sensing network structures. Network supersites, distributed around the world, preferably in hotspot regions of anthropogenic activities and climate change as well as in rural background regions, need to cover profiling of aerosol mixtures and their aerosol-type properties, cloud microphysical, optical, and cloud-type (phase) properties, and meteorological parameters such as temperature, relative humidity, and wind, especially of the vertical wind component and thus of updraft, downdraft, and wave characteristics. Aerosol influences on low-level liquid-water clouds over mixed-phase clouds to tropopause cirrus need to be monitored. Measurements of cloud-relevant aerosol parameters must even include heights within the lower stratosphere which may serve as a source for ice-nucleating particles of heterogeneous ice formation in high level cirrus layers. In Europe, ACTRIS (Aerosols, Clouds, and Trace gases Research InfraStructure; https://www.actris.eu/, last access: 2 December 2020) with its network structures Cloudnet (Illingworth et al., 2007) and EARLINET (European Aerosol Research Lidar Network) (Pappalardo et al., 2014) is responsible for the buildup of the necessary aerosol–cloud monitoring infrastructure.

There is still a strong request for the development of new and robust aerosol and cloud profiling techniques (Grosvenor et al., 2018). As a contribution to improved ACI field studies with a focus on liquid-water clouds, we offer a novel lidar measurement concept that permits continuous, vertically resolved observations of cloud-relevant aerosol properties below the cloud base, cloud microphysical properties in the lower part of the cloud layer, and the vertical wind component below and within the cloud parcels with a temporal resolution of 30–120 s. The methodological framework is presented in Part 1 (Jimenez et al., 2020). The selected measurement concept of combining aerosol lidar, cloud lidar, and wind Doppler lidar observations was already outlined and applied by Schmidt et al. (2014, 2015). However, a fast lidar technique for cloud observation (day and night and with updraft-resolving temporal resolution) was introduced only recently (Jimenez et al., 2017, 2018). In Part 1 (Jimenez et al., 2020), we presented the theoretical framework of the novel dual-field-of-view (dual-FOV) polarization lidar method, which allows us to derive microphysical properties of liquid-water clouds such as droplet number concentration N_d, effective radius R_e of the droplets, and liquid-water content w_l as well as the cloud extinction coefficient α in the cloud base region at 50 to 100 m above the cloud base. Together with the recently developed method to derive height profiles of cloud condensations nuclei (CCN) concentrations (N_{CCN}) from aerosol extinction coefficients α_{par}, measured with the same polarization lidar (Mamouri and Ansmann, 2016) below the cloud base, detailed studies of the impact of aerosol particles on the microphysical properties of droplets in the cloud base region of liquid-water cloud layers have become possible.

The instrumental setup can be easily integrated into existing ground-based aerosol and cloud remote sensing network supersites as already demonstrated in the case of the mobile ACTRIS Cloudnet station LACROS (Leipzig Aerosol and Cloud Remote Observation System; http://lacros.rsd.tropos.de/, last access: 2 December 2020), which is presently deployed for a long-term campaign in Punta Arenas, Chile, in the pristine marine environment of southernmost South America. Network observations of aerosol–cloud interaction on a continental scale offer new possibilities of co-operations between the measuring science community performing long-term observations of aerosols and clouds and the modeling community developing and improving atmospheric and Earth system models with the goal to better consider natural and anthropogenic aerosols and their impact on radiative transfer and cloud evolution in weather and climate forecast simulations. The models can be confronted with a continuous flow of aerosol and cloud observations for very different aerosol and meteorological conditions. This would probably lead to a significant step forward in the understanding of the role of aerosols in the atmospheric system. Furthermore, dual-FOV lidars can provide constraints for cloud radar retrievals (e.g., Frisch et al., 2002) so that full cloud profiling throughout cloud layers is possible. The new dual-FOV polarization lidar technique can be easily implemented in widespread aerosol polarization lidars (of, e.g., EARLINET) with near-range and far-range receiver telescopes, as will be discussed below, and can then contribute to the long-term monitoring of droplet microphysical properties in the lower part of liquid-water clouds within network structures.

In this second article (Part 2), we apply the new dual-FOV polarization lidar technique to recent aerosol and cloud observations at Punta Arenas, Chile, discuss the cloud retrieval uncertainties, compare the results with independent alternative cloud observations, and highlight the new potential of the lidar technique to significantly contribute to atmospheric and climate research in the field of ACI. Part 2 is organized as a stand-alone publication. Part 1 is therefore not needed as a prerequisite to follow the presentations and discussions in Part 2. In Sect. 2, we briefly summarize the data analysis procedure to retrieve the aerosol and cloud parameters for in-depth ACI studies as extensively discussed and explained in Part 1 (Jimenez et al., 2020). Sect. 3 provides details of the integration of the dual-FOV polarization lidar technique into a Polly (portable lidar system) instrument (Engelmann et al., 2016; Baars et al., 2016). The upgraded Polly is part of LACROS and consists of an aerosol–cloud lidar, a Doppler lidar for profiling of the vertical wind component, and a cloud radar as the main profiling instruments. LACROS was continuously operated at Punta Arenas, Chile, in the framework of the long-term field campaign DACAPO-PESO (Dynamics, Aerosol, Cloud And Precipitation Observations in the Pristine Environment of the Southern Ocean; https://dacapo.tropos.de, last access: 2 December 2020) from November 2018 to the end of 2020. Details of the campaign

and the goals of the investigations are outlined in Sect. 3.3. In the measurement section (Sect. 4), two case studies are presented. Case 1 (Sect. 4.1) is shown to discuss the basic and principle features of the new cloud retrieval technique. The potential of the new dual-FOV lidar to contribute to ACI research is then illuminated in Sect. 4.2 (case study 2). Concluding remarks and an outlook are given in Sect. 5.

2 Data processing scheme

As outlined in Part 1 (Jimenez et al., 2020), the basic motivation for the development of the dual-FOV polarization lidar technique was the need for simultaneous aerosol and cloud observations at day- and nighttime, with high temporal resolutions of the order of 30–120 s. The developed novel lidar method for liquid-water cloud observations is based on the measurement of the so-called volume linear depolarization ratio in the lower part of the water cloud at two different receiver FOVs. The required dual-FOV polarization lidar transmits linearly polarized laser pulses and detects the so-called cross- and co-polarized signal components. "Co" and "cross" denote the planes of polarization parallel and orthogonal to the plane of linear polarization of the transmitted laser pulses, respectively. The volume linear depolarization ratio is defined as the ratio of the cross- to the co-polarized signal and yields the basic information on the ratio of the cross- to the co-polarized backscatter coefficient. In water clouds, the depolarization ratio is sensitively influenced by multiple scattering and varies, e.g., with receiver FOV, cloud height, and cloud droplet number concentration and size of the droplets as explained in detail in Part 1. These relationships are used in the dual-FOV polarization lidar technique to retrieve the effective radius R_e of the droplets and the cloud extinction coefficient α in the cloud base region at 50 to 100 m above the cloud base by means of measured depolarization ratios at two FOVs, and, in the next step, to compute the liquid-water content w_l and the cloud droplet number concentration N_d from the R_e and α values.

Table 1 provides an overview of all steps of the comprehensive analysis of cloud and aerosol data obtained with the new dual-FOV polarization lidar developed in Part 1 (Jimenez et al., 2020). The overall concept of lidar-based aerosol–cloud-interaction studies with a focus on liquid-water clouds is illustrated in Fig. 4 in Part 1. The dual-FOV polarization lidar technique allows us to derive simultaneously the microphysical properties of liquid-water clouds at a height of $z_{ref} = z_{bot} + 75$ m above the cloud base height z_{bot} and the aerosol proxies α_{par} and N_{CCN} at height z_{aer} which can be freely selected and is typically about 250–750 m below the cloud base to avoid aerosol water-uptake effects (Skupin et al., 2016; Haarig et al., 2017) on the ACI studies.

In this article (Part 2), we apply the full methodology to a DACAPO-PESO measurement case collected at Punta Arenas on 22 March 2019 and explain all retrieval steps listed in Table 1. The second case, measured on 23 February 2019, is then presented to highlight the new potential of this novel lidar approach to significantly improve ACI studies in the case of liquid-water clouds. Before that, we describe the lidar hardware needed for such observations and the way to obtain the required depolarization ratios from the measured lidar signals that serve as the basic input in the cloud data analysis scheme.

3 Instrument and experiment

3.1 Polly with dual-FOV capability

We implemented the dual-FOV polarization lidar technique in several lidars of the Leibniz Institute for Tropospheric Research (TROPOS) during recent years. The dual-FOV polarization lidar technique was firstly integrated into the EARLINET (European Aerosol Research Lidar Network) lidar MARTHA (Multiwavelength Atmospheric Raman lidar for Temperature, Humidity, and Aerosol profiling) (Jimenez et al., 2019). MARTHA was already equipped with the dual-FOV Raman lidar technique (Schmidt et al., 2013, 2014), so direct comparisons of cloud observations with the Raman lidar and the polarization lidar method were possible. We found in general good agreement in the retrieval of cloud optical and microphysical properties (Jimenez et al., 2017, 2018). Encouraged by this successful comparison, we stepped forward and equipped four Polly (portable lidar system) instruments (Engelmann et al., 2016) with the new dual-FOV polarization lidar technique. These four lidar systems are and were involved in several long-term field activities at very different aerosol and environmental conditions, namely at Dushanbe, Tajikistan, in Central Asia (continuous measurements since June 2019), aboard the German ice breaker Polarstern (North Pole, a 1-year campaign from October 2019 to September 2020), at Punta Arenas (a 2-year campaign from November 2018 to the end of 2020), and at Limassol, Cyprus (continuous measurements since October 2020). Aerosol retrieval methods and measurement examples can be found in Baars et al. (2016) and Hofer et al. (2017, 2020). Improved water vapor observations (water vapor mixing ration, relative humidity) by combining lidar and regular photometer observations were recently discussed by Dai et al. (2018). In this section, we concentrate on the new approach of cloud measurements at two FOVs.

Figure 1 shows the transmitter and receiver configuration of the Polly instrument of the Punta Arenas remote sensing facility. The lidar is described in detail by Engelmann et al. (2016) and Hofer et al. (2017). Laser beam diameter and divergence are 45 mm and 0.2 mrad, respectively, after beam expansion. The polarization impurity (fraction of nonlinear polarized light) of the transmitted laser beam is less than 0.1 %. The receiver unit consists of the near-range re-

Table 1. Overview of the cloud and aerosol retrieval procedure (step-by-step data analysis). The retrieval procedure starts with the determination of the cloud base height z_{bot}. The cloud depolarization ratios $\overline{\delta}_{in}$ and $\overline{\delta}_{out}$ and the ratio $\overline{\delta}_{rat} = \overline{\delta}_{in}/\overline{\delta}_{out}$, integrated over the height range from the cloud base at z_{top} to the cloud retrieval or reference height z_{ref}, are calculated from the height profiles of measured volume linear depolarization ratios (see Sect. 3.2). The cloud products R_e, α, w_l, and N_d are given for the reference height z_{ref}, 75 m above the cloud base height z_{bot}. The computation of the aerosol–cloud-interaction (ACI) efficiencies E_{ACI} is based on N_d, particle extinction coefficient α_{par}, and CCN concentration N_{CCN} at z_{aer}, usually several hundreds of meters below the cloud base. The aerosol proxies are determined from aerosol measurements with the same dual-FOV lidar. All equations refer to Part 1 (Jimenez et al., 2020).

Parameter	Symbol	Equation	Uncertainty
Cloud base height	z_{bot}		0.1 %–1 %
Cloud depolarization ratios	$\overline{\delta}_{in}(z_{bot}, z_{ref})$	Eq. (23)	5 %
	$\overline{\delta}_{out}(z_{bot}, z_{ref})$	Eq. (24)	5 %
	$\overline{\delta}_{rat}(z_{bot}, z_{ref})$	Eq. (25)	10 %–15 %
Droplet effective radius	$R_e(z_{ref})$	Eq. (26)	15 %
Cloud extinction coefficient	$\alpha(z_{ref})$	Eq. (27)	15 %–20 %
Liquid-water content	$w_l(z_{ref})$	Eq. (4)	25 %
Cloud droplet number concentration	$N_d(z_{ref})$	Eq. (6)	25 %–75 %
Aerosol depolarization ratio	$\delta_{par}(z)$		5 %–10 %
Aerosol extinction coefficient	$\alpha_{par}(z_{aer})$		20 %
Cloud condensation nuclei concentration	$N_{CCN}(z_{aer})$	Eqs. (36)–(38)	30 %–100 %
Aerosol–cloud-interaction efficiency	$E_{ACI,\alpha_{par}}(N_d, \alpha_{par})$	Eq. (39)	
Aerosol–cloud-interaction efficiency	$E_{ACI,N_{CCN}}(N_d, N_{CCN})$	Eq. (40)	

ceiver part (purple frame in Fig. 1), optimized to deliver particle backscatter and extinction profiles almost down to the ground determined from measured total and nitrogen Raman backscatter signals at 355, 387, 532, and 607 nm, and a far-range receiver part (blue frame). The diameter of the primary mirror of the far-range Newtonian telescope is 30 cm. The overlap of the laser beam with the receiver FOV is incomplete for heights below about 800 m above ground level (a.g.l.) and allows for accurate aerosol and cloud profiling for heights above about 400 m a.g.l. only (after the correction of the overlap effects). For the far-range channels, the selected FOV_{in} is 1.0 mrad. The FOV for the near-range channels is FOV_{out}= 2.0 mrad. As can be seen in contrast to a classical polarization lidar as described above, the Polly instrument measures the cross-polarized and the total (co- plus cross-polarized) signal components with the far-range telescope. The reasons for this specific design are explained below.

The near-range receiver part was not designed for polarization-sensitive lidar return observations. A 50 mm fiber-wired telescope collects the total (co- plus cross-polarized) backscatter signals. To realize the dual-FOV polarization lidar technique, we installed another receiver unit (with 50 mm telescope) that permits measurements of the cross-polarized signal at 532 nm at FOV_{out}= 2.0 mrad (top part, purple frame, in Fig. 1). The details of the optical elements and the design of this cross-polarized channel are described by Jimenez et al. (2019). Only a polarizer and a collimation lens are used to collect the backscattered cross-polarized laser photons which are then counted by a photomultiplier tube.

3.2 Determination of calibrated depolarization ratios at two FOVs

As mentioned, all Polly instruments measure the cross-polarized and the total (co- plus cross-polarized) signal components. The co-polarized signal component is not recorded. The measurement of the total backscatter coefficient facilitates the determination of the particle backscatter coefficient and, more importantly, guarantees a direct observation of the extinction-to-backscatter ratio without introducing uncertainties by composing the total backscatter signal from the two (cross and co-polarized) signal components, measured with different receiver channel efficiencies which need to be measured on a regular basis. To be widely in line with the notation in Engelmann et al. (2016), we switch from indices $\perp$, $\parallel$, and $\perp + \parallel$ (for the total backscatter signal) to c (cross), p (parallel), and t (total), respectively. Because of measuring the cross-polarized and total backscatter signal components, we introduce

$$\delta'(z) = \frac{S_c(z)}{S_t(z)} \tag{1}$$

to distinguish this signal ratio from the volume depolarization ratio as defined by Eq. (8) in Part 1. According to Engelmann et al. (2016), the volume depolarization ratio is given by

$$\delta(z) = \frac{1 - \delta'(z)/C}{\delta'(z)F_t/C - F_c}, \tag{2}$$

with the transmission ratio F and the absolute calibration parameter C (explained below). The transmission ratio F is de-

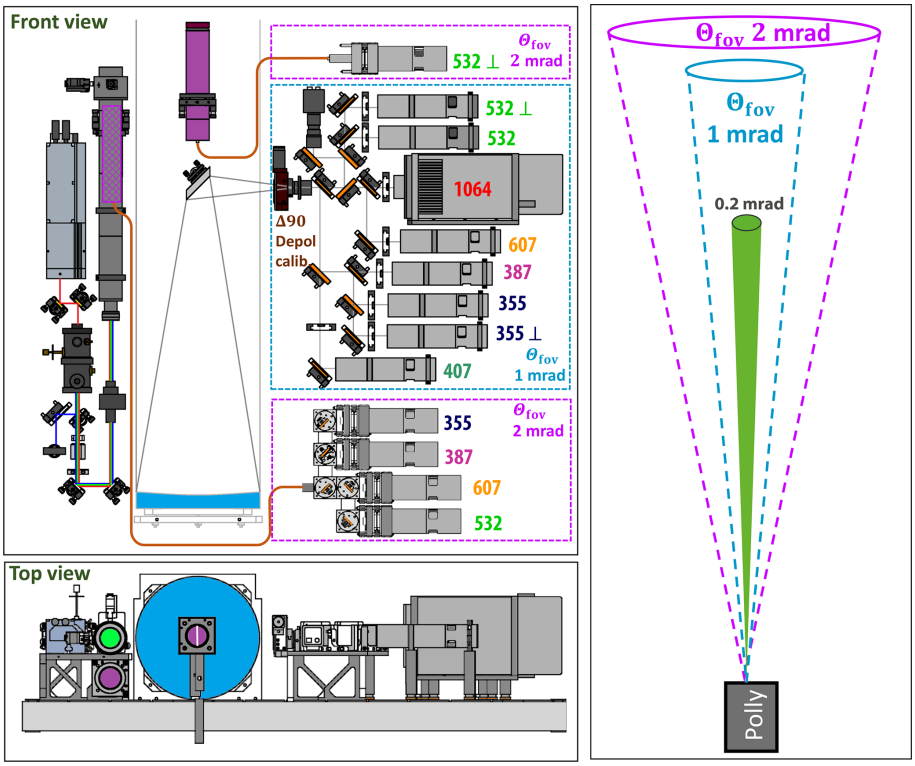

Figure 1. Optical setup of the Polly lidar (left side, same as in Fig. 3 of Engelmann et al., 2016). The upper left part displays the front view of the system, the lower left part a top view. The transmitter unit is mounted to the left of the main lidar telescope (in blue). Laser light transmission is indicated by a green circle in the top-view sketch. Backscattered light is collected with a Newtonian telescope (blue area in the top-view sketch, FOV = 1 mrad, far-range telescope) and then passed towards the far-range receiver unit to the right. All optical elements and detector channels belonging to the 1 mrad FOV receiver block are given in a blue frame. The numbers indicate the wavelength in nanometers of the detection channels, and ⊥ denotes the cross-polarized channels. A polarizer is mounted in front of the pinhole (entrance of the far-range receiver unit) and used for the absolute calibration of the depolarization measurements at 1 mrad FOV (for details, see Engelmann et al., 2016). The purple parts and the purple frame (top view, front view sketch) belong to the 2 mrad FOV receiver unit (near-range receiver unit). An additional 5 cm receiver telescope (purple; for details, see Jimenez et al., 2019) is mounted above the secondary mirror of the far-range telescope and collects the cross-polarized signal component at FOV = 2 mrad. To the right of the optical setup, the dual-FOV polarization lidar geometrical configuration is illustrated, sketching the footprints of the laser beam and FOVs with height.

fined as

$$F_i = \frac{\eta_{i,\mathrm{c}}}{\eta_{i,\mathrm{p}}}, \tag{3}$$

with channels $i = \mathrm{c}$ (cross-polarized signal) and $i = \mathrm{t}$ (total backscatter signal). As mentioned, the index p indicates here the plane of laser polarization (parallel-polarized signal channel). F_i describes the ratio of transmission η for cross-polarized light to the transmission for co-polarized light for channel i. For the Polly system at Punta Arenas (used here), the F_i values were determined from measurements with an artificial light source with a polarizer mounted in front of each channel (Mattis et al., 2009). The values are $F_\mathrm{t} = 1.09$ and $F_\mathrm{c} = 800$ for the far-range channels ($\mathrm{FOV_{in}}$) and $F_\mathrm{t} = 1$ and $F_\mathrm{c} = 500$ for the near-range channels ($\mathrm{FOV_{out}}$).

The absolute calibration parameter C in Eq. (2) is defined as

$$C = \frac{1 + F_\mathrm{t}}{1 + F_\mathrm{c}} \sqrt{\delta'(z)_{45^\circ} \delta'(z)_{-45^\circ}} \tag{4}$$

and obtained from regular and automated clear-sky measurements. The so-called $\Delta 90^\circ$ calibration method (formerly known as $\pm\Delta 45^\circ$ calibration) (Freudenthaler et al., 2009; Freudenthaler, 2016; Engelmann et al., 2016) is applied to obtain highly accurate depolarization ratio observations for the $\mathrm{FOV_{in}}$ channels (far-range receiver). In order to include this method in the automated measurement procedure of Polly, a remote-controlled rotary mount with a so-called sheet polarizer close to the focal plane of the receiver telescope was added to the system. This sheet polarizer is equipped with an off-center hole to measure without the polarizer into the light path in normal mode by rotating the hole onto the optical axis. Three times per day, the polarizer is rotated automatically by -45 and 45° with respect to the laser polarization plane in the light path for calibration to determine the signal ratios $\delta'(z)_{-45^\circ}$ and $\delta'(z)_{45^\circ}$. The resulting profile of C slightly varies with height because of signal noise and slightly different conditions during the measure-

ment periods with −45 and 45° polarization. Thus, the most favorable conditions are cloud-free, clear-sky periods for the measurement of C. In practice, profile values over several kilometers in the vertical column are averaged to reduce the impact of signal noise on C.

The uncertainties in the measurements and data analysis in obtaining the volume depolarization ratio are caused, e.g., by the influence of laser linear polarization purity and uncertainties in the determination of the transmission ratios F_i and the procedure to obtain the absolute calibration constant C. The uncertainties are discussed by Engelmann et al. (2016) and Belegante et al. (2018).

In our approach of a dual-FOV polarization lidar, we have to distinguish between measurements with $\mathrm{FOV_{in}}$ and $\mathrm{FOV_{out}}$. Above, we described the retrieval of the volume depolarization ratio for $\mathrm{FOV_{in}}$. To indicate this we specify $C = C_{\mathrm{in}}$, $\delta = \delta_{\mathrm{in}}$, and $F_i = F_{i,\mathrm{in}}$. As in the case of $F_i = F_{i,\mathrm{in}}$, we can obtain $F_{i,\mathrm{out}}$ for $\mathrm{FOV_{out}}$ as well.

The calibration constant C_{out} cannot be measured with the rotating polarizer. C_{out} is obtained under the assumption that the volume depolarization ratios for $\mathrm{FOV_{in}}$ and $\mathrm{FOV_{out}}$ are equal under clear-sky conditions (i.e., in the absence of any cloud layer and related multiple scattering effects). It can be shown that for $\delta_{\mathrm{out}}(z) = \delta_{\mathrm{in}}(z)$,

$$C_{\mathrm{out}} = \delta'_{\mathrm{out}}(z)\left(\frac{1 + F_{\mathrm{t,out}}\delta_{\mathrm{in}}(z)}{1 + F_{\mathrm{c,out}}\delta_{\mathrm{in}}(z)}\right). \tag{5}$$

After careful determination of the F_i and C values for $\mathrm{FOV_{in}}$ and $\mathrm{FOV_{out}}$ we can now proceed to analyze cloud observations, as described in Sect. 4 in Part 1 (Jimenez et al., 2020).

The cloud-integrated volume depolarization ratio for $\mathrm{FOV_{in}}$ signals as defined by Eq. (23) in Part 1 is now given by

$$\overline{\delta}_{\mathrm{in}}(z_{\mathrm{bot}}, z_{\mathrm{ref}}) = \frac{1 - \overline{\delta}'_{\mathrm{in}}/C_{\mathrm{in}}}{\overline{\delta}'_{\mathrm{in}}F_{\mathrm{t,in}}/C_{\mathrm{in}} - F_{\mathrm{c,in}}}, \tag{6}$$

with $\overline{\delta}'_{\mathrm{in}}$ calculated from the cross-polarized and the total signal components:

$$\overline{\delta}'_{\mathrm{in}} = \frac{\int_{z_{\mathrm{bot}}}^{z_{\mathrm{ref}}} S_{\mathrm{c,in}}(z)\mathrm{d}z}{\int_{z_{\mathrm{bot}}}^{z_{\mathrm{ref}}} S_{\mathrm{t,in}}(z)\mathrm{d}z}. \tag{7}$$

For $\mathrm{FOV_{out}}$, we obtain correspondingly

$$\overline{\delta}_{\mathrm{out}}(z_{\mathrm{bot}}, z_{\mathrm{ref}}) = \frac{1 - \overline{\delta}'_{\mathrm{out}}/C_{\mathrm{out}}}{\overline{\delta}'_{\mathrm{out}}F_{\mathrm{t,out}}/C_{\mathrm{out}} - F_{\mathrm{c,out}}}, \tag{8}$$

with $\overline{\delta}'_{\mathrm{out}}$ calculated from the cross-polarized and the total signal components:

$$\overline{\delta}'_{\mathrm{out}} = \frac{\int_{z_{\mathrm{bot}}}^{z_{\mathrm{ref}}} S_{\mathrm{c,out}}(z)\mathrm{d}z}{\int_{z_{\mathrm{bot}}}^{z_{\mathrm{ref}}} S_{\mathrm{t,out}}(z)\mathrm{d}z}. \tag{9}$$

The cloud-integrated depolarization ratios $\overline{\delta}_{\mathrm{in}}(z_{\mathrm{bot}}, z_{\mathrm{ref}})$ and $\overline{\delta}_{\mathrm{out}}(z_{\mathrm{bot}}, z_{\mathrm{ref}})$ and the ratio $\overline{\delta}_{\mathrm{rat}} = \overline{\delta}_{\mathrm{in}}/\overline{\delta}_{\mathrm{out}}$ as defined by Eqs. (23)–(25) in Part 1 are the input in the retrieval of cloud microphysical properties as described in Sect. 4 in Part 1 and summarized in Table 1.

3.3 DACAPO-PESO and LACROS

The lidar observations at Punta Arenas (53.2° S, 70.9° W, 9 m above sea level, a.s.l.), Chile, were conducted in the framework of the DACAPO-PESO campaign from November 2018 to the end of 2020. DACAPO-PESO belongs to a series of long-term ACI-related field studies performed with the mobile LACROS station. Before that, we deployed LACROS for the 17-month field campaign CyCARE (Cyprus Clouds, Aerosol and Rain Experiment) at Limassol, Cyprus (October 2016 to March 2018) (Bühl et al., 2019; Ansmann et al., 2019), in the highly polluted and dusty eastern Mediterranean. All these campaigns are aimed at the central question: how do aerosol particles influence the evolution and microphysical properties of liquid-water, mixed-phase, and ice clouds and precipitation in different meteorological regimes and at contrasting levels of anthropogenic and natural aerosol concentrations? The novel dual-FOV polarization lidar fills an important gap and covers the ACI research in the case of liquid-water clouds.

We upgraded meanwhile several Polly instruments to dual-FOV polarization lidars. Besides the lidar at Punta Arenas, another upgraded dual-FOV Polly was operated at the North Pole (aboard the German ice breaker Polarstern in the framework of the MOSAiC campaign (September 2019–September 2020). MOSAiC (Multidisciplinary Drifting Observatory for the Study of Arctic Climate; https://mosaic-expedition.org, last access: 2 December 2020) is the largest Arctic field campaign ever realized. A new Polly, designed as dual-FOV polarization lidar from the beginning, is now operated at Dushanbe, Tajikistan, in a dusty and polluted region of Central Asia in the framework of a long-term (unlimited) CADEX follow-up campaign (since June 2019). CADEX (Central Asian Dust Experiment) (Hofer et al., 2017, 2020) was conducted from March 2015 to August 2016. In the framework of the 7-year project EXCELSIOR (EXcellence Research Center for Earth SurveiLlance and Space-Based MonItoring Of the EnviRonment; https://excelsior2020.eu/the-project/, last access: 2 December 2020), we deployed a new dual-FOV Polly, integrated into the new EXCELSIOR supersite at Limassol, in October 2020. Finally, the fourth new dual-FOV Polly will be set up at Cabo Verde (in the summer of 2021) in the outflow regime of African dust and biomass burning smoke, as part of ACTRIS.

The mobile Leipzig Cloudnet supersite LACROS (Bühl et al., 2013, 2016; Ansmann et al., 2019) was run continuously at the University of Magallanes (UMAG) at Punta Arenas and covered two summer and winter seasons of aerosol

and cloud observations during the DACAPO-PESO campaign. LACROS is equipped with the dual-FOV polarization lidar, a wind Doppler lidar, 35 GHz Doppler cloud radar, ceilometer, disdrometer, and microwave radiometer. In addition, an Aerosol Robotic Network (AERONET) sun photometer (AERONET, 2020; Holben et al., 1998) was operated.

4 Measurements

We discuss two measurement cases of the DACAPO-PESO campaign. The first case study (22 March 2019) deals with the development of an extended altocumulus field in the pristine free troposphere over Punta Arenas, Chile, during the autumn season. The full aerosol and cloud data analysis scheme is applied, the uncertainties in the cloud products obtained with the dual-FOV lidar are discussed, and the basic results (cloud extinction coefficient, effective radius) are compared with alternative independent retrievals. On 23 February 2019 (case 2), a long-lasting evolution of a stratocumulus deck at the top of the convective summertime boundary layer was observed. This case is used to illuminate the full potential of a dual-FOV polarization lidar regarding ACI studies in the case of liquid-water clouds.

4.1 Case study of 22 March 2019

Figure 2 provides an overview of the cloud conditions over Punta Arenas on 22 March 2019. The narrow FOV signal channels of the Polly lidar are used here. A complex layering of low-level liquid-water clouds, mid-level mixed-phase and upper tropospheric ice clouds was found on this autumn day. In Fig. 2a, optically thin, transparent ice clouds prevailed at heights above about 5 km, whereas optically thick liquid and mixed-phase clouds, indicated by dark blue columns above the clouds in Fig. 2a, dominated at heights below 4 km. The depolarization ratio was high with values of about 0.4 in the ice clouds caused by strong light depolarization by hexagonal ice crystals. Cloud droplets dominate light depolarization in the liquid-water clouds at heights below 4 km. The depolarization ratio monotonically increase from values around zero (for ideal spheres) to values around 0.15–0.2 caused by strong multiple scattering by water droplets. It should be mentioned that all POLLY instruments are tilted to an off-zenith angle of 5° to avoid a strong impact of specular reflection by falling, horizontally aligned ice crystals which lead to rather low depolarization ratios and, in this way, considerably disturb cloud observations and the separation of liquid-water, mixed-phase, and ice cloud layers.

The results of the Cloudnet classification (Cloudnet, 2020) in Fig. 3a are in good agreement with Fig. 2. The Cloudnet identification and classification method is based on cloud radar, microwave radiometer, and ceilometer observations (Illingworth et al., 2007; Bühl et al., 2016; Baars et al., 2017). According to the Cloudnet classification, the clouds below 3.5 km height were mostly liquid-water clouds (blue layers), partly mixed-phase clouds in the height range from 4–6 km, and pure ice clouds (yellow layers) higher up. The 0 and −10 °C temperature levels were observed at about 2 and 3.5 km height according to the radiosonde launched at Punta Arenas on 22 March 2019, 12:00 UTC. Some artifacts are visible. For example, the detection of ice crystals in the liquid layers at 3–3.5 km around 06:00 UTC and after 09:00 UTC is wrong and caused by missing ceilometer observations. The ceilometer laser beam could not penetrate the lower, optically dense cloud layer around 06:00 UTC.

Figure 3b shows the respective dual-FOV polarization lidar observations. These measurements widely confirm the Cloudnet classification results. The observations are shown in terms of the ratio $\delta_{\mathrm{rat}} = \delta_{\mathrm{in}}/\delta_{\mathrm{out}}$ with $\mathrm{FOV_{in}} = 1$ mrad and $\mathrm{FOV_{out}} = 2$ mrad. It can be seen that the upper layers contained ice crystals which produce a strong, rather narrow, and non-depolarizing forward scattering peak so that both FOVs measure the same backscattering and depolarization features; therefore, δ_{rat} was mostly close to 1.0 (reddish colors). In contrast, δ_{rat} was clearly < 1.0 in the shallow altocumulus layers between 3 and 3.5 km height (yellow and green color) caused by a larger contribution to the depolarization ratio by droplet multiple scattering in the case of the larger receiver $\mathrm{FOV_{out}} = 2$ mrad. Even the presence of drizzle droplets at 1.5 km is detected in Fig. 2b. These large droplets cause δ_{rat} values close to 1 because of a narrow forward scattering peak and similar multiple scattering effects in both FOVs.

In the following, we concentrate on the liquid-water cloud layer from 3–3.5 km height observed over several hours from about 04:30 UTC (01:30 local time) to 11:00 UTC (08:00 local time). The results of the dual-FOV polarization lidar measurements are shown in Fig. 4. The data analysis procedure was as follows: in the first step, the background and range-corrected total backscatter signals, available with 30 s temporal resolution, were used to obtain the information about the cloud base height z_{bot}. These signals were normalized to the maximum signal value $P_{\mathrm{norm}}(z)$ of the total backscatter profile (in the lower part of the cloud layer). A threshold $P_{\mathrm{norm}}(z) > 0.06$ was set to estimate the cloud base height within the signal profile segment from below the cloud base up to about 100 m within the cloud layer. To avoid the influence of signal noise in the cloud base calculation, a smoothing over five height bins (37.5 m) was applied to the 30 s profiles. This smoothing was only performed for the determination of z_{bot}. The approach is similar to the method of Donovan et al. (2015) to determine z_{bot} of liquid-water clouds. The time series of the estimated cloud base height is shown in Fig. 4a.

In the next step, the cross-polarized and total signal components from the cloud base to 75 m (10 range or height bins) above the cloud base were averaged. A temporal resolution of 2 min was selected (Fig. 4). The integrated depolarization ratios $\overline{\delta}_{\mathrm{in}}$ and $\overline{\delta}_{\mathrm{out}}$ were calculated by using Eqs. (6)–(8) (in

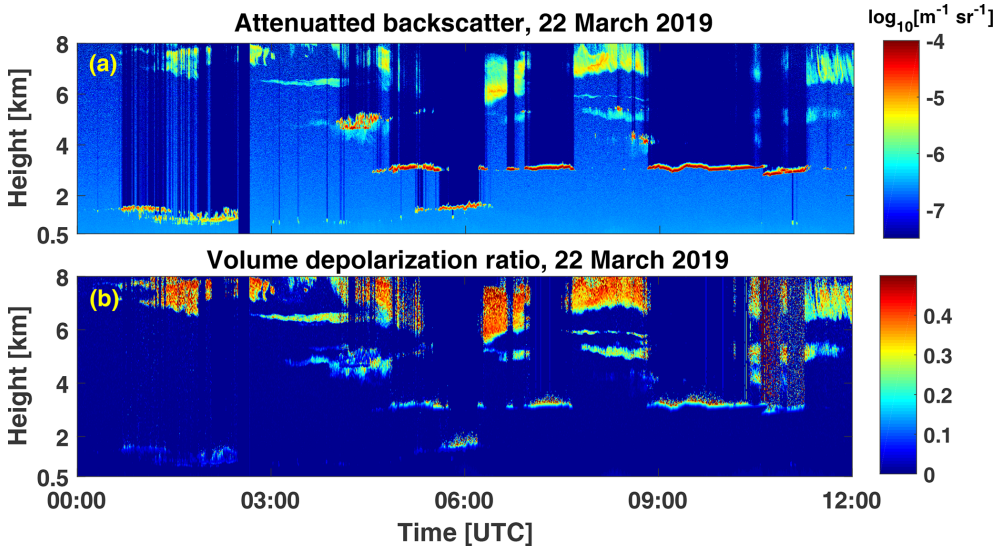

Figure 2. Liquid-water cloud layers at heights < 3.5 km and ice-containing clouds between 4 and 8 km height in the pristine marine atmosphere over Punta Arenas observed with polarization lidar on 22 March 2019. Height–time display of **(a)** attenuated backscatter at 1064 nm and **(b)** volume linear depolarization ratio at 532 nm measured with 30 s temporal and 7.5 m vertical resolution are presented.

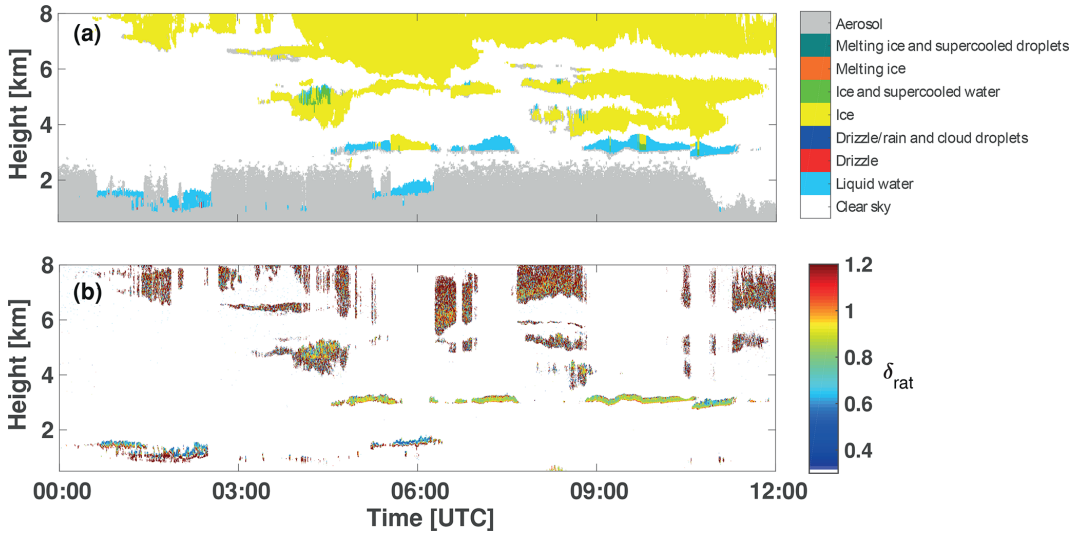

Figure 3. **(a)** Cloudnet target classification of the cloud layers shown in Fig. 2 and **(b)** ratio $\delta_{rat} = \delta_{in}/\delta_{out}$ measured with the dual-FOV polarization lidar Polly ($FOV_{in} = 1$ mrad, $FOV_{out} = 2$ mrad).

Sect. 3.2). Then, we followed the data analysis strategy as illustrated in Fig. 8 in Part 1 and summarized in Table 1. We used $\overline{\delta}_{rat} = \overline{\delta}_{in}/\overline{\delta}_{out}$ for $\Delta z_{ref} = 75$ m to determine $R_e(z_{ref})$ by means of Eq. (26) (Part 1), and afterwards, $\overline{\delta}_{in}$ and R_e to determine $\alpha(z_{ref})$ with Eq. (27). By means of the cloud extinction coefficient and the droplet effective radius, we finally obtained the liquid-water content $w_l(z_{ref})$ with Eq. (4) and the droplet number concentration $N_d(z_{ref})$ with Eq. (6), again in Part 1.

As can be seen in Fig. 4 the shallow altocumulus field which developed in the pristine free troposphere in the Punta Arenas area showed cloud extinction coefficients around 20 km^{-1} (75 m above the cloud base) and droplet effective radii of initially 10 µm and later on around 7 µm. The liquid-water content was around 0.1 $g\,m^{-3}$, and the cloud droplet number concentrations increased from initially 30 cm^{-3} to 50–80 cm^{-3} later on. The properties found are typical of stratiform cloud layers (stratocumulus, altocumulus) in the marine environment (Miles et al., 2000; Revell et al., 2019).

In Fig. 5, the uncertainties in the cloud retrieval products are shown. The impact of the different error contributions discussed in Sect. 5 of Part 1 is given. The influence of un-

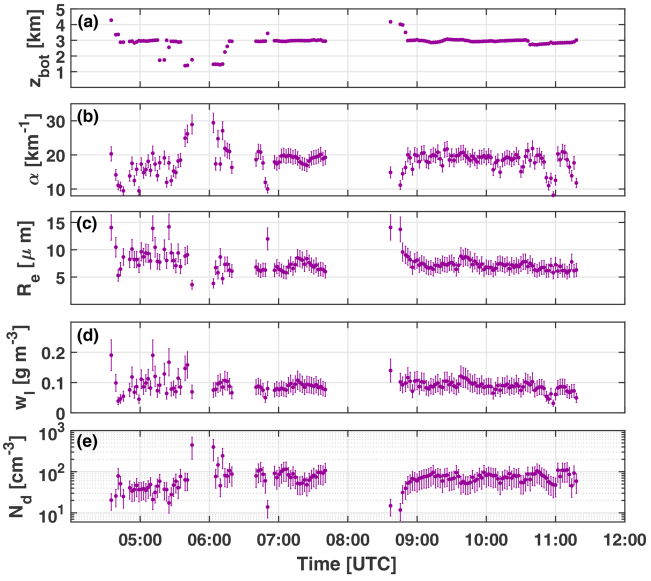

Figure 4. Dual-FOV polarization lidar observation of **(a)** cloud base height z_{bot} of detected liquid cloud layers, **(b)** cloud extinction coefficient $\alpha(z_{ref})$, **(c)** droplet effective radius $R_e(z_{ref})$, **(d)** liquid-water concentration $w_l(z_{ref})$, and **(e)** droplet number concentration $N_d(z_{ref})$ for the liquid-water clouds mostly located between 3.0 and 3.5 km height shown in Fig. 2. z_{ref} is 75 m above the cloud base. Time resolution is 120 s. Error bars indicate the estimated overall uncertainty in the retrieved values.

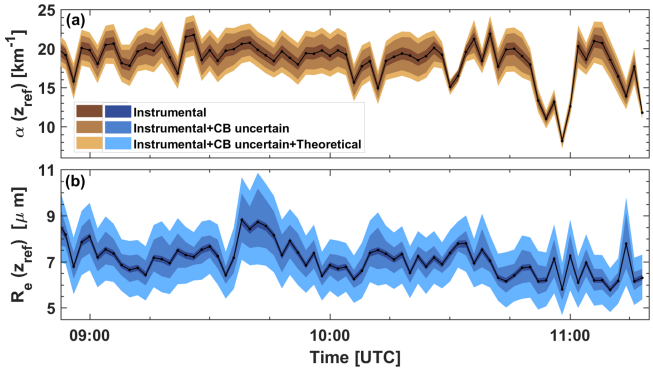

Figure 5. Contribution of the different error sources in the retrieval of the cloud extinction coefficient **(a)** and droplet effective radius **(b)** shown in Fig. 4. In **(a)**, the impact of instrumental uncertainties is calculated with Eq. (32) in Part 1 (Jimenez et al., 2020), the uncertainty in the cloud base (CB) determination with Eq. (34), and theoretical uncertainties with Eq. (33) in Part 1. In **(b)**, the impact of instrumental uncertainty is calculated with Eq. (28), the influence of the CB uncertainty with Eq. (30), and theoretical uncertainties with Eq. (29). The uncertainty in the CB determination and the methodological (theoretical) uncertainties dominate the overall retrieval uncertainties.

certainties in the measured depolarization ratio profiles for the two FOVs computed using Eqs. (28) and (32) in Part 1 is in general small (on the order of $< 5\,\%$ relative error). The retrieval uncertainties caused by an error in the estimate of the cloud base (CB) height z_{bot} (± 15 m uncertainty or 10 %–15 % relative error; see Eqs. (30) and (34) in Part 1) and caused by the theoretical (methodological) aspects (8-15 % relative error; see Eqs. (29) and (33) in Part 1) dominate the overall uncertainties in the products. For both the cloud extinction coefficient $\alpha(z_{ref})$ and droplet effective radius $R_e(z_{ref})$, the overall uncertainty is on the order of 15 %–25 %. The uncertainty in the $N_d(z_{ref})$ value depends on the uncertainties in $\alpha(z_{ref})$ and $R_e(z_{ref})$ and is on the order of 50 % according to the law of error propagation as indicated by a 50 % uncertainty bar in Fig. 4e.

As discussed by Schmidt et al. (2013, 2014) a bias can be introduced when backscatter signals during periods with varying cloud base height resulting from up and downward motions are averaged. Then, in the lowest part of the cloud, signals from cloud-free and cloudy air parcels may be averaged which causes this bias. Such an effect cannot be excluded when using the dual-FOV Raman lidar method, whereby signals over 10–30 min must be averaged before cloud microphysical properties can be derived. However, the high temporal resolution now achievable with the new dual-FOV polarization technique is of advantage in this respect, so we assume that related uncertainties are small.

Another uncertainty aspect arises from the fact that we observe the cloud layers with two different field of views (i.e., with two different eyes) and, thus, monitor two different portions (or cross sections) of the cloud in the horizontal plane. Our method assumes horizontally homogeneous cloud conditions, so that the multiple scattering effect is the only reason for differences in the measurements at the two different FOVs. However, in reality, horizontal variations in terms of droplet number concentration, size distribution, and cloud extinction coefficient always occur and can, in principle, affect the quality of the cloud retrieval products. We checked this potential impact by correlating the separately measured values of depolarization ratios for FOV_{in} and FOV_{out}. The scatter in the data was very low and did not indicate any significant influence of horizontal cloud inhomogeneities on the ratio $\overline{\delta}_{rat}$ from which the effective radius of the cloud droplets is retrieved. The necessary signal averaging over 30 to 120 s may smooth out most of the existing inhomogeneities so that the overall impact is further decreased. A good sign for a negligible impact of horizontal fluctuations in the cloud properties is finally when the time series of the derived values for the different cloud parameters show a coherent behavior.

Figure 6 shows comparisons of our solutions for the cloud extinction coefficient and droplet effective radius with respective results obtained with the single-FOV (SFOV) polarization lidar method (Donovan et al., 2015) and a technique solely based on cloud radar observations of the radar reflectivity factor (Frisch et al., 2002). Here, we used our

35 GHz cloud radar measurements simultaneously conducted at Punta Arenas. The SFOV lidar method is based on cloud simulations with a Monte Carlo multiple scattering model (Donovan et al., 2010) and, as a result of the lidar simulations, on computed lookup tables of the cross- and co-polarized signal strengths as a function of cloud microphysical properties. In the case of the Polly instruments, the co-polarized signal is given by the difference of the total minus the cross-polarized signal. The SFOV technique searches for the optimum solution of cloud microphysical properties (cloud extinction coefficient, droplet effective radius) which are consistent with the measured height profiles of the co-polarized and cross-polarized lidar backscatter signals. The products are given as mean values for the lowest 100 m of the liquid-water cloud layer. For the comparison, we used our solutions for 75 m above the cloud base and the profile structures shown in Fig. (4) in Part 1 to compute the respective mean values of α and R_e for the lowest 100 m within the cloud layers. Note that we started from the SFOV lidar approach to develop the dual-FOV (DFOV) polarization lidar technique. One advantage of the SFOV polarization technique is that it can directly be used by widely distributed polarization lidars (with one FOV). The technique however requires a complicated treatment of the lidar data to perform the retrieval. On the other hand, the DFOV polarization technique allows a much more straightforward retrieval, exploiting the direct relationship between $\bar{\delta}_{rat}$ and R_e.

As can be seen in Fig. 6a, the SFOV polarization lidar slightly underestimates the effective radius of the droplets compared to the other two methods. We used the 1 mrad FOV channel here, as commonly used by widespread polarization lidars. If we use the 2 mrad FOV channel, which is more sensitive to depolarization features caused by multiple scattering in water clouds, the agreement with the SFOV approach may improve.

The good agreement of our results with the respective cloud radar solution in Fig. 6b corroborates the quality (accuracy) of our retrieval products. The radar method simply uses the high correlation between the radar reflectivity factor and effective radius. In this retrieval procedure, a lognormal droplet size distribution is assumed, and the cloud droplet number concentration N_d and the width of the size distribution are needed as input parameters. However, the dependence of the solutions on these input parameters is weak as the solution with different input values indicates. In Fig. 6, we assumed $N_d = 100\,cm^{-3}$ (as a typical value for liquid-water clouds) and a logarithmic width of 0.29 as reported for marine stratocumulus over the Southern Ocean (Martin et al., 1994).

The agreement between the SFOV and DFOV solutions is very good in the case of the cloud extinction coefficient. The SFOV polarization lidar technique is obviously robust enough to retrieve the cloud extinction coefficient with good accuracy from the measured cloud depolarization ratio values. This observation is also consistent with Fig. 7 of Donovan et al. (2015). The retrieved extinction coefficient was found to be not very sensitive to depolarization ratio calibration errors, in contrast to the retrieved values of the effective radius of the droplets.

4.1.1 Aerosol and CCN conditions

Figure 7 shows the aerosol conditions determined from the lidar observations at $FOV_{in} = 1$ mrad for this cloud event. We analyzed the altocumulus-free period from 07:45 to 08:45 UTC (see Fig. 2). It was still dark during this time, so we could use the Raman lidar option to determine the height profiles of the particle extinction coefficient at 355 and 532 nm wavelength (Baars et al., 2016; Hofer et al., 2017).

As can be seen in Fig. 7a, the particle extinction coefficient α_{par} at 532 nm was in the range of 5–10 Mm^{-1} for the height range from 1.5 to 2.5 km height and even lower at the cloud base at 3 km of the cloud layer developing after this cloud-free period. The lidar-derived 532 nm aerosol optical thickness (AOT) was low, with values of 0.04, consistent with the 500 nm AOT of 0.03 from the AERONET sun photometer observations on 22 March 2019 after sunrise (13:00–16:00 UTC) (AERONET, 2020).

The different relative humidity profiles in Fig. 7c indicated a comparably low relative humidity ($< 70\,\%$) and thus a low particle water-uptake effect (Skupin et al., 2016; Haarig et al., 2017) in the height range from 1.6–2.2 km marked by dashed lines in Fig. 7. Our extinction-to-N_{CCN} conversion model, described in Sect. 6 in Part 1 (Jimenez et al., 2020) (see also Table 1), is applicable for these conditions. By assuming pure marine conditions and sea salt particles as CCN, the conversion yields $N_{CCN} = 40\,cm^{-3}$ for an assumed water supersaturation of 0.2 % during droplet formation at the cloud base. Such low supersaturation values correspond to the occurrence of weak updrafts with vertical velocities of about $20\,cm\,s^{-1}$ at the cloud base. By applying the continental fine-mode aerosol model, we obtain $160\,cm^{-3}$ assuming urban haze or fire smoke conditions in the lower free troposphere above Punta Arenas. As shown in Fig. 4e, the cloud droplet number concentration N_d ranged from 50–100 cm^{-3}.

HYSPLIT backward trajectories (Hybrid Single-Particle Lagrangian Integrated Trajectory Model) (Stein et al., 2015; Rolph et al., 2017; HYSPLIT, 2020), not shown here, indicated westerly winds from the Southern Ocean during the last 5 d before the air mass crossed the lidar station. According to the Ångström exponent in Fig. 7b, describing the wavelength dependence of the extinction coefficient in the short-wavelength range (355 to 532 nm), traces of continental aerosol (haze or smoke) may have been present in the free troposphere over the lidar site. One option for the occurrence of fine-mode particles could be severe bush fires on the east coast of Australia in February and March 2019. The Ångström exponent is defined as $\ln(\alpha_{par}(\lambda_1)/\alpha_{par}(\lambda_2))/\ln(\lambda_2/\lambda_1)$ and typically 0.35 ± 0.2 for the 355–532 nm wavelength range and 0.45 ± 0.2 in the case

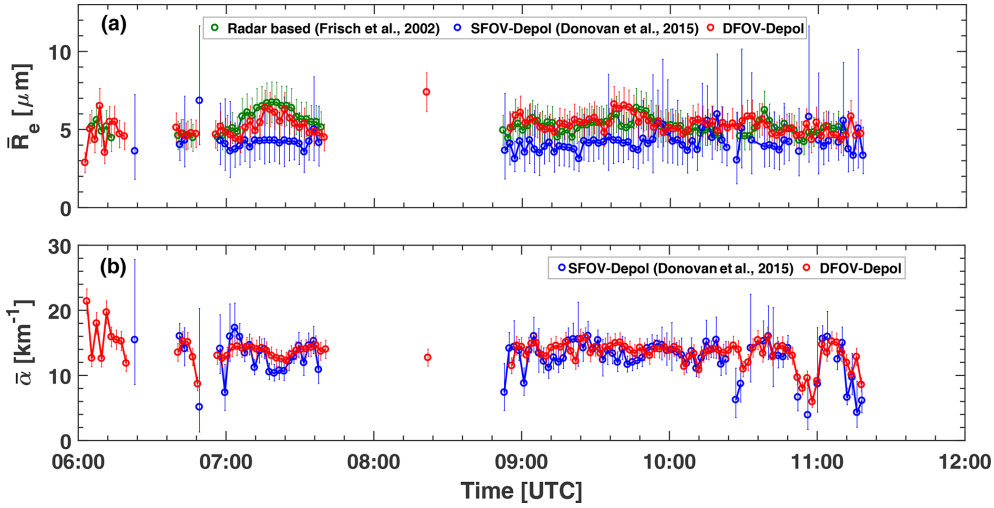

Figure 6. Comparison of **(a)** droplet effective radius values $\overline{R}_e$ (mean values for the lowest 100 m in the liquid-water cloud layer) and **(b)** respective mean extinction coefficient values $\overline{\alpha}$ obtained with the single-FOV polarization lidar method (SFOV-Depol) (Donovan et al., 2015) and the dual-FOV polarization lidar technique (DFOV-Depol) for the case shown in Fig. 4. In addition, the results (in green) obtained with a cloud radar approach (Frisch et al., 2002) are shown in **(a)**. Observations of the radar reflectivity factor performed with the LACROS 35 GHz cloud radar at Punta Arenas are used here. Error bars indicate the uncertainty range.

of the widely used Ångström exponent for the visible-near-IR wavelength spectrum (440–870 nm spectral range). Such low Ångström exponents clearly below 1 were observed at heights below 1 km in Fig. 7b.

However, it is more likely that pure marine conditions prevailed but that the marine coarse-mode particle fraction (large sea salt particles) was widely removed by sedimentation or cloud events in which the large sea salt particles were preferably consumed as CCN and then removed by rainout. As a response to the removal of coarse-mode particles, the Ångström exponent increases. The apparent discrepancy between the low marine N_{CCN} of about 40 cm^{-3} and the much higher N_d values (80–100 cm^{-3}) is possibly caused by the 0.2 % supersaturation assumption in our N_{CCN} retrieval. The Doppler lidar of LACROS showed the occurrence of gravity wave structures with a pronounced updraft period (45 min) from about 08:45 to 09:30 UTC on 22 March 2019 (when a cloud layer formed after the cloud-free period) and vertical winds mostly between 0.5 and 1 m s^{-1}, and partly exceeding 1 m s^{-1}, so that the water supersaturation was probably clearly higher than 0.5 %. At these higher supersaturation conditions the CCN concentration is higher by a factor of about 2 than the value for the 0.2 % supersaturation level, as discussed in Mamouri and Ansmann (2016) and recently in Regayre et al. (2020) for Southern Ocean marine CCN conditions. In addition, at such strong vertical winds, even non-sea-salt marine sulfate particles (nss-SO_4^{2-}) (Fossum et al., 2020) may have served as CCN. The sulfate-particle-related CCN concentration can be 1 to 2 orders of magnitude higher than the sea-salt-particle-related CCN numbers (Fossum et al., 2020). This aerosol species is not considered in the marine conversion model (Mamouri and Ansmann, 2016) presented in Sect. 6 of Part 1.

4.2 Case study of 23 February 2019

The second case of the DACAPO-PESO campaign is selected to highlight the significantly improved potential of lidar to contribute to ACI studies with a focus on liquid-water clouds. By means of the new dual-FOV polarization lidar technique, cloud and aerosol information can be derived with high temporal resolution which allows us to resolve different phases of the cloud evolution and life cycle and to investigate the impact of individual updrafts on the droplet nucleation rate, droplet growth, and corresponding evolution of the effective radius and the N_d–N_{CCN} relationship in great detail.

Schmidt et al. (2014, 2015) developed a new strategy to investigate ACI by integrating vertical wind observations with a Doppler lidar. The closest relationship between the number of CCN below the cloud base and the freshly formed cloud droplets was found during updraft periods. The ACI parameter $E_{ACI,\alpha_{par}}(N_d, \alpha_{par})$ (see Table 1 and the discussion in Sect. 6 in Part 1) was around 0.4 when ignoring the meteorological impact (vertical motion) and about 0.8 when lidar observations exclusively performed during updraft times were considered (Schmidt et al., 2015). However, the database of Schmidt et al. (2014, 2015) was small (< 30 individual cloud cases). When using the dual-FOV Raman lidar technique, long signal averaging times are required. More than 200 cloud events were collected, but only in 27 cases were the observational constraints fulfilled (need for clear skies below the cloud layers over the long signal averaging times of 10–30 min and also a relatively constant cloud base height

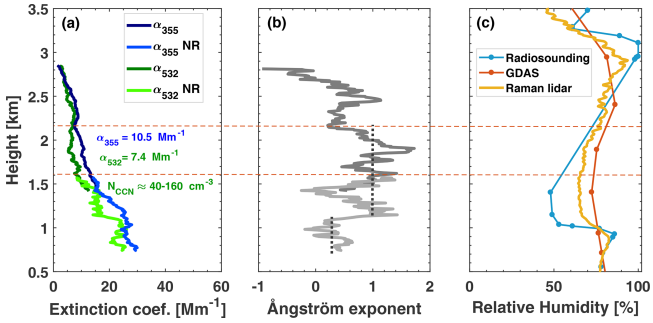

Figure 7. Aerosol observation with the dual-FOV polarization Raman lidar on 22 March 2019 during the altocumulus-free period from 07:45–08:45 UTC (see Figs. 2 and 4). **(a)** Particle extinction coefficient at 355 and 532 nm (NR indicates the determination from Raman signal profiles measured with the near-range of FOV_{out} telescope), **(b)** Ångström exponent (355–532 nm spectral range) computed from the extinction profiles in (a), and **(c)** relative humidity profiles, calculated from the Raman lidar observation of the water vapor mixing ratio (for the time period from 07:45–08:45 UTC, in yellow), by using the respective GDAS temperature profile (not shown), relative humidity taken from the GDAS data set (orange), and as measured with the Punta Arenas radiosonde (blue, launched at 12:00 UTC). The mean values of the particle extinction coefficients α_{355} at 355 nm and α_{532} at 532 nm for the height range from 1.6–2.15 km (driest region, indicated by dashed horizontal lines) are given as numbers in **(a)**. The layer mean 532 nm extinction coefficient is used to derive the N_{CCN} range by assuming pure marine conditions (minimum value) and pure urban haze conditions (maximum value) and a supersaturation of 0.2 % during droplet nucleation events. The dashed vertical lines in **(b)** indicate different Ångström values for the boundary layer and for the relatively dry part of the free troposphere below the cloud deck.

during these 10–30 min). These restrictions were required to avoid biases in the data analysis and thus allow a trustworthy ACI study. All these shortcomings are widely overcome now by using the new dual-FOV polarization lidar technique.

We start with Fig. 8a which shows a 6 h cloud measurement at Punta Arenas on 23 February 2019. Liquid-water cloud parcels permanently formed at the top of the convective summertime planetary boundary layer (PBL) between 15:00 and 21:00 local time (18:00–24:00 UTC). HYSPLIT backward trajectories (not shown) indicated pure marine conditions with an airflow from southwest (from the Southern Ocean). GDAS relative humidity (RH) values ranged from 60 %–65 % (at 500 m height) and 75 %–85 % (at 1000 m height) and were around > 95 % about 100 m below the cloud base during the 18:00–24:00 UTC period (GDAS, 2020). The aerosol particle extinction coefficient α_{par} decreased with time and indicated a significant reduction of aerosol particles during the last 2 h of the measurement period (22:00–24:00 UTC; see Table 2). The particle extinction coefficient is calculated from the measured aerosol backscatter coefficient multiplied by a typical marine extinction-to-backscatter ratio of 25 sr at 532 nm (more details of the determination of backscatter coefficient profiles below a cloud deck are given in Sect. 6.1 in Part 1).

Table 2. Mean values and standard deviations of cloud properties observed in the liquid-water cloud layer at 3 km height on 23 February 2019. The aerosol properties for the height range from 375–600 m below the cloud base are given in addition. During the selected averaging periods (before and after 22:00 UTC), very different cloud and aerosol properties were found.

	18:00–22:00 UTC	22:00–24:00 UTC
N_d, cm^{-3}	42.4 ± 46.3	21.4 ± 15.4
R_e, µm	8.5 ± 2.7	10.4 ± 2.7
α, km^{-1}	10.0 ± 2.3	9.3 ± 1.8
w_l, gm^{-3}	0.054 ± 0.015	0.063 ± 0.02
N_{CCN}, cm^{-3}	110 ± 21	72 ± 14
α_{par}, km^{-1}	0.025 ± 0.006	0.015 ± 0.003

Figure 8b shows the convective structures of the PBL in terms of the vertical wind component measured with the zenith-pointing Doppler lidar of LACROS (Cloudnet, 2020). Varying periods with upward (orange) and downward motions (green) were observed. Most updraft velocities were < 0.5–0.7 m s^{-1}; however some strong updrafts with velocities > 1 m s^{-1} occurred as well. The up- and downdrafts modulated cloud formation and cloud base height variations. Water uptake by the aerosol particles at relative humidity > 75 % (close to the cloud base) influenced the strength of the lidar return signals, especially during upwind situations. The dashed lines in Fig. 8a follow the variations of the cloud base height z_{bot} and indicate 10 further height levels from 75–750 m below the cloud base. These height levels (z_{aer} in the ACI sketch in Fig. 4 of Part 1) are used in the discussion of the results regarding ACI below.

Figure 9 presents the time series of the cloud droplet number concentration N_d for the height $z_{ref} = z_{bot} + 75$ m (see Fig. 4 of Part 1) obtained from the dual-FOV polarization lidar measurements together with the vertical wind indicator (orange for updraft, green for downdraft) and the aerosol proxies α_{par} and N_{CCN}. The aerosol proxies are mean values for the height range from 375–600 m below the cloud base at z_{bot} and thus for the height range from $z_{aer} = z_{bot} - 375$ m to $z_{aer} = z_{bot} - 600$ m according to Fig. 4 in Part 1. The temporal resolution in Fig. 9 is 1 min. The marine aerosol conversion parameterization (Mamouri and Ansmann, 2016) is applied to obtain N_{CCN} (see Table 1; more explanations are given in Sect. 6 in Part 1). This conversion corrects for aerosol water-uptake effects for a typical marine RH of 80 % and holds for the water supersaturation level of 0.2 %. Error bars indicate the retrieval uncertainty of 20 % (marine particle extinction coefficient α_{par}) and 50 % (N_d, N_{CCN}).

Figure 9 shows that the cloud droplet number concentration N_d varied strongly and was clearly correlated with updraft occurrence during the 19:30–24:00 UTC time period,

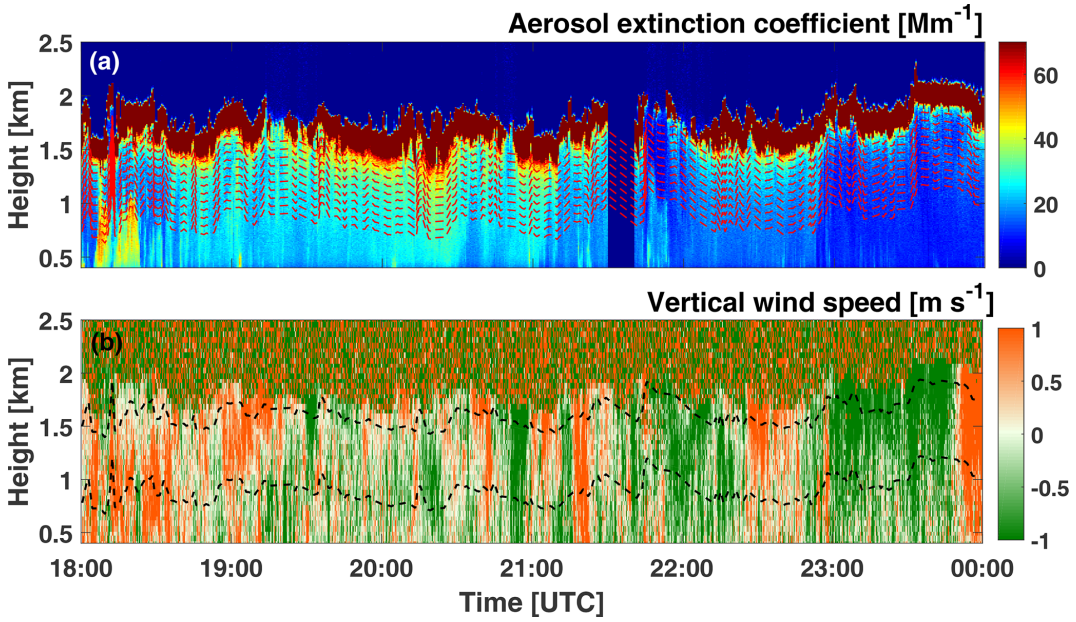

Figure 8. Lidar observation of the convective cloud-topped planetary boundary layer in the afternoon and evening of the summer day of 23 February 2019. **(a)** Aerosol extinction coefficient (blue to yellow colors) up to the base of the stratocumulus layer (dark red) at around 1500 m height and **(b)** vertical wind component (orange: upward motion, green: downward motion) measured with the zenith-pointing Doppler lidar of the LACROS facility. The cloud base strongly varies with the permanently changing updraft and downdraft conditions. Dashed red curves in **(a)** show height levels of constant distance of 75 to 750 m from the cloud base. The dashed black lines in **(b)** show the cloud base height z_{bot} and the height level 750 m below the cloud base. For these height levels, aerosol proxies for the ACI studies are computed as discussed below.

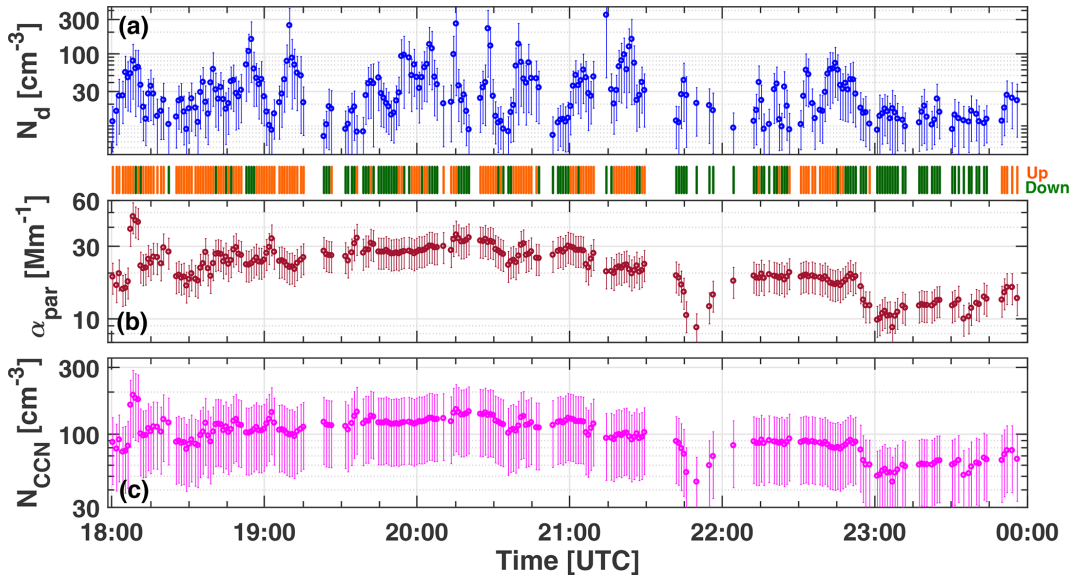

Figure 9. **(a)** Cloud droplet number concentration N_d for the height of $z_{ref} = z_{bot} + 75$ m within the stratocumulus layer shown in Fig. 8. Below **a**, the vertical wind indicator (orange: updraft, green: downdraft) is shown. **(b)** Particle extinction coefficient α_{par} (mean value for the height range from 375 to 600 m below the cloud base). **(c)** CCN concentration N_{CCN} obtained from the extinction coefficient (in **b**) by using the marine conversion parameters (Sect. 6 in Part 1) (Jimenez et al., 2020). Temporal resolution is 1 min. Error bars indicate the uncertainty range.

whereas the aerosol proxies N_{CCN} and α_{par} were likewise smooth functions of time. However, the true or actual N_{CCN} values probably showed large variations because the CCN level (actually occurring) depends on actual updraft speed and the related actually occurring supersaturation level. For updraft velocities of 1 m s^{-1} and corresponding supersaturation exceeding 0.5 %, N_{CCN} is approximately a factor of 2 higher than the ones shown for the fixed 0.2 % water supersaturation as outlined in Mamouri and Ansmann (2016) and already pointed out in Sect. 4.1.

On average, N_d ranged from 20–100 cm^{-3} before 21:30 UTC and 10–30 cm^{-3} later on. Peak values exceeded 200 cm^{-3}. The aerosol parameters N_{CCN} and α_{par}, indicating clean conditions (with horizontal visibility $>$ 50 km), were mostly in the range of 20–40 Mm^{-1} before 21:15 UTC and 10–25 Mm^{-1} later on in the case of α_{par} and $>$ 100 cm^{-3} before 21:15 UTC and clearly $<$ 100 cm^{-3} later on in the case of N_{CCN}. The decrease of N_d with time is in line with the decrease of N_{CCN} and α_{par}. Table 2 summarizes the aerosol and cloud observations and contains mean values of all derived aerosol and cloud properties for two time periods characterized by different aerosol conditions.

Besides aerosol and cloud correlations, our measurements allow us to look into the effect of vertical wind velocity (especially of updrafts) on the observed cloud products. The number of aerosol particles and the updraft velocity (and accompanying adiabatic cooling) (Reutter et al., 2009) controls CCN activation and droplet growth. Upward movements affect the water vapor saturation pressure in the cloud base region. The stronger the updraft is, the larger the water supersaturation is, enabling aerosol particles to become activated and grow. In Fig. 10, the impact of upward (and downward) motions on the measured cloud properties N_d, R_e, and α_{par} is illuminated for the observation on 23 February 2019. For comparison, we also included the respective variations of the aerosol proxy N_{CCN}.

Such correlations of N_d and R_e with vertical velocity at the cloud base are new options of combined dual-FOV and Doppler lidar profiling. As can be seen, very clear correlations were not found. A pronounced influence of updraft speed on N_d and R_e cannot be expected in this case of a long-lived, well-developed stratocumulus cloud deck. At such pre-existing cloud conditions there is a competition between droplet nucleation and water uptake by the existing droplets in the case of a given supersaturation. Advection and diffusion processes mix different droplet concentrations together. Besides condensation of water vapor on existing droplets and new droplet formation, collision–coalescence processes shape the size distribution measured over the lidar station. All cloud features observed are related to processes that occurred upstream of the lidar. However, even in these cases of complex cloud processes, we expect that a residual effect of the aerosol concentration variations found on the droplet microphysical properties during updraft periods should be detectable. Updraft speeds of 0–70 cm s^{-1} occurred most often. For these weak to moderate updraft velocities N_d and N_{CCN} (for the supersaturation of 0.2 %) were then found in the range from 15–100 and 75–200 cm^{-3}, respectively. Obviously the true supersaturation was about 0.1 %–0.15 % (to obtain an activation ratio N_d/N_{CCN}=1). New droplet formation and growth of existing droplets by water uptake led to a slight increase of the cloud extinction coefficient in many

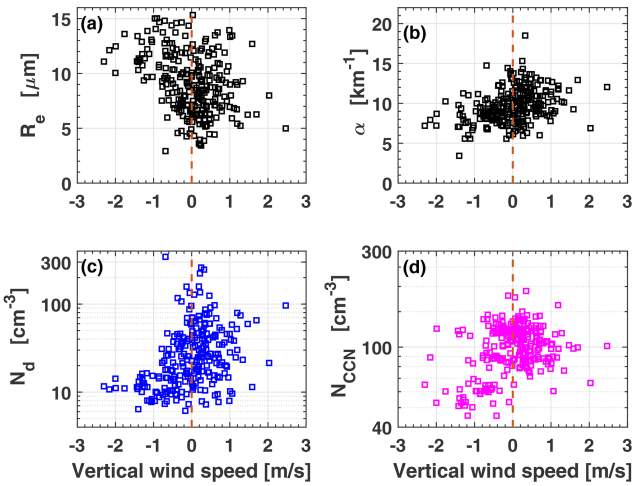

Figure 10. Correlation of retrieved cloud properties (droplet effective radius R_e, number concentration N_d, and 532 nm light-extinction coefficient α) and aerosol CCN concentration N_{CCN} (for a fixed water supersaturation level of 0.2 %) vs. vertical wind measured with Doppler lidar at the cloud base. The data in Fig. 9 are used. The data are observed with 1 min temporal resolution in a well-developed stratocumulus deck at the top of the pristine marine boundary layer.

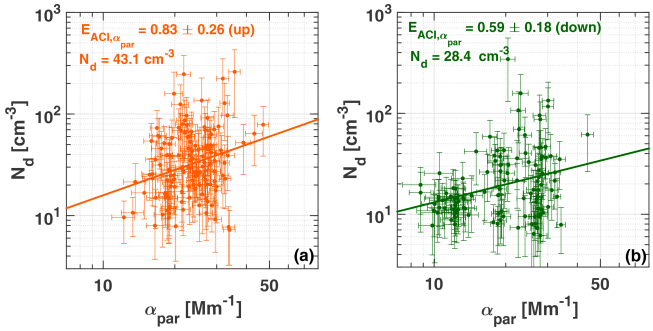

Figure 11. Cloud droplet number concentration N_d (for height z_{ref} = 75 m above the cloud base) vs. aerosol particle extinction coefficient α_{par}, separately for **(a)** updraft and **(b)** downdraft periods. The N_d and α_{par} values shown in Fig. 9 are used (375–600 m below the cloud base). In total, almost 260 values were available for the regression analysis. Error bars show the uncertainties in the N_d and α_{par} values. The linear regression fits a straight line to the logN_d–logα_{par} data field with the slope $E_{ACI,\alpha_{par}} = 0.87 \pm 0.26$ (orange slope) and 0.58 ± 0.17 (green slope). The mean droplet number concentration (given as numbers) was about 50 % higher during the updraft periods than during the downdraft periods.

cases. A weak reduction of the mean effective radius during upward motions may indicate new droplet nucleation in the presence of existing droplets.

Our observations of N_d and N_{CCN} are in good agreement with values presented by Revell et al. (2019). In this model-based study, simulated N_{CCN} values (for a supersaturation of 0.2 %) were in the range from 50–80 cm^{-3} during the late summer season (February and March), and N_d showed values from 30–50 cm^{-3} for boundary layer clouds at 800 m height under pure marine conditions of the Southern Ocean. According to the recent publication of Regayre et al. (2020), N_{CCN} is usually underestimated by a factor of 2 in models focusing on aerosols and clouds in the Southern Ocean. Our lidar-derived N_{CCN} values are in very good agreement with the CCN numbers presented by Regayre et al. (2020) of usually 100–200 cm^{-3}. These authors constrained their simulations to recent CCN observations aboard a Russian research vessel traveling around the entirety of Antarctica (Schmale et al., 2019). Our findings are also in reasonable agreement with airborne in situ observations of N_d and N_{CCN} over the Southeast Pacific stratocumulus cloud regime west of northern Chile (Zheng et al., 2011; Painemal and Zuidema, 2013).

Some caution has to be exercised in the interpretation of the results in Fig. 10 because of the uncertainties in the retrieval products discussed above (case study 1) and because of the assumptions made in the development of the dual-FOV polarization lidar technique. We assume subadiabatic conditions and corresponding profile structures for the different cloud parameters as shown in Fig. 4 of Part 1 for the lowermost 75 m of the cloud layer. We also assume a gamma size distribution to describe the droplet size spectrum. These assumptions may no longer hold for an aged, preexisting cloud layer (especially not during downdraft periods) in which droplet collision and coalescence processes, entrainment, and droplet evaporation take place. However, the gamma size distribution and subadiabatic cloud conditions were introduced to develop our dual-FOV lidar method with a focus on the most interesting scenarios (updraft periods). The new method is primarily based on the strong relationship between the measured ratio $\overline{\delta}_{rat} = \overline{\delta}_{in}/\overline{\delta}_{out}$ and the droplet effective radius R_e and the clear relationship between the depolarization ratio $\overline{\delta}_{in}$ (for FOV_{in}) and the cloud extinction coefficient α for a given R_e value, known from the first part of the retrieval procedure.

Disregarding the complex cloud structures, processes, and features found, we computed the ACI parameter $E_{ACI,\alpha_{par}}(N_d, \alpha_{par})$ (see Table 1 and Sect. 6 in Part 1 for more explanations). In Fig. 11, the correlation between the derived N_d and measured α_{par} values (in Figs. 9 and 10) are considered separately for updraft and downdraft periods. We use the particle extinction coefficient α_{par} (and not N_{CCN}) in the correlation because this quantity is directly obtained from the lidar observations with a low uncertainty of 20 %. Disregarding the aerosol proxy used, we notice a large scatter in the correlated data. This is typical of aerosol and cloud

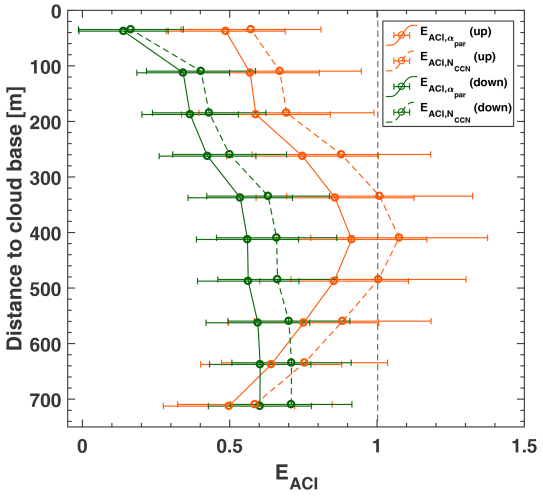

Figure 12. ACI efficiency parameter E_{ACI} (see Table 1 and Sect. 6 in Part 1 for detailed explanations) as a function of N_d and α_{par} (solid curves, $E_{ACI,\alpha_{par}}$) and as a function of N_d and N_{CCN} (dashed curve, $E_{ACI,N_{CCN}}$), separated for updraft periods (orange) and downdraft periods (green). Different values of aerosol proxies α_{par} and N_{CCN} for different layers (with 75 m vertical depth and increasing distance from the cloud base towards lower heights) are considered in the calculations of the four E_{ACI} parameters (as explained in Fig.11). The ACI efficiencies are assigned to the center heights of these 75 m deep aerosol layers for which the aerosol proxies were determined. E_{ACI} values around 400 m below the cloud base are obviously not affected by aerosol water-uptake effects which tend to widely smooth out a well-defined and strong correlation between aerosol proxy and cloud droplet number concentration. Error bars indicate the uncertainty in the determination of the slopes of the linear regression analysis.

parameters determined in well-developed, preexisting liquid-water cloud layers (McComiskey et al., 2009). As mentioned above, the large scatter is caused by the strong variability of N_d (as a function of the varying vertical wind conditions) compared to the low variability in the particle extinction coefficient which is not a function of vertical wind velocity. To obtain $E_{ACI,\alpha_{par}}(N_d, \alpha_{par})$ a linear regression analysis is applied to the $\log(N_d)$–$\log(\alpha_p)$ data field. $E_{ACI,\alpha_{par}}(N_d, \alpha_{par})$ is equal to the slope of the regression line. As expected, the aerosol impact on N_d is stronger for upward motions. However, we should emphasize again that we present just one case study (in order to show the potential of the dual-FOV lidar) so that general conclusions on the relationship between N_d and N_{CCN} can not be drawn in this stage of data analysis. Presently we analyze the entire Punta Arenas data set (collected in 2019–2020) along the data analysis steps presented here.

As a final task, we applied such correlation studies and regression analysis as presented in Fig. 11 to the full sets of N_d, α_{par}, and N_{CCN} data. We performed regression analyses with different sets of aerosol proxies for different height levels z_{aer} below the cloud base height z_{bot} (as illustrated in Fig. 4 in

Part 1 and indicated by the 10 dashed lines in Fig. 8a) to investigate to what extent water uptake corrupts the ACI study. The result is shown in Fig. 12.

The respective ACI efficiency values E_{ACI} are assigned to the heights of the aerosol layers (with respect to the cloud base) of which the aerosol proxies were considered in the E_{ACI} computations. This way of presenting the ACI efficiency values allows us to check the impact of water uptake by the marine particles when the relative humidity steadily increases and reaches 100 % at the cloud base. As can be seen, the ACI efficiency E_{ACI} for well-defined updraft conditions decreases from values close to 1 (the optimum value for the expected strong impact of marine particles on the droplet number concentration) at heights around 400 m below the cloud base to values around 0.5 very close to the cloud base. Obviously, water uptake leads to a broadening of the range of observable extinction coefficients. For dry or almost dry particles, the extinction coefficients vary over a more narrow range, so the relative increase of the directly measured $\log(\alpha_{\mathrm{par}})$ is proportional to the relative increase in $\log N_{\mathrm{d}}$. This is no longer the case when all particles grow by water uptake. Then the increase of $\log(\alpha_{\mathrm{par}})$ is linked to a much lower relative increase of the droplet number concentration (lower by a factor of almost 2). For downdraft periods the decrease of E_{ACI} with water-uptake effects is less clear and pronounced as can be seen in Fig. 11 because of the generally not well-defined link between droplet nucleation and available CCN.

It is interesting to note at the end that Shinozuka et al. (2015) found that the maximum value of $E_{\mathrm{ACI},\alpha_{\mathrm{par}}}(N_{\mathrm{d}}, \alpha_{\mathrm{par}})$ can only be about 0.8–0.85, i.e., when the aerosol particle extinction coefficient α_{p} is used as aerosol proxy. $E_{\mathrm{ACI}} = 0.9$–1.0 is only possible when N_{CCN} is considered as shown in Fig. 12. The reason for this is that N_{CCN} is proportional to $\alpha_{\mathrm{par}}^{0.85}$ and not to α_{par} in Eq. (36) in Part 1.

5 Summary, conclusions, and outlook

In a companion article (Jimenez et al., 2020), we presented a new polarization-lidar-based approach to derive microphysical properties in the lower part of pure liquid-water clouds. Extended simulations were performed regarding the relationship between cloud microphysical and light-extinction properties and the cloud depolarization ratio measured with lidar at two different FOVs. These simulations served as the basis for the development of the new dual-FOV polarization lidar method. The effective radius of the cloud droplets and the cloud light-extinction coefficient in the lowest 50–100 m of the cloud layer can be derived with a relative error of 20 %–25 %. From the quantities, the cloud droplet number concentration can be computed with an error of the order of 50 %.

In Part 2, the new lidar technique was combined with the aerosol polarization lidar method, which enables the retrieval of CCN concentrations below the cloud base, and with Doppler lidar observations of the vertical wind component and thus of updraft and downdraft occurrence at the cloud base. We integrated the novel dual-FOV polarization lidar technique into a multiwavelength polarization Raman lidar (Polly), which is now involved in the long-term DACAPO-PESO field campaign in Punta Arenas, southern Chile, at the southernmost tip of South America.

Two case studies were presented. Case 1 was used to discuss the basic and principle features of the new cloud retrieval technique. This case study included an uncertainty discussion and comparisons with alternative approaches to derive cloud microphysical properties such as the single-FOV polarization lidar technique (Donovan et al., 2015) and a cloud-radar-based approach (Frisch et al., 2002). Good agreement was found.

Case 2 highlighted the new and extended potential of lidar to contribute to detailed ACI studies in the case of liquid-water clouds. Profiling of aerosol-relevant aerosol parameters close to the cloud base, cloud microphysical properties just above the cloud base, and vertical wind with 1 min resolution was possible and enabled a detailed updraft- and downdraft-resolved ACI study. For typical updraft conditions with vertical velocities < 50–$70\,\mathrm{cm\,s^{-1}}$, we found N_{d} and N_{CCN} values (for 0.2 % water supersaturation) ranging from 15–100 $\mathrm{cm^{-3}}$ and 75–200 $\mathrm{cm^{-3}}$, respectively, in the well-developed, preexisting stratocumulus deck at the top of the pristine marine boundary layer over Punta Arenas. ACI studies were performed separately for updraft and downdraft conditions with the particle extinction coefficient α_{par} as well as with N_{CCN} as aerosol proxy. High ACI values of 0.8–1.0 were found. The impact of aerosol water uptake on the ACI studies was illuminated with the result that the highest ACI values were obtained by considering the aerosol proxies α_{par} or N_{CCN} measured at heights about 500 m below the cloud base (and thus for dry aerosol conditions) in the ACI computations.

As an outlook, we will extend our ACI studies by means of the dual-FOV lidar method. We equipped three further Polly instruments with the dual-FOV polarization lidar technique. These lidars are or were operated at the North Pole (at 85–90° N) on board the German ice breaker Polarstern from September 2019 to September 2020, at Dushanbe, Tajikistan, at polluted and dusty conditions in Central Asia since June 2019, and at Limassol, Cyprus, in the polluted and dusty eastern Mediterranean since October 2020. A fourth dual-FOV Polly lidar will start long-term monitoring at Mindelo, Cabo Verde, in the outflow regime of pollution and dust from western and central Africa in 2021. A mobile dual-FOV Polly will be moved to New Zealand for further ACI studies in the Southern Ocean in 2021. All these field activities will be used to characterize ACI in the case of liquid-water clouds at very different aerosol and meteorological conditions.

We are presently analyzing the data of Punta Arenas and Dushanbe and are preparing a follow-up paper (tentative title: "Aerosol effects in liquid-water clouds: contrasting lidar ob-

servations in dusty, polluted Central Asia and clean, southern South America"). Another goal is to initiate the further upgrading of the existing European lidar–radar network by implementing the dual-FOV lidar technique at several network supersites.

The integration of the dual-FOV-polarization lidar technique into the LACROS infrastructure can be regarded as the next systematic step to improve the capability of state-of-the-art ground-based remote sensing towards an overall monitoring of aerosol–cloud interaction in liquid-water clouds as presented here and mixed-phase clouds and cirrus layers as presented recently by Bühl et al. (2019) and Ansmann et al. (2019).

Data availability. Polly lidar observations (level 0 data, measured signals) are in the PollyNET database (http://polly.rsd.tropos.de/; PollyNET, 2020). LACROS observations (level 0 data) are stored in the Cloudnet database of LACROS (http://lacros.rsd.tropos.de/; Cloudnet, 2020). All the analysis products are available at TROPOS upon request (info@tropos.de). Backward trajectory analysis has been supported by air mass transport computation with the NOAA (National Oceanic and Atmospheric Administration) HYSPLIT (HYbrid Single-Particle Lagrangian Integrated Trajectory) model (http://ready.arl.noaa.gov/HYSPLIT_traj.php; HYSPLIT, 2020). AERONET photometer observations of Punta Arenas are in the AERONET database (http://aeronet.gsfc.nasa.gov/; AERONET, 2020).

Author contributions. CJ and AA prepared the manuscript. CJ developed the new method and analyzed all field campaign observations. CJ, RE, and RW upgraded the Polly instrument. CJ, RE, PS, MR, BB, and JB took care of the DACAPO PESO campaign and the field campaign instrumentation. ZY determined the lidar calibration constants (for the aerosol retrieval below the cloud base). JB took care of the vertical wind retrievals. DD developed the code to analyze single-FOV polarization measurements. PS took care of the radar-based retrieval. DD, AM, PS, JS, and UW supported the discussion and interpretation of the observations.

Competing interests. The authors declare that they have no conflict of interest.

Special issue statement. This article is part of the special issue "EARLINET aerosol profiling: contributions to atmospheric and climate research". It is not associated with a conference.

Acknowledgements. The authors wish to thank TROPOS and UMAG for their logistic and infrastructural support during the preparation phase and during the DACAPO-PESO campaign at Punta Arenas. We are grateful to the technicians of the mechanical workshop of TROPOS for the always prompt and careful assistance when upgrading the Polly instruments. We thank AERONET for their continuous efforts in providing high-quality measurements and products. Aerosol source apportionment analysis has been supported by air mass transport computation with the rather convenient NOAA (National Oceanic and Atmospheric Administration) HYSPLIT (HYbrid Single-Particle Lagrangian Integrated Trajectory) model.

Financial support. This research has been supported by the DAAD/Becas Chile (grant no. 57144001) and the ACTRIS Research Infrastructure (EU H2020-R&I) (grant no. 654109).

The publication of this article was funded by the Open Access Fund of the Leibniz Association.

Review statement. This paper was edited by Eduardo Landulfo and reviewed by three anonymous referees.

References

AERONET: Aerosol Robotic Network aerosol data base, available at: http://aeronet.gsfc.nasa.gov/, last access: 22 Februray 2020.

Ansmann, A., Mamouri, R.-E., Bühl, J., Seifert, P., Engelmann, R., Hofer, J., Nisantzi, A., Atkinson, J. D., Kanji, Z. A., Sierau, B., Vrekoussis, M., and Sciare, J.: Ice-nucleating particle versus ice crystal number concentrationin altocumulus and cirrus layers embedded in Saharan dust:a closure study, Atmos. Chem. Phys., 19, 15087–15115, https://doi.org/10.5194/acp-19-15087-2019, 2019.

Baars, H., Kanitz, T., Engelmann, R., Althausen, D., Heese, B., Komppula, M., Preißler, J., Tesche, M., Ansmann, A., Wandinger, U., Lim, J.-H., Ahn, J. Y., Stachlewska, I. S., Amiridis, V., Marinou, E., Seifert, P., Hofer, J., Skupin, A., Schneider, F., Bohlmann, S., Foth, A., Bley, S., Pfüller, A., Giannakaki, E., Lihavainen, H., Viisanen, Y., Hooda, R. K., Pereira, S. N., Bortoli, D., Wagner, F., Mattis, I., Janicka, L., Markowicz, K. M., Achtert, P., Artaxo, P., Pauliquevis, T., Souza, R. A. F., Sharma, V. P., van Zyl, P. G., Beukes, J. P., Sun, J., Rohwer, E. G., Deng, R., Mamouri, R.-E., and Zamorano, F.: An overview of the first decade of PollyNET: an emerging network of automated Raman-polarization lidars for continuous aerosol profiling, Atmos. Chem. Phys., 16, 5111–5137, https://doi.org/10.5194/acp-16-5111-2016, 2016.

Baars, H., Seifert, P., Engelmann, R., and Wandinger, U.: Target categorization of aerosol and clouds by continuous multiwavelength-polarization lidar measurements, Atmos. Meas. Tech., 10, 3175–3201, https://doi.org/10.5194/amt-10-3175-2017, 2017.

Belegante, L., Bravo-Aranda, J. A., Freudenthaler, V., Nicolae, D., Nemuc, A., Ene, D., Alados-Arboledas, L., Amodeo, A., Pappalardo, G., D'Amico, G., Amato, F., Engelmann, R., Baars, H., Wandinger, U., Papayannis, A., Kokkalis, P., and Pereira, S. N.: Experimental techniques for the calibration of lidar depolarization channels in EARLINET, Atmos. Meas. Tech., 11, 1119–1141, https://doi.org/10.5194/amt-11-1119-2018, 2018.

Bühl, J., Seifert, P., Wandinger, U., Baars, H., Kanitz, T., Schmidt, J., Myagkov, A., Engelmann, R., Skupin, A., Heese, B., Kle-

pel, A., Althausen, D., and Ansmann, A.: LACROS: the Leipzig Aerosol and Cloud Remote Observations System, Proc. SPIE, 8890, 889002, https://doi.org/10.1117/12.2030911, 2013.

Bühl, J., Seifert, P., Myagkov, A., and Ansmann, A.: Measuring ice- and liquid-water properties in mixed-phase cloud layers at the Leipzig Cloudnet station, Atmos. Chem. Phys., 16, 10609–10620, https://doi.org/10.5194/acp-16-10609-2016, 2016.

Bühl, J., Seifert, P., Radenz, M., Baars, H., and Ansmann, A.: Ice crystal number concentration from lidar, cloud radar and radar wind profiler measurements, Atmos. Meas. Tech., 12, 6601–6617, https://doi.org/10.5194/amt-12-6601-2019, 2019.

Cloudnet: Cloudnet data base, available at: http://lacros.rsd.tropos.de/, last access: 20 April 2020.

Dai, G., Althausen, D., Hofer, J., Engelmann, R., Seifert, P., Bühl, J., Mamouri, R.-E., Wu, S., and Ansmann, A.: Calibration of Raman lidar water vapor profiles by means of AERONET photometer observations and GDAS meteorological data, Atmos. Meas. Tech., 11, 2735–2748, https://doi.org/10.5194/amt-11-2735-2018, 2018.

Donovan, D., Voors, R., van Zadelhoff, G.-J., and Acarreta, J.-R.: ECSIM Model and Algorithms Document, KNMI Tech. Rep.: ECSIM-KNMI-TEC-MAD01-R, availanle at: https://www.academia.edu/33712449/ECSIM_Model_and_Algorithms_Document (last access: 2 December 2020), 2010.

Donovan, D. P., Klein Baltink, H., Henzing, J. S., de Roode, S. R., and Siebesma, A. P.: A depolarisation lidar-based method for the determination of liquid-cloud microphysical properties, Atmos. Meas. Tech., 8, 237–266, https://doi.org/10.5194/amt-8-237-2015, 2015.

Engelmann, R., Kanitz, T., Baars, H., Heese, B., Althausen, D., Skupin, A., Wandinger, U., Komppula, M., Stachlewska, I. S., Amiridis, V., Marinou, E., Mattis, I., Linné, H., and Ansmann, A.: The automated multiwavelength Raman polarization and water-vapor lidar PollyXT: the neXT generation, Atmos. Meas. Tech., 9, 1767–1784, https://doi.org/10.5194/amt-9-1767-2016, 2016.

Fossum, K. N., Ovadnevaite, J., Ceburnis, D., Preißler, J., Snider, J. R., Huang, R.-J., Zuend, A., and O'Dowd, C.: Sea-spray regulates sulfate cloud droplet activation over oceans, npj Clim. Atmos. Sci., 3, 14, https://doi.org/10.1038/s41612-020-0116-2, 2020.

Freudenthaler, V., Esselborn, M., Wiegner, M., Heese, B., Tesche, M., Ansmann, A., Müller, D., Althausen, D., Wirth, M., Fix, A., Ehret, G., Knippertz, P., Toledano, C., Gasteiger, J., Garhammer, M., and Seefeldner, M.: Depolarization ratio profiling at several wavelengths in pure Saharan dust during SAMUM 2006, Tellus B, 61, 165–179, https://doi.org/10.1111/j.1600-0889.2008.00396.x, 2009.

Freudenthaler, V.: About the effects of polarising optics on lidar signals and the $\Delta 90$ calibration, Atmos. Meas. Tech., 9, 4181–4255, https://doi.org/10.5194/amt-9-4181-2016, 2016.

Frisch, S., Shupe, M., Djalalova, I., Feingold, G., and Poellot, M.: The retrieval of stratus cloud droplet number effective radius with cloud radars, J. Atmos. Ocean. Tech., 19, 835–842, https://doi.org/10.1175/1520-0426(2002)019<0835:TROSCD>2.0.CO;2, 2002.

GDAS: Global Data Assimilation System, meteorological data base, available at: https://www.ready.noaa.gov/gdas1.php, last access: 20 March 2020.

Grosvenor, D. P., Sourdeval, O., Zuidema, P., Ackerman, A., Alexandrov, M. D., Bennartz, R., Boers, R., Cairns, B., Chiu, J. C., Christensen, M., Deneke, H., Diamond, M., Feingold, G., Fridlind, A., Hünerbein, A., Knist, C., Kollias, P., Marshak, A., McCoy, D., Merk, D., Painemal, D., Rausch, J., Rosenfeld, D., Russchenberg, H., Seifert, P., Sinclair, K., Stier, P., van Diedenhoven, B., Wendisch, M., Werner, F., Wood, R., Zhang, Z., and Quaas, J.: Remote sensing of droplet number concentration in warm clouds: A review of the current state of knowledge and perspectives, Rev. Geophys., 56, 409–453, https://doi.org/10.1029/2017RG000593, 2018.

Haarig, M., Ansmann, A., Gasteiger, J., Kandler, K., Althausen, D., Baars, H., Radenz, M., and Farrell, D. A.: Dry versus wet marine particle optical properties: RH dependence of depolarization ratio, backscatter, and extinction from multiwavelength lidar measurements during SALTRACE, Atmos. Chem. Phys., 17, 14199–14217, https://doi.org/10.5194/acp-17-14199-2017, 2017.

Hofer, J., Althausen, D., Abdullaev, S. F., Makhmudov, A. N., Nazarov, B. I., Schettler, G., Engelmann, R., Baars, H., Fomba, K. W., Müller, K., Heinold, B., Kandler, K., and Ansmann, A.: Long-term profiling of mineral dust and pollution aerosol with multiwavelength polarization Raman lidar at the Central Asian site of Dushanbe, Tajikistan: case studies, Atmos. Chem. Phys., 17, 14559–14577, https://doi.org/10.5194/acp-17-14559-2017, 2017.

Hofer, J., Ansmann, A., Althausen, D., Engelmann, R., Baars, H., Abdullaev, S. F., and Makhmudov, A. N.: Long-term profiling of aerosol light extinction, particle mass, cloud condensation nuclei, and ice-nucleating particle concentration over Dushanbe, Tajikistan, in Central Asia, Atmos. Chem. Phys., 20, 4695–4711, https://doi.org/10.5194/acp-20-4695-2020, 2020.

Holben, B. N., Eck, T. F., Slutsker, I., Tanré, D., Buis, J. P., Setzer, A., Vermote, E., Reagan, J. A., Kaufman, Y. J., Nakajima, T., Lavenu, F., Jankowiak, I., and Smirnov, A.: AERONET – a federated instrument network and data archive for aerosol characterization, Remote Sens. Environ., 66, 1–16, 1998.

Hu, Y., Vaughan, M., Liu, Z., Lin, B., Yang, P., Flittner, D., Hunt, B., Kuehn, R., Huang, J., Wu, D., Rodier, S., Powell, K., Trepte, C., and Winker, D.: The depolarization – attenuated backscatter relation: CALIPSO lidar measurements vs. theory, Opt. Express 15, 5327–5332, 2007.

HYSPLIT: HYbrid Single-Particle Lagrangian Integrated Trajectory model, backward trajectory calculation tool, available at: http://ready.arl.noaa.gov/HYSPLIT_traj.php, last access: 20 February 2020.

Illingworth, A. J., Hogan, R. J., O'Connor, E. J., Bouniol, D., Delanoe, J, Pelon, J., Protat, A., Brooks, M. E., Gaussiat, N., Wilson, D. R., Donovan, D. P., Klein Baltink, H., van Zadelhoff, G.-J., Eastment, J. D., Goddard, J. W. F., Wrench, C. L., Haeffelin, M., Krasnov, O. A., Russchenberg, H. W. J., Piriou, J.-M., Vinit, F., Seifert, A., Tompkins, A. M., and Willen, J.: CLOUDNET: Continuos evaluation of cloud profiles in seven operational models using ground-based observations, B. Am. Meteorol. Soc., 88, 883–898, https://doi.org/10.1175/BAMS-88-6-883, 2007.

Jimenez, C., Ansmann, A., Donovan, D., Engelmann, R., Malinka, A., Schmidt, J., and Wandinger, U.: Retrieval of microphysical properties of liquid water clouds from atmospheric lidar measurements: Comparison of the Raman dual field of view

and the depolarization techniques, Proc. SPIE, 10429, 1042907, https://doi.org/10.1117/12.2281806, 2017.

Jimenez, C., Ansmann, A., Donovan, D., Engelmann, R., Schmidt, J., and Wandinger, U.: Comparison between two lidar methods to retrieve microphysical properties of liquid water clouds, EPJ Web Conf., 176, 01032, https://doi.org/10.1051/epjconf/201817601032, 2018.

Liu, M., Lin, J., Boersma, K. F., Pinardi, G., Wang, Y., Chimot, J., Wagner, T., Xie, P., Eskes, H., Van Roozendael, M., Hendrick, F., Wang, P., Wang, T., Yan, Y., Chen, L., and Ni, R.: Improved aerosol correction for OMI tropospheric NO_2 retrieval over East Asia: constraint from CALIOP aerosol vertical profile, Atmos. Meas. Tech., 12, 1–21, https://doi.org/10.5194/amt-12-1-2019, 2019.

Jimenez, C., Ansmann, A., Engelmann, R., Donovan, D., Malinka, A., Schmidt, J., Seifert, P., and Wandinger, U.: The dual-field-of-view polarization lidar technique: a new concept in monitoring aerosol effects in liquid-water clouds – theoretical framework, Atmos. Chem. Phys., 20, 15247–15263, https://doi.org/10.5194/acp-20-15247-2020, 2020.

Mamouri, R.-E. and Ansmann, A.: Potential of polarization lidar to provide profiles of CCN- and INP-relevant aerosol parameters, Atmos. Chem. Phys., 16, 5905–5931, https://doi.org/10.5194/acp-16-5905-2016, 2016.

Martin, G. M., Johnson, D. W., and Spice, A.: The measurement and parameterization of effective radius of droplets in warm stratocumulus clouds, J. Atmos. Sci., 51, 1823–1842, https://doi.org/10.1175/1520-0469(1994)051<1823:TMAPOE>2.0.CO;2, 1994.

Mattis, I., Tesche, M., Grein, M., Freudenthaler, V., and Müller, D.: Systematic error of lidar profiles caused by a polarization-dependent receiver transmission: quantification and error correction scheme, Appl. Optics, 48, 2741–2751, https://doi.org/10.1364/AO.48.002742, 2009.

McComiskey, A., Feingold, G., Frisch, A. S., Turner, D. D., Miller, M. A., Chiu, J. C., Min, Q., and Ogren, J. A.: An assessment of aerosol-cloud interactions in marine stratus clouds based on surface remote sensing, J. Geophys. Res., 114, D09203, https://doi.org/10.1029/2008JD011006, 2009.

Miles, N., Verlinde, J., Clothiaux, E.: Cloud droplet size distributions in low-level stratiform clouds, J. Atmos. Sci., 57, 295–311, 2000.

Painemal, D. and Zuidema, P.: The first aerosol indirect effect quantified through airborne remote sensing during VOCALS-REx, Atmos. Chem. Phys., 13, 917–931, https://doi.org/10.5194/acp-13-917-2013, 2013.

Pappalardo, G., Amodeo, A., Apituley, A., Comeron, A., Freudenthaler, V., Linné, H., Ansmann, A., Bösenberg, J., D'Amico, G., Mattis, I., Mona, L., Wandinger, U., Amiridis, V., Alados-Arboledas, L., Nicolae, D., and Wiegner, M.: EARLINET: towards an advanced sustainable European aerosol lidar network, Atmos. Meas. Tech., 7, 2389–2409, https://doi.org/10.5194/amt-7-2389-2014, 2014.

PollyNet: PollyNET lidar data base, available at: http://polly.rsd.tropos.de/, last access: 20 April 2020.

Regayre, L. A., Schmale, J., Johnson, J. S., Tatzelt, C., Baccarini, A., Henning, S., Yoshioka, M., Stratmann, F., Gysel-Beer, M., Grosvenor, D. P., and Carslaw, K. S.: The value of remote marine aerosol measurements for constraining radiative forcing uncertainty, Atmos. Chem. Phys., 20, 10063–10072, https://doi.org/10.5194/acp-20-10063-2020, 2020.

Reutter, P., Su, H., Trentmann, J., Simmel, M., Rose, D., Gunthe, S. S., Wernli, H., Andreae, M. O., and Pöschl, U.: Aerosol- and updraft-limited regimes of cloud droplet formation: influence of particle number, size and hygroscopicity on the activation of cloud condensation nuclei (CCN), Atmos. Chem. Phys., 9, 7067–7080, https://doi.org/10.5194/acp-9-7067-2009, 2009.

Revell, L. E., Kremser, S., Hartery, S., Harvey, M., Mulcahy, J. P., Williams, J., Morgenstern, O., McDonald, A. J., Varma, V., Bird, L., and Schuddeboom, A.: The sensitivity of Southern Ocean aerosols and cloud microphysics to sea spray and sulfate aerosol production in the HadGEM3-GA7.1 chemistry–climate model, Atmos. Chem. Phys., 19, 15447–15466, https://doi.org/10.5194/acp-19-15447-2019, 2019.

Rolph, G., Stein, A., and Stunder, B.: Real-time Environmental Applications and Display sYstem: READY, Environ. Modell. Softw., 95, 210–228, https://doi.org/10.1016/j.envsoft.2017.06.025, 2017.

Schmale, J., Baccarini, A., Thurnherr, I., Henning, S., Efraim, A., Regayre, L., Bolas, C., Hartmann, M., Welti, A., Lehtipalo, K., Aemisegger, F., Tatzelt, C., Landwehr, S., Modini, R. L., Tummon, F., Johnson, J. S., Harris, N., Schnaiter,M., Toffoli, A., Derkani, M., Bukowiecki, N., Stratmann, F., Dommen, J., Baltensperger, U., Wernli, H., Rosenfeld, D., Gysel-Beer, M. and Carslaw, K. S.: Overview of the Antarctic Circumnavigation Expedition: Study of Preindustrial-like Aerosols and Their Climate Effects (ACE-SPACE), B. Am. Meteorol. Soc., 100, 2260–2283, https://doi.org/10.1175/BAMS-D-18-0187.1, 2019

Schmidt, J., Wandinger, U., and Malinka, A.: Dual-field-of-view Raman lidar measurements for the retrieval of cloud microphysical properties, Appl. Optics 52, 2235–2247, https://doi.org/10.1364/AO.52.002235, 2013.

Schmidt, J., Ansmann, A., Bühl, J., Baars, H., Wandinger, U., Müller, D., and Malinka, A. V.: Dual-FOV Raman and Doppler lidar studies of aerosol-cloud interactions: simultaneous profiling of aerosols, warm-cloud properties, and vertical wind, J. Geophys. Res., 119, 5512–5527, https://doi.org/10.1002/2013JD020424, 2014.

Schmidt, J., Ansmann, A., Bühl, J., and Wandinger, U.: Strong aerosol–cloud interaction in altocumulus during updraft periods: lidar observations over central Europe, Atmos. Chem. Phys., 15, 10687–10700, https://doi.org/10.5194/acp-15-10687-2015, 2015.

Shinozuka, Y., Clarke, A. D., Nenes, A., Jefferson, A., Wood, R., McNaughton, C. S., Ström, J., Tunved, P., Redemann, J., Thornhill, K. L., Moore, R. H., Lathem, T. L., Lin, J. J., and Yoon, Y. J.: The relationship between cloud condensation nuclei (CCN) concentration and light extinction of dried particles: indications of underlying aerosol processes and implications for satellite-based CCN estimates, Atmos. Chem. Phys., 15, 7585–7604, https://doi.org/10.5194/acp-15-7585-2015, 2015.

Skupin, A., Ansmann, A., Engelmann, R., Seifert, P., and Müller, T.: Four-year long-path monitoring of ambient aerosol extinction at a central European urban site: dependence on relative humidity, Atmos. Chem. Phys., 16, 1863–1876, https://doi.org/10.5194/acp-16-1863-2016, 2016.

Stein, A. F., Draxler, R. R, Rolph, G. D., Stunder, B. J. B., Cohen, M. D., and Ngan, F.: NOAA's HYSPLIT atmospheric transport and dispersion modeling system, B. Am. Meteorol. Soc., 96, 2059–2077, https://doi.org/10.1175/BAMS-D-14-00110.1, 2015

Zheng, X., Albrecht, B., Jonsson, H. H., Khelif, D., Feingold, G., Minnis, P., Ayers, K., Chuang, P., Donaher, S., Rossiter, D., Ghate, V., Ruiz-Plancarte, J., and Sun-Mack, S.: Observations of the boundary layer, cloud, and aerosol variability in the southeast Pacific near-coastal marine stratocumulus during VOCALS-REx, Atmos. Chem. Phys., 11, 9943–9959, https://doi.org/10.5194/acp-11-9943-2011, 2011.

Chapter 5

Discussion and further applications – Long-term observations of aerosol-cloud interaction

Motivated by the questions raised in Chapter 2, in the cumulative part, several developments based on lidar to unambiguously assess cloud and aerosol properties were introduced and tested. Emphasis was put onto the technical aspects to assure the quality of the products and the replicability in standard lidar systems. The potential of the technique to study ACI in liquid clouds and the importance of considering vertical wind was illuminated in a case study [Jimenez et al., 2020b]. The focus of this Chapter 5 is to answer the last three research questions: How different are the aerosol and cloud conditions in different regions of the planet when tackled with the same approach? How does the temporal scale affect the assessment of the efficiency index $E_{\mathrm{aci}}^{N_{\mathrm{d}}}$? And how relevant are these results for estimations of the Twomey effect?

To deal with these questions, this chapter provides a preliminary analysis of the measurement campaign DACAPO-PESO in Punta Arenas, Chile (2019) and also the first results obtained with the DFOV Polly system located in Dushanbe, Tajikistan (June 2019–January 2020). To further discuss the potential of the new approach, a measurement case from the RV Polarstern close to the North Pole is presented. All three lidar systems were upgraded into DFOV polarization lidars right before the respective campaigns.

The reason to choose those locations lies in their contrasting environments. Punta Arenas (PA) is located at the southernmost tip of South America. Here, westerly winds prevail, being strong during the whole year, especially during the summer. Surrounded by the Pacific and Atlantic Oceans, daily and seasonal variations of the weather in PA are weak, and as one of the cleanest locations on the planet, PA is considered as a reference for pre-industrial aerosol conditions in climate studies [Carslaw et al., 2017; Hamilton et al., 2014]. Despite the low aerosol concentrations, the Southern Ocean region is known for its perpetual high cloud fraction (about 60% for low clouds) [Haynes et al., 2011].

On the other hand, Dushanbe is a hot spot for aerosol research. Pollution and mineral

dust are important components in the environmental and atmospheric system in this region, which belongs to the northern hemispheric dust belt extending from the Sahara in northern Africa to the Taklamakan and Gobi deserts in China [Hofer et al., 2020a]. Contrary to PA, concentrations of aerosol particles are high, but the dry continental environment makes clouds scarce, with cloud fractions of about 10–20% [Jin et al., 2009].

5.1 Observations on cloud scale

As mentioned in Chapter 2, to improve the representation of cloud processes, in awareness of aerosol-cloud interactions, there is a need of closure studies in which models can be confronted with reliable measurements [Rosenfeld et al., 2014b]. Such measurement scenes can be provided with the DFOV-Depol approach currently available in several instruments operated by TROPOS.

By means of the DFOV-Depol approach, explained in Sect. 4.2, the optical and microphysical properties of the lowest part of liquid-cloud layers can be obtained. The provided products are the profiles of extinction coefficient (α), effective radius (R_e), liquid-water content (w_l), and droplet number concentration (N_d) from the cloud base (z_bot) to 75 meters above z_bot. Via the methodology presented in Appendix A, the aerosol products that can be obtained are the backscattering and extinction coefficients as profiles from 500 m above ground to the cloud base z_bot. Below 500 m, uncertainties due to overlap correction make the retrieval highly uncertain. A mean value of the extinction coefficient from 500 m to 300 m below z_bot is computed, and it is used to estimate the CCN concentration (N_CCN) [Mamouri and Ansmann, 2016]. Above ($z_\mathrm{bot} - 300$ m), the parameterization may overestimate N_CCN due to the hygroscopic growth of particles at high relative humidities, usually >80% as seen in the cloudy cases analyzed, including the cases reported in Jimenez et al. [2020b]. At the PA station, vertical-wind measurements with two-second resolution, obtained with a commercial Doppler lidar Halo Streamline, are also available.

Case 1: Punta Arenas

Fig. 5.1 shows two cloud measurements at PA on 13 and 16 December 2018. HYSPLIT backward trajectories [Stein et al., 2015; HYSPLIT, 2020] indicated an airflow out of the Pacific Ocean, from the west on the first day and from the southwest on the second day. Thus, pure marine conditions are assumed for the aerosol retrieval and for the estimations of N_CCN.

The liquid-cloud layers were detected at about 1.8 and 1.4 km height for the 13 and 16 December, respectively. GDAS relative humidity (RH) values ranged from 45–80% (at 500–1500 m height) on the 13 December and from 50–80% (at 500–1100 m height) on the 16 December [GDAS, 2020].

The retrieval was performed at 3-min resolution, and the time series of the products are presented in Fig. 5.1. The left panels show the results for the 13 December 2018 and the right panels the results from three days later, the 16 December. Panel (c) shows the indication

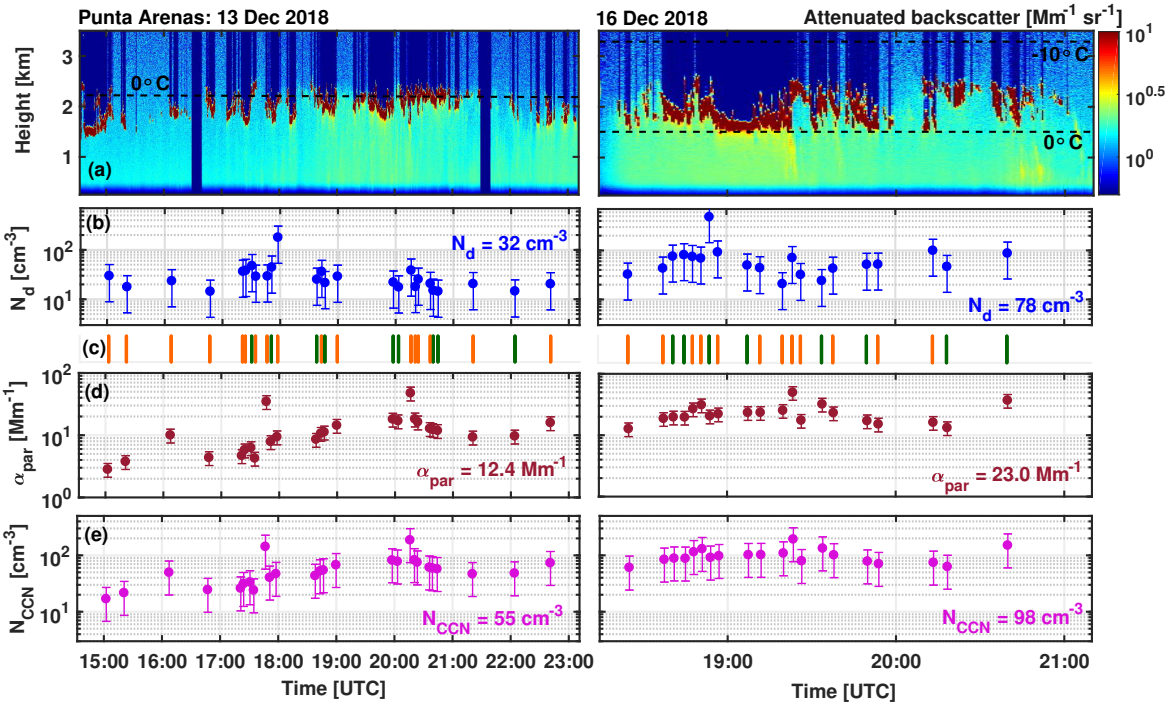

Figure 5.1: (a) Lidar attenuated backscatter of the convective cloud-topped planetary boundary layer in the afternoon and evening of the summer days of 13 December (left) and 16 December 2018 (right), (b) cloud droplet number concentration N_d for the height of $z_\mathrm{ref} = z_\mathrm{bot} + 75$ m within the stratocumulus layer shown in (a), (c) vertical-wind indicator (orange: updraft, green: downdraft), (d) particle extinction coefficient α_par (mean value for the height range from 500 m to 300 m below cloud base), and (e) CCN concentration N_CCN obtained from the extinction coefficient in (d). Temporal resolution is three minutes. Error bars indicate the uncertainty range. The mean value of each panel is written as number.

for updraft or downdraft movements for each 3-min period. On both days, updraft periods prevailed and make this case ideal to study the activation of droplets and the relation with the aerosol situation during the observation. The notorious correlation over time between the cloud and aerosol properties, considering both periods, corroborates this statement.

As one may expect for this pristine location, the droplet concentration (Fig. 5.1b) and aerosol extinction coefficient (Fig. 5.1d) generally take low values. Between the two days clear differences can be noted. The 12 Mm^{-1} of aerosol extinction almost doubled three days later. This change yielded an increase in the droplet number concentration from about 32 cm^{-3} to 78 cm^{-3}.

The conversion of particle extinction into N_CCN was done with the following parameterization:

$$N_\mathrm{CCN} = f_\mathrm{ss} n_{50}, \tag{5.1}$$

with n_{50} the number concentration of particles with size above 50 nm at dry conditions. This value is given by:

$$n_{50} = c_\mathrm{m} \alpha_\mathrm{par}^{\chi}. \tag{5.2}$$

For pure marine aerosol conditions, the values $c_{\mathrm{m}} = 7$ and $\chi = 0.85$ provided by Mamouri and Ansmann [2016] were used. In such pure marine conditions, all particles larger than 50 nm can activate when reaching a maximum supersaturation of 0.2%, as concluded by Mamouri and Ansmann [2016]. At higher supersaturation, even smaller particles can reach the critical size and activate. To adjust the parameterization to other supersaturation levels an enhancement factor f_{ss} is employed. This parameterization holds for an ambient RH of 70–80%.

The N_{CCN} values obtained with Eq. (5.1), and shown in Fig. 5.1(d), are a bit larger than the actual N_{d} values obtained with the DFOV-Depol approach. The ratio $N_{\mathrm{d}}/N_{\mathrm{CCN}}$ was about 0.74 and 0.83 for the 13 and 16 December, respectively. From this result, we can conclude that the mean maximum water supersaturation was about 0.15–0.2% [Mamouri and Ansmann, 2016].

The final product obtained for this scene is the N_{d}–N_{CCN} efficiency index $E_{\mathrm{aci}}^{N_{\mathrm{d}}}$, defined in Eq. (2.6). A value of 0.52 was obtained, and in terms of α_{par} an $E_{\mathrm{aci}}^{N_{\mathrm{d}},\alpha_{\mathrm{par}}} = 0.44$ was obtained. This clear cloud-aerosol correlation and the large ratio $N_{\mathrm{d}}/N_{\mathrm{CCN}}$ suggest that an aerosol-limited regime [Reutter et al., 2009] might govern cloud formation in this case at PA, i.e., maximum supersaturations are high and the low CCN concentrations makes a 1:1 correlation more likely. However, caution needs always be exercised when analyzing such aerosol-cloud scenes because, besides droplet activation, other processes such as entrainment, collision/coalescence or evaporation of droplets can play a role. This measurement case could provide the observational scene to evaluate cloud-resolving models, such as the Aerosol Cloud Precipitation Interaction Model [Connolly et al., 2012], which has been recently used as reference to evaluate the parameterizations being currently used in climate models [Simpson et al., 2014].

Case 2: Dushanbe

A measurement case to illuminate the contrasting situation in Dushanbe (DB), with respect to PA, is shown in Fig. 5.2. The lidar registered an altocumulus layer at the top of the PBL at 4 km height, which extended over 8 hours from the evening of the 15 September 2019 to the morning of the next day. The situation here is quite different compared to PA. Large droplet concentrations (shown in Fig. 5.2b) of about 213 cm^{-3} are in agreement with the large particle extinction values observed, shown in panel (a) as attenuated backscatter [Baars et al., 2017], in (c) as mean extinction coefficient, and in panel (d) as CCN concentration estimate.

Additionally, using the particle depolarization, dust and non-dust contributions to the total aerosol extinction were separated according to Tesche et al. [2009]. For this case, the ratio of extinction values between dust and non-dust particles $\alpha_{\mathrm{par,non\text{-}dust}}/\alpha_{\mathrm{par,dust}}$ was about 1/9.

In the case of dust particles, which are much less hygroscopic than marine particles, only particles with radius larger than about 100 nm can become droplets after water-vapor condensation when reaching a supersaturation of 0.2%. In the case of non-dust particles,

here assumed as anthropogenic, 50 nm is the size from which particles can reach activation, as concluded by Mamouri and Ansmann [2016]. At those continental conditions, the N_{CCN} parameterization holds for RH of 50–70%.

During the measurement period, GDAS RH values remained almost constant with time and height, at about 65% from the ground up to 3 km [GDAS, 2020]. Under these ambient humidity conditions, the CCN concentration of dust and non-dust particles can be computed according to Mamouri and Ansmann [2016] by using the conversion factors for typical aerosol conditions in Tajikistan, provided by long-term observations in Hofer et al. [2020a].

As shown in Fig. 5.2(c), non-dust particles represent about 10% of the total extinction. As dust particles are not very efficient as CCN, more than half of the total N_{CCN} comes from non-dust particles as shown in Fig. 5.2(d). On average, a total amount of N_{CCN}= 418 cm^{-3} was obtained. With a median N_d of 213 droplets per cm^3, a ratio N_d/N_{CCN} of 0.5 was obtained. This low ratio suggests that the supersaturation level was actually around 0.1% instead of 0.2% as assumed in the parameterization.

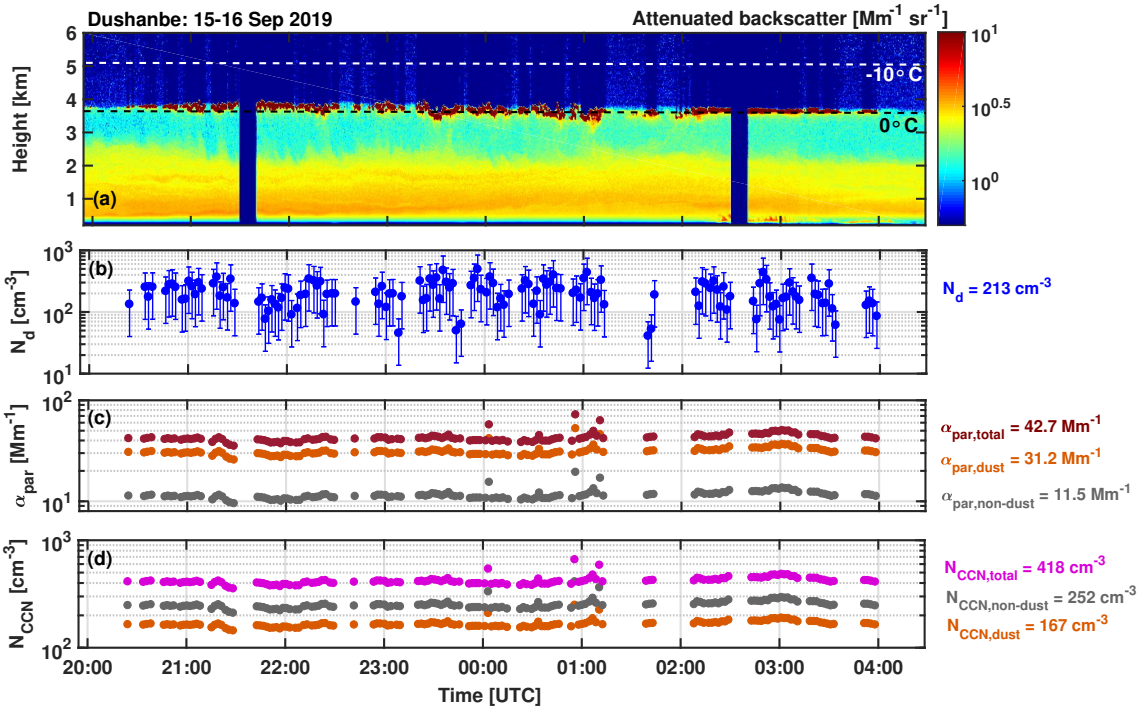

Figure 5.2: (a) Lidar attenuated backscatter of the stratocumulus-topped planetary boundary layer during the evening/night of the 15 and 16 September 2019, (b) cloud droplet number concentration N_d for the height of $z_{ref} = z_{bot} + 75$ m within the stratocumulus layer shown in (a), (c) particle extinction coefficient α_{par} (mean value for the height range from 300 to 1000 m below cloud base). Here, the contributions of dust and non-dust have been separated using the particle depolarization ratio (according to Tesche et al. [2009]). (d) CCN concentration N_{CCN} obtained from the extinction coefficient and the dust and non-dust fractions, shown in (c), by using the conversion parameters provided by Mamouri and Ansmann [2016]. Temporal resolution is three minutes. Error bars indicate the uncertainty range.

Regarding the index $E_{\mathrm{aci}}^{N_{\mathrm{d}}}$, no clear correlation between N_{CCN} and N_{d} can be noted for this case. In the dry region of DB, where many particles compete for the little amount of available water vapor, low correlation in the short temporal scales can be expected.

According to the criteria proposed by Reutter et al. [2009], cloud formation can be considered here as an updraft-limited regime, in which particle and cloud droplet number concentrations are weakly correlated and the updraft velocity plays a major role in the activation of droplets. Maximum supersaturation of about 0.2% can be hardly reached, which explains the low number of droplets compared to the number of available aerosol particles. Such as for PA, vertical-wind measurements might be important as well.

Case 3: High Arctic

As an outlook and to further explore the potential of the DFOV-Depol approach, a third case of a mixed-phase cloud is briefly described in this section. The measurements were conducted on board the RV Polarstern during the 1-year measurement campaign MOSAiC (Multidisciplinary drifting Observatory for the Study of Arctic Climate, `https://mosaicexpedition.org/`), the largest Arctic campaign in history. The rapid sea ice loss, unusual warming, and our incomplete knowledge about the complex processes controlling the Arctic motivated this big collective effort [Engelmann et al., 2020]. Multi-layer and mixed-phase clouds dominate the scene in this region [Griesche et al., 2020]. Due to the difficulties to measure in the polar region and the poorly understood web of processes and feedbacks involved, the radiative effect of arctic clouds remains highly uncertain [Morrison et al., 2011].

The DFOV-Depol approach was initially developed to analyze pure liquid layers in which depolarization is entirely produced by multiple scattering. In mixed-phase clouds, such as the layer shown in Fig. 5.3, ice virga at the bottom of the cloud can produce strong depolarization of light, buffering the multiple-scattering effect on light depolarization. At the top of the cloud, however, a well-defined supercooled liquid layer can be noted, and here the scattering increases abruptly. The strong backscattering at droplets, about two orders of magnitude higher than for ice, reduces the ice contribution to negligible levels, so that depolarization due to multiple scattering can be properly observed (Fig. 5.3b). After careful determination of the cloud base, using both signal and depolarization, the retrieval of the liquid-cloud microphysical properties is possible. On panels (c) and (d) of Fig. 5.3, the obtained cloud droplet number concentration and effective radius at 75 meters above the liquid-cloud base are displayed.

The relevant feature in this case is the strong reduction of droplet size and increase of droplet number after 8:00 UTC. This change correlates with a strong reduction of ice virga, as can be seen in Fig. 5.3(a) and (b), likely due to the removal of large liquid and ice particles, which enables also the formation of new droplet populations and explains the increase of N_{d}.

As mentioned in Chapter 2, aerosol effects on mixed-phase clouds, such as the glaciation and deactivation effects (explained in Sect. 2.1.2), are poorly understood, and being involved in both effects, supercooled water plays a major role. The DFOV-Depol approach, in com-

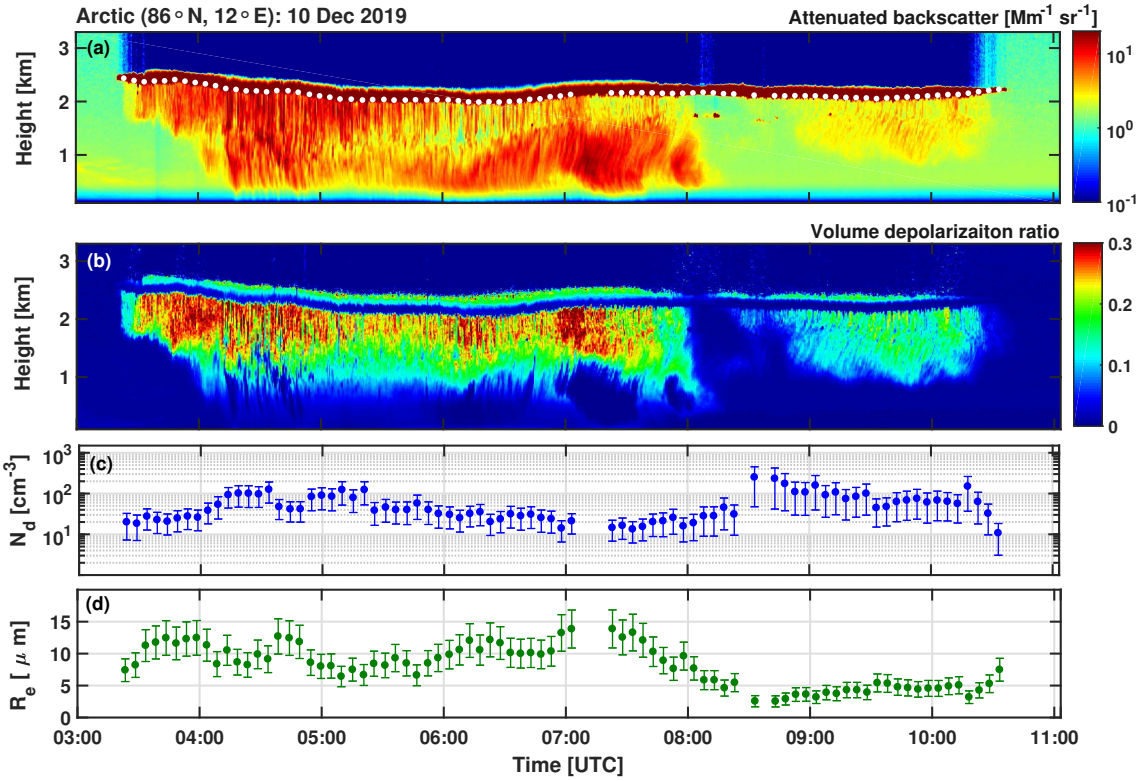

Figure 5.3: (a) Lidar attenuated backscatter for a mixed-phase cloud observed on 10 December 2019, (b) volume depolarization ratio of the same period, (c) cloud droplet number concentration, (d) the cloud droplet effective radius 75 meters above z_{bot}.

bination with radar-based methods, can contribute to respective investigations by providing a full picture of mixed-phase clouds, in both its liquid and ice phases. Such research is out of the scope of this work, but an open door remains for future studies by means of new technique developed in the framework of this thesis.

5.2 Long-term results

In the previous section, research possibilities based on three example cloud cases were presented. Contrasting properties at PA and DB could be seen in those cases, which respond partially to the sixth research questions regarding the situation in both regions in terms of aerosol and liquid-water-cloud properties. Despite in-situ and spaceborne observations are available in the literature, a long-term data set with collocated observations of aerosol and cloud properties does not exist. This section provides an overview of the results obtained at the two locations.

One year of observations at PA and eight months at DB are summarized in Table 5.1 and in Fig. 5.4 and 5.5. The contrast seen in the case studies is more pronounced in the long-term observations. Larger effective radii and smaller extinction coefficients were observed at

PA, which is then reflected in low droplet number concentrations with a mean of 97 cm^{-3} and median of 56 cm^{-3}. The median is provided as a more representative value, as it smoothes out the effect of large and uncertain values in the case of N_d and N_{CCN}. The observations of N_d are in agreement with the slightly larger N_{CCN} estimations (with mean and median of 96 and 59 cm^{-3} respectively). The ratio N_d/N_{CCN} is about 1, indicating that 0.2% supersaturation can be easily reached for the Southern Ocean conditions with strong winds and a vast moisture source. At DB, the number concentrations of CCN are about one order of magnitude larger than at PA. The droplet number concentrations are, however, only about about four times larger. A ratio N_d/N_{CCN} of about one third was observed here, corroborating the finding that in a polluted ambience, a large amount of particles can activate into droplets, but even more remain unactivated, as shown in Sect. 5.1 (case 2).

Table 5.1: Mean values of cloud and aerosol properties at both locations. For number concentrations the median was computed as well and written in brackets (). 304 hours of observations are considered for PA and 266 hours for DB.

Products	Units	Punta Arenas		Dushanbe	
		Mean	SD	Mean	SD
Liquid-cloud products					
$\overline{z}_{bot}$	[km]	2.12	1.5	3.35	1.5
$\overline{\alpha}$	[km^{-1}]	14.8	4.2	19.6	6.4
$\overline{R}_e$	[μm]	7.3	3.2	4.9	1.98
$\overline{w}_l$	[gm^{-2}]	0.071	0.038	0.062	0.029
$\overline{N}_d$	[cm^{-3}]	97 (56)	112	292 (196)	305
Below-cloud aerosol products					
$\overline{\alpha}_{par}$	[km^{-1}]	23.5	27.1	101.3	71.5
$\overline{N}_{ccn}$	[cm^{-3}]	96 (59)	102	872 (743)	534

5.2.1 Comparison of DFOV-Depol products with available estimations and observations

The values obtained with the new lidar approach are in agreement with modeling and observational results. Revell et al. [2019], based on spaceborne observations [Grosvenor et al., 2018], reported N_d values for the Southern Ocean in the range of 20–100 cm^{-3} and values of 25–60 cm^{-3} obtained from the chemistry-climate model HadGEM3-GA7.1 [Walters et al., 2019]. Satellite observations of N_d provide on average similar values in the range of 50–160 cm^{-3} for PA and 200–300 for DB [Quaas et al., 2006; Li et al., 2018]. Based on the ECHAM5/MESSy Atmospheric Chemistry (EMAC) model [Jöckel et al., 2006], Karydis et al. [2017] obtained annual droplet concentrations between 10–100 cm^{-3} for the region of PA and values in the range of 600–1500 cm^{-3} for the Central Asian desert area.

Regarding the concentrations of CCN, the same study of Karydis et al. [2017] reported values in the range 0–200 cm^{-3} for PA and 1000–4000 cm^{-3} for DB, and maximum supersatu-

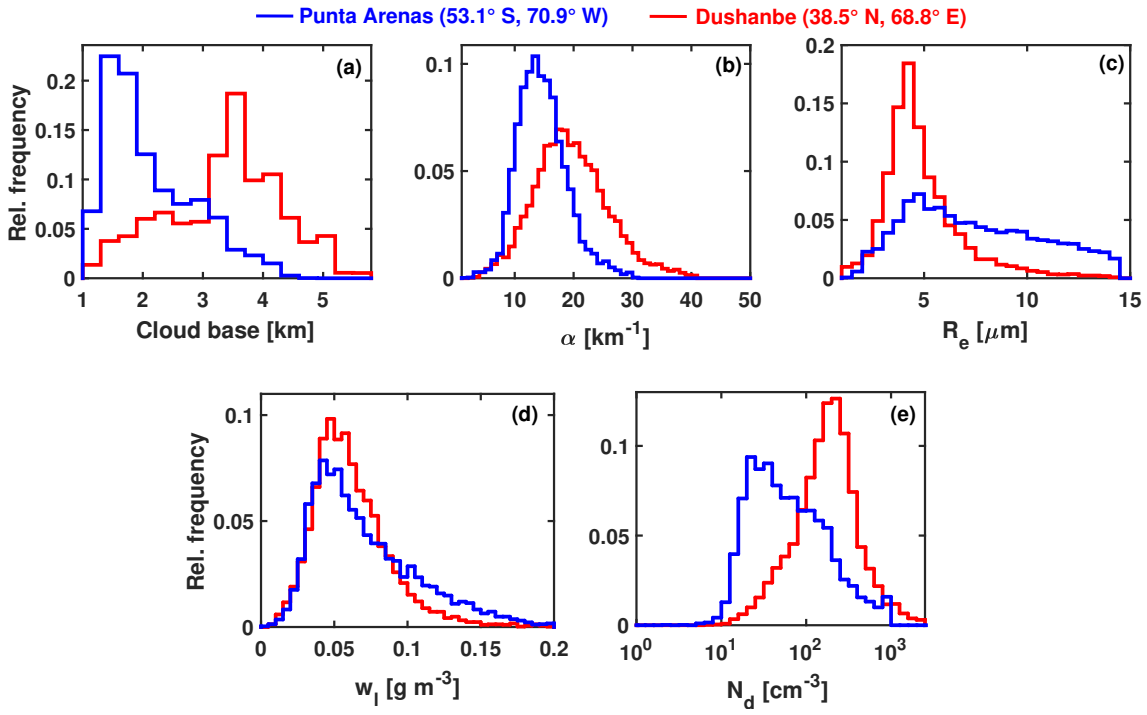

Figure 5.4: Histograms of the cloud microphysical properties obtained with the DFOV-Depol technique at PA (blue) and at DB (red). From (a) to (e) the properties presented are respectively: cloud base height, cloud extinction coefficient, effective radius, liquid-water content , and droplet number concentration (all at 75 m above z_{bot}).

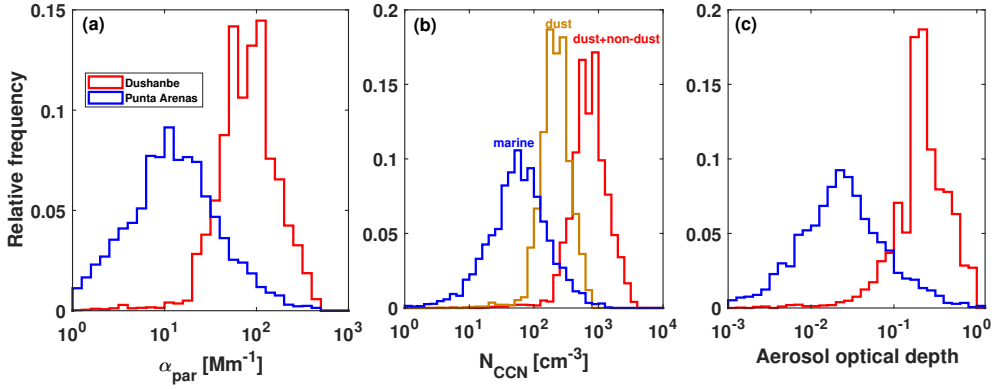

Figure 5.5: Histograms of the aerosol properties obtained for PA (blue) and for DB (red). (a) Mean extinction coefficient below cloud base, (b) CCN concentration. For DB the CCN concentration was separated into dust (yellow) and non-dust. Panel (c) presents the aerosol optical depth from the surface to the cloud base.

ration (ss) at the lowest cloud-forming level of 0.5% for PA and 0.05–0.1% for DB. Westervelt et al. [2014], based on the GEOS-Chem model [Bey et al., 2001], derived CCN concentrations in the range of 50–100 cm^{-3} at 0.2% (ss) for PA and values of 100–200 cm^{-3} at 1% (ss). For DB the values found are in the range of 300–1000 cm^{-3} at 0.2% supersaturation and 1000–3000 cm^{-3} at 1% (ss). In-situ shipborne observations around the Antarctic continent showed that the CCN values in the Southern Ocean are in the range of 50–200 cm^{-3} at 0.2% (ss) [Regayre et al., 2020], which is also in agreement with results of the observations performed by Zheng et al. [2011] and Painemal and Zuidema [2013].

In general, there is agreement between our value ranges and other observational and modeling results. It seems there is a little underestimation of the CCN concentrations at PA and an overestimation at DB in models. Our results offer a constraint opportunity for models dealing with aerosol and clouds in the analyzed regions.

5.3 Assessment of $E_{\mathrm{aci}}^{N_{\mathrm{d}}}$

As shown in Chapter 2, there is a variety of approaches to empirically assess $E_{\mathrm{aci}}^{N_{\mathrm{d}}}$, either using remote-sensing and in-situ, only in-situ, or satellite observations. The reported $E_{\mathrm{aci}}^{N_{\mathrm{d}}}$ values cover the whole range of possible results, but clear tendencies can be seen among the platforms used (see Fig. 2.1). One important reason , which likely explains those differences among the platforms, ignoring systematical issues as explained in Chapter 2, lies in the observational scale of aerosol and clouds.

According to McComiskey and Feingold [2012], differences between process and analysis scales may incur biases in quantification of $E_{\mathrm{aci}}^{N_{\mathrm{d}}}$ and therefore of the albedo effect. Combined ground-based remote-sensing and in-situ observations cover scales from 20 s to 1 hour, airborne in-situ approaches stretch over temporal scales of 10–60 minutes and spatial scales from 12–30 km, and satellite estimates cover spatial scales of 0.5°–4° and either daily, seasonal, or annual scales, as summarized in McComiskey and Feingold [2012].

With our ground-based lidar instruments, we can observe one spot over time. The aerosol/cloud products have a temporal resolution of 3 min. With the long-term continuous flow of observations, we have the possibility to evaluate the efficiency index $E_{\mathrm{aci}}^{N_{\mathrm{d}}}$ at several temporal scales and can thus answer the seventh research question about how the considered scale affects the derived cloud-aerosol relationships. One year of measurements at PA (2019) and eight months, from June 2019 to January 2020, at DB were considered for the assessment of $E_{\mathrm{aci}}^{N_{\mathrm{d}}}$. All clouds with a duration of less than one hour were filtered out. Only strato- and altocumulus layers were considered. In total, 218 single liquid-water clouds remained for the analysis for PA and 72 for DB.

The first evaluation approach consists of finding $E_{\mathrm{aci}}^{N_{\mathrm{d}}}$ via a log-log regression of the 3-min-resolution products in single clouds. Additionally, by using the vertical velocity provided by the Doppler lidar in the case of PA, updraft and downdraft periods were selected and $E_{\mathrm{aci}}^{N_{\mathrm{d}}}$ was also computed for each cloud layer.

A large spread of $E_{\mathrm{aci}}^{N_{\mathrm{d}}}$ was found at this scale when considering all clouds. Cases with a clear correlation between aerosol and cloud properties, such as the 13 and 16 of December

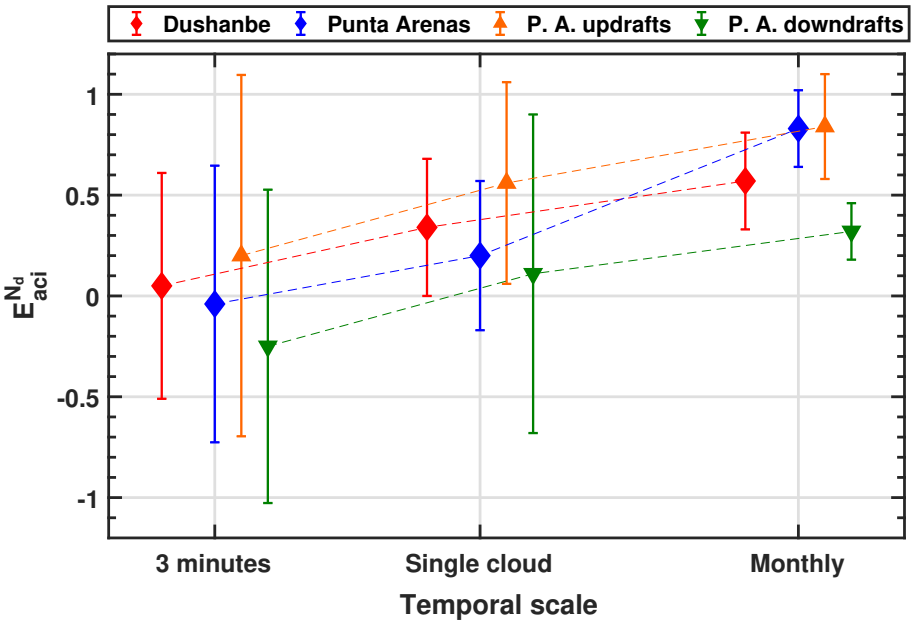

Figure 5.6: $E_{\mathrm{aci}}^{N_{\mathrm{d}}}$ values obtained at different temporal resolutions. Punta Arenas with no wind consideration is plotted in blue, only for updrafts in orange and only for downdrafts in green.

presented in Sect. 5.1 and the 23 of February 2019 presented in Jimenez et al. [2020b], in which aerosol properties vary on the scale of cloud microphysics, i.e, some minutes, are rather scarce. In the Troposphere, significant variations of aerosol properties likely occur at a horizontal scale of 40–400 km or temporal scales of 2–48 h [Anderson et al., 2003]. Thus, finding individual scenes in which aerosol-cloud interaction can be observed is a difficult task. As shown in Fig. 5.6, mean $E_{\mathrm{aci}}^{N_{\mathrm{d}}}$ values of -0.04 ± 0.7 and 0.05 ± 0.6 were obtained for the clouds at PA and DB respectively. When considering only updraft periods, a slightly larger mean $E_{\mathrm{aci}}^{N_{\mathrm{d}}}$ value of 0.2 ± 0.9 was found for PA. These results suggest that caution needs to be exercised when evaluating ACI in high-resolution observations of single clouds. $E_{\mathrm{aci}}^{N_{\mathrm{d}}}$ values of 0.45–0.8 were found in selected updraft-dominated cases at PA.

A more attractive scale to estimate the index $E_{\mathrm{aci}}^{N_{\mathrm{d}}}$ is to take the mean values for each single cloud as individual points and evaluate Eq. (2.6) on a monthly basis. At this scale, a mean $E_{\mathrm{aci}}^{N_{\mathrm{d}}}$ value of 0.35 ± 0.3 was obtained for DB and a value of 0.2 ± 0.35 for PA, both with no consideration of vertical wind. A remarkable feature here is the stronger correlation at DB than at PA. When considering only clouds in which updrafts prevailed, the susceptibility index at PA increased to about 0.56 ± 0.5. This feature corroborates the need to consider wind information to derive aerosol-cloud relationships in an aerosol- and updraft-sensitive regime [Reutter et al., 2009], which is likely the regime governing cloud formation at PA and in the Southern Ocean. No correlation between N_{d} and N_{CCN} with the ambient relative humidity was found at the studied locations.

The most accurate value of the ACI index was obtained when considering monthly averages over the whole period, 8 months at DB and 1 year at PA, as shown in the right side of

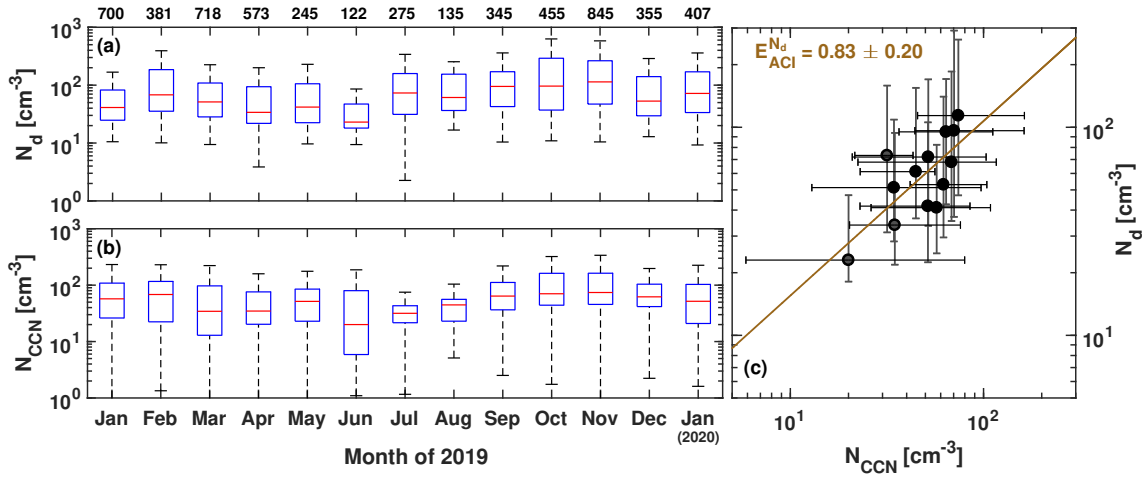

Figure 5.7: Box plot of the monthly statistical results for (a) the cloud droplet number concentration and (b) CCN concentration at Punta Arenas. The boxes represent the first and third quantiles, the red line the median, and the error bars the maximum and minimum values for each month. The number of points for each month is displayed on the top of panel (a). Panel (c) shows a scatter plot with the monthly median values and the log-log regression to determine $E^{N_d}_{aci}$.

Fig. 5.6. The monthly results are summarized in Fig. 5.7 and 5.8 by using box plots for both locations. Log-log regressions were applied to the median values as shown in panel (c). $E^{N_d}_{aci}$ values of 0.83 ± 0.20 and 0.57 ± 0.26 were obtained for PA and DB, respectively, suggesting that this scale is the most suitable one to quantify $E^{N_d}_{aci}$. Additionally, values of 0.84 ± 0.26 and 0.32 ± 0.14 were obtained when considering either only updraft or only downdraft periods, respectively (at PA). These N_d–N_{CCN} relationships are one of the most relevant results of this thesis, as they can provide an accurate constraint for $\frac{\partial_{\ln} N_d}{\partial_{\ln} N_{CCN}}$ to evaluate Eq. (2.5) for observation-based estimations of the radiative effect of aerosol via aerosol-cloud interactions.

$E^{N_d}_{aci}$ values at seasonal and annual scales can in principle be assessed by means of the DFOV-Depol approach, but the current data sets are still too small to explore aerosol-cloud interactions at these scales. Such investigations are a potential topic for future works.

5.4 Relevance of $E^{N_d}_{aci}$ for the radiative effect

To get an idea of the impact of our results on the instantaneous cloud-mediated aerosol radiative effect, i.e., the Twomey effect [Twomey, 1959, 1977], this section aims to estimate the change of cloud albedo at both locations, PA and DB. Eqs. (2.1)–(2.5) described in Section 2.2 are employed. By ignoring the so-called adjustments related to changes in cloud fraction f_c and liquid-water path L_w, Eq. (2.1) takes the form:

$$F^{\text{Twomey}}_{aci} = -\frac{1}{3} f_c A_c (1 - A_c) E^{N_d,\text{Twomey}}_{aci} F^{\downarrow} \Delta \ln N_{CCN}. \tag{5.3}$$

Here, information about the cloud albedo and cloud fraction is needed, and such data can be provided from satellite observations. For this purpose, monthly means from the second

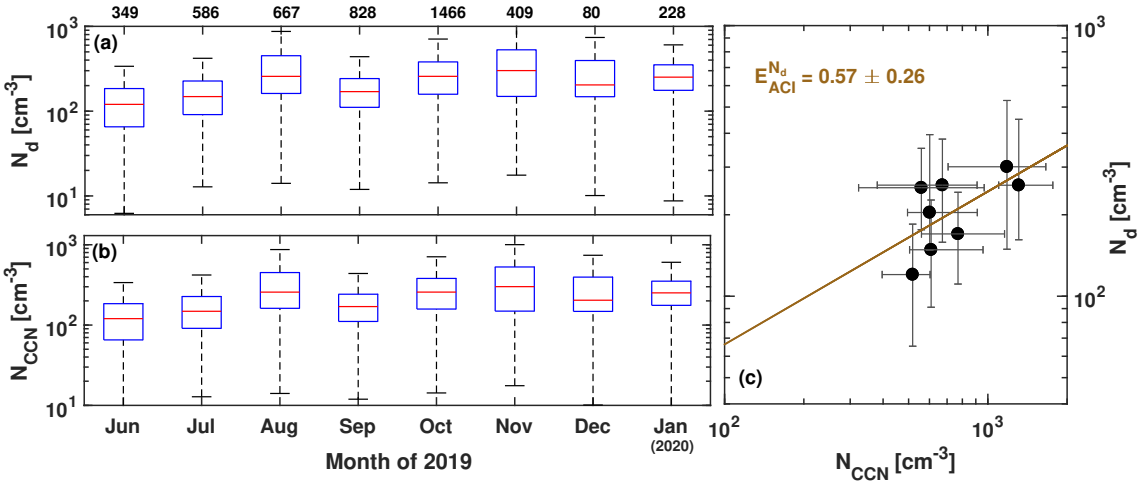

Figure 5.8: Same as Fig. 5.7, but for Dushanbe.

Modern-Era Reanalysis for Research and Applications (MERRA-2) [Gelaro et al., 2017] were collected and, in order to extract representative data at both locations, 12.5° in longitude and 8° in latitude (10 × 8 grid points) were averaged. An annual mean of the cloud albedo of 0.58 for PA and 0.46 for DB, a liquid-cloud fraction of 0.22 for PA and 0.07 for DB, and a down-welling shortwave radiance at the top of the atmosphere of 300 and 322 Wm^{-2} were respectively obtained for PA and DB. These values were considered for the evaluation of Eq. (5.3). The most accurate $E^{N_\mathrm{d}}_\mathrm{aci}$ values for PA and DB shown in the previous section are used for these calculations, i.e., 0.83 ± 0.20 and 0.57 ± 0.26, respectively.

However, these $E^{N_\mathrm{d}}_\mathrm{aci}$ values were obtained from measurements of the lowest 75–100 meters in liquid-water clouds, which is where the Twomey effect originates. During the upward transport of the aerosol-affected cloud parcels, these are exposed to a number of other processes diminishing the overall influence of aerosol on droplet number concentration. According to the investigations of Schmidt [2014], most of instantaneous ACI occur in the first 100 meters. To provide realistic calculations, a constant $E^{N_\mathrm{d}}_\mathrm{aci}$ in the first 100 meters and a quadratic decreasing one in the next 100 meters is assumed, as shown in Fig. 5.9. Finally, considering a mean extension of liquid layers of 250 meters, a mean of

$$E^{\mathrm{N_d,Twomey}}_\mathrm{aci} \approx \frac{2}{3} E^{N_\mathrm{d}}_\mathrm{aci} \tag{5.4}$$

is obtained. Investigations on this penetration factor of 2/3 could be conducted when measuring cloud layers on a vertical basis from the base to the top. To step towards this direction, one could explore the synergy of lidar, by means of the DFOV-Depol approach, and radar instruments, which can reach larger penetration depths [e.g., Donovan et al., 2001; Frisch et al., 2002].

The remaining factor in Eq. (5.3) is the variation of CCN concentrations to account for the change between pre-industrial and present-day conditions, i.e., $\Delta \ln N_\mathrm{CCN}$. This value

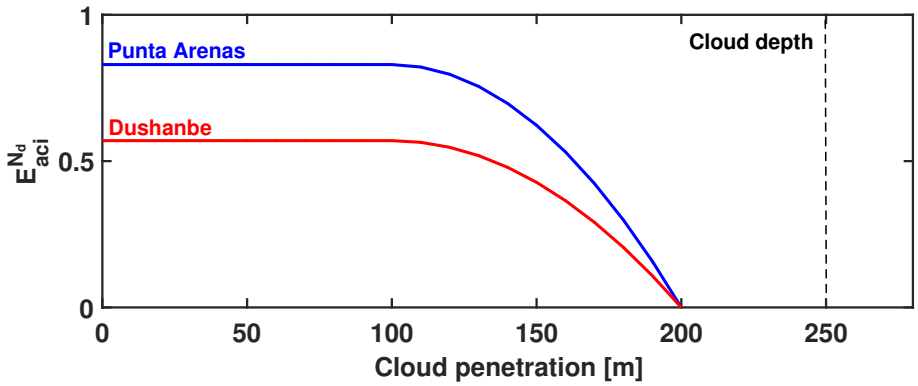

Figure 5.9: Schematic view of the aerosol-cloud-interaction efficiency in dependence of cloud penetration depth.

can be expressed in terms of the anthropogenic fraction f_{anth} as:

$$\Delta \ln N_{\mathrm{CCN}} = -\ln(1 - f_{\mathrm{anth}}), \tag{5.5}$$

with

$$f_{\mathrm{anth}} = \frac{N^{\mathrm{anth}}_{\mathrm{CCN}}}{N^{\mathrm{nat}}_{\mathrm{CCN}} + N^{\mathrm{anth}}_{\mathrm{CCN}}}. \tag{5.6}$$

$N^{\mathrm{nat}}_{\mathrm{CCN}}$ and $N^{\mathrm{anth}}_{\mathrm{CCN}}$ are the natural and anthropogenic contribution to the total CCN, respectively. The anthropogenic fraction f_{anth} is a challenging parameter to determine and it is in fact one of the greatest sources of uncertainty for aerosol radiative effects [Boucher et al., 2013; Rosenfeld et al., 2014b]. For a first estimation of the Twomey effect, average values obtained from models are used.

By considering six different aerosol schemes, Wang and Penner [2009] found values of f_{anth} between 0.05 and 0.15 for PA and between 0.6 and 0.85 for DB. With these values we obtain an anthropogenic radiative forcing due to ACI from -0.70 to -0.17 Wm^{-2} at PA and between -1.89 and -0.66 Wm^{-2} at DB as shown in Fig. 5.10.

These values agree with model estimates of the global mean ACI radiative effect [Myhre et al., 2013; Lohmann and Feichter, 2005], but they are larger in magnitude than those values obtained for the specific locations. Values roughly between –0.5 and 0.0 Wm^{-2} have been reported for PA and between –1.5 and 0.0 Wm^{-2} for DB [Zelinka et al., 2000; Regayre et al., 2018; Wang et al., 2020]. On the other hand, the choice of CCN concentrations as aerosol proxy, instead of aerosol extinction coefficient, is reflected in the radiative-forcing calculations. The $F^{\mathrm{Twomey}}_{\mathrm{aci}}$ values obtained in this work are considerably larger than those obtained when using the AOD as aerosol proxy, e.g., in Quaas et al. [2004] and Quaas et al. [2006], who reported values between –0.5 and –0.2 Wm^{-2}. However, satellite-based estimates can be substantially improved by using the so-called aerosol index (AOD × Ångström exponent) to account for the strong contribution of fine-mode aerosol to CCN concentrations, which is the physical quantity affecting N_{d}. This approach can yield to considerably larger radiative-forcing values as shown by Hasekamp et al. [2019], who found global mean values between -1.72 and -0.84 Wm^{-2}.

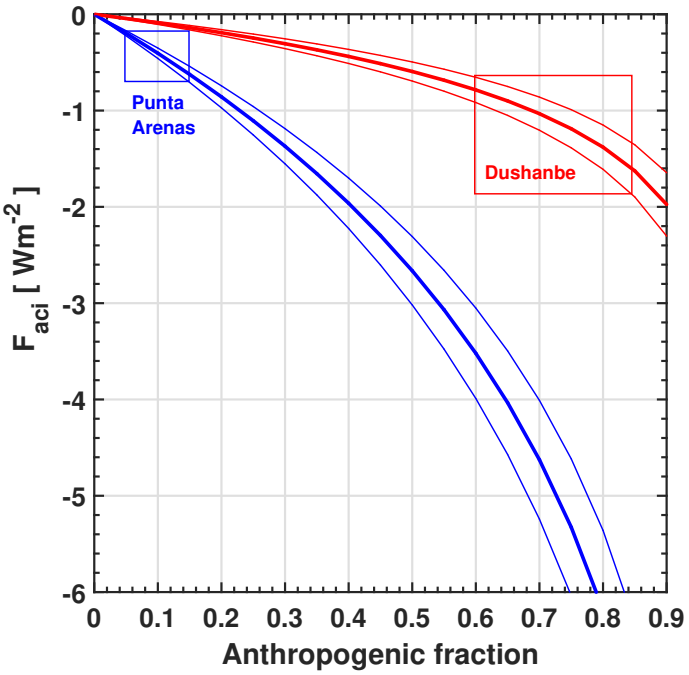

Figure 5.10: Estimated radiative effect for 2019 at the two study locations considering only the Twomey effect. The thin lines indicate the error coming from the assessment of the susceptibility index $E_{\mathrm{aci}}^{N_{\mathrm{d}}}$ and the rectangles the range in which the anthropogenic fraction varies for those regions.

Our results show that the pristine region of PA is specially sensitive to CCN perturbations due to the perpetually large cloud cover and low CCN concentrations. The low anthropogenic fraction of CCN at Punta Arenas and in the Southern Ocean keeps the $F_{\mathrm{aci}}^{\mathrm{Twomey}}$ values small, but increases in the CCN budget, e.g., from increased wildfires driven by climate change, would lead to a much stronger cooling effect. As shown by Ohneiser et al. [2020] and Ansmann et al. [2020], fine-mode particles emitted by recent wildfires in Australia and advected by pyrocumulus clouds can stay from the upper troposphere to 30 km height in the stratosphere over the entirely Southern Ocean for months. Sedimentation of this high-altitude aerosol layer would eventually serve as a CCN source increasing the so-called anthropogenic fraction, or more precisely, the ratio between present-day and pre-industrial CCN concentrations.

In DB the situation is quite different. Although this region is not as sensitive to CCN changes as the region of the Southern Ocean, the large anthropogenic fraction leads to a strong cooling. Looking at this region, the need of considering CCN concentrations, beyond the aerosol extinction, as aerosol proxy is confirmed. Because of the smaller sizes of anthropogenic particles compared to natural aerosol particles, not more than 30% of the extinction coefficient is contributed by anthropogenic particles, but considering the total CCN concentration, 80–90% of the CCN originate from anthropogenic sources, as shown by Hofer et al. [2020a] from long-term measurements at DB. By using the extinction coefficient as aerosol proxy, the values of $F_{\mathrm{aci}}^{\mathrm{Twomey}}$ obtained are between –0.43 and –0.15 Wm^{-2}, i.e., about four

times smaller than when using the CCN concentration as aerosol proxy. In conclusion, a robust separation of the natural and anthropogenic CCN sources is essential and can only be achieved from continuous long-term observations [Hofer et al., 2017, 2020a,b] and with proper conversion factors to retrieve CCN concentrations based on extinction-coefficient values [Mamouri and Ansmann, 2016; Ansmann et al., 2019].

Chapter 6

Summary and outlook

A better understanding of the impact of aerosol particles on cloud properties, relevant for the role of clouds in weather and climate, has been the main motivation of this thesis. The main task was to provide observational, collocated data sets of aerosol and liquid-water clouds under ambient conditions by means of ground-based lidar instruments. Metrics of aerosol-cloud interaction (ACI), such as the so-called ACI efficiency index $E_{\mathrm{aci}}^{N_{\mathrm{d}}}$ [Feingold et al., 2003; Schmidt et al., 2015], can be assessed with the observational approaches developed during this PhD work. The overall concept is sketched in Fig. 6.1.

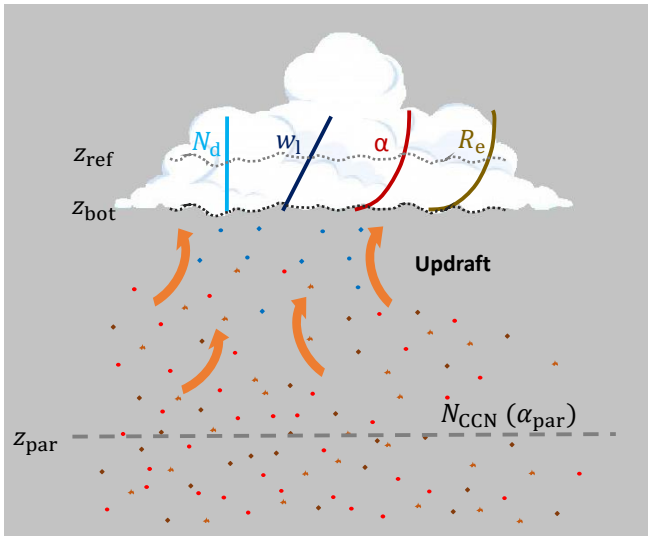

Figure 6.1: Illustration of the overall concept to investigate aerosol-cloud interaction by combining observations of cloud microphysical properties at height z_{ref}, 50–100 m above cloud base z_{bot}, with aerosol properties (α_{par}, N_{CCN}) measured at height z_{par} several 100 m below cloud base. The indicated height profiles of cloud microphysical properties were used in the simulations to develop the new retrieval scheme. Subadiabatic conditions in the lowest part of the cloud layer are assumed with a height-independent droplet number concentration $N_{\mathrm{d}}(z)$ and a linearly increasing liquid-water content $w_{\mathrm{l}}(z)$.

The major challenge was to obtain unambiguous information about the microphysics of liquid-water clouds. A new retrieval scheme to obtain cloud properties was conceived and implemented in the course of this work. The new DFOV-Depol approach allows us to obtain cloud microphysical properties from observations of the volume depolarization ratio at two different fields of view (FOVs). The retrieval is done by employing direct relationships between the depolarization at two FOVs with cloud extinction coefficient (α) and effective radius (R_e), from which the liquid-water content (w_l) and droplet number concentration (N_d) can be derived. Those relations were obtained from extended simulations using a multiple-scattering model with polarization capabilities, and they are now available for different system configurations and cloud base heights [Jimenez et al., 2020a].

The DFOV-Depol solution emerges from the need of daytime and high-temporal-resolution capabilities, as concluded by Schmidt [2014]. Prior to this thesis, a novel DFOV Raman technique was developed and tested at TROPOS to conduct ACI studies [Schmidt et al., 2013, 2014, 2015]. In the present work, several developments to assure the robust and unsupervised retrieval of both cloud and aerosol properties were presented, all of them motivated by the questions raised in Chapter 2. The following paragraphs aim to give concrete answers to these questions, summarizing the most important aspects of the investigations done during the PhD work.

1. How can we improve the assessment of $E_\mathrm{aci}^{N_\mathrm{d}}$ using ground-based lidar systems?

2. Is it possible to extend the DFOV concept proposed by Schmidt et al. [2013] to polarization measurements in a practical way to assess cloud microphysical properties with high temporal resolution and towards daytime?

With the array of developments presented in Chapters 3–5 and in Appendices A and B, new measurement possibilities were provided, which allow an accurate assessment of N_d, N_CCN, and thus of $E_\mathrm{aci}^{N_\mathrm{d}}$. The coarse resolution and limitation to nighttime of the DFOV-Raman technique, additionally to the difficulty to retrieve the aerosol information in cloudy periods, are issues that have been successfully overcome with the new DFOV-Depol approach and with a new approach named bottom-up approximation and outlined in Appendix A.

The extensive simulations and measurements have shown that it is possible to extend the DFOV concept to polarization measurements. The implementation of the method is straight forward, and its accuracy to retrieve cloud properties has been demonstrated by comparing the products firstly with the DFOV Raman approach, implemented in the MARTHA system at Leipzig, and then also with radar-based retrievals of effective radii, which was possible via the upgrade of a portable lidar system (Polly) into a DFOV depolarization system. Comparisons with model outputs from the large-domain large-eddy model ICON-LEM corroborated the accuracy of the new method as well [Costa-Surós et al., 2020].

3. How can a lidar instrument be calibrated to obtain accurate retrievals of aerosol and cloud properties?

The problem of calibrating such a system was solved for different scenarios. In the case of the MARTHA system, the three-signal calibration approach was developed and used for the accurate retrieval of the linear depolarization ratio from lidar measurements at one FOV. This approach was the content of the first publication [Jimenez et al., 2019]. The accuracy of the method was evaluated against collocated observations done with the state-of-the-art three-wavelength polarization lidar BERTHA [Haarig et al., 2017, 2018]. The instrumental constant determined with this approach showed stable values over time. No extra measurement period is needed to calibrate the system, because the calibration is done directly on the basis of the lidar measurements. The three-signal calibration approach can deliver depolarization ratios with an uncertainty of 3–5%.

In the case of the Polly systems, the calibration of the small FOV is performed via a $\Delta 90^\circ$ calibration [Freudenthaler, 2016a; Engelmann et al., 2016] and the transmission ratio is measured by using an artificial light source and a rotating polarization filter [Mattis et al., 2009]. Depolarization ratios with an uncertainty of 1–5% can be obtained.

To calibrate the second, larger FOV a simple method was developed. Here, the calculations of the inter-channel constants are done in the no-cloud height range, where single scattering produces the same depolarization at both FOVs. As shown in the second and third publications [Jimenez et al., 2020a,b], the method is robust enough to provide accurate depolarization ratios. A previously unknown parameter for the larger FOV is the so-called transmission ratio [Engelmann et al., 2016]. By means of the method presented in Appendix B, this parameter can be determined from lidar measurements that exhibit strong contrast in the depolarization values with height, such as in cases with dust particles or cirrus clouds next to clear air. The volume depolarization ratio measured with the second FOV showed uncertainties of 3–5%.

The calibration of the elastic channels to retrieve the aerosol products from our lidar measurements was needed as well. Because the well-known Klett–Fernald [Fernald, 1984] and Raman solutions [Ansmann et al., 1990, 1992] cannot be properly applied in cloudy scenarios, a new method named bottom-up approximation and presented in Appendix A, was developed and tested. To apply the method a cloud-free period is employed to perform the traditional aerosol retrieval and to compute the lidar calibration constant, which is then used to initialize the bottom-up retrieval. Two versions of the method were presented. One is based on Raman and elastic signals and is highly accurate with an uncertainty of about 5%, but only applicable during nighttime. The second version based only on elastic signals can be applied during day and night, but it needs previous knowledge about the extinction-to-backscatter ratio and a precise overlap function to correct the signal in the first height bins. For the long-term analysis, the second method was chosen and extinction-to-backscatter values obtained from previous campaigns were used to initialize the retrieval [Haarig et al., 2017; Bohlmann et al., 2018; Hofer et al., 2017, 2020b]. The overlap function was determined by combining the elastic and Raman signals [Wandinger and Ansmann, 2002]. The method for daytime has provided extinction values within an uncertainty range of 10–20%.

The quality of all the products was assured by comparing the aerosol and cloud properties with alternative observational and modeling methods. The most relevant equations to apply

the developed methods are listed in Table 6.1.

4. How can a standard lidar be upgraded into a DFOV polarization lidar?

The hardware requirement to apply the DFOV-Depol method is to possess polarization measurements at two FOVs. Several setups were studied, but the case of FOVs of 1.0 and 2.0 mrad was studied in deep detail, as it is the pair of FOVs implemented in the Polly systems. By means of the numerical simulations we concluded that at other FOV configurations the retrieval would also be possible, as shown in the second publication [Jimenez et al., 2020a]. Regardless which channels or calibration methods are used to apply the method, only depolarization profiles with an uncertainty of not more than 5–10% are needed.

In polarization lidars, such as the Polly systems [Engelmann et al., 2016; Baars et al., 2016], which already possess polarization channels, the upgrade to a DFOV system is straight forward. If a near-range telescope is used to measure the total backscattering, an additional telescope can be employed to detect cross-polarized light. No instrumental setup is needed for the calibration, as the calibrated depolarization ratio measured by the inner FOV can be used to calibrate the second FOV. If no near-range telescope is available, two telescopes for the outer FOV would be needed and the procedure to calibrate them is the same. If no polarization channels are available at all, a five-channel receiver would be needed. Three channels for the inner FOV, which may be calibrated by means of the three-signal method [Jimenez et al., 2019], and two channels for the outer FOV. Two-inch-diameter telescopes have given us strong enough returns to analyze cloudy periods.

Besides the MARTHA system, used as a testbed for the new approach, the technique was implemented in several Polly systems with equivalent features used as workhorse to provide long-term data at different strategic locations over the globe. The collected data helped us to evaluate the potential of the DFOV-Depol technique for aerosol-cloud-interaction research.

5. How important is it to consider vertical-wind information in the assessment of E_{aci}^{X}?

The vertical wind has shown to be a crucial parameter when analyzing single cases at Punta Arenas (PA), Chile. In this region, as expected, low CCN and droplet concentrations were observed. The prevailing clean conditions and the strong winds at PA, allow cloud formation likely in an aerosol- and updraft-sensitive regime [Reutter et al., 2009]. If updrafts prevailed in a cloud scene, strong correlations between N_{CCN} and N_{d} could be observed. As found in the cases analyzed, about 50% higher slopes were found for measurements with prevailing updraft movements (vertical velocity > 0.05 ms^{-1}) compared to the case when no wind information is taken into account. To improve cloud-resolving models, updraft measurements have to be considered in closure studies to evaluate the overall evolution of liquid-water clouds for all processes that may shape the cloud droplet number besides the particle number concentration.

6. How different are the aerosol and cloud conditions in different regions of the planet,

when observed with lidar systems possessing equivalent capabilities? And how large is the cloud response to aerosol in each of these regions?

Fourteen months of observations at the pristine location of Punta Arenas (PA), Chile, and eight months at the polluted location of Dushanbe (DB), Tajikistan, were considered to investigate the cloud response to different environmental conditions. A clear contrast in the aerosol and cloud properties was found. Larger droplet effective radii and smaller droplet number concentrations were observed at PA, with a mean of 97 cm^{-3} and a median of 56 cm^{-3}. From the retrieved aerosol extinction coefficient below the cloud base, estimations of the CCN concentration at 0.2% supersaturation were performed according to Mamouri and Ansmann [2016]. The ratio between this estimate and the obtained droplet number concentration was about one at PA, which indicates that 0.2% supersaturation can be easily reached at the Southern-Ocean conditions, with strong winds and a vast moisture source. At DB the number concentrations of droplets and CCN are much larger. Droplet concentrations are on the order of 200–400 cm^{-3} and CCN concentrations on the order of 700–900 cm^{-3}, leading to a N_d/N_{CCN} ratio of about 1/3, which corroborates that in a polluted environment a large amount of particles can activate into droplets, but many more remain unactivated. According to Reutter et al. [2009], the low activation ratios and ACI index that we found at DB suggest that an updraft-limited regime governs cloud formation here, whereas at PA cloud formation follows an aerosol- and updraft-sensitive regime, with large activation ratios and correlations between aerosol and cloud properties when the vertical wind is also considered. The long-term observations also showed consistency with observational reports based on space-borne and on in-situ measurements, and also with model-based studies. Our results suggest however that models slightly underestimate the CCN concentrations at PA and overestimate them at DB.

The data sets provided have the potential to evaluate microphysical schemes via closure studies. In the scope of this thesis, only the observational part was provided, leaving the confrontation with models as an outlook for future works. The high-resolution and long-term capabilities may help us to improve models from the scale of minutes (10–10^2 m horizontal scale), in which clouds can be resolved by large-eddy simulations and microphysics is usually parameterized [Morrison et al., 2005; Kretzschmar et al., 2020; Zhang et al., 2021], to larger scales of days to months relevant for climate simulations, in which both microphysics and clouds are parameterized [Morrison et al., 2020].

7. How does the temporal scale affect the estimation of $E_{aci}^{N_d}$? And what are the consequences of considering data sets of different scales in ACI research?

Using the data obtained from December 2018 to January 2020 at PA, the ACI index $E_{aci}^{N_d}$ was computed at different scales via log-log regressions of the N_{CCN} and N_d data. The shortest scale was 3 minutes. Here, the ACI index was calculated for each individual cloud detected. Considering all clouds, a large spread of the values was found. In a few cases, such as the measurements presented in Sect. 5.1 and in Jimenez et al. [2020b], we

obtained values between 0.4 and 0.8, when considering only updraft periods. However, such scenes are rare, and this is simply because tropospheric aerosol amount varies significantly only on the temporal scale of 2–48 h [Anderson et al., 2003]. To be able to observe the response of the cloud state to the aerosol state, abundant updraft periods have shown to be a robust indicator. Thus, caution needs to be exercised when evaluating ACI in high-resolution observations of single clouds.

The second scale considered for these calculations was the temporal scale of single clouds. Here, the average values of single clouds over the different months were used. When no wind information was considered, slopes of 0.35 ± 0.3 for DB and 0.2 ± 0.35 for PA were obtained. When considering only clouds in which updrafts prevailed, the susceptibility index at PA increased to about 0.56 ± 0.5. The most robust estimate of the $E_{\mathrm{aci}}^{N_{\mathrm{d}}}$ was obtained when considering monthly means over the whole measurement periods. Values of 0.83 ± 0.20 and 0.57 ± 0.26 were obtained for PA and DB, respectively.

The temporal scale used for the analysis of $E_{\mathrm{aci}}^{N_{\mathrm{d}}}$ was found to be an important issue to consider, corroborating McComiskey and Feingold [2012], who stated that differences between cloud microphysical processes and analysis scale may incur biases when assessing $E_{\mathrm{aci}}^{N_{\mathrm{d}}}$. The most accurate value obtained at the coarsest scale was used to answer the last question regarding the relevance of our results for the radiative effect at the two locations.

8. How relevant are the $E_{\mathrm{aci}}^{N_{\mathrm{d}}}$ values that can be obtained with the new approach for the aerosol-cloud-albedo effect?

The relevance of the $E_{\mathrm{aci}}^{N_{\mathrm{d}}}$ values was illuminated in Chapter 5. Radiative-forcing calculations were done using our results and data obtained from the second Modern-Era Reanalysis for Research and Applications (MERRA-2) [Gelaro et al., 2017], i.e., the cloud albedo and cloud fraction. A radiative cooling due to the Twomey effect from -0.70 to -0.17 Wm^{-2} was found for PA and between -1.89 and -0.66 Wm^{-2} for DB. These values agree with global estimates of the cloud-mediated aerosol effect, but are slightly larger than those values usually found at the specific locations considered [Myhre et al., 2013]. These results show the potential of the new approach to address questions regarding the radiative effect of aerosols via the Twomey effect, opening a door towards improvements of models dealing with the effects of aerosol on the radiative budget.

The products that can be obtained after this PhD work respond to the strong request of new, robust, and replicable aerosol and cloud profiling techniques [Grosvenor et al., 2018]. Such schemes can become an essential part of aerosol-cloud monitoring infrastructures, such as ACTRIS (https://www.actris.eu/), which is in charge of building up the necessary aerosol-cloud monitoring infrastructure to improve our knowledge about atmospheric processes with focus on climate change.

As an outlook of this work, an extension of the ACI studies by means of the DFOV-Depol method is foreseen. Already five lidar instruments have been upgraded with the new technique. These lidars are or were operated at Punta Arenas for a two-year campaign from 2019 to 2021, at the High Arctic (at 85–90° N) on board the German icebreaker Polarstern

from September 2019 to September 2020, at Dushanbe, Tajikistan, under polluted and dusty conditions in Central Asia since June 2019, and at Limassol, Cyprus, in the polluted and dusty Eastern Mediterranean since the summer of 2020. A fifth DFOV polarization lidar will start long-term monitoring at Mindelo, Cabo Verde, in the outflow regime of pollution and dust from western and central Africa in the summer of 2021. A mobile DFOV Polly will be moved to New Zealand for further ACI studies in the Southern Ocean in 2022. All these field activities will be used in the near future to characterize ACI in the case of liquid-water clouds under very different aerosol and meteorological conditions.

Cloud adjustments manifested in the cloud fraction [Gryspeerdt et al., 2016] and in liquid-water path [Gryspeerdt et al., 2019] could also be investigated by combining the N_{d} values that we can observe with reanalysis data. Longer measurement periods will be needed to obtain representative data, and ambient humidity would be an important parameter to be considered here. Lidar systems can provide this property as a profile as well [Dai et al., 2018], which again highlights the potential of the lidar platform. The new lidar methods, combined with newly developed radar/lidar techniques to provide information about clouds [e.g., Bühl et al., 2019] and aerosol [Radenz et al., 2021], could become a valuable framework to conduct aerosol-cloud-precipitation interaction studies.

A further application of the new approach could be the support of geoengineering experiments with the aim to modify marine cloud properties by artificially emitting sea spray with autonomous vessels in order to enhance the albedo of already formed low-level marine clouds [Latham, 1990; Latham et al., 2008]. Field experiments to test such approaches will need observational platforms to continuously track cloud properties as a response to the artificial aerosol emissions.

Table 6.1: Overview of the cloud and aerosol retrieval procedure (step-by-step data analysis). The data analysis starts with a precise calibration of the depolarization products, either via the three-signal approach for the MARTHA system or via the two-signal approach for the Polly system. The cloud retrieval starts with the determination of the cloud base height z_{bot}. The cloud products are given at the reference height z_{ref}, 75 m above cloud base height z_{bot}. In the estimation of the ACI efficiency, particle extinction and cloud condensation nucleus concentration at z_{par}, several 100 m below cloud base, are considered. Equations from the respective publications have been indicated as p1, p2, and p3.

Parameter	**Symbol**	**Equation**	**Uncertainty**
To be used in a three-channel polarization system			
Inter-channel constant (cross to co)	X_δ	Eq. (35) p1	3–5%
Cross-talk parameter	ξ_{tot}	Eq. (42) p1	1%
Volume depolarization ratio	$\delta_{\mathrm{in}}(z)$	Eq. (41) p1	3–5%
To be used in a two-channel polarization system			
Inter-channel constant (cross to total)	C_{in}	Eq. (4) p3	1–3 %
Volume depolarization ratio	$\delta_{\mathrm{in}}(z)$	Eq. (2) p3	1–5 %
Calibration of second FOV			
Inter-channel constant	C_{out}	Eq. (B.4)	1–4%
Transmission ratio	$F_{\mathrm{c,out}}$	Eq. (B.5)	5–15%
Volume depolarization ratio	$\delta_{\mathrm{out}}(z)$	Eq. (B.6)	3–5 %
Cloud products from DFOV-Depol approach			
Cloud base height	z_{bot}	Sect. 4.1 p3	0.1–1%
Cloud depolarization ratios	$\overline{\delta}_{\mathrm{in}}(z_{\mathrm{bot}}, z_{\mathrm{ref}})$	Eq. (23) p1	5%
	$\overline{\delta}_{\mathrm{out}}(z_{\mathrm{bot}}, z_{\mathrm{ref}})$	Eq. (24) p2	5%
	$\overline{\delta}_{\mathrm{rat}}(z_{\mathrm{bot}}, z_{\mathrm{ref}})$	Eq. (25) p2	10–15%
Droplet effective radius	$R_{\mathrm{e}}(z_{\mathrm{ref}})$	Eq. (26) p2	15%
Cloud extinction coefficient	$\alpha(z_{\mathrm{ref}})$	Eq. (27) p2	15–20%
Liquid-water content	$w_{\mathrm{l}}(z_{\mathrm{ref}})$	Eq. (4) p2	25%
Cloud droplet number concentration	$N_{\mathrm{d}}(z_{\mathrm{ref}})$	Eq. (6) p2	25–75%
Aerosol products from bottom-up approach			
Particle extinction coefficient (daytime)	$\alpha_{\mathrm{par}}(z_{\mathrm{par}})$	Sect. A.3	10–20%
Particle extinction coefficient (nighttime)	$\alpha_{\mathrm{par}}(z_{\mathrm{par}})$	Sect. A.2	5%
Particle depolarization ratio	$\delta_{\mathrm{par}}(z)$	Eq. (A.6)	5–10%
CCN concentration	$N_{\mathrm{CCN}}(z_{\mathrm{par}})$	Eq. (5.1)	30–100%
ACI products			
ACI $N_{\mathrm{CCN}} - N_{\mathrm{d}}$ efficiency (monthly scale)	$E_{\mathrm{aci}}^{N_{\mathrm{d}}}$	Eq. (2.6)	25–40%
ACI $\alpha_{\mathrm{par}} - N_{\mathrm{d}}$ efficiency (monthly scale)	$E_{\mathrm{aci}}^{N_{\mathrm{d}},\alpha_{\mathrm{par}}}$	Eq. (2.11)	25–35%

Appendix A

Aerosol properties with lidar

In the present work a novel lidar-based approach to observe cloud microphysical properties was presented. The final goal was to study the relation between cloud and aerosol properties measured by the same lidar system. This Appendix provides an overview of the analytical treatment of lidar returns for assessing aerosol properties. New alternative methodologies to solve the lidar problem in cloudy periods are presented.

A lidar system is an active optoelectronical instrument that provides vertically resolved information about the atmosphere, it consists on a vertically-pointing light source and a receiver that collects the light scattered back to the light source. The returned photons can be recorded within a temporal window of the order of microseconds, enabling the acquisition of profiles with spatial resolution of a few meters. Lidar instruments has been widely used to obtain valuable information about aerosol particles, such as the extinction and backscattering coefficient [Ansmann et al., 1990, 1992], thermodynamical information such as relative humidity and temperature [Dai et al., 2018; Weitkamp, 2005], and dynamic information such as the vertical and horizontal wind [Bühl et al., 2013]. Multiwavelength and depolarization information can be useful for aerosol and cloud typing [Baars et al., 2017]. The potential of the lidar technique to characterize aerosol particles at small temporal and spatial resolutions, makes the technique suitable to provide valuable observations to study the interaction between aerosol and clouds. In this chapter an overview of current techniques to retrieve optical properties of aerosol, using ground-based lidar, is given. Most of current approaches to invert lidar signals have shown to not be very eligible for cloudy scenarios [Ansmann and Müller, 2005]. A novel methodology to retrieve the optical properties in those cases is proposed and described in this appendix.

A.1 Lidar principles of elastic and Raman lidar

We talk about an elastic signal when the system detects the same wavelength that it emits, i.e. it measures only elastic scattered photons. The equation to describe the vertical evolution of the lidar return is given by the Lambert-Beer law and takes the following form [Wandinger,

2005]:

$$P_{\lambda_0}(z) = C_{\lambda_0} \frac{O(z)}{z^2} \beta_{\lambda_0}(z) \exp\left[-2 \int_0^z \alpha_{\lambda_0}(\zeta) \mathrm{d}\zeta\right] \tag{A.1}$$

In Eq. (A.1) C_{λ_0} is a constant that comprises system parameters describing among others the efficiency of the reception unit and the energy of the laser pulse. This constant can change with time as the laser source and the detectors efficiency usually decay, with noticeable changes within a few days. $O(z)$ denotes the fraction of the outgoing laser section inside the receiver field of view and increases from the ground level with height z until it reach the full overlap (0 to 1) [Malinka and Schmidt, 2010; Stelmaszczyk et al., 2005; Wandinger and Ansmann, 2002], $1/z^2$ counts for the decrease of the solid angle that can be catch by the telescope area. As for optical properties of the atmospheric constituents are the parameters β_λ and α_λ introduced and denote backscattering and the extinction coefficient respectively. The extinction counts the fraction of light that is scattered and absorbed by unit of distance (m^{-1}), and the backscattering coefficient the fraction scattered within a solid angle of 1 sr in the backward direction and it is measured in $\mathrm{m}^{-1}\mathrm{sr}^{-1}$.

The atmosphere is composed by air molecules and aerosol particles. For molecules the interaction can be well described by the Rayleigh theory, whereas for aerosol particles the scattering and absorption generally follows a Mie regime [Mie, 1908]. Thereby the extinction and backscattering coefficient can be decomposed into two terms:

$$\alpha_{\lambda_0}(z) = \alpha_{\lambda_0}^{\mathrm{par}}(z) + \alpha_{\lambda_0}^{\mathrm{mol}}(z), \tag{A.2}$$

$$\beta_{\lambda_0}(z) = \beta_{\lambda_0}^{\mathrm{par}}(z) + \beta_{\lambda_0}^{\mathrm{mol}}(z). \tag{A.3}$$

Here the subscript mol denotes molecules and par aerosol particles. The molecular backscattering coefficient can be written as the multiplication of the differential cross section for backward scattering and the number density.

$$\beta_{\lambda_0}^{\mathrm{mol}}(z) = \frac{\mathrm{d}\sigma_{\lambda_0}^{\mathrm{mol}}}{\mathrm{d}\Omega}(\pi) N^{\mathrm{mol}}(z) \tag{A.4}$$

The cross section $\frac{\mathrm{d}\sigma_{\lambda_0}^{\mathrm{mol}}}{\mathrm{d}\Omega}(\pi)$ depends on the wavelength and is set constant as the composition of air molecules in the Troposphere does not change with height, varying only the number density N^{mol} with height. These two quantities can be obtained analytically from temperature and pressure profiles [Teillet, 1990].

For air molecules, the extinction coefficient is the sum of scattering and absorption coefficients. Given the usual wavelengths used in backscatter lidar systems, the absorption of air molecules can be neglected [Gordon et al., 2017]. The corresponding extinction and bascattering coefficients can then be related by the molecular extinction-to-backscattering ratio [Collis and Russel, 1976]:

$$S^{\mathrm{mol}} = \frac{\alpha_{\lambda_0}^{\mathrm{mol}}}{\beta_{\lambda_0}^{\mathrm{mol}}} = \frac{8\pi}{3} K, \tag{A.5}$$

where K is the so-called King's factor that describes the anisotropy of air molecules. In this work a value of K=1.049 is used [Young, 1981]. Yet, Eq. (A.1) has several unknowns which are the particle extinction $\alpha_{\lambda_0}^{\text{par}}$ and backscattering coefficients $\beta_{\lambda_0}^{\text{par}}$, the so-called lidar constant C_{λ_0} and the overlap function $O(z)$. In the next sections different methodologies to solve the lidar problem are presented and discussed.

A.2 Raman lidar

When the lidar laser beam goes towards the atmosphere, not only elastic scattering takes place, but also Raman scattering at air molecules. A Raman channel is dedicated to measure at the vibrational and/or rotational lines of, e.g., nitrogen or water vapor molecules, which are well documented in the literature, and the equation to describe such a Raman return has the following form [Wandinger, 2005]:

$$P_{\lambda_{\text{Ra}}}(z) = C_{\lambda_{\text{Ra}}} \frac{O(z)}{z^2} \beta_{\lambda_{\text{Ra}}}^{\text{N}_2}(z) \exp\left\{ -\int_0^z \left[\alpha_{\lambda_0}(\zeta) + \alpha_{\lambda_{\text{Ra}}}(\zeta)\right] \mathrm{d}\zeta \right\}. \tag{A.6}$$

The difference with Eq. (A.1) is that the argument of the exponential has two terms, as the light has a shifted wavelength λ_{Ra} after being backscattered. $\beta_{\lambda_{\text{Ra}}}^{\text{N}_2}(z)$ denotes the Raman backscattering coefficient of nitrogen molecules, which can be calculated multiplying the backscattering raman differential cross section with the number density.

As air molecules are composed by approximately 78 % of Nitrogen, in remote sensing it is commonly used as a reference for air. Using equation A.4 the Raman backscattering of nitrogen molecules can be expressed as follows

$$\beta_{\lambda_{\text{Ra}}}^{\text{N}_2} = N^{\text{N}_2} \times \frac{\mathrm{d}\sigma_{\lambda_{\text{Ra}}}^{\text{N}_2}}{\mathrm{d}\Omega}(\pi) = 0.78 N^{\text{mol}} \times \frac{\mathrm{d}\sigma_{\lambda_{\text{Ra}}}^{\text{N}_2}}{\mathrm{d}\Omega}(\pi) = 0.78 \frac{\frac{\mathrm{d}\sigma_{\lambda_{\text{Ra}}}^{\text{N}_2}}{\mathrm{d}\Omega}(\pi)}{\frac{\mathrm{d}\sigma_{\lambda_0}^{\text{mol}}}{\mathrm{d}\Omega}(\pi)} \times \beta_{\lambda_0}^{\text{mol}}, \tag{A.7}$$

where N^{N_2} denotes the number concentration of nitrogen molecules, $\frac{\mathrm{d}\sigma_{\lambda_{\text{Ra}}}^{\text{N}_2}}{\mathrm{d}\Omega}(\pi)$ the cross section for Raman backscattering of nitrogen molecules, N^{mol} the number concentration of air molecules and $\frac{\mathrm{d}\sigma_{\lambda_0}^{\text{mol}}}{\mathrm{d}\Omega}(\pi)$ the cross section for Rayleigh backscattering of air molecules. The factors accompanying $\beta_{\lambda_0}^{\text{mol}}$ are constant, and together with the lidar constant $C_{\lambda_{\text{Ra}}}$ can define a new constant:

$$C_{\lambda_{\text{Ra}}}^{*} = 0.78 \frac{\frac{\mathrm{d}\sigma_{\lambda_{\text{Ra}}}^{\text{N}_2}}{\mathrm{d}\Omega}(\pi)}{\frac{\mathrm{d}\sigma_{\lambda_0}^{\text{mol}}}{\mathrm{d}\Omega}(\pi)} C_{\lambda_{\text{Ra}}}, \tag{A.8}$$

so that Eq. (A.6) can be written in the following simple form

$$P_{\lambda_{\text{Ra}}}^{\text{rc}}(z) = P_{\lambda_{\text{Ra}}}(z) z^2 / O(z) = C_{\lambda_{\text{Ra}}}^{*} \beta_{\lambda_0}^{\text{mol}}(z) \exp\left\{ -\int_0^z \left[\alpha_{\lambda_0}(\zeta) + \alpha_{\lambda_{\text{Ra}}}(\zeta)\right] \mathrm{d}\zeta \right\}. \tag{A.9}$$

$P_{\lambda_{\text{Ra}}}^{\text{rc}}$ is the so-called range-corrected signal.

A.2.1 Retrieval of extinction coefficient

Applying natural logarithms to equation A.9 and differentiating respect to z, a solution for the extinction coefficient, without assumptions concerning the extinction to backscattering ratio, can be derived [Ansmann et al., 1990]:

$$\alpha_{\lambda_0}^{\mathrm{par}}(z) = \frac{\frac{\mathrm{d}}{\mathrm{dz}} \ln \frac{\beta_{\lambda_0}^{\mathrm{mol}}}{P_{\lambda_{\mathrm{Ra}}}^{\mathrm{rc}}(z)} - \alpha_{\lambda_0}^{\mathrm{mol}}(z) - \alpha_{\lambda_{\mathrm{Ra}}}^{\mathrm{mol}}(z)}{1 + \left(\frac{\lambda_0}{\lambda_{Ra}}\right)^{\mathring{\mathrm{a}}}}. \tag{A.10}$$

In this equation, the Ångström exponent is introduced. This parameters reflects the spectral dependency of the aerosol properties [Ångström, 1964], closely related to the size of the scatterer:

$$\frac{\alpha_{\lambda_{\mathrm{Ra}}}^{\mathrm{par}}}{\alpha_{\lambda_0}^{\mathrm{par}}} = \left(\frac{\lambda_0}{\lambda_{\mathrm{Ra}}}\right)^{\mathring{\mathrm{a}}}. \tag{A.11}$$

For aerosol particles and water droplets with diameters comparable with the measurement wavelength, $\mathring{\mathrm{a}} = 1$ is an appropriate value to use [Ansmann et al., 1990].

A.2.2 Retrieval of backscattering coefficient

Considering a system that measures elastic and Raman scattering, the independent variables $\alpha_{\lambda_0}^{\mathrm{par}}$ and $\beta_{\lambda_0}^{\mathrm{par}}$ can be resolved. Diving Eq. (A.1) by Eq. (A.6) and taking the new constant $C_{\lambda_{\mathrm{Ra}}}^{*}$ we obtain:

$$\frac{P_{\lambda_0}(z)}{P_{\lambda_{\mathrm{Ra}}}(z)} = \frac{C_{\lambda_0}}{C_{\lambda_{\mathrm{Ra}}}^{*}} \frac{\beta_{\lambda_0}^{\mathrm{par}} + \beta_{\lambda_0}^{\mathrm{mol}}}{\beta_{\lambda_0}^{\mathrm{mol}}} \exp\left\{ -\int_0^z \left[\alpha_{\lambda_0}^{\mathrm{mol}}(\zeta) - \alpha_{\lambda_{\mathrm{Ra}}}^{\mathrm{mol}}(\zeta) + \alpha_{\lambda_0}^{\mathrm{par}}(\zeta) - \alpha_{\lambda_{\mathrm{Ra}}}^{\mathrm{par}}(\zeta)\right] \mathrm{d}\zeta \right\}. \tag{A.12}$$

The molecular extinction and backscattering are needed so that boundary conditions have to be applied, namely the upper Troposphere at z_0, where the aerosol contribution can usually be neglected. To calculate the backscatterig coefficient, the extinction must be previously computed evaluating Equation A.10, although it influences on the retrieval of $\beta_{\lambda}^{\mathrm{par}}(z)$ is rather small, because the term $\left[1 - (\lambda_0/\lambda_{\mathrm{Ra}})^{\mathring{\mathrm{a}}}\right]$ is $<< 1$. Equation A.13 shows the solution of the backscattering coefficient using the ratio of elastic and Raman signals [Ansmann et al., 1992].

$$\begin{aligned} \beta_{\lambda}^{\mathrm{par}}(z) &= \left[\beta_{\lambda_0}^{\mathrm{par}}(z_0) + \beta_{\lambda_0}^{\mathrm{mol}}(z_0)\right] \frac{P_{\lambda_0}(z) P_{\lambda_{\mathrm{Ra}}}(z_0) \beta_{\lambda_0}^{\mathrm{mol}}(z)}{P_{\lambda_{\mathrm{Ra}}}(z) P_{\lambda_0}(z) \beta_{\lambda_0}^{\mathrm{mol}}(z_0)} \\ &\times \frac{\exp\left\{ \int_{z_0}^{z} \left[1 - (\lambda_0/\lambda_{\mathrm{Ra}})^{\mathring{\mathrm{a}}}\right] \alpha_{\lambda_0}^{\mathrm{par}}(\zeta) \mathrm{d}\zeta \right\}}{\exp\left\{ \int_{z_0}^{z} \left[\alpha_{\lambda_{\mathrm{Ra}}}^{\mathrm{mol}}(\zeta) - \alpha_{\lambda_0}^{\mathrm{mol}}(\zeta)\right] \mathrm{d}\zeta \right\}} - \beta_{\lambda}^{\mathrm{mol}}(z). \end{aligned} \tag{A.13}$$

Equations A.10 and A.13 represent a general solution to resolve the extinction and backscattering coefficients independently. The solutions are highly accurate, but in the case of the extinction coefficient a robust overlap function is required to cover the lowest range bins. Long averaging periods are needed to retrieve the extinction coefficient making a product with high temporal resolution difficult to achieve. This could be achieve with the particle backscattering, but in the presence of liquid-water clouds, Eqs. (A.1) and (A.6) do not hold anymore because of the multiple-scattering effect that take place in liquid-cloud layers.

A.2.3 Bottom-up approximation for Raman Signals

This section propose an alternative method to resolve the optical properties with high temporal resolution using elastic and Raman returns. This can be done when a neighbor period without clouds is available, so that the optical parameters $\alpha_{\lambda}^{\mathrm{par}}(z)$ and $\beta_{\lambda}^{\mathrm{par}}(z)$ can be obtained using Eqs. (A.10) and (A.13). With knowledge about the these optical properties, the constants ratio from Equation A.12 can be computed:

$$\frac{C_{\lambda_0}}{C^{*}_{\lambda_{\mathrm{Ra}}}} = \frac{P_{\lambda_0}(z)}{P_{\lambda_{\mathrm{Ra}}}(z)} \frac{\beta^{\mathrm{mol}}_{\lambda_0}}{\beta^{\mathrm{par}}_{\lambda_0} + \beta^{\mathrm{mol}}_{\lambda_0}} \exp\left\{ \int_0^z \left[\alpha^{\mathrm{mol}}_{\lambda_0}(\zeta) - \alpha^{\mathrm{mol}}_{\lambda_{\mathrm{Ra}}}(\zeta) + \alpha^{\mathrm{par}}_{\lambda_0}(\zeta) - \alpha^{\mathrm{par}}_{\lambda_{\mathrm{Ra}}}(\zeta) \right] \mathrm{d}\zeta \right\}. \tag{A.14}$$

With this constant, the backscattering coefficient can be calculated without boundary condition as follows:

$$\begin{aligned} \beta^{\mathrm{par}}_{\lambda_0} &= \left[\frac{C^{*}_{\lambda_{\mathrm{Ra}}}}{C_{\lambda_0}} \frac{P_{\lambda_0}(z)}{P_{\lambda_{\mathrm{Ra}}}(z)} \frac{\exp\left\{ \int_0^z \left[\alpha^{\mathrm{mol}}_{\lambda_0}(\zeta) - \alpha^{\mathrm{mol}}_{\lambda_{\mathrm{Ra}}}(\zeta) \right] \mathrm{d}\zeta \right\}}{\exp\left\{ - \int_0^z \left[1 - (\lambda_0/\lambda_{\mathrm{Ra}})^{\mathring{\mathrm{a}}} \right] \alpha^{\mathrm{par}}_{\lambda_0}(\zeta) \mathrm{d}\zeta \right\}} - 1 \right] \beta^{\mathrm{mol}}_{\lambda_0} \\ &\approx \left[\frac{C^{*}_{\lambda_{\mathrm{Ra}}}}{C_{\lambda_0}} \frac{P_{\lambda_0}(z)}{P_{\lambda_{\mathrm{Ra}}}(z)} \frac{\exp\left\{ \int_0^z \left[\alpha^{\mathrm{mol}}_{\lambda_0}(\zeta) - \alpha^{\mathrm{mol}}_{\lambda_{\mathrm{Ra}}}(\zeta) \right] \mathrm{d}\zeta \right\}}{\exp\left\{ - \int_0^{z-\Delta z} \left[1 - (\lambda_0/\lambda_{\mathrm{Ra}})^{\mathring{\mathrm{a}}} \right] \alpha^{\mathrm{par}}_{\lambda_0}(\zeta) \mathrm{d}\zeta \right\}} - 1 \right] \beta^{\mathrm{mol}}_{\lambda_0}. \end{aligned} \tag{A.15}$$

To apply this equation, knowledge about the extinction coefficient to the range z is needed, but because the term $\left[1 - (\lambda_0/\lambda_{\mathrm{Ra}})^{\mathring{\mathrm{a}}}\right]$ is $<< 1$. The integration up to $z - \Delta z$, with Δz the height resolution, is a robust approximate of the transmission up to z. In this way, the retrieval of the backscattering coefficient can be extended to the cloudy periods, performing the calculations bin by bin from the ground base up to the cloud base. Furthermore, the calibration constant enables the high temporal-resolution retrieval of the optical properties in a straight forward way.

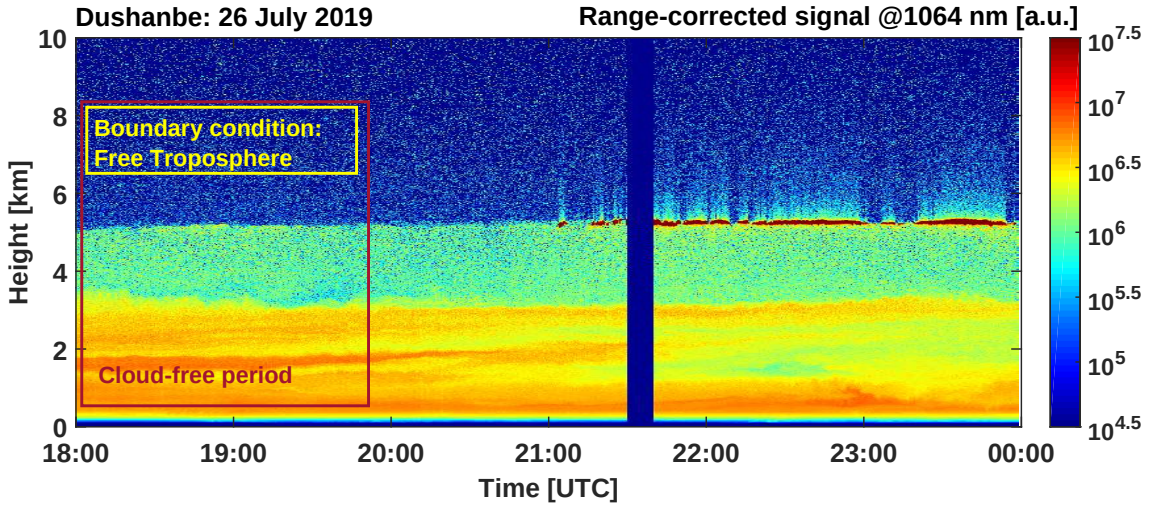

Figure A.1: Logarithms of range corrected signal for the measurement example 26 July 2019. A cloud layer is observed i the first two hour. A cloud-free period was selected to apply the traditional Raman method and compute the aerosol properties, from which the lidar constants can be obtained.

A.2.4 Evaluation of Raman methods

To show the applicability of the methods outlined in Sections A.2.1, A.2.2 and A.2.3, a measurement case was analyzed. The data was obtained with the 3+2+2 lidar system Polly system [Engelmann et al., 2016; Hofer et al., 2020a]. 3+2+2 stands for three-wavelength Backscatter, two-wavelength extinction and two-wavelength depolarization. The system is equipped with two FOVs, both measuring depolarization.

The system is deployed in Dushanbe (38.6 ° N, 68.9 ° E, 864 m a.s.l.), capital of Tajikistan, and it is running automatically around the clock since June 2019. In Figure A.1 the range corrected data $P_{1064}(z)z^2$ for the 16 July 2019 between 18 and 24 UTC, is presented.

Strong presence of aerosol in the boundary layer and a cloud layer between 21 and 24 UTC at 5 km height can be seen. The cloud-free period from 18:00 to 19:58 UTC was averaged and Raman method was applied to obtain $\alpha^{\text{par}}_{\lambda_0}(z)$ and $\beta^{\text{par}}_{\lambda_0}(z)$. The calculations from the molecular backscattering was done as outlined in section A.1 and the profiles of pressure and temperature were obtained from the Global Data Assimilation System [GDAS, 2020]. In the selected free-aerosol range (white rectangle) the boundary condition is applied, i.e background values of aerosol backscattering at 8 km are assumed: 5×10^8 ,2×10^8 and 10^8 m^{-1} sr^{-1} for 355, 532 and 1064 nm respectively.

Using the outlined approach, the extinction and then backscattering coefficient was retrieved. Figure A.2a shows the backscattering profiles obtained evaluating Equation A.13 for the three observed wavelengths in dark colors. The extinction profiles from the Raman signals and with smoothing lenght 60 bins (450 meters) are shown in Figure A.2b. The corresponding lidar ratio $S^{\text{par}}_{\lambda_0}$ (extinction to backscattering ratio) is presented in Figure A.2c. The values obtained, in average 40 sr for 532 nm and 60 sr for 355 nm, are in agreement

with typical values observed in the region [Hofer et al., 2020a]. These values of lidar ratio were used in Section A.3.4 to derive the properties using only the elastic signals.

The calibraiton constants were calculated from the extinction and backscattering profiles, obtaining values of $\frac{C_{355}}{C^*_{\lambda_{387}}} = 0.9898$, $\frac{C_{532}}{C^*_{\lambda_{607}}} = 0.4686$ and $\frac{C_{1064}}{C^*_{\lambda_{607}}} = 0.0575$. The profiles of backsctattering using Eq. (A.15) were recalculated, and as expected, they agree completely with the previous profiles, since both, Eq. (A.13) and (A.15) are derived from the same same equation, i.e., Eq. (A.12). Eq. (A.15), however, permits calculations without boundary condition, making the methodology outlined in Section A.2.3 suitable to analyze cloudy periods.

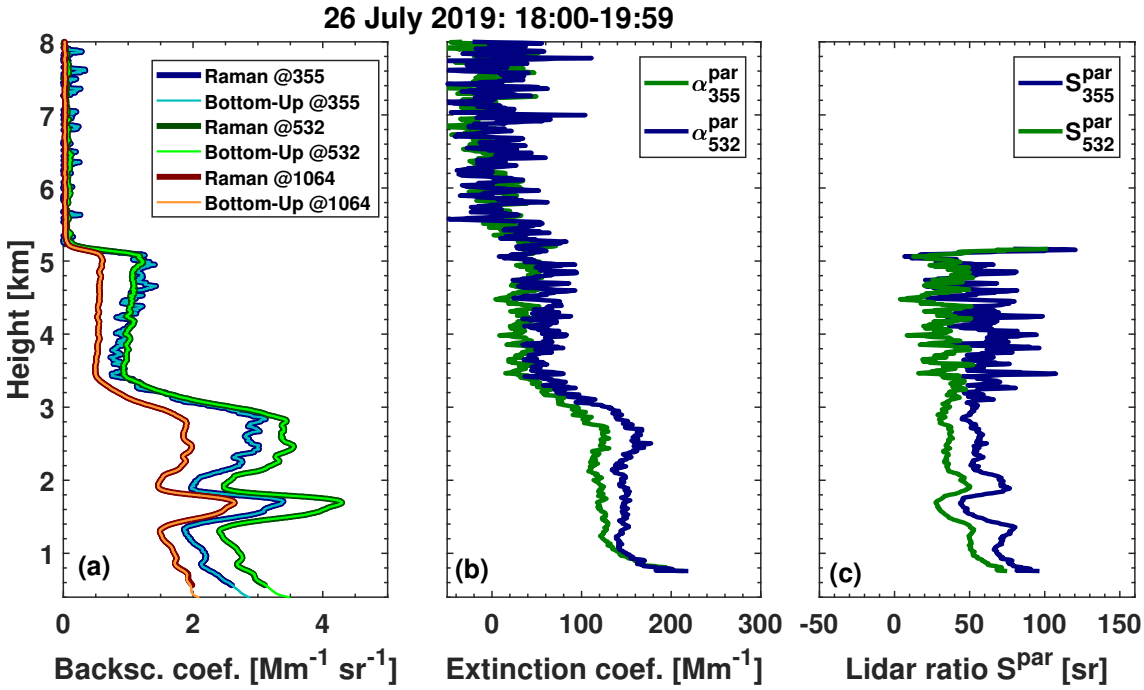

Figure A.2: Profiles of the aerosol backscattering coefficient obtained from the Raman and elastic signals. The dark colored curves are the solutions obtained with the traditional method [Ansmann et al., 1992], the bright colored lines the solutions with the method proposed in this chapter, starting from the calibration constants.

In Figure A.3 the backscattering profiles for the 16 July 2019 between 00:00 and 06:00 UTC are presented. Equation A.15 was evaluated, assuming that the ratio of exponential remains constant with time. This ratio was previously calculated for the average of the whole period. This assumption induce minimal error in the high temporal resolution retrieval as it varies little with height (about 0.001 each 100 meters). The values are consistent with the values obtained using only the elastic signals (Figure A.7).

These results are highly accurate since no assumptions were made. The method can however only be applied during nighttime. To evaluate long-term measurements, a second bottom-up method was developed and have been applied to all cases. The approach based solely on elastic signals is presented in Section A.3.3.

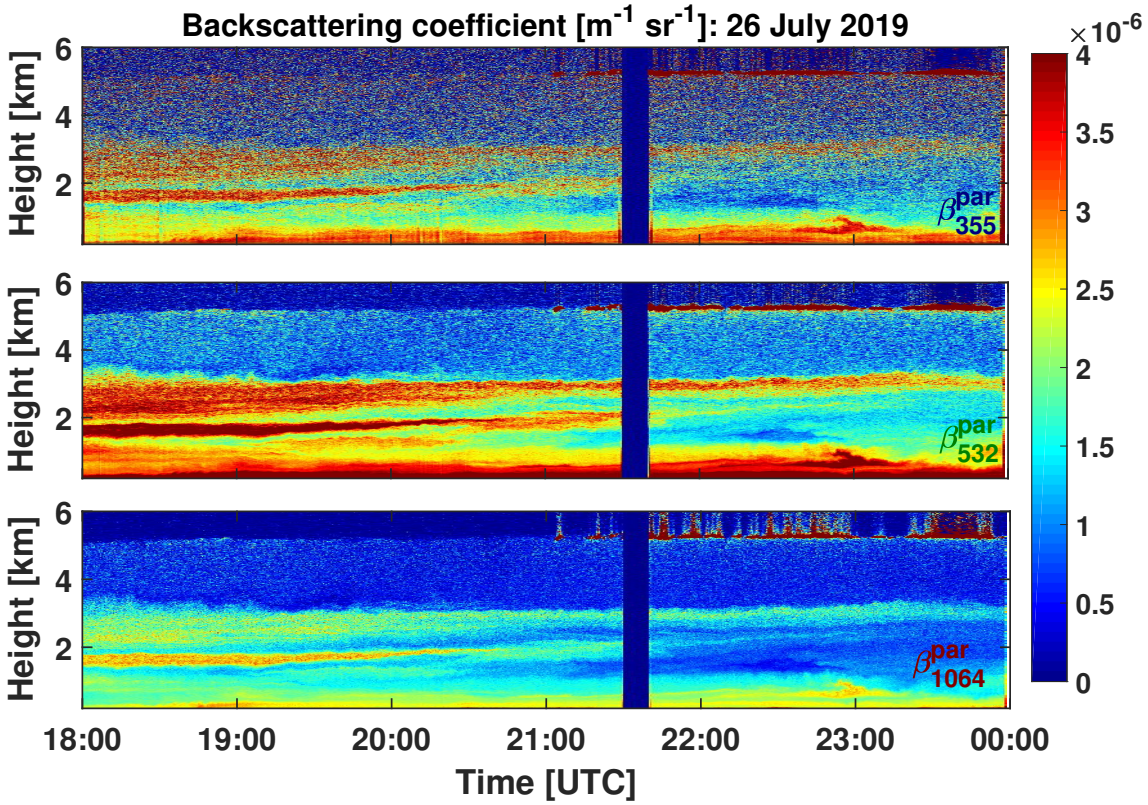

Figure A.3: High resolved backscattering profiles obtained with our methodology using the elastic and Raman signals. The measurement period is the 26 July 2019 18:00-24:00, with temporal resolution of 30 seconds.

A.3 Elastic Lidar

The Raman method is very accurate but it works only if good Raman echoes are available, i.e., during nighttime. Many lidar systems possess only elastic channels and there is a path to solve the lidar problem from one single signal, which have been widely used in aerosol lidars.

A.3.1 Klett-Fernald Solution

With the outlined considerations, i.e. having knowledge about the molecular structure of the atmosphere and a robust overlap function to characterize the system, still three unknown remain in Eq. (A.1), the lidar constant and the aerosol extinction and backscattering coefficients. To resolve the optical properties from one signal, additional information is needed. A widely used parameter to relate these las two properties is the so-called extinction-to-backscatter ratio, also known as lidar ratio.

$$S^{\mathrm{par}}_{\lambda_0}(z) = \frac{\alpha^{\mathrm{par}}_{\lambda_0}(z)}{\beta^{\mathrm{par}}_{\lambda_0}(z)}. \tag{A.16}$$

This quantity depends mainly on the absorption properties of the aerosols, but also on its size. Thus, by assuming a known and vertically-constant value of $S^{\text{par}}_{\lambda_0}$, a Bernoulli-type equation can be derived from Eq. (A.1), and applying boundary conditions the equation can be solved without needing the lidar calibration constant. Klett [1981] presented a solution for an atmosphere with one disperser type, and Fernald [1984] proposed a more general approach separating the atmosphere into aerosol and molecules. The backscattering can be calculated with the following equation:

$$\beta^{\text{par}}_{\lambda_0} = \frac{U(z_0, z)}{V(z_0) - 2S^{\text{par}}_{\lambda_0} \int_{z_0}^{z} U(z_0, \zeta)\mathrm{d}\zeta} - \beta^{\text{mol}}_{\lambda_0}, \tag{A.17}$$

whit

$$U(z_0, z) = P_{\lambda_0}(z) z^2 \exp\left\{ -2\left[S^{\text{par}}_{\lambda_0} - S^{\text{mol}}\right] \int_{z_0}^{z} \beta^{\text{mol}}_{\lambda_0}(\zeta)\mathrm{d}\zeta \right\} \tag{A.18}$$

and

$$V(z_0) = \frac{P_{\lambda_0}(z_0) z_0^2}{\beta^{\text{par}}_{\lambda_0}(z_0) + \beta^{\text{mol}}_{\lambda_0}(z_0)}. \tag{A.19}$$

A reference height z_0 with known aerosol properties is needed to solve Eqs. (A.17)–(A.19). The reference height is commonly set at the aerosol-free Troposphere, with an aerosol burden so low, that assuming it as zero (or a very low value, e.g. order of 10^{-8} m^{-1} sr^{-1}), is a fair-enough boundary condition to solve the lidar equation.

To apply the Klett-Fernald approach it is assumed an atmospheric scene where the extinction-to-backscatter ratio (or lidar ratio) does not change with height. This is not the case of a cloud layer present below the reference height. More importantly, the strong attenuation of light throughout the liquid layer makes the lidar return practically useless, so that a retrieval using the signal above the cloud is not possible. Nevertheless, this solution serves as a basis for further methodologies, aiming to analyze cloudy scenarios. This information, vertically resolved and as uncertain as possible, comprises an essential part for the study presented in this thesis: To evaluate the relation between cloud properties and the aerosol particles below the cloud. Alternative methods to derive the aerosol properties in cloudy periods are described in the next sections. First, the so-called Quasi-backscattering approach is presented and then a new, here named bottom-up, approximation for elastic signals is introduced.

A.3.2 Quasi-backscattering for high resolved retrievals

With the assumption of a constant and known lidar ratio (Equation A.16), the Klett-Fernald approach outlined in Section A.3.1, i.e. evaluating Eqs. (A.17), (A.18) and (A.19), enables the retrieval of the extinction and backscattering coefficient . This is a practical solution for single "'well behaving"' time-averaged profiles, but for small temporal resolutions the signal-noise does not allow stable retrievals making the calculations slow and noisy. To achieve

highly-temporally resolved retrievals, the so-called lidar calibration constant C_{λ_0} is an useful parameter which can be computed from Equation A.1, if the profiles of backscattering and extinction are previously computed in a cloud-free period.

$$C_{\lambda_0}(z) = \frac{P_{\lambda_0}(z)z^2}{\left[\beta^{\mathrm{par}}_{\lambda_0}(z) + \beta^{\mathrm{mol}}_{\lambda_0}(z)\right] O(z)} \exp\left\{2\int_0^z \left[\alpha^{\mathrm{par}}_{\lambda_0}(\zeta) + \alpha^{\mathrm{mol}}_{\lambda_0}(\zeta)\right] \mathrm{d}\zeta\right\}. \tag{A.20}$$

This constant can be used to compute the so-called attenuated backscatter, which depends only on the optical properties of the atmosphere:

$$\beta^{\mathrm{att}}_{\lambda}(z) = \frac{P_{\lambda_0}(z)z^2}{C_{\lambda_0}O(z)} = \left[\beta^{\mathrm{par}}_{\lambda_0}(z) + \beta^{\mathrm{mol}}_{\lambda_0}\right] T^{\mathrm{par}}_{\lambda_0}(z) T^{\mathrm{mol}}_{\lambda_0}(z) \tag{A.21}$$

Here the terms $T^{\mathrm{par}}_{\lambda_0}(z)$ and $T^{\mathrm{mol}}_{\lambda_0}(z)$ are introduced, and denote the round-trip transmission through aerosol particles and molecules respectively, i.e.:

$$T^{\mathrm{par}}_{\lambda_0}(z) = \exp\left[-2\int_0^z \alpha^{\mathrm{par}}_{\lambda_0}\mathrm{d}\zeta\right] \tag{A.22}$$

and

$$T^{\mathrm{mol}}_{\lambda_0}(z) = \exp\left[-2\int_0^z \alpha^{\mathrm{mol}}_{\lambda_0}\mathrm{d}\zeta\right] \tag{A.23}$$

Starting with the attenuated backscatter, [Baars et al., 2017] proposed a method to derive the optical properties of aerosol particles. The method begins with a first guess of the aerosol transmission, hence the aerosol contribution is initially neglected, i.e. $T^{\mathrm{par}}_{\lambda_0}(z) = 1$. Then, a first guess of the particle backscattering $\beta^{\mathrm{par*}}_{\lambda_0}(z)$ can be obtained from equation A.21.

$$\beta^{\mathrm{par*}}_{\lambda_0}(z) = \frac{\beta^{\mathrm{att}}_{\lambda_0}(z)}{T^{\mathrm{mol}}_{\lambda_0}(z)} - \beta^{\mathrm{mol}}_{\lambda_0}(z). \tag{A.24}$$

Calculations with Equation A.24 can be performed fast for a whole measurement period, without the need for temporal averaging. From Equation A.16 now a first guess of the extinction coefficient can be calculated by assuming a value of $S^{\mathrm{par}}_{\lambda_0}$, i.e. $\alpha^{\mathrm{par*}}_{\lambda_0}(z) = S^{\mathrm{par}}_{\lambda_0}\beta^{\mathrm{par*}}_{\lambda_0}(z)$. This quasi extinction is then used to calculate the transmission of aerosol particles as follows:

$$T^{\mathrm{par*}}_{\lambda_0}(z) = \exp\left[-2\int_0^z \alpha^{\mathrm{par*}}_{\lambda_0}\mathrm{d}\zeta\right] = \exp\left[-2\int_0^z S^{\mathrm{par}}_{\lambda_0}\beta^{\mathrm{par*}}_{\lambda_0}(z)\mathrm{d}\zeta\right]. \tag{A.25}$$

Evaluating then Eq. (A.21), a robust approximation of the aerosol backscattering coefficient can be obtained.

$${}^{\mathrm{quasi}}\beta^{\mathrm{par}}_{\lambda_0}(z) = \frac{\beta^{\mathrm{att}}_{\lambda_0}(z)}{T^{\mathrm{mol}}_{\lambda_0}(z)T^{\mathrm{par*}}_{\lambda_0}(z)} - \beta^{\mathrm{mol}}_{\lambda_0}(z). \tag{A.26}$$

Eq. (A.26) enables fast calculations of the aerosol optical properties. This has been tested and implemented in the Pollynet processing chain for automatic calculations at the wavelengths 1064, 532 and 355 nm [Baars et al., 2016; Engelmann et al., 2016]. This properties allow the calculation of further high resolved products such as the particle depolarization ratio at 532 and 355 nm, providing valuable information about the aerosol type with high temporal resolution [Baars et al., 2017].

Although the solution outlined in this section can be easily implemented, it would not suit in all cases because of the first assumption of $T^{\mathrm{par}}_{\lambda_0}(z) = 1$ for all the height range from the bottom to the reference height, Eq. (A.24) can deliver negative values, and then transmission values larger than one. Furthermore, the assumption of a lidar ratio needs a priori knowledge of the existing aerosol type. Similar to the Klett-Fernald solution, it can become unstable when the assumed lidar ratio is too high compared to reality.

To overcome this drawback, Eqs. (A.24), (A.25) and (A.26) can be evaluated iteratively, so that the aerosol contribution to the total transmission approaches towards the real profile. The number of iterations will depend on the situation. The larger the particle extinction and vertical extension of the aerosol layer are, the more iterations are needed. Furthermore, in cases when the Rayleigh scattering has a large contribution, such as for the case of $\lambda_0 =$ 355 nm, a considerable larger number of iterations are needed to obtain valid profiles of the backscattering coefficient.

A.3.3 Bottom-up approximation for elastic signals

To avoid the underestimation of $\beta^{\mathrm{par}*}_{\lambda_0}(z)$ because of the assumption of $T^{\mathrm{par}}_{\lambda_0}(z) = 1$, an alternative method is proposed in this section. Instead of calculating a first guess for the whole height range, the backscattering coefficient can be built up starting from the bottom. To perform this, knowledge of the extinction from the ground-base to z is needed.

Calculating the profiles starting from the bottom, $\beta^{\mathrm{aer}}_{\lambda_0}$ and hence $\alpha^{\mathrm{aer}}_{\lambda_0} = S^{\mathrm{par}}_{\lambda_0}\beta^{\mathrm{aer}}_{\lambda_0}$ from 0 to $z - \Delta z$ is available, with Δz the height resolution. To calculate the transmission until z, an approximation can be obtained by assuming the extinction at z equal to the extinction at $z - \Delta z$. The transmission of aerosol particles can be then calculated as follows:

$$\begin{aligned} T^{\mathrm{par}**}_{\lambda_0}(z) &= \exp\left[-2\int_0^z \alpha^{\mathrm{aer}}_{\lambda_0}(\zeta)\mathrm{d}\zeta\right] \\ &= \exp\left[-2\int_0^{z-\Delta z} \alpha^{\mathrm{aer}}_{\lambda_0}(\zeta)\mathrm{d}\zeta - 2\int_{z-\Delta z}^{z} \alpha^{\mathrm{aer}}_{\lambda_0}(\zeta)\mathrm{d}\zeta\right] \\ &\approx \exp\left[-2\int_0^{z-\Delta z} \alpha^{\mathrm{aer}}_{\lambda_0}(\zeta)\mathrm{d}\zeta - 2\Delta z\alpha^{\mathrm{aer}}_{\lambda_0}(z-\Delta z)\right], \end{aligned} \tag{A.27}$$

and it is illustrated in Figure A.4.

With the transmission value obtained from Eq. (A.27), Eq. (A.26) can be evaluated for

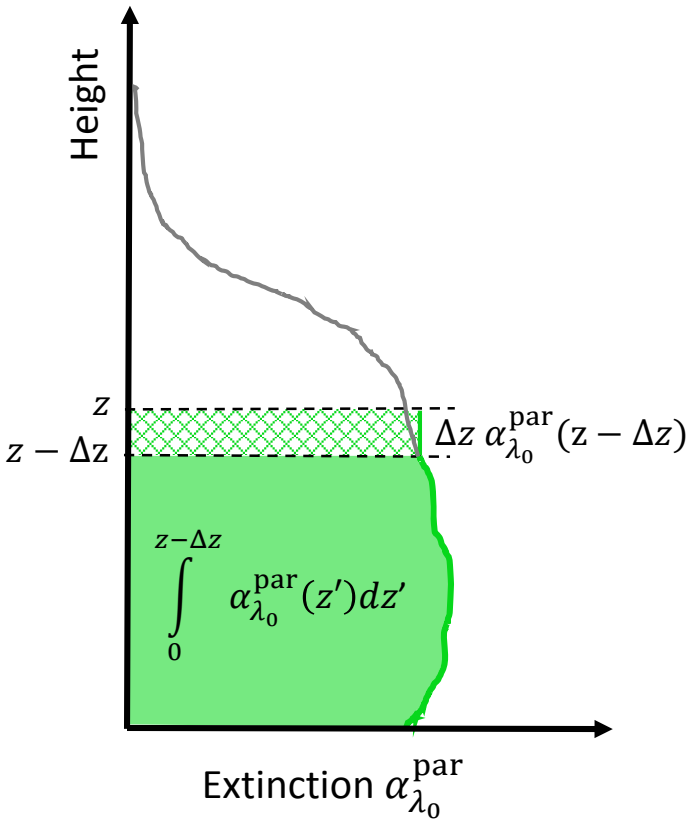

Figure A.4: Schematic view of the bottom-built approximation. The integral from 0 to z is approximated as the sum of the integral from 0 to $z - \Delta z$ plus the grid-area

each height bin starting from the first one on the ground-base using the following expression:

$$^{\text{bottom}-\text{up}}\beta^{\text{par}}_{\lambda_0}(z) = \frac{\beta^{\text{att}}_{\lambda_0}(z)}{T^{\text{mol}}_{\lambda_0}(z)T^{\text{par}**}_{\lambda_0}(z)} - \beta^{\text{mol}}_{\lambda_0}(z). \tag{A.28}$$

First, it shall be noted that the term $-2\Delta z\alpha^{\text{aer}}_{\lambda_0}(z - \Delta z)$ in Eq. (A.27) is really small compared the integral term, so that one could also neglect it and simply consider only the left term in the exponential. To corroborate the validity of this simplification, a simple simulation using an artificial aerosol backscattering profile, as shown in Fig. A.5a, was considered. It was found that the retrieval of the backscattering coefficient using Eq. (A.28), when neglecting previously the second term in Eq. (A.27), is in average 0.07% smaller than when considering also the second term in Eq. (A.27). The largest difference was found for the first height bins, about 0.2% in first 1000 meters, and smaller as height increases, as shown in Fig. A.5b. This difference is so small that the term $-2\Delta z\alpha^{\text{aer}}_{\lambda_0}(z - \Delta z)$ can just be neglected.

One strength of this methodology is that the retrieval can be performed at cloudy periods and with high temporal resolution. A possible drawback relies on the first meters where the most backscattered photons does not get into the receiver FOV. As lights goes up more and

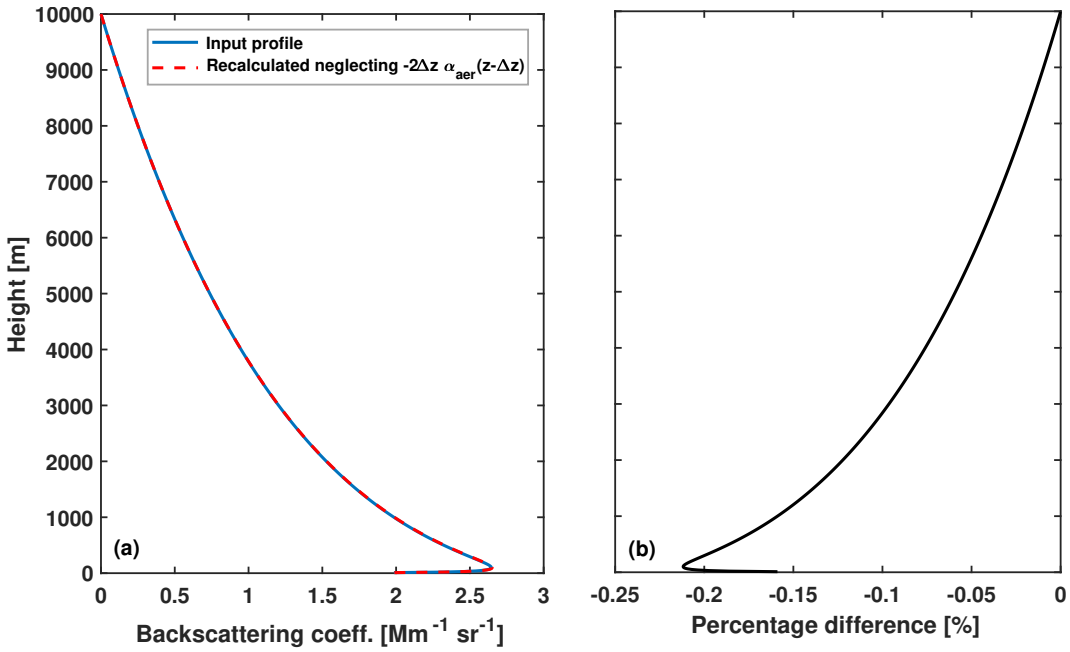

Figure A.5: (left) Synthetic backscattering profiles considered as example, the corresponding extinction profiles was computed as $\alpha^{\text{aer}}_{\lambda_0} = 40\beta^{\text{aer}}_{\lambda_0}$. (b) Percentage difference between the backscattering profiles obtained when evaluating Eq. (A.27) without the second term, compared to the values obtained when including it.

more of the backscattered light can then be observed until at a given height, the whole laser horizontal section is fully inside the footprint of the receiver. A retrievable function, called overlap function, can be used to describe the fraction of backscattered light that the lidar measures, so that the signal at the first hundreds of meters can also be used. In the Polly systems and in the lidar MARTHA the overlap function can be determined experimentally according to [Wandinger and Ansmann, 2002], allowing the correction of the overlap on the lidar signal. However, the smaller the value of this function is (i.e. first height bins), the more inaccurate it is, making the signal in the very first tens of meters useless. In this work we assume the first 15 bins (112.5 meters) as equal to the 15th bin, to at least account for a non-zero aerosol attenuation in the first meters.

A.3.4 Evaluation of methods based on elastic lidar

The same measurement example analyzed in the previous section was analyzed using the methods described in this section as well. The assumption of the lidar ratio value can produce large errors in the results, in fact, the wrong lidar ratio can induce errors of more than 100% in the backscattering coefficient [Sasano et al., 1985]. To avoid large errors the lidar ratios were calculated from the independent retrievals of the extinction and backscattering coefficients using elastic and Raman signals [Ansmann et al., 1990, 1992], as shown in the previous section. Mean values of 55 and 40 sr were obtained for 355 and 532 nm. For

1064 nm a lidar ratio of 40 was assumed. The backscattering coefficient was then computed using Eqs. (A.4)–(A.19). The resulting backscattering profiles at 355, 532 and 1064 nm are presented in Figure A.6 (a), (b) and (c) respectively.

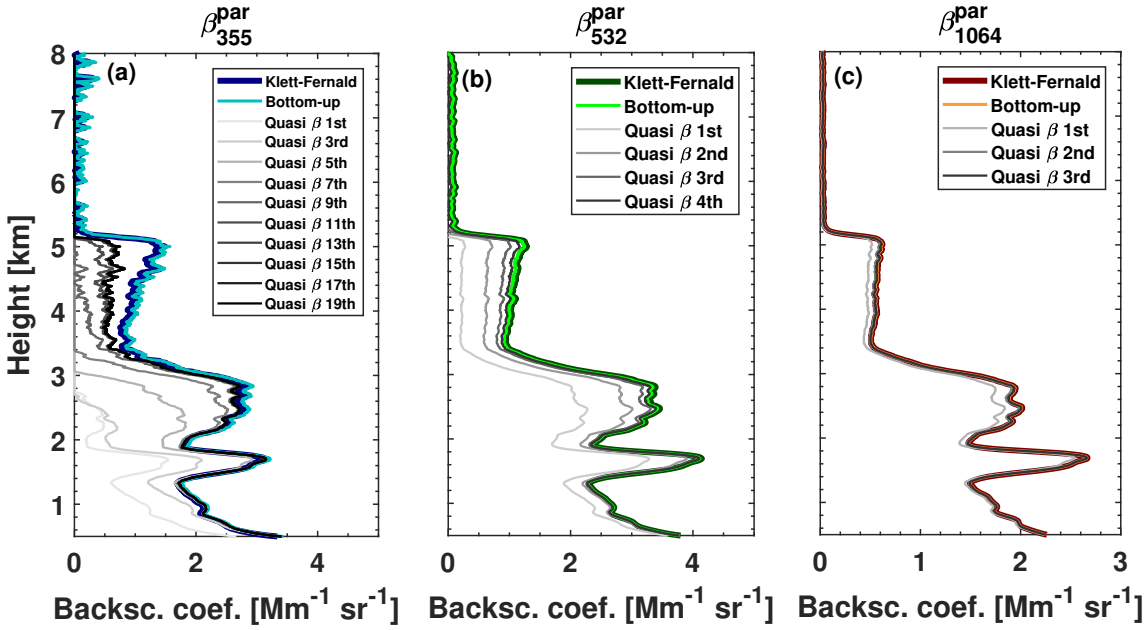

Figure A.6: Profiles of the aerosol backscattering coefficient obtained by different methods. The dark colored curves are the solutions obtained with the Klett-Fernald method, the bright colored lines the solutions obtained with the approximation proposed in this chapter, and the grey lines are the solutions obtained from Baars et al. [2017]. This solutions have been obtained iteratively.

The optical properties can be used now to calculate the lidar constants using Eq. (A.20). In this example the following mean values were obtained: $C_{355} = 5.113 \times 10^{11}$, $C_{532} = 1.242 \times 10^{12}$, $C_{1064} = 3.075 \times 10^{12}$ MHz m^{-3}sr. Making use of these constants, the inversion process with the schemes outlined in Sections A.3.2 and A.3.3 can be done. The backscattering profiles are presented in Figure A.6. The so-called quasi-approximation is shown in greyish colors, and the bottom-up approximation is shown in bright colors. The Klett-Fernald solutions are showed in darker colors. In the case of the first iteration using the quasi-approximation, an underestimation is present at the three wavelengths. Further iterations were done to match the profiles retrieved with the Klett-Fernald Method, considered as true profile. In the case of 1064 nm, a second iteration is enough to match the Klett-Fernald result, at 532 nm four iterations are needed. At 355 nm however, even after 8 iterations, the approach still has issues matching the reference profile, given the large contribution of Rayleigh scattering($\beta^{mol}_{\lambda_0}$), so that neglecting the aerosol transmission in Eq. (A.24) leads to negative values. On the other hand, the profiles obtained with the bottom-up approximation agrees with the reference profiles, showing the accuracy of the proposed approximation. There are little differences in the case of 355 nm mainly due to the accuracy of the calibration constant, which exhibit especially large variations at this wavelength.

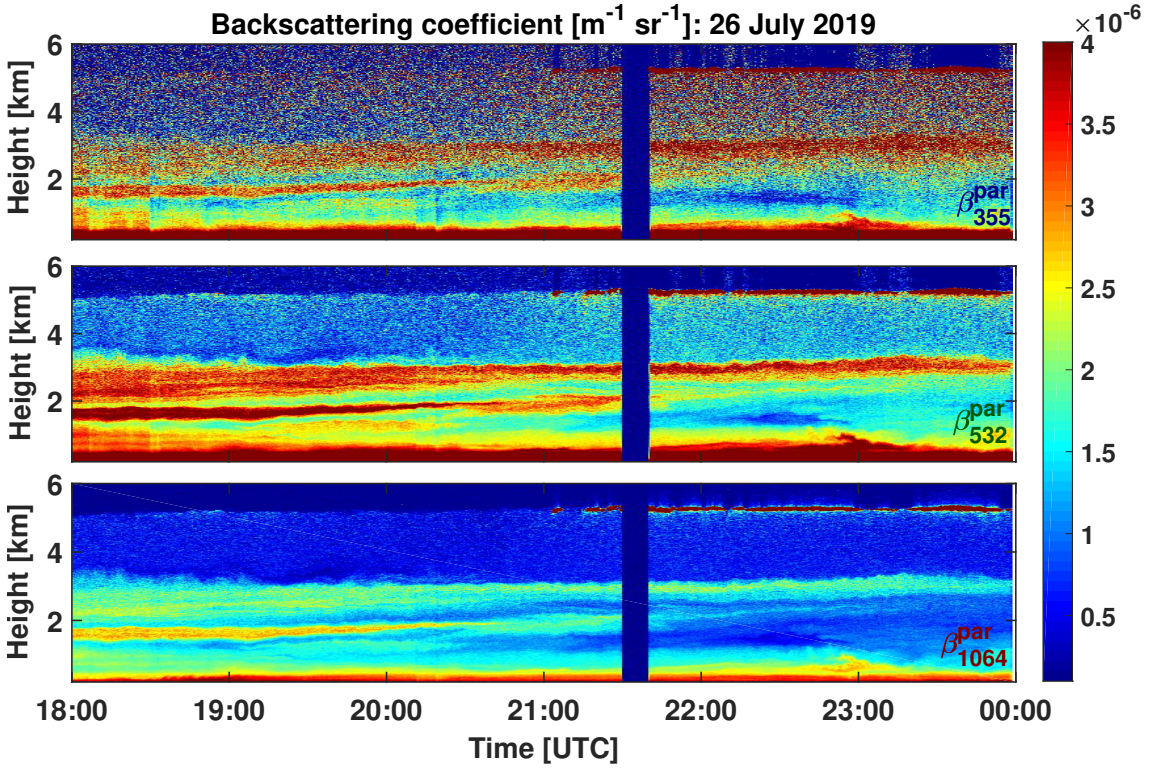

Figure A.7: High resolved backscattering profiles obtained with the methodology outlined in seciton A.3.3. The measurement period is the 26 July 2019 18:00-24:00, with temporal resolution of 30 seconds.

The bottom-up approach was applied to the whole measurement period, obtaining the profiles shown in Figure A.7. This method provides valid profiles, but only up to the cloud layer, as here a different lidar ratio and multiple scattering effect plays an important role. The goal of the so-called bottom-up approximation is however only the retrieval of extinction coefficients below the cloud base of clouds, where the interaction between aerosol particles and the cloud layer takes place. The inability to assess information in and above the cloud is not harmful for the porpoises of this work.

A.3.5 Microphysical properties from optical properties

With high-resolved extinction profiles ($S^{\text{par}}_{\lambda_0}\beta^{\text{par}}_{\lambda_0}$), further products, such as the particle number concentration can be estimated [Mamouri and Ansmann, 2016]. Using conversion values for desert dust, i.e. $c_{100,\text{d}} = 11.8$ and $x_\text{d} = 0.76$, the particle number concentration can be estimated as follows:

$$n_{100,\text{d}} = c_{100,\text{d}} \times (\alpha^{\text{par}}_{532})^{x_\text{d}}\,, \tag{A.29}$$

where 100 denotes particles with radius larger than 100 nm, the input value of the extinction is in Mm^{-1}, and the number concentration output in cm^{-3}. Figure A.8 shows the number concentrations os particles larger than 100 nm obtained with Eq. (A.29). The cloud is

removed from the calculation.

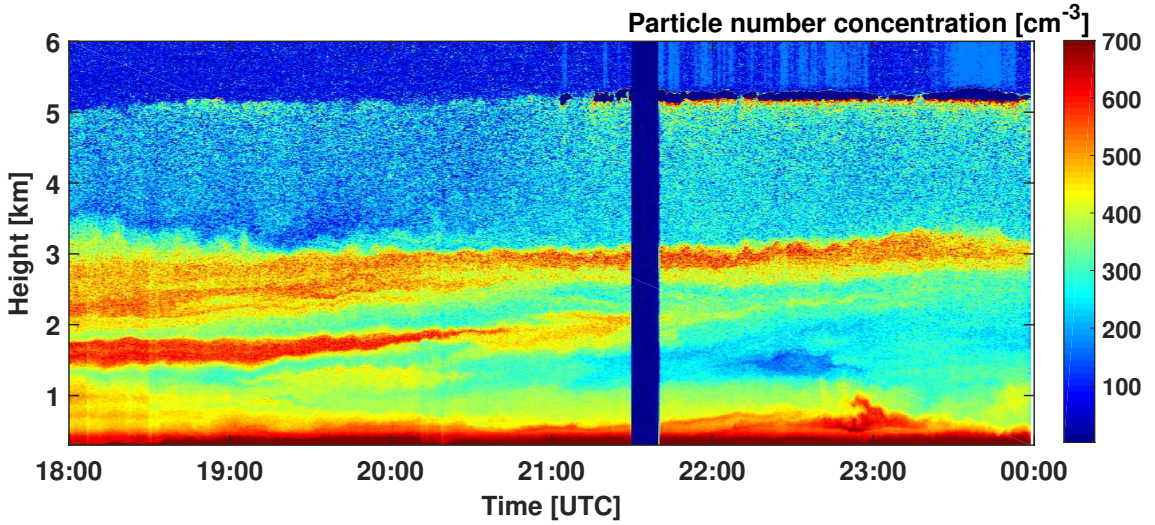

Figure A.8: High resolved particle number concentration according to [Mamouri and Ansmann, 2016]. The calculations are based on the extinction profiles at 532 nm.

Conversion factors $c_{100,\mathrm{d}}$ and x_{d} are available in the literature for several aerosol types and locations. The particle number concentration can be then used to estimate CCN (cloud condensation nuclei) concentrations by multiplying a enhancement factor $f_{\mathrm{ss,d}}$, that will depend in the level of supersaturation in the ambient cloud layer. The supersaturation (ss) depends mostly on the updraft velocities and typically is in the range of ss from 0.1 to 1 % [Mamouri and Ansmann, 2016].

$$N_{\mathrm{CCN,ss,d}} = f_{\mathrm{ss,d}} \times n_{100,\mathrm{d}} \tag{A.30}$$

Not only concentrations of dust particles can be obtained from lidar observations, but also marine and continental aerosol can be obtained by using the respective conversion parameters provided in Mamouri and Ansmann [2016]. The individual contributions of dust and non-dust particles in well mixed aerosol layers can be assessed with a simple mixing rule, as proposed by Tesche et al. [2009], in which the particle depolarization ratio is the intensive parameter used to separate the aerosol load between dust and non-dust particles. The particle depolarization ratio δ_{par} can be obtained from the measured volume depolarization ratio $\delta_{\mathrm{in}}(z)$ (at the $\mathrm{FOV_{in}}$) and the particle and molecular backscattering coefficients $\beta^{\mathrm{par}}_{\lambda_0}(z)$ and $\beta^{\mathrm{mol}}_{\lambda_0}(z)$.

$$\delta_{\mathrm{par}} = \frac{R\delta_{\mathrm{in}}(\delta_{\mathrm{mol}}+1) - \delta_{\mathrm{mol}}(\delta_{\mathrm{in}}+1)}{R(\delta_{\mathrm{mol}}+1) - (\delta_{\mathrm{in}}+1)}, \tag{A.31}$$

with

$$R = \frac{\beta^{\mathrm{par}}_{\lambda_0} + \beta^{\mathrm{mol}}_{\lambda_0}}{\beta^{\mathrm{mol}}_{\lambda_0}}. \tag{A.32}$$

δ_{mol} denotes the depolarization ratio produced by air molecules, which is well known to be about 0.005 for visible light [Behrendt et al., 2002; Freudenthaler et al., 2016b].

With the individual contributions separated, the individual and then total concentration of CCN can be derived with high temporal resolution. This was an important feature of the data analysis for the instrument at Dushanbe, Tajikistan.

Appendix B

Characterization of DFOV-Depol lidar

Another important aspect of this research was the characterization the new polarization channels to expand a SFOV into a DFOV system. Two unknown parameters have to be determined to derive the volume depolarization ratio from the lidar measurements.

We start with the volume depolarization ratio at the inner FOV, which can be easily retrieved from the cross and total signals after performing the so called ±45◦ calibration [Freudenthaler, 2016a; Engelmann et al., 2016].

$$\delta_{\mathrm{in}}(z) = \frac{1 - \delta'_{\mathrm{in}}(z)/C_{\mathrm{in}}}{\delta'_{\mathrm{in}}(z)F_{\mathrm{t,in}}/C_{\mathrm{in}} - F_{\mathrm{c,in}}}, \tag{B.1}$$

where C_{in} represent the calibration constant of the $\mathrm{FOV_{in}}$ defined in Engelmann et al. [2016], and $F_{\mathrm{t,in}}$ and $F_{\mathrm{t,in}}$ denote the so-called transmission ratio of the total and cross channel at the $\mathrm{FOV_{out}}$, respectively. This parameter is defined as

$$F_{\mathrm{c,in}} = \frac{\eta_{\mathrm{c,in},\perp}}{\eta_{\mathrm{c,in},\parallel}}, \tag{B.2}$$

where the subindex c,in denotes cross channel of the $\mathrm{FOV_{in}}$. For the inner FOV these parameters are determined via an experimental setup with an artificial light source [Mattis et al., 2009].

The same equation (B.3) can be used to determine the depolarization ratio at the second FOV ($\mathrm{FOV_{out}}$).

$$\delta_{\mathrm{out}}(z) = \frac{1 - \delta'_{\mathrm{out}}(z)/C_{\mathrm{out}}}{\delta'_{\mathrm{out}}(z)F_{\mathrm{t,out}}/C_{\mathrm{out}} - F_{\mathrm{c,out}}}, \tag{B.3}$$

To calibrate the polarization channels of the second FOV, the observed depolarization ratio at the first FOV can be exploited. Assuming that in the cloud-free range, the depolarization values does not depend on the FOV size, the calibration constant C_{out} can be calculated evaluating Eq. (B.3).

$$C_{\mathrm{out}} = \delta'_{\mathrm{out}}(z)\left(\frac{1 + F_{\mathrm{t,out}}\delta_{\mathrm{in}}(z)}{1 + F_{\mathrm{c,out}}\delta_{\mathrm{in}}(z)}\right). \tag{B.4}$$

To evaluate this equation, the transmission ratios $F_{\mathrm{t,out}}$ and $F_{\mathrm{c,out}}$ are needed. In the case of the total-channel, the constant $F_{\mathrm{t,out}}$ is assumed as one, since the receiver consist of a mirror and an optical fiber, after which all polarization information is lost. The value of $F_{\mathrm{c,out}}$ is in a first instance unknown. To determine this constant, an usual method is to use an artificial light-source in combination with a rotating polarization filter in front of the receiver[Mattis et al., 2009]. Because the current system is not capable yet to perform this measurement (in the case of the $\mathrm{FOV_{out}}$), an alternative way of calculate the transmission ratio is to make use of a measured depolarization profile, that varies on a wide range of values. Similar as done in [Jimenez et al., 2019], the determination of two calibration constants, namely C_{out} and $F_{\mathrm{c,out}}$ is possible given the non-linearity of the depolarization equation. Evaluation of Eq. (B.3) at two heights, with strong contrast on the depolarization values, for the $\mathrm{FOV_{out}}$ we can obtain:

$$F_{\mathrm{c,out}} = \frac{[\delta_{\mathrm{in}}(z_i)+1]\,[1-\delta_{\mathrm{in}}(z_j)/\delta_{\mathrm{in}}(z_i)]\,\delta'_{\mathrm{out}}(z_i)}{[\delta_{\mathrm{in}}(z_j)+1]\,\delta_{\mathrm{in}}(z_i)\delta'_{\mathrm{out}}(z_j) - \delta_{\mathrm{in}}(z_j)\,[\delta_{\mathrm{in}}(z_i)+1]\,\delta'_{\mathrm{out}}(z_i)} - 1/\delta_{\mathrm{in}}(z_i). \tag{B.5}$$

Here the two height bins z_i and z_j must have a strong contrast on their depolarization values, e.g. cases with cirrus clouds or mineral dust. The parameter δ_{in} is the retrieved depolarization ratio at the $\mathrm{FOV_{in}}$ and δ'_{out} the ratio of the cross and total signal of the $\mathrm{FOV_{out}}$.

In this way the volume depolarization ratio at the $\mathrm{FOV_{out}}$ can be obtained as follows:

$$\delta(z)_{\mathrm{out}} = \frac{1-\delta'_{\mathrm{out}}(z)/C_{\mathrm{out}}}{\delta'_{\mathrm{out}}(z)F_{\mathrm{t,out}}/C_{\mathrm{out}} - F_{\mathrm{c,out}}}\,. \tag{B.6}$$

In Figure B.1 is one example presented. The measurement of the 22 March 2019 between 00:00 and 06:00 UTC obtained with the Polly system located in Punta Arenas. In this case a liquid layer with little depolarization was observed at about 1.2 km and an ice cloud with high depolarization values at 6 km height. To evaluate Eq. (B.5), using the signal ratio shown in Figure B.1 (a) and the depolarization ratio δ_{in} in Figure B.1 (b), the height ranges $z_i = 3-3.5$ km and $z_j = 5.8-6.3$ km were chosen. Evaluating Eq. (B.4) and B.5 a mean value of $F_{\mathrm{c,out}} = 462$ and $C_{\mathrm{out}} = 0.0442$ were obtained. With this constants, the volume depolarization ratio δ_{out}, showed in Figure B.1 (b), was computed.

B.1 Transmission ratio based on long-term analysis

This procedure was applied to several measurements among the year, in order to have a more accurate value of the transmission ratio $F_{\mathrm{c,out}}$. This ratio should remain constant with time, as it depends on the optical set up of the polarization channels, and not on the laser energy or detector efficiency, as the calibration constants C_{in} and C_{out} do. A cloud-free range and an ice-cloud range was selected for each case and the transmission ratio was calculated.

In Figure B.2 are the results presented. The values of the transmission ratios obtained using Eq. (B.5) are shown in Figure B.2(a). Small variations in the values can be noted in the

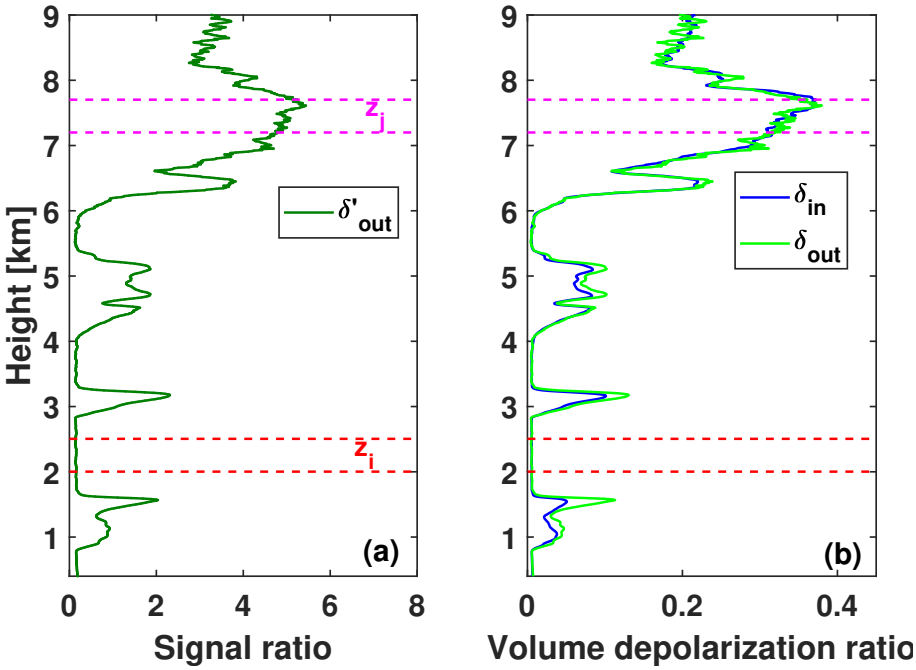

Figure B.1: (a) Profile of the signal ratio S_c/S_t for the $\mathrm{FOV_{out}}$. (b) Profiles of the depolarization ratio. In blue is δ_{in}, and in green δ_{out} computed using the calibration constants $F_{\mathrm{c,out}}$ and C_{out} obtained

course of the year, but there a point at which the transmission ratio seems to have changed to a negative value, which is physically not possible. This results were found to be originated by a change on the transmission efficiency of the $\mathrm{FOV_{in}}$, which is confirmed when considering the mean values of the depolarization of the aerosol particles at Punta Arenas over the year as shown in Fig. B.2(c). Before the 10 of August a depolarization ratio of about 0.006 was obtained, while a value of about 0.011 was obtained afterwards. The reason for this change in the transmission ratio are not all clear, likely, during a maintenance between July and August, changes were induced on the optical system changing the transmission ratio.

In addition, to provide clarity between the approaches outlined in the first publication, panel (b) present the evolution of the so-called cross-talk parameter, which is the constant introduced in Jimenez et al. [2019] to account for the instrumental effects in terms of polarization. The conversion of this constant to the transmission-ratio used here, which was introduced by Engelmann et al. [2016], can be done with the following expression:

$$\xi_{\mathrm{t,out}} = \frac{1 + 1/F_{\mathrm{c,out}}}{1 - 1/F_{\mathrm{c,out}}}. \tag{B.7}$$

The value of this cross-talk parameter is shown on panel (b), which by definition, it can not be smaller than one. But with the wrong transmission ratio, values not allowed were obtained after the 10 August, i.e., $\xi_{\mathrm{t}} < 1$.

To match the values on the second period with the values of the first period, a value of $F_{\mathrm{c,in}} = 150$ after the 10 of August was determined. Figure B.3 show the values obtained,

varying the transmission ratio of the $\mathrm{FOV_{in}}$ to 150. A mean value of $F_{\mathrm{c,out}} = 520$ was obtained for the measurements before 10 of August, and a value of $F_{\mathrm{c,out}} = 480$ afterwards.

The proposed method have been used to calibrate the lidar systems with DFOV-Depol capabilities, such as the Polly in the LACROS [Bühl et al., 2013] and OCEANET [Yin et al., 1981; Griesche et al., 2020] mobile stations, and also on the system located at Dushanbe for long-term observations of central Asia aerosol conditions.

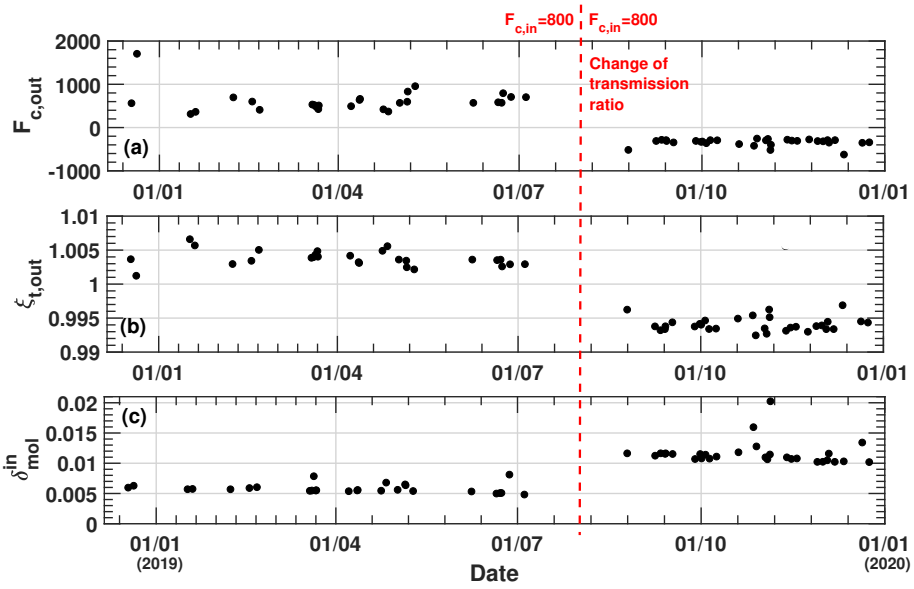

Figure B.2: (a) Time series of the channel cross-talk parameter used in [Jimenez et al., 2019], (b) shows the obtained transmission ratios $F_{\mathrm{c,out}}$ according to [Engelmann et al., 2016]. (c) Mean depolarization values at the cloud-free region. The red line denotes the day when the transmission ratio changed.

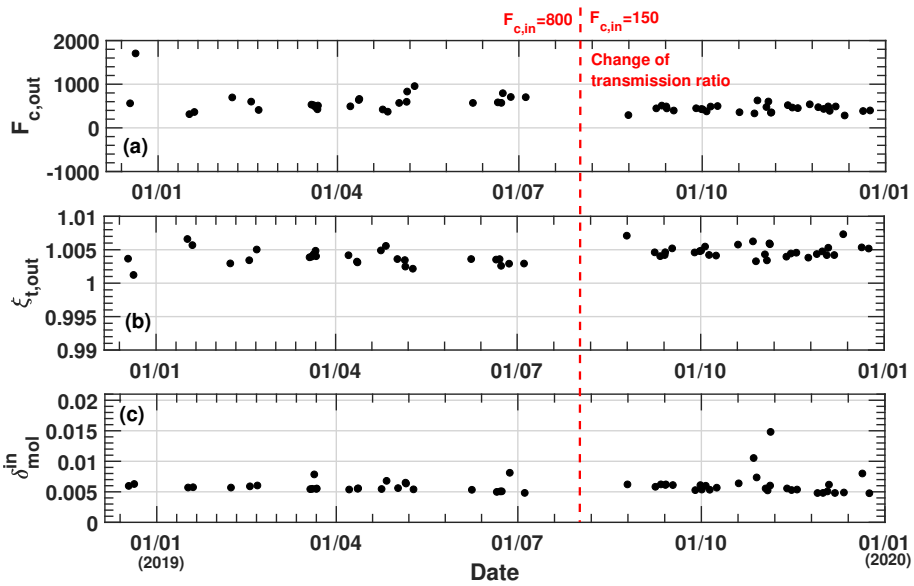

Figure B.3: Same parameters as shown in Figure B.2. Before the 10 August 2010 a value of $F_{\mathrm{c,in}} = 800$ was used for the calculations, afterward a value of $F_{\mathrm{c,in}} = 150$ was used.

Appendix C

Author's contributions to the three publications

First publication: Polarization lidar: an extended three-signal calibration approach

For this publication, I developed the theoretical framework to calibrate a three-channel polarization lidar. I discussed about the analytical details with Albert Ansmann, Moritz Haarig and Ronny Engelmann. To test the proposed approach I built a three-channel lidar receiver in the lab at TROPOS, which we then integrated into the MARTHA system. Ronny Engelmann supported me with this task. The measurements with the MARTHA system during 2017 were performed by me and I wrote the code to analyze the data with the proposed three-signal approach. Moritz Haarig performed simultaneous measurements with the BERTHA system and provided the analyzed data. The comparisons between the MARTHA and BERTHA depolarization products was done by me. I wrote the manuscript in close cooperation with Albert Ansmann. Moritz Haarig contributed with proofreading and his expert view on polarization lidar. Albert Ansmann and I took care of the submission and review process.

Second publication: The dual-field-of-view polarization lidar technique: A new concept in monitoring aerosol effects in liquid-water clouds – Theoretical framework

For this paper, I conceived the idea of a new measurement principle and developed the method DFOV-Depol to retrieve cloud microphysical properties. I performed the multiple-scattering simulations and developed the retrieval scheme based on the simulation results.

Two multiple scattering models were confronted for this publication. Aleksey Malinka developed and provided the analytical multiple-scattering code, which was used to to perform the simulations, and David Donovan performed simulations with the ECSIM multiple-scattering model and provided the outputs, which I then compared with the analytical code outputs. Aleksey Malinka and David Donovan were an great help to better understand the multiple scattering effect. I had long discussions about the design of the simulations study and of the retrieval scheme with Albert Ansmann, Ronny Engelmann, Ulla Wandinger and Joerg Schmidt. I prepared the manuscript and it was reviewed by Albert Ansmann. We both took care of the review process.

Third publication:
The dual-field-of-view polarization lidar technique: A new concept in monitoring aerosol effects in liquid-water clouds – Case studies

For the third publication, I prepared the code to apply the method proposed in the second publication and analyzed all the measurements obtained during 2018-2019 at Punta Arenas, Chile in the framework of the DACAPO-PESO campaign. Before the campaign, and in order to extend the system capabilities, Ronny Engelmann, Robert Wiesen, and I upgraded the Polly instrument into a DFOV-Depol system. Ronny Engelmann, Patric Seifert, Martin Radenz, Boris Barja, and the rest of the DACPO-PESO crew took are of the instruments and the logistic o the two-year field campaign. During 2019, I was in charge of taking care of the equipment at Punta Arenas in two monthly stays. Zhenpping Yin determined the lidar calibration constants, which was used for the aerosol retrieval below the cloud base. Johannes Bühl took care of the vertical wind observations and Patric Seifert analyzed the radar data. For comparison, David Donovan developed and provided to me the code to analyze single-FOV polarization measurements. The discussion and interpretation of the observations was mostly organized by Albert Ansmann and me and it was strongly supported by David Donovan, Aleksey Malinka, Patric Seifert, Jörg Schmidt and Ulla Wandinger. Albert Ansmann and I prepared the manuscript together and we took care of the peer-review.

Appendix D

Lists

D.1 List of Figures

D.2 List of Tables

D.3 List of Symbols (excluding cumulative part)

Symbol	Units	Description
α	m^{-1}	Cloud extinction coefficient.
$\alpha_{\lambda_0}^{\mathrm{mol}}$	m^{-1}	Molecular extinction coefficient at the wavelength λ_0 (subindex may also be λ_{Ra}).
$\alpha_{\lambda_0}^{\mathrm{par}}$	m^{-1}	Particle extinction coefficient at the wavelength λ_0 (subindex may also be λ_{Ra}). α_{par} is also used to denote $\alpha_{\lambda_0}^{\mathrm{par}}$.
$\beta_{\lambda_0}^{\mathrm{mol}}$	$\mathrm{m}^{-1}\ \mathrm{sr}^{-1}$	Molecular backscattering coefficient at the wavelength λ_0 (subindex may also be λ_{Ra}).
$\beta_{\lambda_0}^{\mathrm{par}}$	$\mathrm{m}^{-1}\ \mathrm{sr}^{-1}$	Particle backscattering extinction coefficient at the wavelength λ_0 (subindex may also be λ_{Ra}).
δ_{in}	–	Volume depolarization ratio at the $\mathrm{FOV_{in}}$ (subindex out is used to denote the value at the $\mathrm{FOV_{out}}$).
δ'_{in}	–	Cross-to-total signal ratio at the $\mathrm{FOV_{in}}$ (subindex out is used to denote the value at the $\mathrm{FOV_{out}}$).
ξ	–	Cross talk parameter for a three-channel polarization system.
λ_0	nm	Wavelength of laser beam.
λ_{Ra}	nm	Wavelength of Raman return.
å	–	Ångström exponent.
A	–	Planetary albedo.
A_{c}	–	Cloud albedo.
A_{clr}	–	Clear-sky albedo.
C_{λ_0}	MHz m^3 sr	Calibration constant of an elastic channel.
$C_{\lambda_{\mathrm{Ra}}}$	MHz m^3 sr	Calibration constant of an Raman channel.
C_{in}	–	Inter-channel constant of the polarization channels at the $\mathrm{FOV_{in}}$ (subindex out is used to denote the value at the $\mathrm{FOV_{out}}$).
$\frac{\mathrm{d}\sigma_{\lambda_0}^{\mathrm{mol}}}{\mathrm{d}\Omega}(\pi)$	$\mathrm{m}^2\ \mathrm{sr}^{-1}$	Differential cross section for Rayleigh scattering by air molecules in the backward direction.
$\frac{\mathrm{d}\sigma_{\lambda_{\mathrm{Ra}}}^{\mathrm{N_2}}}{\mathrm{d}\Omega}(\pi)$	$\mathrm{m}^2\ \mathrm{sr}^{-1}$	Differential cross section for Raman scattering by nitrogen molecules in the backward direction.
$E_{\mathrm{aci}}^{N_{\mathrm{d}}}$	–	Aerosol cloud interaction index $\partial_{\ln} N_{\mathrm{d}} / \partial_{\ln} N_{\mathrm{CCN}}$.
$E_{\mathrm{aci}}^{R_{\mathrm{e}}}$	–	Aerosol cloud interaction index in terms of effective radius $-\partial_{\ln} R_{\mathrm{e}} / \partial_{\ln} N_{\mathrm{CCN}}$.
$F_{\mathrm{t,in}}$	–	Transmission ratio of the cross to parallel efficiencies of the total-scattering channel at the $\mathrm{FOV_{in}}$ (subindex t,out is used to denote the value at the $\mathrm{FOV_{out}}$).
$F_{\mathrm{c,in}}$	–	Transmission ratio of the cross to parallel efficiencies of the cross-polarized channel at the $\mathrm{FOV_{in}}$ (subindex c,out is used to denote the value at the $\mathrm{FOV_{out}}$).

Symbol	Unit	Description
$F^{\downarrow}$	Wm^{-2}	Downwelling solar radiation.
F_{aci}	Wm^{-2}	Radiative forcing on the top of the atmosphere due to aerosol-cloud. interactions.
$F_{\mathrm{aci}}^{\mathrm{Twomey}}$	Wm^{-2}	Radiative forcing on the top of the atmosphere only due to the Twomey effect.
f_{anth}	–	Fraction of anthropogenic CCN to the total amount of CCN.
f_{c}	–	Cloud fraction
f_{ss}	–	enhancement factor for Extinction–CCN conversion.
n_{50}	cm^{-3}	Number concentration of particles larger than 50 nm.
N_{CCN}	cm^{-3}	Number concentration of cloud condensation nuclei.
N_{d}	cm^{-3}	Number concentration of cloud droplets.
N^{mol}	cm^{-3}	Number concentration of air molecules.
O	–	lidar overlap function.
P_{λ_0}	MHz	Lidar elastic return (instead of Watt, the unit of detection is used).
$P_{\lambda_{\mathrm{Ra}}}$	MHz	Lidar Raman return.
R_{e}	μm	Cloud effective radius.
S^{mol}	sr	Extinction to backscatter ratio for air molecules.
S^{par}	sr	Extinction to backscatter ratio for aerosol particles.
w_l	gm^{-3}	Liquid-water content.
z	m	Height range respect to the ground base.

D.4 List of Abbreviations

AERONET	Aerosol Robotic Network
AOD	Aerosol Optical Depth
ACI	Aerosol-cloud interaction
BERTHA	Backscatter, Extinction, lidar Ratio, Temperature, Humidity profiling Apparatus
CALIPSO	Cloud-Aerosol Lidar and Infrared Pathfinder Satellite Observations
CCN	Cloud Condensation Nuclei
DB	Dushanbe, Tajikistan
DFOV	Dual Field of view
EARLINET	European Aerosol Research Lidar Network
EarthCARE	Earth Clouds, Aerosol and Radiation Explorer
Eq.	Equation
et al.	*et alii* (latin for 'and others')
Fig.	Figure
GDAS	Global Data Assimilation System
HYSPLIT	Hybrid Single–Particle Lagrangian Integrated Trajectory model
INP	Ice Nucleating Particles
IPCC	International Panel on Climate Change
GDAS	Global Data Assimilation System
ICON-LEM	ICOsahedral Non-hydrostatic Large-Eddy Model
LACROS	Leipzig Aerosol and Cloud Remote Observations System
Laser	Light amplification by stimulated emission of radiation
Lidar	Light detection and ranging
MARTHA	Multiwavelength Atmospheric Raman lidar for Temperature, Humidity, and Aerosol profiling
MERRA-2	Second Modern-Era Reanalysis for Research and Applications
PA	Punta Arenas, Chile
PBL	Planetary Boundary Layer
PollyNET	Portable Lidar NETwork
Polly	Portable Lidar
Radar	Radio Detection and Ranging
RH	Relative Humidity
RF	Radiative forcing
RV	Research Vessel
SFOV	Single Field of view
Sect.	Section
TROPOS	Leibniz Institute for Tropospheric Research
UTC	Universal Coordinated Time

Bibliography

Abdul-Razzak, H., Ghan, S. J., and Rivera-Carpio, C.: A parameterization of aerosol activation. 1. Single aerosol type, J. Geophys. Res., 103, 6123–6131, https://doi.org/10.1029/97JD03735, 1998.

Ackerman, A. S., O. B. Toon, J. P. Taylor, D. W. Johnson, P. V. Hobbs, and R. J. Ferek: Effects of Aerosols on Cloud Albedo: Evaluation of Twomeyś Parameterization of Cloud Susceptibility Using Measurements of Ship Tracks, J. Atmos. Sci., 57, 2684-2695, https://doi.org/10.1175/1520-0469(2000)057<2684:EOAOCA>2.0.CO;2, 2000.

Ackerman, A. S., O. B. Toon, D. E. Stevens, A. J. Heymsfield, V. Ramanathan, and E. J. Welton, Reduction of tropical cloudiness by soot, Science, 288, https://doi.org/10.1126/science.288.5468.1042, 2000.

Ackerman, A.S, M.P. Kirkpatrick, D.E. Stevens, and O.B. Toon: The impact of humidity above stratiform clouds on indirect aerosol climate forcing, Nature, 432, 1014-1017, https://doi.org/10.1038/nature03174 2004

Albrecht, B.: Aerosols, cloud microphysics, and fractional cloudiness, Science, 245, https://doi.org/10.1126/science.245.4923.1227, 1989.

Alterskjaer, K., Kristjánsson, J. E., and Seland, O.: Sensitivity to deliberate sea salt seeding of marine clouds – observations and model simulations, Atmos. Chem. Phys., 12, 2795–2807, https://doi.org/10.5194/acp-12-2795-2012, 2012.

Anderson, T. L., Charlson, R. J., Winker, D. M., Ogren, J. A., and Holmen, K.: Mesoscale variations of tropospheric aerosols, J. Atmos. Sci., 60, 119–136, https://doi.org/10.1175/1520-0469(2003)060%3C0119:MVOTA%3E2.0.CO;2, 2003.

Andreae, M. O., Jones, C. D., and Cox, P. M.: Strong present-day aerosol cooling implies a hot future, Nature, 435, 1187-1190, https://doi.org/10.1038/nature03671, 2005.

Ångström, A.: The parameters of atmospheric turbidity, Tellus, 16, https://doi.org/10.1111/j.2153-3490.1964.tb00144.x, 1964.

Ansmann, A., and Müller, D.: Lidar and atmospheric aerosol particles, in Lidar Range-Resolved Optical Remote Sensing of the Atmosphere, edited by C. Weitkamp, pp. 105-141, Springer, Berlin/Heidelberg, https://doi.org/10.1007/0-387-25101-4_4, 2005.

Ansmann, A., Riebesell, M., Weitkamp, C. : Measurement of atmospheric aerosol extinction profiles with a Raman lidar, Opt. Lett., 15, https://doi.org/10.1364/OL.15.000746, 1990.

Ansmann, A., Wandinger, U., Riebesell, M., Weitkamp, C., Michaelis W.: Independent measurement of extinction and backscatter profiles in cirrus clouds by using a combined Raman elastic-backscatter lidar, Appl. Opt., 31, https://doi.org/10.1364/AO.31.007113, 1992.

Ansmann, A., Mamouri, R.-E., Hofer, J., Baars, H., Althausen, D., and Abdullaev, S. F.: Dust mass, cloud condensation nuclei, and ice-nucleating particle profiling with polarization lidar: updated POLIPHON conversion factors from global AERONET analysis, Atmos. Meas. Tech., 12, 4849–4865, https://doi.org/10.5194/amt-12-4849-2019, 2019.

Ansmann, A., Ohneiser, K., Mamouri. R, Knopf, D., Veselovskii, I., Baars, H., Engelmann, R., Foth, A., Jimenez, C., Seifert, P., Barja, B.: Tropospheric and stratospheric wildfire smoke profiling with lidar: Mass, surface area, CCN and INP retrieval, Atmos. Chem. Phys. Discuss., https://doi.org/10.5194/acp-2020-1093, in review. 2020.

Ansmann, A., Mamouri, R.-E., Bühl, J., Seifert, P., Engelmann, R., Hofer, J., Nisantzi, A., Atkinson, J. D., Kanji, Z. A., Sierau, B., Vrekoussis, M., and Sciare, J.: Ice-nucleating particle versus ice crystal number concentration in altocumulus and cirrus layers embedded in Saharan dust:a closure study, Atmos. Chem. Phys., 19, 15087-15115, https://doi.org/10.5194/acp-19-15087-2019, 2019.

Baars, H., Kanitz, T., Engelmann, R., Althausen, D., Heese, B., Komppula, M., Preißler, J., Tesche, M., Ansmann, A., Wandinger, U., Lim, J.-H., Ahn, J. Y., Stachlewska, I. S., Amiridis, V., Marinou, E., Seifert, P., Hofer, J., Skupin, A., Schneider, F., Bohlmann, S., Foth, A., Bley, S., Pfüller, A., Giannakaki, E., Lihavainen, H., Viisanen, Y., Hooda, R. K., Pereira, S. N., Bortoli, D., Wagner, F., Mattis, I., Janicka, L., Markowicz, K. M., Achtert, P., Artaxo, P., Pauliquevis, T., Souza, R. A. F., Sharma, V. P., van Zyl, P. G., Beukes, J. P., Sun, J., Rohwer, E. G., Deng, R., Mamouri, R.-E., and Zamorano, F.: An overview of the first decade of PollyNET: an emerging network of automated Raman-polarization lidars for continuous aerosol profiling, Atmos. Chem. Phys., 16, 5111-5137, https://doi.org/10.5194/acp-16-5111-2016, 2016.

Baars, H., Seifert, P., Engelmann, R., and Wandinger, U.: Target categorization of aerosol and clouds by continuous multiwavelength-polarization lidar measurements, Atmos. Meas. Tech., 10, 3175-3201, https://doi.org/10.5194/amt-10-3175-2017, 2017.

Barahona, D., and Nenes, A.: Parameterization of cloud droplet formation in large-scale models: Including effects of entrainment. Journal of Geophysical Research, 112, D16206. https://doi.org/10.1029/2007JD00847, 2007

Barlakas, V., Deneke, H., and Macke, A.: The sub-adiabatic model as a concept for evaluating the representation and radiative effects of low-level clouds in a high-resolution atmospheric

model, Atmos. Chem. Phys., 20, 303–322, https://doi.org/10.5194/acp-20-303-2020, 2020.

Behrendt, A., and Nakamura, T.: Calculation of the calibration constant of polarization lidar and its dependency on atmospheric temperature, Opt. Express, 10, 805-817, https://doi.org/10.1364/OE.10.0008052002.

Belegante, L., Bravo-Aranda, J. A., Freudenthaler, V., Nicolae, D., Nemuc, A., Ene, D., Alados-Arboledas, L., Amodeo, A., Pappalardo, G., D'Amico, G., Amato, F., Engelmann, R., Baars, H., Wandinger, U., Papayannis, A., Kokkalis, P., and Pereira, S. N.: Experimental techniques for the calibration of lidar depolarization channels in EARLINET, Atmos. Meas. Tech., 11, 1119-1141, https://doi.org/10.5194/amt-11-1119-2018, 2018.

Bissonnette, L. R., Bruscaglioni, P., Ismaelli, A., Zaccanti, G., Cohen, A., Benayahu, Y., Kleiman, M., Egert, S., Flesia, C., Schwendimann, P., Starkov, A. V., Noormohammadian, M., Oppel, U. G., Winker, D. M., Zege, E. P., Katsev, I. L., and Polonsky, I. N.: LIDAR multiple scattering from clouds, Appl. Phys. B, 60, 355-362, https://doi.org/10.1007/BF01082271, 1994.

Bissonnette, L. R., Bruscaglioni, P., Ismaelli, A., Zaccanti, G., Cohen, A., Benayahu, Y., Kleiman, M., Egert, S., Flesia, C., Schwendimann, P., Starkov, A. V., Noormohammadian, M., Oppel, U. G., Winker, D. M., Zege, E. P., Katsev, I. L., and Polonsky, I. N.: LIDAR multiple scattering from clouds, Appl. Phys. B, 60, 355-362, https://doi.org/10.1007/BF01082271, 1995.

Bissonnette, L. R., Roy, G., Roy, N.: Multiple-scattering-based lidar retrieval: method and results of cloud probings, Appl. Optics, 44, 26, 5565-5581, 2005.

Bissonnette, L. R., Roy, G., Tremblay, G.: Lidar-Based Characterization of the Geometry and Structure of Water Clouds, J. Atmospheric Ocean. Technol., 24, 1364-1376,https://doi.org/10.1175/JTECH2045.1, 2006.

Bey, I., Jacob, D. J., Yantosca, R. M., Logan, J. A., Field, B. D., Fiore, A. M., Li, Q. B., Liu, H. G. Y., Mickley, L. J., and Schultz, M. G.: Global modeling of tropospheric chemistry with assimilated meteorology: Model description and evaluation, J. Geophys. Res., 106, 23073–23095, https://doi.org/10.1029/2001JD000807, 2001.

Bohlmann, S., Baars, H., Radenz, M., Engelmann, R., and Macke, A.: Ship-borne aerosol profiling with lidar over the Atlantic Ocean: from pure marine conditions to complex dust–smoke mixtures, Atmos. Chem. Phys., 18, 9661–9679, https://doi.org/10.5194/acp-18-9661-2018, 2018.

Boucher, O., Randall, D.,Artaxo, P., Bretherton, C., Feingold, G., Forster, P., Kerminen, V.-M. , Kondo, Y., Liao, H., Lohmann, U., Rasch, P., Satheesh, S.K., Sherwood, S., Stevens,

B., and Zhang, X.Y.: Clouds and Aerosols. In: Climate Change 2013: The Physical Science Basis. Contribution of Working Group I to the Fifth Assessment Report of the Intergovernmental Panel on Climate Change. Cambridge University Press, Cambridge, United Kingdom and New York, NY, USA, https://doi.org/10.1017/CBO9781107415324.016, 2013.

Braga, A.L.F., Zanobetti, A. and Schwartz, J.: The lag structure between particulate air pollution and respiratory and cardiovascular deaths in 10 US cities, Journal of Occupational and Environmental Medicine, 43(11): 927-933, 2001.

Bühl, J., Seifert, P., Wandinger, U., Baars, H., Kanitz, T., Schmidt, J., Myagkov, A., Engelmann, R., Skupin, A., Heese, B., Klepel, A., Althausen, D., Ansmann, A.: LACROS: the Leipzig Aerosol and Cloud Remote Observations System, Proc. SPIE 8890, 889002, https://doi.org/10.1117/12.2030911, 2013

Bühl, J., Leinweber, R., Görsdorf, U., Radenz, M., Ansmann, A., and Lehmann, V.: Combined vertical-velocity observations with Doppler lidar, cloud radar and wind profiler, Atmos. Meas. Tech., 8, 3527-3536, https://doi.org/10.5194/amt-8-3527-2015, 2015.

Bühl, J., Seifert, P., Myagkov, A., and Ansmann, A.: Measuring ice- and liquid-water properties in mixed-phase cloud layers at the Leipzig Cloudnet station, Atmos. Chem. Phys., 16, 10609-10620, https://doi.org/10.5194/acp-16-10609-2016, 2016.

Block, K.: Aerosol-Cloud-Radiation interactions in regimes of liquid water clouds, Phd thesis, University Leipzig, https://nbn-resolving.org/urn:nbn:de:bsz:15-qucosa2-319314, 2018.

Bühl, J., Seifert, P., Radenz, M., Baars, H., and Ansmann, A.: Ice crystal number concentration from lidar, cloud radar and radar wind profiler measurements, Atmos. Meas. Tech., 12, 6601-6617, https://doi.org/10.5194/amt-12-6601-2019, 2019.

Cao, L., Gao, C., Yhao, L.: Geoengineering: Basic science and ongoing research efforts in China, Advances in Climate Change Research 6 (2015) 188 - 196, https://doi.org/10.1016/j.accre.2015.11.002, 2015.

Carslaw, K. S., Boucher, O., Spracklen, D. V., Mann, G. W., Rae, J. G. L., Woodward, S., and Kulmala, M.: A review of natural aerosol interactions and feedbacks within the Earth system, Atmos. Chem. Phys., 10, 1701-1737, https://doi.org/10.5194/acp-10-1701-2010, 2010.

Carslaw, K., Lee, L., Reddington, C., Pringle, K., Rap, A., Forster, P., Mann, G., Spracklen, D., Woodhouse, M., Regayre, L., Pierce, J.: Large contribution of natural aerosols to uncertainty in indirect forcing, Nature, 503, 67, https://doi.org/10.1038/nature12674, 2013.

Carslaw, K. S., Gordon, H., Hamilton, D. S., Johnson, J. S., Regayre, L. A., Yoshioka, M., and Pringle, K. J.: Aerosols in the Pre-industrial Atmosphere, Current Climate Change Reports, 3, 1–15, https://doi.org/10.1007/s40641-017-0061-2, 2017.

Chaikovskaya, L., Zege, E., Theory of polarized lidar sounding including multiple scattering, J. Quantitative Spectroscopy & Radiative Transfer 88 21-35, https://doi.org/10.1016/j.jqsrt.2004.01.002, 2004.

Chaikovskaya, L.: Remote sensing of clouds using linearly and circularly polarized laser beams: techniques to compute signal polarization, In: Kokhanovsky A.A. (eds) Light Scattering Reviews 3. Springer Praxis Books. Springer, Berlin, Heidelberg, 191-228, https://doi.org/10.1007/978-3-540-48546-9_6, 2008.

Chen, Y.-C., Christensen, M. W., Xue, L., Sorooshian, A., Stephens, G. L., Rasmussen, R. M., and Seinfeld, J. H.: Occurrence of lower cloud albedo in ship tracks, Atmos. Chem. Phys., 12, 8223-8235, http://dx.doi.org/10.5194/acp-12-8223-2012, 2012.

Collis, R. T. H., and Russel , P. B: Lidar measurement of particles and gases by elastic backscattering and differential absorption, in Laser Monitoring of the Atmosphere, edited by E. D. Hinkley, pp. 71-151, Springer, Berlin/Heidelberg, https://doi.org/10.1007/3-540-07743-X, 1976

Conant, W. C., VanReken, T. M., Rissman, T. A., Varutbangkul, V., Jonsson, H. H., Nenes, A., et al.: Aerosol-cloud drop concentration closure in warm cumulus. Journal of Geophysical Research, 109, D13204. https://doi.org/10.1029/2003JD004324, 2006.

Connolly, P. J., Emersic, C., and Field, P. R.: A laboratory investigation into the aggregation efficiency of small ice crystals, Atmos. Chem. Phys., 12, 2055–2076, https://doi.org/10.5194/acp-12-2055-2012, 2012.

Cooper, G., Johnston, D., Foster, J., Galbraith, L., Neukermans, A., Ormond, R., Rush J., and Wang, Q.: A review of some experimental spray methods for marine cloud brightening. Int. J. Geosci. 4, 78-97 , http://dx.doi.org/10.4236/ijg.2013.41009, 2013.

Costa-Surós, M., Sourdeval, O., Acquistapace, C., Baars, H., Carbajal Henken, C., Genz, C., Hesemann, J., Jimenez, C., König, M., Kretzschmar, J., Madenach, N., Meyer, C. I., Schrödner, R., Seifert, P., Senf, F., Brueck, M., Cioni, G., Engels, J. F., Fieg, K., Gorges, K., Heinze, R., Siligam, P. K., Burkhardt, U., Crewell, S., Hoose, C., Seifert, A., Tegen, I., and Quaas, J.: Detection and attribution of aerosol–cloud interactions in large-domain large-eddy simulations with the ICOsahedral Non-hydrostatic model, Atmos. Chem. Phys., 20, 5657–5678, https://doi.org/10.5194/acp-20-5657-2020, 2020.

Costantino, L. and Bréon, F.-M.: Aerosol indirect effect on warm clouds over South-East Atlantic, from co-located MODIS and CALIPSO observations, Atmos. Chem. Phys., 13, 69–88, https://doi.org/10.5194/acp-13-69-2013, 2013.

Dai, G., Althausen, D., Hofer, J., Engelmann, R., Seifert, P., Bühl, J., Mamouri, R.-E., Wu, S., and Ansmann, A.: Calibration of Raman lidar water vapor profiles by means of AERONET photometer observations and GDAS meteorological data, Atmos. Meas. Tech., 11, 2735–2748, https://doi.org/10.5194/amt-11-2735-2018, 2018.

Donner, L. J., O'Brien, T. A., Rieger, D., Vogel, B., and Cooke, W. F.: Are atmospheric updrafts a key to unlocking climate forcing and sensitivity?, Atmos. Chem. Phys,, 16, 12,983-12,992. https://doi.org/10.5194/acp-16-12983-2016, 2016.

Donovan, D. P. and van Lammeren, A. C. A. P.: Cloud effective particle size and water content profile retrievals using combined lidar and radar observations – 1. Theory and examples, J. Geophys. Res., 106, 27425–27448, https://doi.org/10.1029/2001JD900243, 2001.

Donovan, D., Voors, R., van Zadelhoff, G.-J., and Acarreta, J.-R.: ECSIM Model and Algorithms Document, KNMI Tech. Rep.: ECSIM-KNMI-TEC-MAD01-R, https://www.academia.edu/33712449/ECSIM_Model_and_Algorithms_Document, 2010.

Donovan, D. P., Klein Baltink, H., Henzing, J. S., de Roode, S. R., and Siebesma, A. P.: A depolarisation lidar-based method for the determination of liquid-cloud microphysical properties, Atmos. Meas. Tech., 8, 237–266, https://doi.org/10.5194/amt-8-237-2015, 2015.

Dufresne, J., and S. Bony: An Assessment of the Primary Sources of Spread of Global Warming Estimates from Coupled Atmosphere-Ocean Models. J. Climate, 21, 5135-5144, https://doi.org/10.1175/2008JCLI2239.1, 2008.

Dusek, U., G. Frank, L. Hildebrandt, J. Curtius, J. Schneider, S. Walter, D. Chand, F. Drewnick, S. Hings, D. Jung, S. Borrmann, and M. Andreae.: Size matters more than chemistry for cloud-nucleating ability of aerosol particles, Science, 312, https://doi.org/10.1126/science.1125261, 2006.

Eloranta, E. W.: Practical model for the calculations of multiply scattered lidar returns, Appl. Optics, 37, 2464–2472, https://doi.org/10.1364/AO.37.002464, 1998.

Engelmann, R., Kanitz, T., Baars, H., Heese, B., Althausen, D., Skupin, A., Wandinger, U., Komppula, M., Stachlewska, I. S., Amiridis, V., Marinou, E., Mattis, I., Linné, H., and Ansmann, A.: The automated multiwavelength Raman polarization and water-vapor lidar PollyXT: the neXT generation, Atmos. Meas. Tech., 9, 1767-1784, https://doi.org/10.5194/amt-9-1767-2016, 2016.

Engelmann, R., Ansmann, A., Ohneiser, K., Griesche, H., Radenz, M., Hofer, J., Althausen, D., Dahlke, S., Maturilli, M., Veselovskii, I., Jimenez, C., Wiesen, R., Baars, H., Bühl, J., Gebauer, H., Haarig, M., Seifert, P., Wandinger, U., and Macke, A.: Wildfire smoke, Arctic haze, and aerosol effects on mixed-phase and cirrus clouds over the North Pole region during MOSAiC: an introduction, Atmos. Chem. Phys., 21, 13397–13423, https://doi.org/10.5194/acp-21-13397-2021, 2021.

Fan J., Wang Y., Rosenfeld D., and Liu X.: Review of Aerosol-Cloud Interactions: Mechanisms, significance, and Challenges, J. Atmospheric Sci., 73, 4221-4252, https://doi.org/10.1175/JAS-D-16-0037.1, 2016.

Feingold, G., Wynn, L. E., Veron, D. E., and Previdi, M.: First measurements of the Twomey indirect effect using ground-based remote sensors, Geophys. Res. Lett., 30, https://doi.org/10.1029/2002GL016633, 2003.

Fernald, F. G.: Analysis of atmospheric lidar observations - some comments, Appl. Opt., 23 (5), https://doi.org/10.1364/AO.23.000652, 1984.

Findeisen, W.: Die kolloidmeteorologischen Vorgänge bei der Niederschlagsbildung (Colloidal meteorological processes in the formation of precipitation). – Meteorol. Z. 55, 121–133. (translated and edited by Volken, E., A.M. Giesche, S. Brönnimann. – Meteorol. Z. 24 (2015), https://doi.org/10.1127/metz/2015/0675, 1938.

Floutsi, A., Baars, H., Radenz, M., Haarig, M., Yin, Z., Seifert, P., **Jimenez, C.**, Ansmann, A., Engelmann, R., Barja, B., Zamorano, F., and Wandinger, U.: Advection of biomass burning berosols towards the southern hemispheric mid-latitude station of Punta Arenas as observed with multiwavelength polarization Raman lidar, Remote Sensing, 13(1):138, https://doi.org/10.3390/rs13010138, 2021.

Foth, A. and Pospichal, B.: Optimal estimation of water vapour profiles using a combination of Raman lidar and microwave radiometer, Atmos. Meas. Tech., 10, 3325–3344, https://doi.org/10.5194/amt-10-3325-2017, 2017.

Forster, P., V. Ramaswamy, P. Artaxo, T. Berntsen, R. Betts, D.W. Fahey, J. Haywood, J. Lean, D.C. Lowe, G. Myhre, J. Nganga, R. Prinn, G. Raga, M. Schulz and R. Van Dorland: Changes in Atmospheric Constituents and in Radiative Forcing. In: Climate Change 2007: The Physical Science Basis. Contribution of Working Group I to the Fourth Assessment Report of the Intergovernmental Panel on Climate Change [Solomon, S., D. Qin, M. Manning, Z. Chen, M. Marquis, K.B. Averyt, M.Tignor and H.L. Miller (eds.)]. Cambridge University, Press, Cambridge, United Kingdom and New York, NY, USA, http://www.cambridge.org/catalogue/catalogue.asp?isbn=9780521705967, 2007

Freudenthaler, V.: About the effects of polarising optics on lidar signals and the $\Delta 90$ calibration, Atmos. Meas. Tech., 9, 4181-4255, https://doi.org/10.5194/amt-9-4181-2016, 2016.

Freudenthaler, V., Seefeldner, M., Groß, S., and Wandinger., U.: Accuracy of Linear Depolarisation Ratios in Clean Air Ranges Measured with POLIS-6 at 355 and 532 NM, EPJ Web of Conferences 119, 25013, https://doi.org/10.1051/epjconf/201611925013, 2016.

Frisch, S., Shupe, M., Djalalova, I., Feingold, G., and Poellot, M.: The retrieval of stratus cloud droplet number effective radius with cloud radars, J. Atmospheric Ocean. Tech-

nol., 19, 6, 835-842, https://doi.org/10.1175/1520-0426(2002)019<0835:TROSCD>2.0.CO;2, 2002.

Gasparini, B., and U. Lohmann: Why cirrus cloud seeding cannot substantially cool the planet, J. Geophys. Res. Atmos., 121, 4877-4893, https://doi.org/10.1002/2015JD024666, 2016.

GDAS: Global Data Assimilation System, meteorological data base, available at: https://www.ready.noaa.gov/gdas1.php, last access: 20 March, 2020.

Gelaro, R., McCarty, W., Suárez, M., Todling, R., Molod, A., Takacs., L., et al.: The Modern-Era Retrospective Analysis for Research and Applications, Version 2 (MERRA-2), J. Climate, 30, 5419–5454, https://doi.org/10.1175/JCLI-D-16-0758.1, 2017.

Ghan, S. J., Guzman, G., and Abdul-Razzak, H.: Competition between sea salt particles as cloud condensation nulcei, J. Atmos. Sci., 55, 3340-3347, https://doi.org/10.1175/1520-0469(1998)055<3340:CBSSAS>2.0.CO;2, 1998.

Ghan, S., Wang, M., Zhang, S., Ferrachat, S. Gettelman, A., Griesfeller, Jan, Kipling, Z., Lohmann, U., Morrison, H., Neubauer, D., Partridge, D., Stier, P., Takemura, T., Wang, H., and Zhang, K.: Challenges in constraining anthropogenic aerosol effects on cloud radiative forcing using present-day spatiotemporal variability, PNAS, 113, 5804-5811, https://doi.org/10.1073/pnas.1514036113, 2016.

Glanemann, N., Willner, S.N. & Levermann, A.: Paris Climate Agreement passes the cost-benefit test, Nature Commun 11, 110, https://www.nature.com/articles/s41467-019-13961-1, 2020.

Gong, X., Wex, H., Voigtländer, J., Fomba, K. W., Weinhold, K., van Pinxteren, M., Henning, S., Müller, T., Herrmann, H., and Stratmann, F.: Characterization of aerosol particles at Cabo Verde close to sea level and at the cloud level - Part 1: Particle number size distribution, cloud condensation nuclei and their origins , Atmos. Chem. Phys., 20, 1431-1449, https://doi.org/10.5194/acp-20-1431-2020, 2020.

Goren, T., and Rosenfeld, D.: Decomposing aerosol cloud radiative effects into cloud cover, liquid water path and Twomey components in marine stratocumulus, Atmospheric Research, 138, 378–393, https://doi.org/10.1016/j.atmosres.2013.12.008, 2014.

Gordon, I., Rothman, L., Hill, C., Kochanov, R., Tana, Y., et al.: The HITRAN2016 molecular spectroscopic database, Journal of Quantitative Spectroscopy and Radiative Transfer, 203, 3–69, https://doi.org/10.1016/j.jqsrt.2017.06.038, 2017.

Grabowski, W., Morrison, H., Shima, S., Abade, G., Dziekan, P, and Pawlowska, H.: Modeling of Cloud Microphysics: Can We Do Better?, Bull. Amer. Meteor. Soc., 100, 655–672, https://doi.org/10.1175/BAMS-D-18-0005.1, 2019.

Griesche, H. J., Seifert, P., Ansmann, A., Baars, H., Barrientos Velasco, C., Bühl, J., Engelmann, R., Radenz, M., Zhenping, Y., and Macke, A.: Application of the shipborne remote sensing supersite OCEANET for profiling of Arctic aerosols and clouds during Polarstern cruise PS106, Atmos. Meas. Tech., 13, 5335–5358, https://doi.org/10.5194/amt-13-5335-2020, 2020.

Grosvenor, D. P., Sourdeval, O., Zuidema, P., Ackerman, A., Alexandrov, M. D., Bennartz, R., et al.: Remote sensing of droplet number concentration in warm clouds: A review of the current state of knowledge and perspectives, Reviews of Geophysics, 56, 409- 453. https://doi.org/10.1029/2017RG000593, 2018.

Gryspeerdt, E., Quaas, J.,and Bellouin, N.: Constraining the aerosol influence on cloud fraction, J. Geophys. Res. Atmos., 121, 3566–3583, https://doi.org/10.1002/2015JD023744, 2016.

Gryspeerdt, E., Quaas, J., Ferrachat, S., Gettelman, A., Ghan, S., Lohmann, U., Morrison, H., Neubauer, D., Partridge, D. G., Stier, P., Takemura, T., Wang, H., Wang, M., and Zhang, K.: Constraining the instantaneous aerosol influence on cloud albedo, P. Natl. Acad. Sci. USA, 114, 4899–4904, https://doi.org/10.1073/pnas.1617765114, 2017.

Gryspeerdt, E., Goren, T., Sourdeval, O., Quaas, J., Mülmenstädt, J., Dipu, S., Unglaub, C., Gettelman, A., and Christensen, M.: Constraining the aerosol influence on cloud liquid water path, Atmos. Chem. Phys., 19, 5331–5347, https://doi.org/10.5194/acp-19-5331-2019, 2019.

Guichard, F., and Couvreux, F.:A short review of numerical cloud-resolving models, Tellus A: Dynamic Meteorology and Oceanography, 69:1, https://doi.org/10.1080/16000870.2017.1373578, 2017

Haarig, M., Ansmann, A., Althausen, D., Klepel, A., Groß, S., Freudenthaler, V., Toledano, C., Mamouri, R.-E., Farrell, D. A., Prescod, D. A., Marinou, E., Burton, S. P., Gasteiger, J., Engelmann, R., and Baars, H.: Triple-wavelength depolarization-ratio profiling of Saharan dust over Barbados during SALTRACE in 2013 and 2014, Atmos. Chem. Phys., 17, 10767-10794, https://doi.org/10.5194/acp-17-10767-2017, 2017.

Haarig, M., Ansmann, A., Gasteiger, J., Kandler, K., Althausen, D., Baars, H., Radenz, M., and Farrell, D. A.: Dry versus wet marine particle optical properties: RH dependence of depolarization ratio, backscatter, and extinction from multiwavelength lidar measurements during SALTRACE, Atmos. Chem. Phys., 17, 14199–14217, https://doi.org/10.5194/acp-17-14199-2017, 2017.

Haarig, M., Ansmann, A., Baars, H., Jimenez, C., Veselovskii, I., Engelmann, R., and Althausen, D.: Depolarization and lidar ratios at 355, 532 and 1064 nm and microphysical properties of aged tropospheric and stratospheric Canadian wildfire smoke, Atmos. Chem. Phys., 18, 11847-11861, https://doi.org/10.5194/acp-18-11847-2018, 2018.

Hansen, J. E., Sato, M., and Ruedy, R.: Radiative forcing and climate response. J. Geophys. Res, 102, 6831-6864, https://doi.org/10.1029/96JD03436, 1997.

Haynes, J. M., Jakob, C., Rossow, W. B., Tselioudis, G., and Brown, J.: Major Characteristics of Southern Ocean Cloud Regimes and Their Effects on the Energy Budget, J. Climate, 24, 5061–5080, https://doi.org/10.1175/2011JCLI4052.1, 2011.

Hamilton, D. S., Lee, L. A., Pringle, K. J., Reddington, C. L., Spracklen, D. V., and Carslaw, K. S.: Occurrence of pristine aerosol environments on a polluted planet, P. Natl. Acad. Sci. USA, 111, 18466–18471, https://doi.org/10.1073/pnas.1415440111, 2014

Hasekamp, O., Gryspeerdt, E., and Quaas, J.: Analysis of polarimetric satellite measurements suggests stronger cooling due to aerosol-cloud interactions, Nature Comm., 10, 5405, https://doi.org/10.1038/s41467-019-13372-2, 2019.

Heyn, I., Block, K., Mülmenstädt, J., Gryspeerdt, E., Kühne, P., Salzmann, M., and Quaas, J.: Assessment of simulated aerosol effective radiative forcings in the terrestrial spectrum. Geophysical Research Letters, 44, 1001-1007. https://doi.org/10.1002/2016GL071975, 2017.

Hofer, J., Althausen, D., Abdullaev, S. F., Makhmudov, A. N., Nazarov, B. I., Schettler, G., Engelmann, R., Baars, H., Fomba, K. W., Müller, K., Heinold, B., Kandler, K., and Ansmann, A.: Long-term profiling of mineral dust and pollution aerosol with multiwavelength polarization Raman lidar at the Central Asian site of Dushanbe, Tajikistan: case studies, Atmos. Chem. Phys., 17, 14559-14577, https://doi.org/10.5194/acp-17-14559-2017, 2017.

Hofer, J., Ansmann, A., Althausen, D., Engelmann, R., Baars, H., Abdullaev, S. F., and Makhmudov, A. N.: Long-term profiling of aerosol light extinction, particle mass, cloud condensation nuclei, and ice-nucleating particle concentration over Dushanbe, Tajikistan, in Central Asia, Atmos. Chem. Phys., 20, 4695–4711, https://doi.org/10.5194/acp-20-4695-2020, 2020.

Hofer, J., Ansmann, A., Althausen, D., Engelmann, R., Baars, H., Fomba, K. W., Wandinger, U., Abdullaev, S. F., and Makhmudov, A. N.: Optical properties of Central Asian aerosol relevant for spaceborne lidar applications and aerosol typing at 355 and 532?nm, Atmos. Chem. Phys., 20, 9265–9280, https://doi.org/10.5194/acp-20-9265-2020, 2020b.

Hogan, R. J.: Fast Lidar and Radar Multiple-Scattering Models. Part I: Small-Angle Scattering Using the Photon Variance-Covariance Method, J. Atm. Sci., 65, 3621-3635, https://doi.org/10.1175/2008JAS2642.1, 2008.

Hogan, R. J., and Battaglia, A., Fast Lidar and Radar Multiple-Scattering Models. Part II: Wide-Angle Scattering Using the Time-Dependent Two-Stream Approximation, J. Atmos. Sci., 65, 12,3636-3651, https://doi.org/10.1175/2008JAS2643.1, 2008.

Hoose, C., Lohmann, U., Erdin, R., and Tegen, I.: The global influence of dust mineralogical composition on heterogeneous ice nucleation in mixed-phase clouds, Environ. Res. Lett., 3, 025003, doi:10.1088/1748-9326/3/2/025003, 2008.

HYSPLIT: HYbrid Single-Particle Lagrangian Integrated Trajectory model, backward trajectory calculation tool, available at: http://ready.arl.noaa.gov/HYSPLIT_traj.php, last access: 20 February, 2020.

Illingworth, A. J., Hogan, R. J., O'Connor, E., Bouniol, D., Brooks, M. E., Delanoé, J., Donovan, D. P., Eastment, J. D., Gaussiat, N., Goddard, J. W. F., Haeffelin, M., Baltink, H. K., Krasnov, O. A., Pelon, J., Piriou, J. M., Protat, A., Russchenberg, H. W. J., Seifert, A., Tompkins, A. M., van Zadelhoff, G. J., Vinit, F., Willén, U., Wilson, D. R., and Wrench, C. L.: Cloudnet: Continuous Evaluation of Cloud Profiles in Seven Operational Models Using Ground-Based Observations, Bulletin of the American Meteorological Society, 88, 883–898, https://doi.org/10.1175/BAMS-88-6-883, 2007.

Illingworth, A. J., Barker, H. W., Beljaars, A., Ceccaldi, M., Chepfer, H., Clerbaux, N., Cole, J., Delanoe, J., Domenech, C., Donovan, D. P., Fukuda, S., Hirakata, M., Hogan, R. J., Huenerbein, H., Kollias, P., Kubota, T., Nakajima, T., Nakajima, T. Y., Nishizawa, T., Ohno, Y., Okamoto, H., Oki, R., Sato, K., Satoh, M., Shephard, M., Velázquez-Blázquez, A., Wandinger, U., Wehr, T., and Zadelhoff, G.-J.: The EARTHCARE satellite: the next step forward in global measurements of clouds, aerosols, precipitation and radiation, B. Am. Meteorol. Soc., 96, 1311–1332, https://doi.org/10.1175/BAMS-D-12-00227.1, 2015.

IPCC: Climate Change 2014: Synthesis Report. Contribution of Working Groups I, II and III to the Fifth Assessment Report of the Intergovernmental Panel on Climate Change, edited by: Core Writing Team, Pachauri, R.K., and Meyer, L.A., IPCC, Geneva, Switzerland, 151 pp; available at: https://www.ipcc.ch/pdf/assessment-report/ar5/syr/SYR_AR5_FINAL_full.pdf, 2014.

Jenkins, A. K. L., and Forster, P. M: The inclusion of water with the injected aerosol reduces the simulated effectiveness of marine cloud brightening, Atmos. Sci. Lett., 14, 164–169, https://doi.org/10.1002/asl2.434, 2013.

Jenkins, A. K. L., Forster, P. M. and Jackson, L. S. The effects of timing and rate of marine cloud brightening aerosol injection on albedo changes during the diurnal cycle of marine stratocumulus clouds. Atmos. Chem. Phys. 13, 1659–1673, https://doi.org/10.5194/acp-13-1659-2013, 2013.

Jiang, H., Xue, H., Teller, A., Feingold, G., and Levin, Z.: Aerosol effects on the lifetime of shallow cumulus, Geophys. Res. Lett., 33, L14806, https://doi.org/10.1029/2006GL026024, 2006.

Jickells, T. D., Z. S. An, K. K. Andersen, A. R. Baker, G. Bergametti, N. Brooks, J. J. Cao, P. W. Boyd, R. A. Duce, K. A. Hunter, H. Kawahata, N. Kubilay, J. LaRoche, P. S.

Liss, N. Mahowald, J. M. Prospero, A. J. Ridgwell, I. Tegen, and R. Torres.: Global iron connections between desert dust, ocean biogeochemistry, and climate, Science, 308, 67-71, https://doi.org/10.1126/science.1105959, 2005.

Jimenez, C., Ansmann, A., Donovan, D., Engelmann, R., Malinka, A., Schmidt, J., and Wandinger, U.: Retrieval of microphysical properties of liquid water clouds from atmospheric lidar measurements: Comparison of the Raman dual field of view and the depolarization techniques, Proc. SPIE 10429, 1042907, https://doi.org/10.1117/12.2281806, 2017.

Jimenez, C., Ansmann, A., Donovan, D., Engelmann, R., Schmidt, J., and Wandinger, U.: Comparison between two lidar methods to retrieve microphysical properties of liquid water clouds, EPJ Web Conf., 176, 01032, https://doi.org/10.1051/epjconf/201817601032, 2018.

Jimenez, C., Ansmann, A., Engelmann, R., Haarig, M., Schmidt, J., Wandinger, U.: Polarization lidar: an extended three-signal calibration approach, Atmos. Meas. Tech., 12, 1-17, https://doi.org/10.5194/amt-12-1077-2019, 2019.

Jimenez, C., Ansmann, A., Engelmann, R., Donovan, D., Malinka, A., Schmidt, J., Seifert, P., and Wandinger, U.: The dual-field-of-view polarization lidar technique: A new concept in monitoring aerosol effects in liquid-water clouds – theoretical framework, Atmos. Chem. Phys., 20, 15247–15263, https://doi.org/10.5194/acp-20-15247-2020, 2020a.

Jimenez, C., Ansmann, A., Engelmann, R., Donovan, D., Malinka, A., Seifert, P., Radenz, M., Yin, Z., Wiesen, R., Bühl, J., Schmidt, J., Wandinger, U., and Barja, B.: The dual-field-of-view polarization lidar technique: A new concept in monitoring aerosol effects in liquid-water clouds – Case studies, Atmos. Chem. Phys., 20, 15265-15284,https://doi.org/10.5194/acp-20-15265-2020, 2020b.

Jimenez, C., Ansmann, A., Engelmann, R., Seifert, P., Wiesen, R., Radenz, M., and Wandinger, U.: Continuos Monitoring of Liquid Water Clouds and Aerosols with Dual-FOV Lidar Polarization Technique, EPJ Web Conf.,237, https://doi.org/10.1051/epjconf/202023707005, 2020c.

Jimenez, C., Ansmann, A., and Malinka, A.: Files to retrieve effective radius and extinction coefficient in liquid clouds from depolarization observations at two FOVs, [Data set] Zenodo, https://doi.org/10.5281/zenodo.4107137, 2020d.

Jin, X., Wu, T., Li, L., and Shi, C.: Cloudiness characteristics over Southeast Asia from satellite FY?2C and their comparison to three other cloud data sets, J. Geophys. Res. Atmos., 114, D17207, https://doi.org/10.1029/2008JD011422, 2009.

Jöckel, P., Tost, H., Pozzer, A., Brühl, C., Buchholz, J., Ganzeveld, L., Hoor, P., Kerkweg, A., Lawrence, M. G., Sander, R., Steil, B., Stiller, G., Tanarhte, M., Taraborrelli, D., van Aardenne, J., and Lelieveld, J.: The atmospheric chemistry general circulation model

ECHAM5/MESSy1: consistent simulation of ozone from the surface to the mesosphere, Atmos. Chem. Phys., 6, 5067–5104, https://doi.org/10.5194/acp-6-5067-2006, 2006.

Johnson, B. T., Shine, K. P., and Forster, P. M.: The semidirect aerosol effect: Impact of absorbing aerosols on marine stratocumulus, Q. J. R. Meteorol. Soc., 130, 1407-1422, https://doi.org/10.1256/qj.03.61, 2004.

Karydis, V. A., Tsimpidi, A. P., Bacer, S., Pozzer, A., Nenes, A., and Lelieveld, J.: Global impact of mineral dust on cloud droplet number concentration, Atmos. Chem. Phys., 17, 5601–5621, https://doi.org/10.5194/acp-17-5601-2017, 2017.

Kaufman, Y. J., and R. S. Fraser: The effect of smoke particles on clouds and climate forcing, Science, 277, https://doi.org/10.1126/science.277.5332.1636, 1997.

Katsev, L., Zege, E., Prikhach, A., Polonsky, I.: Efficient technique to determine backscattered light power for various atmospheric and oceanic sounding and imaging systems, JOSA A,14, 1338-46, https://doi.org/10.1364/JOSAA.14.001338, 1997.

Kiehl, J.: Geoengineering climate Change: Treating the symptom over the cause?, Climatic Change, August 2006, https://doi.org/10.1007/s10584-006-9132-4, 2006.

Kim, B., Schwartz, S., Miller, M. Min, Q.: Effective radius of cloud droplets by ground-based remote sensing: Relationship to aerosol, J. of Geophys. Res., 108, D23, 4740 https://doi.org/10.1029/2003JD00372, 2003.

Kim, B., Miller, M. A., Schwartz, S. E., Liu, Y., and Min, Q.: The role of adiabaticity in the aerosol first indirect effect, J. Geophys. Res., 113, https://doi.org/10.1029/2007JD008961, 2008.

Kim, D., Cheong, H., Kim, Y., Volkov, S., Lee, J.: Optical Depth and Multiple Scattering Depolarization in Liquid Clouds, Optical Review, 17, 507-512, 2010

Klett, J.: Stable analytical inversion solution for processing lidar returns, Appl. Opt., 20, https://doi.org/10.1364/AO.20.000211, 1981.

Köhler, H.: The nucleus in and the growth of hygroscopic droplets, T. Faraday Soc., 32, 1152-1161, https://doi.org/10.1039/TF9363201152, 1936.

Koren, I., Kaufman, Y. J., Rosenfeld, D., Remer, L. A., and Rudich, Y.: Aerosol invigoration and restructuring of Atlantic convective clouds, Geophys. Res. Lett., 32, L14828, https://doi.org/10.1029/2005GL023187, 2005.

Korhonen, H., Carslaw, K. S. and Romakkaniemi, S.: Enhancement of marine cloud albedo via controlled sea spray injections: a global model study of the influence of emission rates, microphysics and transport. Atmos. Chem. Phys. 10, 4133–4143, https://doi.org/10.5194/acp-10-4133-2010, 2010.

Kretzschmar, J., Stapf, J., Klocke, D., Wendisch, M., and Quaas, J.: Employing airborne radiation and cloud microphysics observations to improve cloud representation in ICON at kilometer-scale resolution in the Arctic, Atmos. Chem. Phys., 20, 13145–13165, https://doi.org/10.5194/acp-20-13145-2020, 2020.

Latham, J.: Control of global warming?, Nature 347, 339-340. https://doi.org/10.1038/347339b0, 1990.

Latham, J., Rasch, P., Chen, C.-C. J., Kettles, L., Gadian, A., Gettelman, A., Morrison, H., Bower, K., and Choularton, T.: Global temperature stabilization via controlled albedo enhancement of low-level maritime clouds. Phil. Trans. R. Soc. A 366, 3969-3987, https://doi.org/10.1098/rsta.20080137, 2008.

Lawrence, M.G., Schäfer, S., Muri, H., Scott, V., Oschlies, A., Vaughan, N.E., Boucher, O., Schmidet, H., Haywood, J., and Scheffran, J.: Evaluating climate geoengineering proposals in the context of the Paris Agreement temperature goals, Nat. Commun., 9, 3734, https://doi.org/10.1038/s41467-018-05938-3, 2018.

Li, J., Jian, B., Huang, J., Hub, Y., Zhao, C.,Kawamoto, K., Liao, S., Wu, M.: Long-term variation of cloud droplet number concentrations from spacebased Lidar, R. Sens. Envir., 213, 144-161, https://doi.org/10.1016/j.rse.2018.05.011, 2018.

Lohmann, U. and Feichter, J.: Global indirect aerosol effects: a review, Atmos. Chem. Phys., 5, 715-737, https://doi.org/10.5194/acp-5-715-2005, 2005.

Lohmann, U., Quaas, J., Kinne, S., and Feichter, J.: Different approaches for constraining global climate models of the anthropogenic indirect aerosol effect, Bull. Am. Meteorol. Soc., 88, Specialty Conference on the Indirect Effect of Aerosols on Climate, Manchester, https://doi.org/10.1175/BAMS-88-2-243, 2007.

Lohmann, U., Lüönd, F., Mahrt, F.: An introduction to clouds from the microscale to climate, Cambridge University Press, ISBN 978-1-107-01822-8, https://de1lib.org/book/3374990/9dbd99, 2016.

Lohmann, U.: Anthropogenic Aerosol Influences on Mixed-Phase Clouds, Curr Clim Change Rep (2017) 3:32-44, https://doi.org/10.1007/s40641-017-0059-9, 2017.

Lu, M., and J. H. Seinfeld: Study of the Aerosol Indirect Effect by Large-Eddy Simulation of Marine Stratocumulus. J. Atmos. Sci., 62, 3909-3932, https://doi.org/10.1175/JAS3584.1, 2005.

Lu, M.-L., G. Feingold, H. H. Jonsson, P. Y. Chuang, H. Gates, R. C. Flagan, and J. H. Seinfeld: Aerosol-cloud relationships in continental shallow cumulus, J. Geophys. Res., 113, https://doi.org/10.1029/2007JD009354, 2008.

Malinka, A.V, and Zege, E.P.: Analytical modeling of Raman lidar return, including multiple scattering, Appl. Optics, 42, 1075-1081, https://doi.org/10.1364/AO.42.001075, 2003.

Malinka, A. V., and Zege, E. P.: Possibilities of warm cloud microstructure profiling with multiple-field-of-view Raman lidar, Appl. Optics 46, 8419-8427, https://doi.org/10.1364/AO.46.008419, 2007.

Malinka, A. V., and Schmidt, J.: Overlap function of a lidar with a field stop shifted from the focal plane, in Proceedings of the 25th International Laser Radar Conference (ILRC), G.Matvienko and A. Zemlyanov, eds. (Curran Associates), pp. 79-81, 2010

Mamouri, R. E., and Ansmann, A.: Potential of polarization lidar to provide profiles of CCN- and INP-relevant aerosol parameters, Atmos. Chem. Phys., 16, 5905-5931, https://doi.org/10.5194/acp-16-5905-2016, 2016.

Mattis, I., Ansmann, A., Müller, D., Wandinger, U., and Althausen, D.: Multiyear aerosol observations with dualwavelength Raman lidar in the framework of EARLINET, J. Geophys. Res., 109, D13203, https://doi.org/10.1029/2004JD004600, 2004.

Mattis, I., Müller, D., Ansmann, A., Wandinger, U., Preißler, J., Seifert, P., and Tesche, M.: Ten years of multiwavelength Raman lidar observations of free-tropospheric aerosol layers over central Europe: Geometrical properties and annual cycle, J. Geophys. Res., 113, D20202, https://doi.org/10.1029/2007JD009636, 2008.

Mattis, I., Tesche, M., Grein, M., Freudenthaler, V., and Müller, D.: Systematic error of lidar profiles caused by a polarization-dependent receiver transmission: quantification and error correction scheme, Appl. Optics, 48, 2742-2751, https://doi.org/10.1364/AO.48.002742, 2009.

Matus, A. V. and T. S. L'Ecuyer: The role of cloud phase inEarth's radiation budget, J. Geophys.Res. Atmos., 122, 2559-2578,https://doi.org/10.1002/2016JD025951, 2017.

McComiskey, A., and G. Feingold: Quantifying error in the radiative forcing of the first aerosol indirect effect, Geophys. Res. Lett., 35, https://doi.org/10.1029/2007GL032667, 2008.

McComiskey, A., G. Feingold, A. S. Frisch, D. D. Turner, M. A. Miller, J. C. Chiu, Q. Min, and J. A. Ogren: An assessment of aerosol-cloud interactions in marine stratus clouds based on surface remote sensing, J. Geophys. Res., 114, https://doi.org/10.1029/2008JD011006, 2009.

McComiskey, A., and Feingold, G.: The scale problem in quantifying aerosol indirect effects, Atmos. Chem. Phys., 12, https://doi.org/10.5194/acp-12-1031-2012, 2012.

McFarquhar, G. and Heymsfield, A.: Parameterizations of INDOEX microphysical measurements and calculations of cloud susceptibility: applications for climate studies, J. Geophys. Res., 106, 28675-28698, https://doi.org/10.1029/2000JD900777, 2001.

Merk, D., Deneke, H., Pospichal, B., and Seifert, P.: Investigation of the adiabatic assumption for estimating cloud micro- and macrophysical properties from satellite and ground observations, Atmos. Chem. Phys., 16, 933–952, https://doi.org/10.5194/acp-16-933-2016, 2016.

Mie, G.: Beitrage zur optik truber medien, speziell kolloidaler metallosungen, Ann. d. Physik, 25, 377, https://doi.org/10.1002/andp.19083300302, 1908.

Mitchell, D. L., and W. Finnegan: Modification of cirrus clouds to reduce global warming, Environ. Res. Lett., 4(4), 045102, https://doi.org/10.1088/1748-9326/4/4/045102, 2009.

Mooradian, G., Geller, M., Stotts, L., Stephens, D., Krautwald, R: Blue-green pulsed propagation through fog, Appl. Opt.,18, 4, 429–441 https://doi.org/10.1364/AO.18.000429, 1979.

Morrison, H., Boer, G., Feingold, G., Harrington, J., Shupe, M., and Sulia, K.: Resilience of persistent Arctic mixed-phase clouds, Nature Geoscience, 5, 11–17, https://doi.org/10.1038/NGEO1332, 2011.

Morrison, H., Curry, J. A., and Khvorostyanov, V. I.: A new double-moment microphysics parameterization for application in cloud and climate models. Part I: Description, J. Atmos. Sci., 62, 1665–1677, https://doi.org/10.1175/Jas3446.1, 2005.

Morrison, H., van Lier Walqui, M., Fridlind, A. M., Grabowski, W. W., Harrington, J. Y., Hoose, C., et al. : Confronting the challenge of modeling cloud and precipitation microphysics, JAMES, 12, e2019MS001689, https://doi.org/10.1029/2019MS001689, 2020.

Moses, E., and Akinyemi, M: A short review on the effects of aerosols on visibility impairment, Journal of Physics: Conf. Series 852 (2017) 012006, https://doi.org/10.1088/1742-6596/852/1/012006, 2017.

Mülmenstädt, J., Sourdeval, O., Delanoe, J. and Quaas, J.: Frequency of occurrence of rain from liquid-, mixed- , and ice-phase clouds derived from A-Train satellite retrievals, Geophys. Res. Lett., 42(15), 6502-6509, https://doi.org/10.1002/2015GL064604, 2015.

Mülmenstädt, J., and G. Feingold: The Radiative Forcing of Aerosol-Cloud Interactions in Liquid Clouds: Wrestling and Embracing Uncertainty, Current Climate Change Reports, 4(1), 23-40, https://doi.org/10.1007/s40641-018-0089-y, 2018.

Myhre, G., E. J. Highwood, K. P. Shine, and F. Stordal: New estimates of radiative forcing due to well mixed greenhouse gases. Geophys. Res. Lett., 25, 2715-2718, https://doi.org/10.1029/98GL01908, 1998.

Myhre, G., Shindell, D., Bréon, F.-M., Collins, W., Fuglestvedt, J., Huang, J. , Koch, D., Lamarque, J.-F., Lee, D., Mendoza, B., Nakajima, T., Robock, A., Stephens, G., Takemura, T., and Zhang, H.: Anthropogenic and Natural Radiative Forcing. In: Climate Change 2013: The Physical Science Basis. Contribution of Working Group I to the Fifth Assessment Report of the Intergovernmental Panel on Climate Change. Cambridge University Press, Cambridge, United Kingdom and New York, NY, USA, https://doi.org/10.1017/CBO9781107415324.018, 2013.

Nakajima, T., Higurashi, A., Kawamoto, K., Penner, J.: A possible correlation between satellite-derived cloud and aerosol microphysical parameters, Geophys. Res. Lett., 28:1171–1174, https://doi.org/10.1029/2000GL012186, 2001

Ohneiser, K., Ansmann, A., Baars, H., Seifert, P., Barja, B., Jimenez, C., Radenz, M., Teisseire, A., Floutsi, A., Haarig, M., Foth, A., Chudnovsky, A., Engelmann, R., Zamorano, F., Bühl, J., and Wandinger, U.: Smoke of extreme Australian bushfires observed in the stratosphere over Punta Arenas, Chile, in January 2020: optical thickness, lidar ratios, and depolarization ratios at 355 and 532?nm, Atmos. Chem. Phys., 20, 8003–8015, https://doi.org/10.5194/acp-20-8003-2020, 2020.

Painemal, D. and Zuidema, P.: The first aerosol indirect effect quantified through airborne remote sensing during VOCALSREx, Atmos. Chem. Phys., 13, 917-931, https://doi.org/10.5194/acp-13-917-2013, 2013.

Pappalardo, G., Amodeo, A., Apituley, A., Comeron, A., Freudenthaler, V., Linne, H., Ansmann, A., Bösenberg, J., D'Amico, G., Mattis, I., Mona, L., Wandinger, U., Amiridis, V., Alados-Arboledas, L., Nicolae, D., and Wiegner, M.: EARLINET: towards an advanced sustainable European aerosol lidar network, Atmos. Meas. Tech., 7, 2389-2409, https://doi.org/10.5194/amt-7-2389-2014, 2014.

Pearce, F.: Geoengineer the Planet? More Scientists Now Say It Must Be an Option, Yale School of the Environment, 19 May 2019, https://e360.yale.edu/features/geoengineer-the-planet-more-scientists-now-say-it-must-be-an-option, 2019.

Penner, J. E., Zhou, C., Liu, X.: Can cirrus cloud seeding be used for geoengineering?. Geophysical Research Letters. 42 (20): 8775-8782. https://doi.org/10.1002/2015GL065992, 2015.

Quaas, J., O. Boucher, N. Bellouin, and S. Kinne: Satellite-based estimate of the direct and indirect aerosol climate forcing, J. Geophys. Res., 113,https://doi.org/10.1029/2007JD008962, 2008.

Quaas, J., O. Boucher, and F. Breon: Aerosol indirect effects in POLDER satellite data and the Laboratoire de Meteorologie Dynamique-Zoom (LMDZ) general circulation model, J. Geophys. Res, 109, https://doi.org/10.1029/2003JD004317, 2004.

Quaas, J., O. Boucher, and U. Lohmann (2006), Constraining the total aerosol indirect effect in the LMDZ and ECHAM4 GCMs using MODIS satellite data, Atmos. Chem. Phys., 6, https://doi.org/10.5194/acp-6-947-2006, 2006.

Quaas, J., Ming, Y., Menon, S., Takemura, T., Wang, M., Penner, J. E., Gettelman, A., Lohmann, U., Bellouin, N., Boucher, O., Sayer, A. M., Thomas, G. E., McComiskey, A., Feingold, G., Hoose, C., Kristjiansson, J. E., Liu, X., Balkanski, Y., Donner, L. J., Ginoux, P. A., Stier, P., Grandey, B., Feichter, J., Sednev, I., Bauer, S. E., Koch, D., Grainger, R. G., Kirkevag, A., Iversen, T., Seland, O , Easter, R., Ghan, S. J., Rasch, P. J., Morrison, H., Lamarque, J.-F., Iacono, M. J., Kinne, S., and Schulz, M.: Aerosol indirect effects - general circulation model intercomparison and evaluation with satellite data, Atmos. Chem. Phys.,9, 8697-8717,https://doi.org/10.5194/acp-9-8697-2009, 2009.

Quaas, J., Arola, A., Cairns, B., Christensen, M., Deneke, H., Ekman, A. M. L., Feingold, G., Fridlind, A., Gryspeerdt, E., Hasekamp, O., Li, Z., Lipponen, A., Ma, P.-L., Mülmenstädt, J., Nenes, A., Penner, J., Rosenfeld, D., Schrödner, R., Sinclair, K., Sourdeval, O., Stier, P., Tesche, M., van Diedenhoven, B., and Wendisch, M.: Constraining the Twomey effect from satellite observations: Issues and perspectives, Atmos. Chem. Phys. Discuss., https://doi.org/10.5194/acp-2020-279, in review, 2020.

Radenz, M., Seifert, P., Baars, H., Floutsi, A. A., Yin, Z., and Bühl, J.: Automated time-height-resolved air mass source attribution for profiling remote sensing applications, Atmos. Chem. Phys., 21, 3015–3033, https://doi.org/10.5194/acp-21-3015-2021, 2021.

Ramachandran, S., Srivastava, R., Kedia, S., and Rajesh, T: Contribution of natural and anthropogenic aerosols to optical properties and radiative effects over an urban location, Environ. Res. Lett. 7 (2012) 034028 (11pp), https://doi.org/10.1088/1748-9326/7/3/034028, 2012.

Regayre, L. A., Johnson, J. S., Yoshioka, M., Pringle, K. J., Sexton, D. M. H., Booth, B. B. B., Lee, L. A., Bellouin, N., and Carslaw, K. S.: Aerosol and physical atmosphere model parameters are both important sources of uncertainty in aerosol ERF, Atmos. Chem. Phys., 18, 9975–10006, https://doi.org/10.5194/acp-18-9975-2018, 2018.

Regayre, L. A., Schmale, J., Johnson, J. S., Tatzelt, C., Baccarini, A., Henning, S., Yoshioka, M., Stratmann, F., Gysel-Beer, M., Grosvenor, D. P., and Carslaw, K. S.: The value of remote marine aerosol measurements for constraining radiative forcing uncertainty, Atmos. Chem. Phys., 20, 10063–10072, https://doi.org/10.5194/acp-20-10063-2020, 2020.

Reutter, P., Su, H., Trentmann, J., Simmel, M., Rose, D., Gunthe, S. S., Wernli, H., Andreae, M. O., and Pöschl, U.: Aerosol- and updraft-limited regimes of cloud droplet formation: influence of particle number, size and hygroscopicity on the activation of cloud condensation nuclei (CCN), Atmos. Chem. Phys., 9, 7067-7080, https://doi.org/10.5194/acp-9-7067-2009, 2009.

Revell, L. E., Kremser, S., Hartery, S., Harvey, M., Mulcahy, J. P., Williams, J., Morgenstern, O., McDonald, A. J., Varma, V., Bird, L., and Schuddeboom, A.: The sensitivity of Southern Ocean aerosols and cloud microphysics to sea spray and sulfate aerosol production in the HadGEM3-GA7.1 chemistry–climate model, Atmos. Chem. Phys., 19, 15447–15466, https://doi.org/10.5194/acp-19-15447-2019, 2019

Robock, A., Marquardt, A., Kravitz, B., Stenchikov, G.: Benefits, risks, and costs of stratospheric geoengineering. Geophys. Res. Lett. 36 (19), L19703, https://doi.org/10.1029/2009GL039209, 2009.

Rosenfeld, D., 1999: TRMM observed first direct evidence of smoke from forest fires inhibiting rainfall. Geophys. Res. Lett., 26, 3105-3108, https://doi.org/10.1029/1999GL006066, 1999.

Rosenfeld, D., Andreae, M., Asmi, A., Chin, M., de Leeuw, G., Donovan, D., Kahn, R., Kinne, S., Kivekäs, N., Kulmala, M., Lau, W., Schmidt, S., Suni, T., Wagner, T., Wild, W., and Quaas, J.: Global observations of aerosol-cloud-precipitationclimate interactions, Rev. Geophys., 52, 750-808, https://doi.org/10.1002/2013RG000441, 2014.

Roy, G., Bissonnette, L., Bastille, C., Vallée, G.: Retrieval of droplet-size density distribution from multiple-field-of-view cross-polarized lidar signals: theory and experimental validation, Applied Opt., 38, 5202-5210, https://doi.org/10.1364/AO.38.005202, 1999.

Salter, S., Sortino, G, Latham, J.: Sea-going hardware for the cloud albedo method of reversing global warming, Philosophical Transactions of the Royal Society of London A: Mathematical, Physical and Engineering Sciences. 366 (1882): 3989-4006. https://doi.org/10.1098/rsta.2008.01360, 2008.

Sasano, Y., Browell, E. V., Ismail, S.: Error caused by using a constant extinction backscattering ratio in the lidar solution, Appl. Opt., 24, http://dx.doi.org/10.1364/AO.24.003929, 1985.

Sassen, K., Petrilla,R.: Lidar depolarization from multiple scattering in marine stratus clouds, Appl. Opt., 25, 1450-1459, https://doi.org/10.1364/AO.25.001450, 1986.

Schmidt, J., Wandinger, U., and Malinka, A.: Dual-field-of-view Raman lidar measurements for the retrieval of cloud microphysical properties, Appl. Optics 52, 2235-2247, https://doi.org/10.1364/AO.52.002235, 2013.

Schmidt, J., Ansmann, A., Bühl, J., Baars, H., Wandinger, U., Müller, D., and Malinka, A. V.: Dual-FOV Raman and Doppler lidar studies of aerosol-cloud interactions: Simultaneous profiling of aerosols, warm-cloud properties, and vertical wind, J. Geophys. Res. Atmos., 119, 5512-5527, https://doi.org/10.1002/2013JD020424, 2014.

Schmidt, Joerg: PhD thesis: Dual-field-of-view Raman lidar measurements of cloud microphysical properties Investigation of aerosol-cloud interactions, University of Leipzig, 2014.

Schmidt, J., Ansmann, A., Bühl, J., and Wandinger, U.: Strong aerosol-cloud interaction in altocumulus during updraft periods: lidar observations over central Europe, Atmos. Chem. Phys., 15, 10687-10700, https://doi.org/10.5194/acp-15-10687-2015, 2015.

Schreier, M., H. Mannstein, V. Eyring, and H. Bovensmann: Global ship track distribution and radiative forcing from 1 year of AATSR data. Geophys. Res. Lett., 34, L17814, https://doi.org/10.1029/2007GL030664, 2007.

Schwartz, S. E., Charlson, R. J., Kahn, R. and Rodhe, H.: Earth's Climate Sensitivity: Apparent Inconsistencies in Recent Assessments, Earth's Future, 2, 601-605, https://doi.org/10.1002/2014EF000273, 2014.

Sekiguchi, M., Nakajima, T., Suzuki, K., Kawamoto, K., Higurashi, A., Rosenfeld, D., Sano, I., and Mukai, S.: A study of the direct and indirect effects of aerosols using global satellite data sets of aerosol and cloud parameters, J. Geophys. Res., 108(D22), 4699, https://doi.org/10.1029/2002JD003359, 2003.

Shinozuka, Y., Clarke, A. D., Nenes, A., Jefferson, A., Wood, R., McNaughton, C. S., Ström, J., Tunved, P., Redemann, J., Thornhill, K. L., Moore, R. H., Lathem, T. L., Lin, J. J., and Yoon, Y. J.: The relationship between cloud condensation nuclei (CCN) concentration and light extinction of dried particles: indications of underlying aerosol processes and implications for satellite-based CCN estimates, Atmos. Chem. Phys., 15, 7585-7604, https://doi.org/10.5194/acp-15-7585-2015, 2015.

Silber, I., A. M. Fridlind, J. Verlinde, L. M. Russell, and A. S. Ackerman: Nonturbulent Liquid-Bearing Polar Clouds: Observed Frequency of Occurrence and Simulated Sensitivity to Gravity Waves, Geophysical Research Letters, 47(10), e2020GL087099, https://doi.org/10.1029/2020gl08709, 2020.

Simpson, E., Connolly, P., and McFiggans, G.: An investigation into the performance of four cloud droplet activation parameterisations. Geoscientific Model Development, 7, 1535-1542, https://doi.org/10.5194/gmd-7-1535-2014, 2014.

Small, J. D., P. Y. Chuang, G. Feingold, and H. Jiang: Can aerosol decrease cloud lifetime?, Geophys. Res. Lett., 36, L16806, https://doi.org/10.1029/2009GL038888, 2009.

Snider, J. R., Guibert, S., Brenguier, J.-L., and Putaud, J.-P.: Aerosol activation in marine stratocumulus clouds: 2. Köhler and parcel theory closure studies, J. of Geophys. Res., 108(D15), 8629, https://doi.org/10.1029/2002JD002692, 2003.

Stein, A.F., Draxler, R.R, Rolph, G.D., Stunder, B.J.B., Cohen, M.D., and Ngan, F.: NOAA's HYSPLIT atmospheric transport and dispersion modeling system, Bull. Amer. Meteor. Soc., 96, 2059-2077, http://dx.doi.org/10.1175/BAMS-D-14-00110.1, 2015.

Stelmaszczyk, K., Dell'Aglio, M., Chudzynski, S., Stacewicz, T., and Wöste, L.: Analytical function for lidar geometrical compression form-factor calculations, Appl. Opt., 44, 1323-1331, https://doi.org/10.1364/AO.44.001323, 2005.

Stevens, B., W. R. Cotton, G. Feingold, and C. Moeng: Large-Eddy Simulations of Strongly Precipitating, Shallow, Stratocumulus-Topped Boundary Layers. J. Atmos. Sci., 55, 3616-3638, https://doi.org/10.1175/1520-0469(1998)055<3616:LESOSP>2.0.CO;2, 1998,

Stevens, B., and Feingold, G.: Untangling aerosol effects on clouds and precipitation in a buffered system, Nature, 461, 607-613, https://doi.org/10.1038/nature08281, 2009.

Storelvmo, T.; Herger, N.: Cirrus cloud susceptibility to the injection of ice nuclei in the upper troposphere, J. of Geophys. Res. Atmos., 119 (5): 2375-2389. https://doi.org/10.1002/2013JD020816, 2014.

Teillet, P. M.: Rayleigh optical depth comparisons from various sources, Appl. Opt., 29,1897-1900, https://doi.org/10.1364/AO.29.001897, 1990.

Tesche, M., Ansmann, A., Müller, D., Althausen, D., Engelmann, R., Freudenthaler, V., and Groß, S.: Vertically resolved separation of dust and smoke over Cape Verde by using multiwavelength Raman and polarization lidars during Saharan Mineral Dust Experiment 2008, J. Geophys. Res.-Atmos., 114, D13202, https://doi.org/10.1029/2009JD011862, 2009.

Twomey, S. A.: The nuclei of natural cloud formation. Part II: The supersaturation in natural clouds and the variation of cloud droplet concentrations, Geofis. Pure Appl, 43, 227-242, https://doi.org/10.1007/BF01993560,1959.

Twomey, S.: Influence of pollution on shortwave albedo of clouds. J. Atmos., Sci., 34, 1149-1152, https://doi.org/10.1175/1520-0469(1977)034<1149:TIOPOT>2.0.CO;2, 1977.

Veselovskii, I., Korenskii, M., Griaznov, V., Whiteman, D., McGill, M., Roy, G., Bissonnette, L.: Information content of data measured with a multiple-field-of-view lidar, Appl. Opt., 45, 6839-6847, https://doi.org/10.1364/AO.45.006839, 2006.

Walters, D., Baran, A. J., Boutle, I., Brooks, M., Earnshaw, P., Edwards, J., Furtado, K., Hill, P., Lock, A., Manners, J., Morcrette, C., Mulcahy, J., Sanchez, C., Smith, C., Stratton, R., Tennant, W., Tomassini, L., Van Weverberg, K., Vosper, S., Willett, M., Browse, J., Bushell, A., Carslaw, K., Dalvi, M., Essery, R., Gedney, N., Hardiman, S., Johnson, B., Johnson, C., Jones, A., Jones, C., Mann, G., Milton, S., Rumbold, H., Sellar, A., Ujiie, M., Whitall, M., Williams, K., and Zerroukat, M.: The Met Office Unified Model Global Atmosphere 7.0/7.1 and JULES Global Land 7.0 configurations, Geosci. Model Dev., 12, 1909–1963, https://doi.org/10.5194/gmd-12-1909-2019, 2019.

Wandinger, U.: Multiple-scattering influence on extinction- and backscatter-coefficient measurements with Raman and high-spectral-resolution lidars, Appl. Opt. 37, 417-427, https://doi.org/10.1364/AO.37.000417,1998.

Wandinger, U., and Ansmann, A.: Experimental determination of the lidar overlap profile with Raman lidar. Appl. Opt., Vol. 41, Issue 3, 511-514, https://doi.org/10.1364/AO.41.000511, 2002.

Wandinger, U.: Introduction to lidar, in Lidar Range-Resolved Optical Remote Sensing of the Atmosphere, edited by C. Weitkamp, pp. 1-18, Springer, Berlin/Heidelberg, https://doi.org/10.1007/0-387-25101-4_1, 2005.

Wang, M. and Penner, J. E.: Aerosol indirect forcing in a global model with particle nucleation, Atmos. Chem. Phys., 9, 239–260, https://doi.org/10.5194/acp-9-239-2009, 2009.

Wang, H., Dai, T., Zhao, M., Goto, D., Bao, Q., Takemura, T., Nakajima, T., Shi, G.:Aerosol Effective Radiative Forcing in the Aerosol Coupled CAS-FGOALS-f3-L Climate Model, MDPI Atmosphere, 11, 1115, https://doi.org/10.3390/atmos11101115, 2020.

Werner, F., Ditas, F., Siebert, H., Simmel, M., Wehner, B., Pilewskie, P., Schmeissner, T., Shaw, R. A., Hartmann, S., Wex, H., Roberts, G. C., and Wendisch, M.: Twomey effect observed from collocated microphysical and remote sensing measurements over shallow cumulus, J. Geophys. Res.-Atmos., 119, 1534-1545, https://doi.org/10.1002/2013JD020131, 2014.

WHO: Guidelines for Air Quality, World Health Organization, Geneva, https://apps.who.int/iris/handle/10665/66537, 1999.

Wild, M., Folini, D., Schär, C., Loeb, N., Dutton, E., König-Langlo, G.: The global energy balance from a surface perspective, Clim Dyn 40, 3107-3134, https://doi.org/10.1007/s00382-012-1569-8, 2013

Wang, M., Peng, Y., Liu, Y., Liu, Yu, Xie, X., and Guo, Z.: Understanding cloud droplet spectral dispersion effect using empirical and semi?analytical parameterizations in NCAR CAM5.3, Earth and Space Science, 7, 2020EA001276. https://doi.org/10.1029/2020EA001276, 2020.

Westervelt, D. M., Pierce, J. R., and Adams, P. J.: Analysis of feedbacks between nucleation rate, survival probability and cloud condensation nuclei formation, Atmos. Chem. Phys., 14, 5577–5597, https://doi.org/10.5194/acp-14-5577-2014, 2014.

Weitkamp, K.: Range-Resolved Optical Remote Sensing of the Atmosphere, Springer-Verlag New York, 102, 241-303, https://doi.org/10.1007/b106786, 2005.

Wiesen, R.: Master thesis: Implementation and Test of the Dual-Field-of-View Depolarization Method into Polly XT, University of Leipzig, 2020.

Yin, Z., Ansmann, A., Baars, H., Seifert, P., Engelmann, R., Radenz, M., Jimenez, C., Herzog, A., Ohneiser, K., Hanbuch, K., Blarel, L., Goloub, P., Dubois, G., Victori, S., and Maupin, F.: Aerosol measurements with a shipborne Sun-sky-lunar photometer and collocated multiwavelength Raman polarization lidar over the Atlantic Ocean, Atmos. Meas. Tech., 12, 5685–5698, https://doi.org/10.5194/amt-12-5685-2019, 2019.

Young., A. T.:On the Rayleigh-Scattering Optical Depth of the Atmosphere, Journal of Applied Meteorology, 20, 3, 328-330, https://www.jstor.org/stable/26179545, 1981

Zege, E., Katsev, I., Polonsky, I.: Analytical solution to LIDAR return signals from clouds with regard to multiple scattering, Appl Phys B, 60, 345-353, https://doi.org/10.1007/BF01082270, 1995.

Zege, E., Chaikovskaya, L.: Polarization of multiple-scattered lidar return from clouds and ocean water, JOSA A, 16, 1430-1438, https://doi.org/10.1364/JOSAA.16.001430, 1999.

Zelinka, M. D., Andrews, T., Forster, P., and Taylor, K.: Quantifying components of aerosol-cloud-radiation interactions in climate models, J. Geophys. Res. Atmos., 119, 7599–7615, https://doi.org/10.1002/2014JD021710, 2014.

Zhang, Y., Fan, J., Li, Z., and Rosenfeld, D.: Impacts of cloud microphysics parameterizations on simulated aerosol-cloud interactions for deep convective clouds over Houston, Atmos. Chem. Phys., 21, 2363–2381, https://doi.org/10.5194/acp-21-2363-2021, 2021.

Zheng, X., Albrecht, B., Jonsson, H. H., Khelif, D., Feingold, G., Minnis, P., Ayers, K., Chuang, P., Donaher, S., Rossiter, D., Ghate, V., Ruiz-Plancarte, J., and Sun-Mack, S.: Observations of the boundary layer, cloud, and aerosol variability in the southeast Pacific near-coastal marine stratocumulus during VOCALS-REx, Atmos. Chem. Phys., 11, 9943-9959, https://doi.org/10.5194/acp-11-9943-2011, 2011.

Zheng, X., Xi, B., Dong, X., Logan, T., Wang, Y., and Wu, P.: Investigation of aerosol-cloud interactions under different absorptive aerosol regimes using Atmospheric Radiation Measurement (ARM) southern Great Plains (SGP) ground-based measurements, Atmos. Chem. Phys., 20, 3483-3501, https://doi.org/10.5194/acp-20-3483-2020, 2020.

Acknowledgements

I would like to thank to the German Academic Exchange Service (DAAD) and to the Chilean Science corporation (Conicyt) for their financial support given to me for doing my PhD. I would also thank to the HDCP2 and Excelsior projects for their financial support. I would like to thank to Prof. Johannes Quaas, Prof. Andreas Macke and Prof. Alfred Wiedensholer for taking care of the evaluation of the thesis. I also thank to the eight anonymous referees for the three publications of the cumulative part.

In the following, I would like to express my gratitude to those who took part in my life on my way to start and finish my PhD.

Firstly, I would like to thank to Albert Ansmann. This work would have not been possible without his support and outstanding guidance. His strong commitment and self criticism when exploring new ideas inspired me all these years. He helped me to grow no only as scientist but as a person as well.

I am deeply grateful to Ulla Wandinger for her excellent advice with the structure and content of the thesis. Her sharp eye when proofreading really improved the text and also my English writing skills. I would like to thank to Jörg Schmidt for introducing me into the research field and patiently teaching me about the DFOV technique and to operate and maintain the MARTHA lidar complex. I am also very thankful to Patric Seifert for sharing his knowledge about aerosol and clouds, for his suggestions, and encouraging words whenever there was an opportunity. I would like to thank to Ronny Engelmann for your ideas and assistance when tacking experimental problems. I also thank to Cornelia Kurze and Karsten Handbuch for their technical help during these years. A big thank to Holger Baars for his comments and suggestions regarding the inversion of lidar signals. I also thank to Johannes Bühl, Dietrich Althausen, Birgit Heese and Annett Skupin for all the fruitfully talks during coffe breaks and lunch times. I deepply thank to Heike Kalesse-Los for your advice, for the yoga sessions, and experiences in conferences and campaigns. I would like to thank to the administration team of TROPOS, especially to Kathrin Hoffmann for always giving me a hand in such a kind way.

I am deeply thankful to Moritz Haarig and Julian Hofer for been an incredible holding up during all this years. Thank you for attending all my questions. I would also like to thank to my fellow PhD students of TROPOS, to Martin Radenz, Zhenping Yin, Audrey Teiseire, Athena Floutsi, Hannes Griesche, Guangyao Dai and Majid Hajipour, and from LIM, to

Teresa Vögel and Willy Schimmel. Being surrounded by such great people encouraged me to work hard for making good science. I am very thankful to Robert Wiesen for the long discussions we had about multiple topics related to this research project. I also thank to Lea Kokott, who helped during the data analysis of Dushanbe and Leipzig. I would also thank to the people that took care of the field site in Punta Arenas and in Dushanbe, to Raúl, Ismael, and Abduvosik.

My sincere gratitude to the many scientists for the shared thoughts and discussions during conferences and seminaries. A big thank to Boris Barja, Eduardo Landulfo, Juan Bravo-Aranda, Carmen Córdoba, Dave Turner, Ilya Serikov, Jens Reichardt, Nikolaos Siomos, and to the people from the EARLINET and LALINET communities. I am specially grateful to David Donovan and Aleksey Malinka for sharing their knowledge and experience with me. They really helped me understand the tricky parts of lidar multiple scattering. I also express my gratitude to Olaf Hellmuth for his explanations and suggestions about retrieval schemes. They were of great help. I would like thank to Elena Montilla-Rosero, who taught me the basics about aerosol and lidar and guide me during my Master thesis. She was an incredible support when seeking for a PhD position. I also thank to Antonieta Silva, from whom I learn a lot during our time at the lidar observatory in Concepción.

I am deeply grateful to Friederike Merkel, for her unconditional love, understanding, support and all the sacrifices she made in the last years for me to finish my thesis. I also thank to her family Beatrix, Clara, Almuth, and Hubert for being a fundamental pillar for me in all these years living in Germany.

This work would have not been possible without the affection of my friends and family. I would like to thank to Nicolas González and to Gustavo Rubio, my comrades and friends. Our esperiences and long talks about all kind of topics really feed my curiosity and love for doing science. I also thank to my fellow physics students in Concepcion, to José Vargas, Alvaro Cuevas, Darwin Nahuelpán, Miguel Campos, Robinson Gómez, Marta Ebner, Romina Ahumada, Jorge Fuenzalida, Evelyn Acuña, Ariana Muñoz, and Diana Hidalgo. I am very happy about the nice bond we still have after we parted ways. I am deeply thankful to my friends from Bulnes, Chillán and Concepción, to my mates in the "Casa Estudio", specially to Alexis Gajardo, Guillermo Yeber, Carlos Gutiérrez, Camilo Manríquez, Fernando Roa, and Maria Elena Celedon. Also a big thank to my school gang "The Charizards", to Eduardo Campos, Guillermo Bernales, Angelo Ríos, Jaime Varas, Jorge Palma and Johnatan Labrin. I also thank to my friends in Leipzig, to Cecilia Barrios, Naiya Viveros, Sarah Skölziger, Adrian Lange, Daniel & Annika Steinbach, Sarvenatz Safari, Sebastian Los, Dorothea Faßlrinner and Niklas spiegel. I also thank to Stefanie Feuerstein and Stephan Braig for being such a great company and support during these years.

I am grateful to my mom Claudia Jimenez Torres who have always been there, for her caring and sacrifices for my to grow and study. I also thank my aunts Silvia, Miriam, Virginia, Margarita and Patricia, an to my uncle John. They helped me in many occasions during my life. I thank to my brothers Ramón Troncoso and Javier Zapata and to all my cousins for always being there for me, specially to Luis, Patricio and Yovania. I am very grateful to my

dear grandma Herminia Torres, who worked a lifetime to raise her nine children and latter to help her many grand children. She supported me financially for my education. She didn't got to know that I pursue a PhD abroad in Germany and would start a family there. I thank to my dear brother Esteban Rebolledo Jiménez whose life and and early disease made me the person I am today.